



HAL
open science

Plasticity mechanisms in CoCrFeMnNi alloy : an in situ TEM approach

Daniela Oliveros

► **To cite this version:**

Daniela Oliveros. Plasticity mechanisms in CoCrFeMnNi alloy : an in situ TEM approach. Material chemistry. Université Paul Sabatier - Toulouse III, 2022. English. NNT : 2022TOU30143 . tel-03865180

HAL Id: tel-03865180

<https://theses.hal.science/tel-03865180>

Submitted on 22 Nov 2022

HAL is a multi-disciplinary open access archive for the deposit and dissemination of scientific research documents, whether they are published or not. The documents may come from teaching and research institutions in France or abroad, or from public or private research centers.

L'archive ouverte pluridisciplinaire **HAL**, est destinée au dépôt et à la diffusion de documents scientifiques de niveau recherche, publiés ou non, émanant des établissements d'enseignement et de recherche français ou étrangers, des laboratoires publics ou privés.



THÈSE

En vue de l'obtention du
DOCTORAT DE L'UNIVERSITÉ DE TOULOUSE
Délivré par l'Université Toulouse 3 - Paul Sabatier

Présentée et soutenue par
Daniela OLIVEROS

Le 21 juillet 2022

Mécanismes de plasticité dans l'alliage CoCrFeMnNi :
Une étude *in situ* MET

Ecole doctorale : **SDM - SCIENCES DE LA MATIÈRE - Toulouse**

Spécialité : **Physique de la Matière**

Unité de recherche :

CEMES - Centre d'Elaboration de Matériaux et d'Etudes Structurales

Thèse dirigée par
Marc LEGROS

Jury

M. Jean-Philippe COUZINIE, Rapporteur
M. Philippe CASTANY, Rapporteur
Mme Dominique POQUILLON, Examinatrice
Mme Mayerling MARTINEZ, Examinatrice
M. Marc LEGROS, Directeur de thèse

To You

“Adventures are never fun while you’re having them.”

— C.S. Lewis, *The Voyage of the Dawn Treader*.

Acknowledgements

I would like to start this section by thanking profusely my thesis supervisor, Marc Legros, for his work, his help, his trust in me and specially for his patience. You taught me many things, Marc, and I will be forever grateful.

I would also like to thank Stefan Sandfeld for his trust and amicable discussions as head of the MuDiLingo project, and the rest of the team in Germany (especially to Chen, Hengxu and Kishan) for their help, discussions and good meeting times.

A special thanking to Philippe Castany and Jean-Philippe Couzinié for accepting the referee roles of this manuscript, and Dominique Poquillon and Mayerling Martinez for accepting to be the examiners. You were a super jury and I thank you for the rich and helpful discussions.

My time in CEMES was filled with great discussions with great people, especially during the writing of this manuscript, and I would like to highlight my thanking to Daniel Caillard, Joël Douin, Frédéric Mompiau, Muriel Hantcherli and the rest of the PPM team. A bigger thanking to my friend Camille Thenot for the discussion that led to the writing of Chapter 4.

I also wish to thank Anna Fraczkievicz and Antonin Dlouhy for providing the specimens, and the Sample Preparation, Microscopy and Informatics Services of CEMES for their help and work.

Thanks to the doctorate students and post-doctorates for the nice and amicable lunch and coffee times: Romain for sharing the office and good times with me, Camille, Ségolène, Mia and Silvia for all the girl's nights, friendship and support, the rest of my PPM colleagues turned dear friends: Nico, Liz, Melvyn, Malo, Benoît, Rachma, Clémence. You were all an integral part of my journey. Thank you for sharing this adventure with me.

Thanks to my friends and family, all over the world, for their support. Special thanking to my parents, who raised me to be who I am. I would not be here without you and your love.

And finally, a big thanking to the love of my life, my husband Daniel. This is as much your accomplishment as it is mine. You have always been my rock. Thank you. I love you.

Glossary of terms and symbols

3D	Three-dimensional
APT	Atom-probe tomography
B	Bulk modulus
\vec{b}	Burgers vector
bcc	Body-centred cubic
BF	Bright field image
CAC	Concurrent atomistic-continuum method
CBED	Convergent beam electron diffraction
CCA	Complex concentrated alloy
CRSS	Critical resolved shear stress
CSSA	Concentrated solid solution alloy
DAPB	Diffuse-anti-phase boundary
DD	Dissociated dislocation
DF	Dark field image
DFT	Density functional theory
DIC	Digital image correlation
DP	Diffraction pattern
E	Young's modulus
EAM	Embedded-atom method model
EBSD	Electron backscatter diffraction
EELS	Electron energy loss spectrometry
EFTEM	Energy filtered transmission electron microscopy
ESF	Extrinsic stacking fault
fcc	Face-centred cubic
FF	Friedel-Fleischer strong pinning model
G	Shear modulus
\vec{g}	Beam direction vector / imaging vector
HAAD	High-angle annular dark-field
hcp	Hexagonal close-packed
HEA	High entropy alloy
HRTEM	High resolution transmission electron microscopy
IM	Intermetallic
ISF	Intrinsic stacking fault
LAC	Local atomic configuration
LAL	Local atomic landscape
LCO	Local chemical order
LCF	Local chemical fluctuation
LN₂T	Liquid nitrogen (cryogenic) temperature
LS	Left side of the specimen's hole
μ	Shear modulus

MC	Monte Carlo simulation
MD	Molecular dynamics simulation
ML	Mott-Labusch weak pinning model
MPEA	Multi-principal element alloy
NSD	Nanoscale segment detrapping
P	Perfect dislocation
PD	Partial dislocation
PP	Pinning point
RS	Right side of the specimen's hole
RT	Room temperature
SEM	Scanning electron microscopy
SF	Stacking fault
SFE	Stacking fault energy
SRC	Short-range clustering
SRO	Short range order
SS	Solid solution
SSS	Solid solution strengthening theory
ST	Slip trace
STEM	Scanning transmission electron microscopy
T	Twinning
TEM	Transmission electron microscopy
TRIP	Transformation induced plasticity
TWIP	Twinning induce plasticity
XRD	X-ray diffraction
ν	Poisson's ratio
σ	Strength
σ_{UTS}	Ultimate yield strength
σ_Y	Yield strength
τ	Critical resolved shear stress

Table of Contents

Chapter 1 – THEORETICAL BACKGROUND AND STATE OF THE ART	1
1. Introduction.....	1
2. High Entropy Alloys.....	6
2.1. Brief history of high entropy alloys	6
2.2. Definitions	8
2.3. “Four core effects” that affect HEA microstructure and properties.....	10
2.4. Classification and properties of HEAs	12
2.4.1. Classification of HEAs	12
2.4.2. Properties of HEAs.....	15
2.5. HEA metallurgy and deformation mechanisms	19
2.5.1. Compositional effect	20
2.5.2. Defects and strengthening mechanisms.....	23
2.5.3. Deformation mechanisms.....	24
3. Plasticity in metals.....	31
3.1. Dislocation slip.....	32
3.2. Dislocations behaviour in crystals	34
3.3. Twinning.....	37
4. Cantor Alloy	40
4.1. Definition and microstructure	40
4.2. Mechanical properties of Cantor alloy	42
4.2.1. Dislocation behaviour of Cantor alloy.....	45
4.2.2. Mechanical twinning.....	48
4.2.3. Stacking fault energy and short range order in CoCrFeMnNi.....	53
5. Motivations: MuDiLingo project.....	56
6. References.....	56
Chapter 2 – EXPERIMENTAL METHODOLOGY AND RESULTS	62
1. Specimens	62
2. Experimental procedure	63
2.1. Set-up.....	63
2.2. Electronic diffraction.....	66
2.2.1. Reciprocal lattice.....	70

2.2.2. Diffraction patterns in TEM.....	73
2.3. Imaging in a TEM.....	76
2.4. Crystal orientation determination	77
3. Direct results from <i>in situ</i> TEM straining experiments.....	84
3.1. Indexing dislocations.....	84
3.2. Observation of stacking faults vs. twinning.....	87
3.3. Thickness determination	90
4. Conclusions.....	94
5. Bibliography	95
Chapter 3 – PLASTICITY MECHANISMS IN THE CoCrFeMnNi ALLOY	97
1. Critical resolved shear stress (CRSS) calculation.....	98
2. Dislocation behaviour: comparing the same specimen at two temperatures	105
2.1. Mechanism activation.....	105
2.2. Critical Resolved Shear Stress	109
2.3. Dislocation movement.....	110
3. Dislocation behaviour at room temperature	110
3.1. Planar glide of perfect dislocations	110
3.1.1. Dissociation of perfect dislocations and SFE determination	111
3.1.2. Cross-slip	116
3.2. Twinning	125
4. At cryogenic temperatures	130
4.1. Planar glide of perfect dislocations	130
4.1.1. Dissociation of perfect dislocations and SFE determination	131
4.1.2. Cross-slip	132
4.2. Twinning	137
5. Conclusions.....	142
6. Bibliography	143
Chapter 4 – DISLOCATION MOVEMENT IN THE LOCAL ATOMIC LANDSCAPE.....	146
1. Dislocation movement.....	146
2. Obstacles	156

3. Pairs of perfect dislocations	169
4. Conclusions	175
5. Bibliography	176
Chapter 5 – GENERAL CONCLUSIONS AND PERSPECTIVES.....	180
1. Conclusions	180
2. Perspectives	182
Appendix 1 – Supplementary videos.....	185
Appendix 2 – Critical resolved shear stress calculation.....	188
Appendix 3 – Shape of a dislocation loop	193
Appendix 4 – Stacking fault characterisation	196
Appendix 5 – Abstract – English.....	198
Appendix 6 – Abstract – Français	199
Appendix 7 – Résumé de la thèse en Français	200

Table of Figures

Figure 1-1..... 2
Figure 1-2..... 3
Figure 1-3..... 4
Figure 1-4..... 8
Figure 1-5..... 9
Figure 1-6..... 10
Figure 1-7..... 13
Figure 1-8..... 17
Figure 1-9..... 18
Figure 1-10..... 19
Figure 1-11..... 20
Figure 1-12..... 21
Figure 1-13..... 22
Figure 1-14..... 22
Figure 1-15..... 24
Figure 1-16..... 26
Figure 1-17..... 26
Figure 1-18..... 28
Figure 1-19..... 29
Figure 1-20..... 29
Figure 1-21..... 30
Figure 1-22..... 32
Figure 1-23..... 32
Figure 1-24..... 33
Figure 1-25..... 35
Figure 1-26..... 35
Figure 1-27..... 36
Figure 1-28..... 37
Figure 1-29..... 38
Figure 1-30..... 38
Figure 1-31..... 39
Figure 1-32..... 40
Figure 1-33..... 43
Figure 1-34..... 43
Figure 1-35..... 43
Figure 1-36..... 44
Figure 1-37..... 47
Figure 1-38..... 48
Figure 1-39..... 48
Figure 1-40..... 49
Figure 1-41..... 50

Figure 1-42	51
Figure 1-43	52
Figure 1-44	53
Figure 1-45	54
Figure 1-46	54
Figure 1-47	55
Figure 2-1	63
Figure 2-2	64
Figure 2-3	65
Figure 2-4	67
Figure 2-5	67
Figure 2-6	68
Figure 2-7	69
Figure 2-8	71
Figure 2-9	72
Figure 2-10	72
Figure 2-11	73
Figure 2-12	74
Figure 2-13	75
Figure 2-14	77
Figure 2-15	78
Figure 2-16	78
Figure 2-17	80
Figure 2-18	80
Figure 2-19	82
Figure 2-20	83
Figure 2-21	84
Figure 2-22	85
Figure 2-23	86
Figure 2-24	87
Figure 2-25	88
Figure 2-26	89
Figure 2-27	89
Figure 2-28	92
Figure 2-29	93
Figure 2-30	94
Figure 3-1	99
Figure 3-2	100
Figure 3-3	101
Figure 3-4	101
Figure 3-5	102
Figure 3-6	104
Figure 3-7	106

Figure 3-8.....	107
Figure 3-9.....	108
Figure 3-10.....	108
Figure 3-11.....	109
Figure 3-12.....	110
Figure 3-13.....	112
Figure 3-14.....	114
Figure 3-15.....	115
Figure 3-16.....	116
Figure 3-17.....	117
Figure 3-18.....	118
Figure 3-19.....	119
Figure 3-20.....	120
Figure 3-21.....	121
Figure 3-22.....	122
Figure 3-23.....	123
Figure 3-24.....	124
Figure 3-25.....	126
Figure 3-26.....	127
Figure 3-27.....	128
Figure 3-28.....	131
Figure 3-29.....	132
Figure 3-30.....	133
Figure 3-31.....	134
Figure 3-32.....	134
Figure 3-33.....	135
Figure 3-34.....	136
Figure 3-35.....	137
Figure 3-36.....	138
Figure 3-37.....	139
Figure 3-38.....	141
Figure 4-1.....	149
Figure 4-2.....	150
Figure 4-3.....	152
Figure 4-4.....	155
Figure 4-5.....	155
Figure 4-6.....	156
Figure 4-7.....	157
Figure 4-8.....	158
Figure 4-9.....	159
Figure 4-10.....	161
Figure 4-11.....	162
Figure 4-12.....	163

Figure 4-13 165
Figure 4-14 166
Figure 4-15 167
Figure 4-16 168
Figure 4-17 169
Figure 4-18 170
Figure 4-19 171
Figure 4-20 172
Figure 4-21 173
Figure 4-22 175

Table of Equations

Equation 1-1	5
Equation 1-2	7
Equation 1-3	9
Equation 1-4	9
Equation 1-5	9
Equation 1-6	32
Equation 1-7	33
Equation 1-8	34
Equation 1-9	36
Equation 1-10	36
Equation 1-11	36
Equation 1-12	46
Equation 1-13	48
Equation 2-1	67
Equation 2-2	68
Equation 2-3	68
Equation 2-4	69
Equation 2-5	70
Equation 2-6	70
Equation 2-7	71
Equation 2-8	74
Equation 2-9	74
Equation 2-10	91
Equation 3-1	98
Equation 3-2	102
Equation 3-3	113
Equation 3-4	113
Equation 4-1	158
Equation 4-2	158
Equation 4-3	173

Table of Tables

Table 2-1	62
Table 2-2	75
Table 2-3	76
Table 2-4	81
Table 3-1	99
Table 3-2	102
Table 3-3	103
Table 3-4	103
Table 3-5	110
Table 3-6	115
Table 3-7	120
Table 3-8	125
Table 3-9	129
Table 3-10	131
Table 3-11	140
Table 4-1	147
Table 4-2	159
Table 4-3	174

Chapter 1

THEORETICAL BACKGROUND AND STATE OF THE ART

To characterize the elementary mechanisms for plasticity in CoCrFeMnNi high entropy alloy (HEA) using the *in situ* TEM straining technique, some basic definitions on plasticity and on high entropy alloys are needed. These will be given in this chapter. The *in situ* TEM straining technique will be explained in the next chapter, along with sample preparation and experimental set-up and procedures. Then, chapter 3 will explain the analysis and key results issued from these experiments, as well as the discussion and perspectives derived from them.

This chapter, through the following sections, will set the common thread of this study, starting by describing the current understanding of alloy design and the steps that led to it, by the development of multi-principal element alloys (MPEA), and the vast world of research opportunities it opened. Then, basic concepts on elementary plasticity will be given (dislocation behaviour and twinning), to, at last, introduce the reader to CoCrFeMnNi (the alloy of this study) and the current status of the research works on its deformation mechanisms. This common thread will be constructed in blocks that will allow the introduction, in subsequent chapters, of the experimental work carried on to explain the elementary mechanisms in the studied alloy.

1. Introduction

Understanding the properties of metals, specially their mechanical properties, has led to the development of metallurgy: the study of metals and its alloys (the combination of elements, of which at least one is a metal), how they behave, their properties and how they affect their performance.

The properties of a given material are determined by its structure ^[1] – atomic arrangement (crystal structure), microstructure and macrostructure. They can change based on temperature and external factors. How a material responds to an applied force defines its mechanical properties: strength, ductility, toughness, fatigue resistance, hardness. Under this applied force, the response of the material at crystalline scale can be the deformation of the crystal lattice (the three-dimensional grid formed by the periodic array of atoms) ^[2]. This leads to permanent changes in the crystal solid, called plasticity.

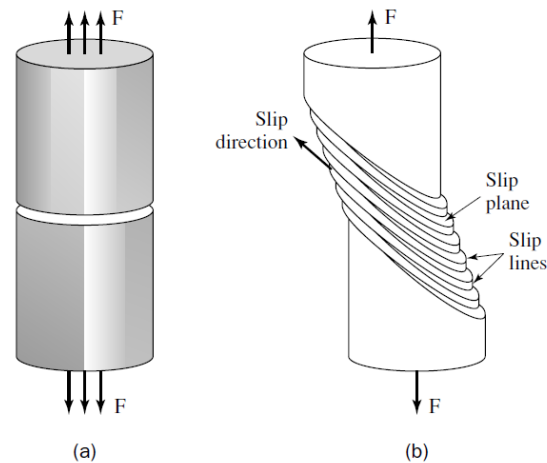


Figure 1-1 – Schematic representation of two mechanisms by which a single crystal is assumed to be stretched when applying a force F : (a) breaking interatomic bonds and (b) considering slip.

From [2].

The adjective *plastic* is a derivative of the Greek noun *Plastikós* (πλαστικός), which means to shape or to form: a material that can have its shape easily changed by the application of appropriately directed forces, and retain its new shape and properties upon removal of such forces [3]. Plasticity in a metallic crystal is primarily caused by two modes of deformation: slip and twinning.

Slip is a process that occurs along specific lattice planes, as depicted in Figure 1-1, where shear deformation moves the atoms through many interatomic distances relative to their initial positions [2]. This movement occurs because the imperfections in the crystal, called dislocations, move under an applied stress [4].

A twin is a defect in the stacking sequence (Figure 1-2), usually of close-packed atomic planes, formed during the growth/heating of a material (annealing twins) or by application of a force onto the crystal (deformation twins) [2]. Such a defect can indeed be created by the movement of partial dislocations on adjacent planes.

Both deformation mechanisms have the same phenomenon at their core: dislocations, a concept that will be further explained in this chapter. Plasticity in metallic alloys, including novel alloys, as the so-called high entropy alloys (HEA), can be described in terms of the operation of atomistic processes and, according to Ashby and Frost [5,6], can be divided as follows:

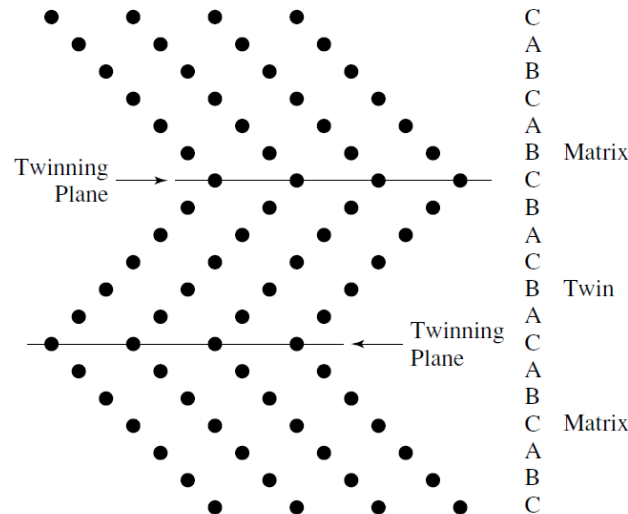


Figure 1-2 – Twin in an fcc metal. The matrix and the twin match at the interface, called twinning plane. The figure shows a $(1\bar{1}0)$ plane normal to the (111) twin plane. From [2].

- Defect-less flow (flow when the ideal shear strength is exceeded).
- Flow by dislocation glide alone (responsible for the yielding of most laboratory and engineering materials). It can happen:
 - Limited by a lattice resistance (Peierls stress).
 - Limited by discrete obstacles.
 - Limited by phonon or other drag.
 - Twinning.
- Flow involving dislocation climb (above $0.3 T_M$ (melting point of a material)). It can be:
 - Glide plus lattice-diffusion controlled climb ("high temperature creep"): generally, occurs above $0.6 T_M$.
 - Glide plus core-diffusion controlled climb ("low temperature creep"): generally occurs at $T < 0.3 T_M$ and at stresses often below the macroscopic yield stress ($\sigma_y^{0.002}$) [7].
- Harper-Dorn creep: occurs under conditions in which the dislocation density does not change with stress.
- Power-law breakdown: it is a transition from the climb-controlled power-law creep to glide-controlled flow which varies exponentially with stress [6].
- Diffusional flow (involving the motion of single ions only): it leads to the Newtonian-viscous creep of a polycrystal, and can be:
 - Lattice-diffusion controlled flow (Nabarro-Herring creep).
 - Grain-boundary-diffusion controlled flow (Coble creep).
 - Interface-reaction controlled diffusional flow.

These mechanisms are summarised for each material in a deformation-mechanism map [5,6], where the temperature ranges for each mechanism is signalled (as well as the shear

stress and strain rate) . An example of such maps is given in Figure 1-3 for pure nickel. In this figure, it is clearly shown that the mechanisms active for the temperature range of this study (between around -175°C and around $+23^{\circ}\text{C}$) are dislocation glide and twinning (not shown in this map [6]). Therefore, this study will only concentrate on the latter two mechanisms without taking the others into consideration.

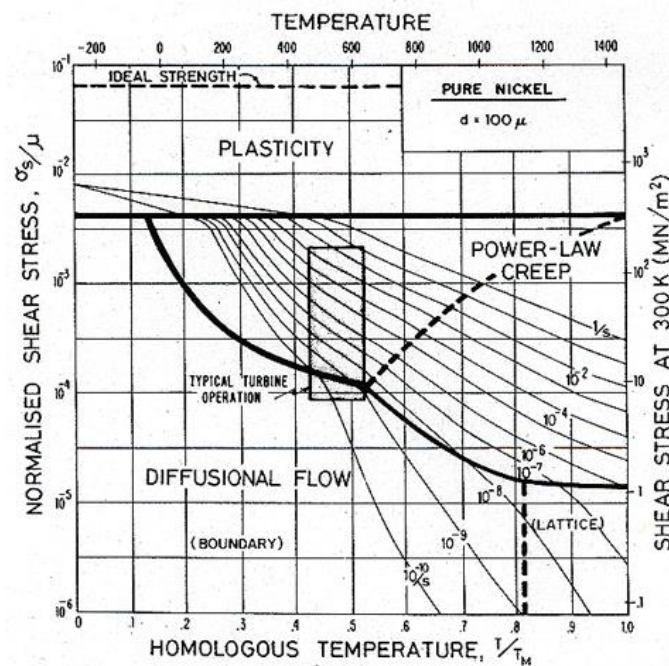


Figure 1-3 – A deformation-mechanism map for pure nickel (of grain size $10\ \mu\text{m}$ and $1\ \text{mm}$). From [6].

A conventional metallic alloy may be a solid solution (a single phase, where all metallic grains are made of the same composition) or a mixture of metallic phases (two or more solutions, forming a microstructure of different crystals within the metal). In contrast, high entropy alloys are multi-element solid solution alloys with no primary solvent metal [8]. They can be defined either by their composition or by their entropy:

Composition-based definition: Yeh et al. defined them to be alloys with “at least five principal elements, each of which has an atomic concentration between 5% and 35%” [9–11]. They can also contain minor elements to modify or enhance the properties of the base alloy [12].

Entropy-based definition: in multiple-element alloys, the configurational entropy (S^{SS}) is maximized when there is an equal atomic proportion of each element [10] and should assist the formation of solid solution (SS) phases over intermetallic (IM) [10,13], since it is claimed to dominate over vibrational, electronic and magnetic terms, hence motivating the separation of low, medium and high entropy alloys:

- Low entropy: $S^{SS,ideal} < 0.69R$
- Medium entropy: $0.069R < S^{SS,ideal} < 1.61R$
- High entropy: $S^{SS,ideal} > 1.61R$

where R is the gas constant and $S^{SS,ideal}$ is the total configurational molar entropy in an ideal SS [12].

The entropy increases as the number of elements increases. From Richards' rule, $\frac{\Delta H_f}{T_m} = \Delta S_f \sim R$; the entropy change per mole, ΔS_f , from solid to liquid during melting is about one gas constant R , and the enthalpy change or latent heat per mole, ΔH_f , can be estimated as RT_m , where T_m is the melting point [14].

Murty et al. [14] also point out that, from the bond number difference in the solid and liquid states (or a regular solid solution state), ΔH_f can be regarded as the energy required to destroy about one-twelfth of all bonds in the close-packed solid of one mole; the mixing entropy of R per mole in random solid solution is large to lower its mixing free energy, ΔG^{mix} , by the amount of RT , since $\Delta G^{mix} = \Delta H^{mix} - T\Delta S^{mix}$. Thus, the free energy lowering causes the solid solution phases to have a greater ability to compete with intermetallic compounds, which usually have much lower ΔS_{conf} due to their ordered nature.

The mixing enthalpy, ΔH^{mix} , can be calculated (from [15-17]) as

$$\Delta H^{mix} = 4 \sum_{i=1, j \neq i}^n \Delta H_{(i,j)}^{mix} X_i X_j + \sum_k \Delta H_k^{trans} X_k$$

Equation 1-1 – Mixing enthalpy in a solid solution.

where X_k is the mole fraction of non-metallic element k in the system and $\Delta H_{(i,j)}^{mix}$ is the mixing enthalpy per mole of an equiatomic i - j alloy in the solid state [14].

In the solid state of an alloy, the equilibrium state is the one having the lowest free energy of mixing according to the second law of thermodynamics. There are three possible categories of competing states: elemental phases (the terminal solid solution based on one metal element), intermetallic compounds (a stoichiometric compound having specific superlattices), and solid solution phases (the phase with the complete mixing or significant mixing of all elements in the structure of bcc – body-centred cubic, fcc – face-centred cubic or hcp – hexagonal close-packed) below the lowest melting point of the alloy [18].

However, most high entropy alloys found on the literature contain more than one phase, because configurational entropy cannot usually overcome enthalpy and non-configurational entropy ^[19]. These definitions will be further discussed in the following section.

Murty et al. ^[14] give details that to reveal the high-entropy effect, which enhances the formation of solid solution phases and inhibits the formation of intermetallic compounds, one needs to consider a HEA composed of those constituent elements with stronger bonding between each other. For simplicity, they suggest to neglect the strain energy contribution (due to atomic size difference) to mixing enthalpy. They continue explaining:

Elemental phases have small negative ΔH^{mix} and ΔS^{mix} because they are based on one major element; compound phases have large negative ΔH^{mix} but small ΔS^{mix} because ordered structures have small configurational entropy; and random solid solution phases containing multicomponents have medium negative ΔH^{mix} and highest ΔS^{mix} , because there exist a proportion of unlike atomic pairs in solution phases. That means the mixing enthalpy in the random solution state is half that of the completely ordered state. Assuming that all heats of mixing for unlike atomic pairs are the same, ΔH^{mix} of the random solution state for quinary equiatomic alloy is 4/5 of that of its completely ordered state. Similarly, for septenary equiatomic alloy, the ratio is 6/7. Therefore, a higher number of elements would allow the random solution state to have the mixing enthalpy much closer to that of the completely ordered state. With the aid of its high mixing entropy in lowering the overall mixing free energy, random solution state would be more favourable in thermal stability than the ordered state. ^[14]

The tendency toward disordered state is stronger at higher temperature due to the temperature dependence of the entropy term: $-T \Delta S^{\text{mix}}$ effect. Miracle et al. ^[20] made an order-of-magnitude thermodynamic analysis to demonstrate this effect, suggesting that the ΔS^{conf} of HEAs may be sufficient to destabilize 5%–10% of intermetallic compounds (with the lowest enthalpies of formation) at room temperature, and an additional 30%–55% of ordered compounds may be suppressed in HEAs at 1500K. Roughly, 50% of the intermetallic compounds may be stable at 300K but unstable at 1500K.

2. High Entropy Alloys

2.1. Brief history of high entropy alloys

An alloy is a metallic solid or liquid formed from an intimate combination of two or more elements. Any chemical element may be used for alloying, but the only ones used in high concentrations are metals.^[21]

According to Murty et al. [14],

The mutual solubility between solvent and solute components in a binary alloy system could be judged by the Hume-Rothery rules, namely, crystal structure, atomic size difference, valence, and electronegativity. In fact, all these factors also influence the interaction between different elements and make the enthalpy of mixing of an atomic pair either negative (attractive interaction leading to ordering and the formation of intermetallic compounds), positive (repulsive interaction leading to clustering and segregation), or near zero (leading to the formation of disordered solid solutions).

As free energy of mixing of a state is determined by enthalpy of mixing and entropy of mixing, the competition of different states also relates with the competition of enthalpy of mixing and entropy of mixing. For a binary alloy system, these two factors affect the solubility between two components at different temperatures. When solubility is limited after competition between two factors, terminal solid solutions based on each component form and can be seen in the phase diagram. When a solid solution forms at all compositions, without a miscibility gap or intermediate phases, it is called an isomorphous system. But continuous solid solutions in binary alloy system are not common because the conditions for its formation are very difficult to fulfil. Similar concept could be applied to higher-order alloy systems in which a greater number of elements are involved in determining enthalpy of mixing and entropy of mixing. [14]

Contrary from traditional ways of making alloys, Cantor et al. [22] and Yeh et al. [10] independently came up with the idea of preparing equiatomic or near equiatomic multicomponent alloys [14]. Yeh popularized the term “HEAs”, indicating that, in thermodynamics, the configurational entropy of a binary alloy

$$\Delta S_{\text{conf}} = -R(X_A \ln X_A + X_B \ln X_B)$$

Equation 1-2 – Configurational entropy of a binary alloy.

is maximum when the elements are in equiatomic proportions, and that the maximum configurational entropy in any system increases with increasing number of elements (N) ($\Delta S_{\text{conf,max}} = R \ln N$), and that it would have an important effect on the kinetics of phase formation, lattice strain and properties of the resulting alloy, enhancing solubility between constituent components and leading to simpler phases and microstructures.

In 1981, Brian Cantor and his undergraduate student Alain Vincent designed several equiatomic alloys. They noticed that only one alloy, $\text{Fe}_{20}\text{Cr}_{20}\text{Ni}_{20}\text{Mn}_{20}\text{Co}_{20}$, formed a single face-centred cubic (fcc) structure. The study was continued by Peter Knight, another undergraduate student, in 1998. The work was again repeated in 2000 by Isaac Chang [23].

These studies led to the publication of the paper “Microstructural development in equiatomic multicomponent alloys” in 2004 [22].

Independently, and since 1995, J. W. Yeh worked with multicomponent alloys [10,24], developing his idea that high mixing entropy factor could reduce the number of phases and contribute new valuable properties. Together with his graduate student, K. H. Huang, he prepared equiatomic alloys of five to nine components. They analysed microstructure, hardness and corrosion resistance of these alloys [23]. This study led to suggestions about the high entropy, lattice distortion and slow diffusion effects.

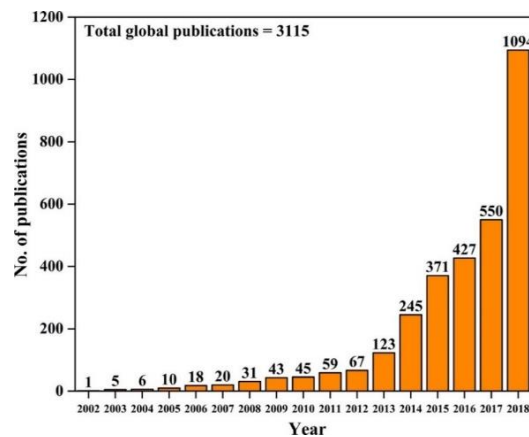


Figure 1-4 – Year-wise publications in the area of HEAs. From [23].

After the publication of these papers, the high entropy alloy community has been a growing domain (as evidenced in the Figure 1-4), grabbing the attention of both the scientific community and the industrial world.

2.2. Definitions

From a compositional point of view, Yeh^[10] defined a high entropy alloy as containing multiple elements (often five or more) in near equiatomic ratios, in atomic percentages between 5% and 35%, with minor elements in less than 5%.

According to Murty et al. [14], the basic principle behind HEAs is that high mixing entropies of solid solution phases can enhance their stability as compared with intermetallic compounds. This enhancement allows them to be easily synthesized, processed, analysed and manipulated. The total mixing entropy has four contributions: configurational, vibrational, magnetic dipole, and electronic randomness. However, configurational entropy is the dominant one [25,26]. Thus, calculating the configurational entropy of a system is critical for HEAs, which can be done from Boltzmann equation:

$$\Delta S_{\text{conf}} = k \ln w$$

Equation 1-3 – Boltzmann equation for configurational entropy.

where k is Boltzmann constant (1.380649×10^{-23} J/K) and w is the number of ways in which the available energy can be arranged on energy levels. Accordingly, ΔS_{conf} per mole to form a solid solution with n elements with x_i mole fraction is:

$$\Delta S_{\text{conf}} = -R \sum_{i=1}^n X_i \ln X_i$$

Equation 1-4 – Configurational entropy to form a solid solution.

where R is the gas constant ($8.134 \text{ J} \cdot \text{K}^{-1} \cdot \text{mole}^{-1}$).

Yeh^[9,10] considered an equiatomic alloy at its regular solid solution state. Its configurational entropy per mole can be calculated as:

$$\Delta S_{\text{conf}} = -k \ln w = -R \left(\frac{1}{n} \ln \frac{1}{n} + \dots + \frac{1}{n} \ln \frac{1}{n} \right) = -R \ln \frac{1}{n} = R \ln n$$

Equation 1-5 – Configurational entropy per mole.

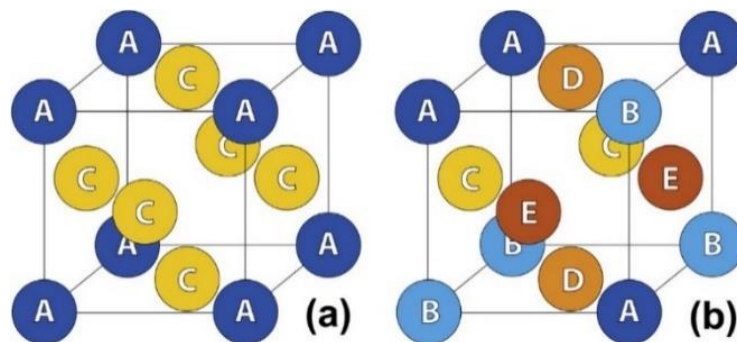


Figure 1-5 – Ordered crystals with (a) $S_{\text{IM,ideal}} = 0$ resulting from perfect order on A and C sub-lattices, and (b) a significant $S_{\text{IM,ideal}}$ due to disordered arrangements of A, B atoms on the A sub-lattice and of C, D, E atoms on the C sub-lattice. From ^[12].

For a quinary equiatomic alloy, ΔS_{conf} can be calculated as $R \ln 5 = 1.61R$. For a non-equiatomic HEA, the mixing entropy would be lower than that for an equiatomic alloy. However, an ideal monatomic gas has an internal energy per mole of $1.5RT$. Therefore,

the free energy lowering gives the solid solution phases an increased ability to compete with intermetallic compounds, which usually have much lower ΔS_{conf} due to their ordered nature^[14]. Hence, Yeh^[18] recommends $\Delta S_{\text{conf}} = 1.5R$ as the limit between high and medium entropy alloys, and $1R$ for medium and low entropy alloys, as a mixing entropy below $1R$ is predicted to be less competitive with strong bonding energies. Therefore, HEAs can also be defined by their configurational entropy.

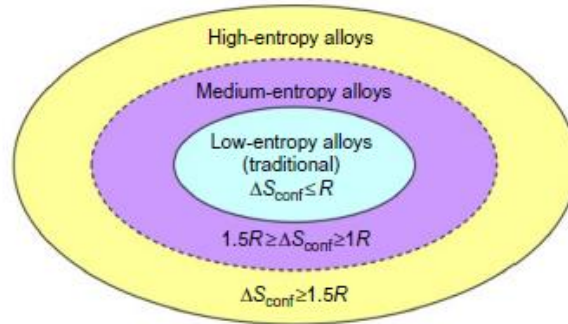


Figure 1-6 – The alloy world divided by the mixing entropy of their random solution states. From ^[18].

Miracle et al. ^[20] suggest that this definition is more effective, since ΔS_{conf} can be calculated for any alloy at the random solid solution state, as well as having more information and reliability than the composition-based. This operational definition also includes HEAs with two or more phases at low temperatures ^[14].

The term “high entropy alloy” (HEA) better describes an alloy where the configurational entropy is important. Other terms that can better explain the complex world of these kind of alloys are “multi-principal element alloys” (MPEAs) or “complex, concentrated alloys” (CCAs), terms that suggest the features of this field without any implications of configurational entropy or types of phases formed ^[12]. In this manuscript, HEA, MPEA and CCA may be used interchangeably for the same definition.

2.3. Proposed “four core effects” that affect HEA microstructure and properties

These hypotheses were proposed in early publications as parts of a multi-principal-element effect ^[9], and are often used to describe HEAs:

1. High-entropy effect:

This hypothesis proposes that increased configurational entropy in near-equimolar alloys with five or more elements may favour solid solution (SS) phases over competing intermetallic (IM) compounds, as, experimentally, the number of phases is far lower than

the maximum number predicted by the Gibbs phase rule ^[12] (Figure 1-5). It also suggests that high mixing entropy increases the solubility among elements and prevents phase separation. Yeh ^[10] and Murty ^[14] claim that configurational entropy dominates over vibrational, electronic and magnetic entropies, thus considering only the configurational term in their theory.

However, although the Gibbs phase rule gives the maximum number of phases that can exist in any given alloy, it does not give probabilities or expectations of the actual number of phases that exist in it, and thus cannot be used to support the 'high entropy' hypothesis, according to Miracle and Senkov ^[12], also because the thermodynamic arguments in the HEA literature are generally based on equilibrium.

2. Severe lattice distortion effect:

In any alloy, the alloying atoms can have different sizes than those constituting the crystal lattice and locally displace the lattice sites. In HEAs, these distortions are claimed to be more severe than in conventional alloys ^[12].

Uncertainty in the atom positions contributes to the excess configurational entropy. Ideal configurational entropy is based on filling identical lattice sites with chemically different but equal-sized atoms. An excess in the configurational entropy can mean there is uncertainty in some atom location, due to the different sizes. The uncertainty in atom location increases with increasing size differences and concentrations. In HEAs, the lattice is expected to be highly distorted, because atoms are usually displaced from their average lattice sites in their pure form (as seen in Figure 1-5).

The degree of lattice distortion influences solid solution hardening models and it is implicated in the difficulty in distinguishing between ordered and disordered phases via standard X-ray diffraction techniques ^[9,10,12,14]. Crystal lattices in HEA phases are in all likelihood distorted, but there are no systematic studies to explore and quantify this feature directly ^[12].

3. Sluggish diffusion effect:

Yeh ^[9,10] proposed that diffusion is sluggish in HEAs, based on the observation of formation of nanocrystals and amorphous phases upon solidification and on qualitative interpretations of microstructural stability upon cooling. The sluggish diffusion in these alloys is supposed to reduce component segregation, creep, defect clustering, and development of heterogeneities ^[27]. However, diffusion is difficult to measure, because of compositional complexity, and early considerations of this hypothesis rely on secondary observations ^[12].

Tsai et al. ^[28] were one of the first teams to study diffusion in HEAs, and they found that the measured diffusion coefficients (in their study conducted on a CoCrFeMn_{0.5}Ni alloy) supported the sluggish diffusion hypothesis. However, Miracle and Senkov ^[12] analysed their data and concluded that the results are not different from diffusion in elements and conventional alloys. This conclusion is supported by Pickering and Jones ^[29]. Since the publication of those articles and reviews, more studies have been conducted, both using experimental and modelling techniques. While there are reports of such sluggish diffusion ^[28,30,31], a number of studies contradict this claim ^[12,32,33].

Osetsky et al. ^[27] (using different modelling techniques), reflected on the governing role of percolation effects and composition dependence of the vacancy migration energy in diffusion, and concluded that the phenomenon of sluggish diffusion (in a Ni-Fe alloy in their study) can be demonstrated by atomistic modelling when the vacancy and the associated atomic diffusion coefficients are smaller than in the corresponding pure metals, and that the maximum effect occurs for the concentration of the fastest element (Fe in Ni) near the site percolation threshold (near the position of a phase transition in a lattice), nonetheless this alone does not provide such a sluggish diffusion. Their results suggest that five is the number of components required to ensure absence of site percolation for each element, hence minimizing atomic diffusion for fcc lattices.

4. Cocktail effect:

Ranganathan ^[34] first used the phrase that came to be associated with a mixture where the end result is unpredictable. The interatomic interactions in HEAs can be diverse, and thus they are expected to show unusual properties as well as a composite-like behaviour ^[35].

Unlike the other “core effects”, this effect is not a hypothesis and requires no proof ^[12]. It suggests that an exceptional combination of structural properties complexly depends on material composition, microstructure, electronic structure and other features, and that unexpected results that can come from unusual combinations of elements and microstructures.

2.4. Classification and properties of HEAs

2.4.1. Classification of HEAs

MPEAs can be classified into seven alloy families: 3d transition metal CCAs, refractory metal CCAs, light metal CCAs, lanthanide (4f) transition metal CCAs, CCA brasses and bronzes, precious metal CCAs and interstitial compound (boride, carbide and nitride) CCAs. This manuscript will be focused on CoCrFeMnNi, an alloy belonging to the 3d transition metal CCAs.

3d transition metal CCAs are the most widely studied alloy family, and they contain at least 4 of the 9 following elements: Al, Co, Cr, Cu, Fe, Mn, Ni, Ti and V [9,10,13,22,36]. According to Miracle and Senkov's review, about 85% of the MPEAs fall in this family [12]. Five of these 9 elements are in the "Cantor alloy" (CoCrFeMnNi) first reported in 2004 [22], which is a classical single-phase disordered solid solution (SS) alloy.

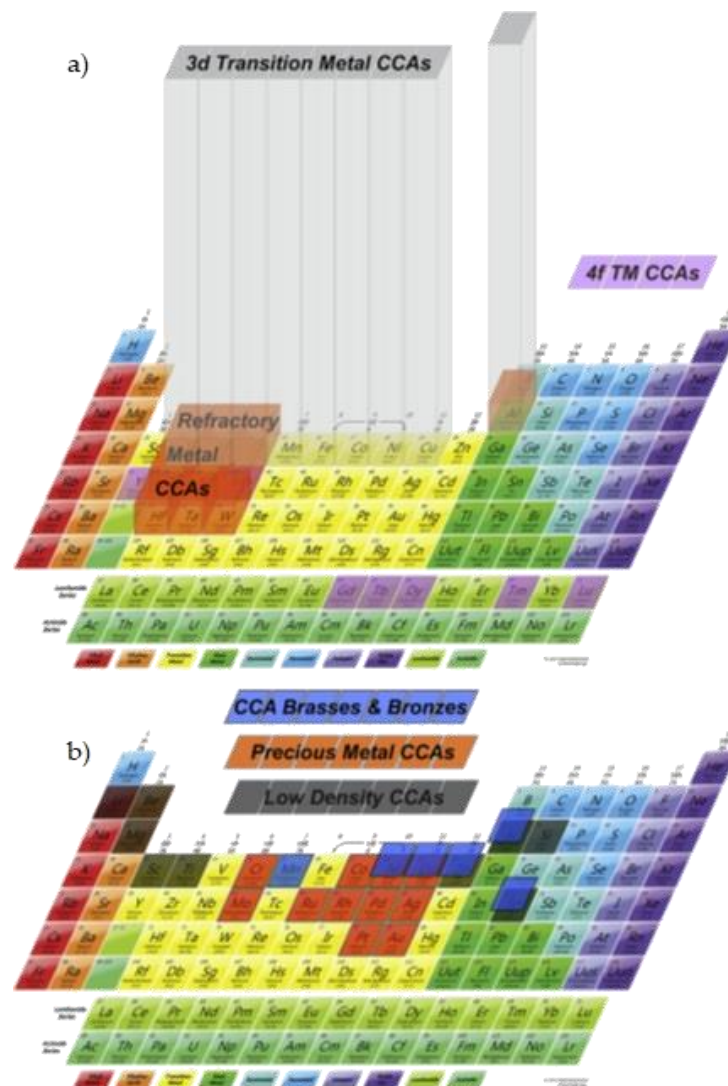


Figure 1-7 – Six of the seven CCA families illustrated by element groupings. a) 345 3d transition metal CCAs, 29 refractory metal CCAs and 2 lanthanide (4f) transition metal CCAs. b) 7 light metal CCAs, as well as precious metal CCAs and CCA brasses and bronzes. The heights of boxes in (a) are proportional to the number of alloys in the two major families. Alloys containing B, C and N are not shown. From [12].

The alloys in this family can be considered extensions of stainless steels and superalloys. Austenitic (fcc), duplex (fcc + bcc) and precipitation hardened stainless steels all have Fe-Cr-Ni as principal elements.[37]

As already presented in previous sections, the configurational entropy of HEAs is suggested to favour disordered solid solutions (SS) with simple crystal structures over the formation enthalpy of intermetallic (IM) phases. Thus, HEA phase classification requires information on whether a phase is: a) ordered or disordered, b) if it is a SS and c) whether it is simple or complex ^[36]:

The order, or “long-range order” (LRO), refers to phases with chemically distinct sub-lattices, distinguishing SS and IM phases. IM are considered LRO alloys, as perfect order occurs when the probability of a given atom species occupying a particular sub-lattice is 0 or 1. Phases with only one lattice are commonly referred to as disordered, when the site occupancy is between 0 and 1 ^[12].

Chemical “short-range order” (SRO) exists in structures that show a preference for a particular pair of atoms to occur as first neighbours. These phases are regular or sub-regular solutions. This disorder can become significant in MPEAs when the number of atom species in a phase is greater than the number of sub-lattices, contributing significantly to configurational entropy. The terms order and disorder are also used to describe local chemistry. Disordered solid solution phases have a single crystal lattice and do not possess LRO; they may or not present SRO ^[12].

According to the International Union of Pure and Applied Chemistry (IUPAC), a solid solution is a solid in which components are compatible and form a unique phase ^[38]. A solid solution forms when, as the solute atoms are added to the host material, the crystal structure is maintained and no new structures are formed. It is compositionally homogeneous; the impurity atoms are randomly and uniformly dispersed within the solid. A solid solution is likely to exist when the elements (generally metals) involved are close together on the periodic table, generally resulting in an intermetallic compound when two metals involved are not near each other on the periodic table ^[21].

Disordered SS phase fields are usually contiguous with at least one pure element; such phases are called terminal solid solutions. However, a single element need not dominate as has been suggested ^[12,36], as demonstrated by alloys such as the single-phase fcc CoCrFeMnNi MPEA, which is a terminal SS, since it is contiguous with all five elemental solid solutions, and yet no single element dominates. The fcc crystal structure in MPEAs also appears to be influenced by high atomic fractions of fcc-stabilizing elements such as Co, Cu, Mn and Ni, as well as small atomic size difference between the alloying elements ^[12].

Simple phases are defined as identical to or derived from face-centred cubic (fcc), body-centred cubic (bcc) or hexagonal close-packed (hcp) structures.

2.4.2. Properties of HEAs

A detailed analysis of MPEA properties is complicated by differences in the number, type and concentration of principal elements in the alloys studied, the extent of post-process deformation processing, and the temperature and duration of post-process thermal treatment. These parameters can have important effects on microstructure and properties [12]. However, families of MPEAs can have several common properties.

As the alloy studied in this work, CoCrFeMnNi, is an fcc belonging to the 3d transition metal alloys family, the focus of this section will be on the mechanical properties (especially tensile) of this family and, more specifically, of its fcc alloys and, finally, of the CoCrFeMnNi alloy.

a) Physical properties:

Most MPEAs for which functional properties are reported are based on the 3d transition metal alloy family [12]. However, there is a lesser amount of work on CCA functional properties than on mechanical properties (roughly a 1:3 proportion [12]).

Thermal conductivity, thermal diffusivity and thermal expansion of 3d transition metal CCAs are generally similar to highly alloyed steels and superalloys [12]. For example, Miracle and Senkov [12] reviewed and compared the thermal conductivity of two alloy systems: $\text{Al}_x\text{CoCrFeNi}$ ($0 \leq x \leq 2$), annealed at 1273 K and water quenched [39], and $\text{Al}_x\text{CrFe}_{1.5}\text{MnNi}_{0.5}\text{Mo}_y$ ($x = 0.3, 0.5; y = 0, 0.1$), studied in the as-cast condition [40]. Thermal conductivity and thermal diffusivity values for these alloys increase when increasing temperature, and the resulting values ($10\text{-}27 \text{ Wm}^{-1}\text{K}^{-1}$ and $2.8\text{-}3.5 \text{ mm}^2\text{s}^{-1}$, respectively) are lower than for pure metallic elements, but are similar to highly alloyed steels and nickel superalloys [12]. The temperature influence is opposite of what it is typically observed for pure metals, but similar to that of alloys such as Inconel and stainless steels [41]. Single-phase fcc alloys (low Al content) have almost half the thermal conductivity of single-phase bcc alloys (high Al content) [12].

The same $\text{Al}_x\text{CoCrFeNi}$ ($0 \leq x \leq 2$) alloys showed electrical resistivity from 100 to 200 $\mu\Omega\text{-cm}$ [12,39], increasing linearly with temperature. Increasing the Al content transforms the microstructures from fcc to bcc + fcc to bcc, giving a non-monotonic dependence of electrical resistivity, it being higher in the fcc phase than in the bcc phase at the same

composition, and the resistivity in the two-phase field follows a linear average of the volume fraction of the bcc and fcc phases ^[12].

According to Miracle and Senkov ^[12], using $\text{Al}_x\text{CoCrFeNi}$ alloys as a baseline allows to infer on other composition effects (without precision, however, since the phases also change): titanium additions give bcc phased $\text{Al}_x\text{CoCrFeNiTi}$ alloys ($0 \leq x \leq 2$), B2 and other intermetallic (IM) phases and show a non-monotonic dependence of resistivity on Al content ^[42]; another example is removing Cr from the baseline to obtain Al_xCoFeNi and CoFeNiSi_x alloys ($0 \leq x \leq 1$) ^[43]. Increasing Al transforms CoFeNi from fcc to bcc + B2, while increasing Si forms silicide phases.

As for the magnetic properties, almost all CCAs studied for magnetic properties contain Co, Fe and Ni ^[12]. CoFeNi is a single-phase SS alloy with an fcc crystal structure and is ferromagnetic with a saturation magnetization (M_s) of 151 emu/g ^[43]. Again, the examples alloys Al_xCoFeNi and CoFeNiSi_x show that the fcc structure transforms to fcc + bcc/B2 with Al additions in Al_xCoFeNi or to fcc + silicides in CoFeNiSi_x ^[43]. These alloys are all ferromagnetic, and M_s decreases to 102 emu/g as Al increases from $x = 0$ to 1, or to 80.5 emu/g as Si increases from $x = 0$ to 0.75 ^[12,43]. Adding Al and Cr to CoFeNi in homogenized $\text{Al}_x\text{CoCrFeNi}$ ($0 \leq x \leq 2$) alloys gives ferromagnetic behaviour at 5 K and 50 K, but paramagnetic properties at 300 K due to changing alloy phases ^[12,44]. Aging increases M_s and coercivity by decomposing Co-Cr-Fe-rich regions into ferromagnetic Co-Fe-rich and antiferromagnetic Cr-rich domains ^[45]. Processing and thermal history also influence magnetic properties through the phases formed. As-processed material typically has different microstructures and magnetic properties compared to annealed materials ^[12].

The exploration of functional materials based on MPEAs is key for future work, including more studies in the functional materials already initiated, exploring a broader range of functional materials such as piezoelectric and optical sensor materials, and a more systematic approach to designing functional MPEAs ^[12].

However, as diverse as these functional properties may be, this work will focus more on detail on the mechanical properties.

b) Mechanical properties:

Mechanical properties strongly depend on composition and microstructure ^[12]. Composition sets elastic properties and atomic interactions that dictate dislocation behaviours. Composition also defines the phases present and their volume fractions, which influence properties through the intrinsic properties of the phases. Even at a fixed

composition and phase content, properties can vary dramatically by changing the size, shape and distribution of phases [12]. Finally, defects are critical microstructural components that play a major role in mechanical properties. Atomic-level defects include vacancies, dislocations and grain boundaries.

- Hardness and compression:

Single-phase fcc alloys have Vickers hardness in the range of 100-200 Hv, single-phase bcc alloys have hardness over 600 Hv and bcc + fcc alloys have hardness values that increase from the lower to the higher levels with increasing bcc content [12]. Compressive yield strengths can be very high in alloys with significant volume fractions of bcc and/or B2 phases, and range from 1300 to 2400 MPa with values as high as 3300 MPa [12]. Malleability is often below 10%. As a general result, it decreases as strength increases.

George et al. [46], show a cohesive review of the compressive properties of MPEAs in Figure 1-8(b). The data they collected shows an ultimate compressive strength of 1000–2300 MPa and a strain of 0.1%–15%, many of the alloys they charted display significantly improved compressive properties compared to conventional engineering alloys [46].

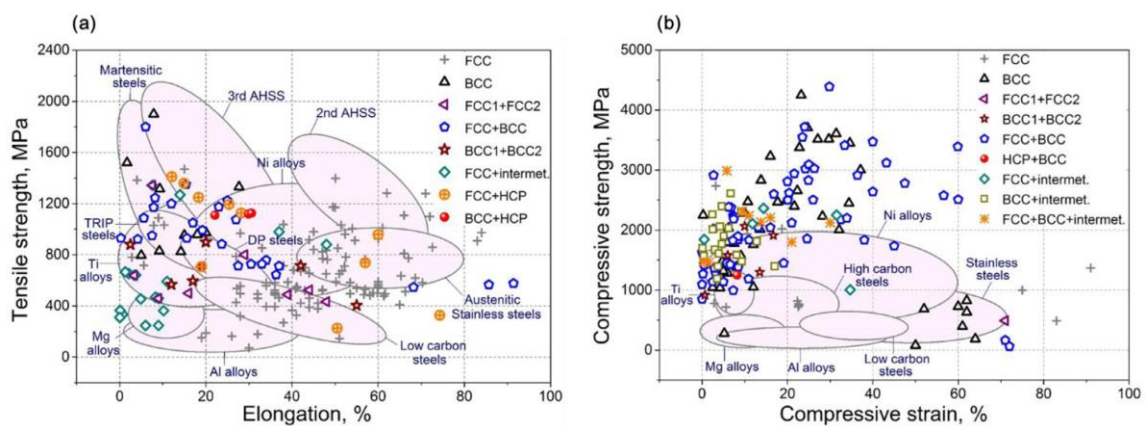


Figure 1-8 – a) Room temperature tensile strength vs elongation to fracture, and b) compressive strength vs compressive strain of HEAs and CCAs reported in literature. 2nd and 3rd AHSS stand for the two generations of advanced high-strength steels, DP steels for dual-phase steels and TRIP steels for transformation-induced plasticity steels. From [46].

- Tensile properties:

George et al. [46] show in Figure 1-8(a) that the mechanical properties observed in the alloys they compared are well within those observed in martensitic steels, advanced high strength steels, nickel-based alloys, etc., and that MPEAs cover nearly the entire property

spectrum of steels, aluminium, titanium, magnesium and nickel alloys, presenting the broadness of the CCA definition.

A comparison of tensile properties of MPEAs with standard alloys of similar phase constitution reveals similar tendencies as those presented in Figure 1-8(a). As seen in Figure 1-9(a), most of the single fcc phase HEAs show comparable properties to Ni-based alloys or austenitic stainless steels, which typically have similar (3d late transition) alloying elements. Compared to 2nd generation advanced high strength steels (2nd AHSS), most single fcc phase HEAs have lower ultimate tensile strengths. HEAs whose properties are comparable to 2nd AHSS benefit from either twinning-induced plasticity (TWIP) effects or the inclusion of interstitial elements [46].

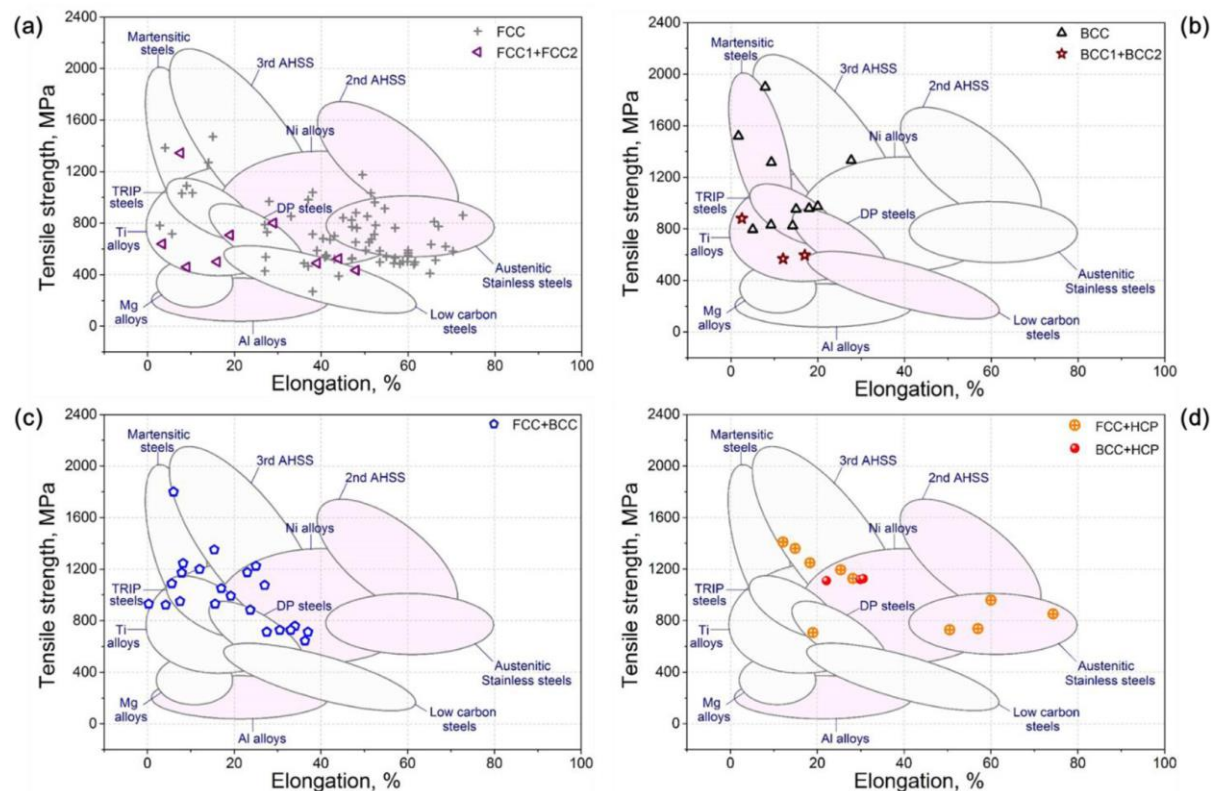


Figure 1-9 – Room temperature uniaxial tension test data of HEAs and CCAs, classified based on phases present in the microstructure: a) fcc, fcc1 + fcc2, b) bcc, bcc1 + bcc2, c) fcc + bcc, d) fcc + hcp. 2nd and 3rd AHSS stand for the two generations of advanced high-strength steels. From [46].

Gorsse et al. [47] compare MPEAs with commercial structural alloys (mg, Al, Ti, Fe and Ni based alloys). Results are shown in Figure 1-10, where the room temperature yield strength is plotted against density using logarithmic scales. In this figure, 3d transition metal and refractory metal CCAs overlap with steels and Ni alloys in room temperature yield strength – density space, especially below the yield strength, σ_Y (around 2000 MPa).

According to Ashby ^[48], at room temperature, steel is the best among other conventional alloy families for uniaxial tension whereas magnesium alloys are the best commercial alloys for beam and panel bending. In terms of the specific yield strength performance index, the room temperature properties of 3d transition metal CCAs are marginally better than the best steels in uniaxial loading ($s = 1$), and so are better than any of the conventional alloys. They are also equivalent to the best Mg alloys in beam bending ($s = 3/2$). Panel bending ($s = 2$) places a premium on low density, and so conventional alloys based on Mg, Al and Ti all significantly out-perform 3d transition metal and refractory CCAs in this loading condition. Thus, the currently available 3d transition metal CCAs do not compete with commercial alloys in panel bending specific strength at room temperature ^[47].

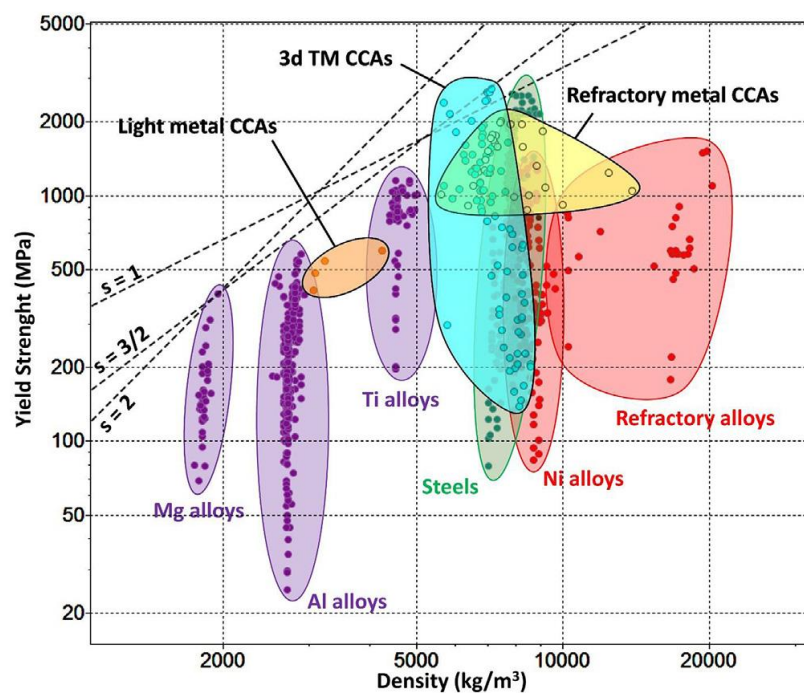


Figure 1-10 – Materials property space for room temperature yield strength vs density of conventional metal alloys and CCAs. The dashed lines give performance indices for uniaxial loading (slope, $s = 1$), beam bending ($s = 3/2$) and panel bending ($s = 2$). From ^[47].

This property is the main focus of this manuscript, thus it will be further discussed on the next section.

2.5. HEA metallurgy and deformation mechanisms

This section will also only focus on the metallurgy of the 3d transition metal alloy family of MPEAs, as the study alloy for this work belongs to that category, and more in detail on their uniaxial tensile properties.

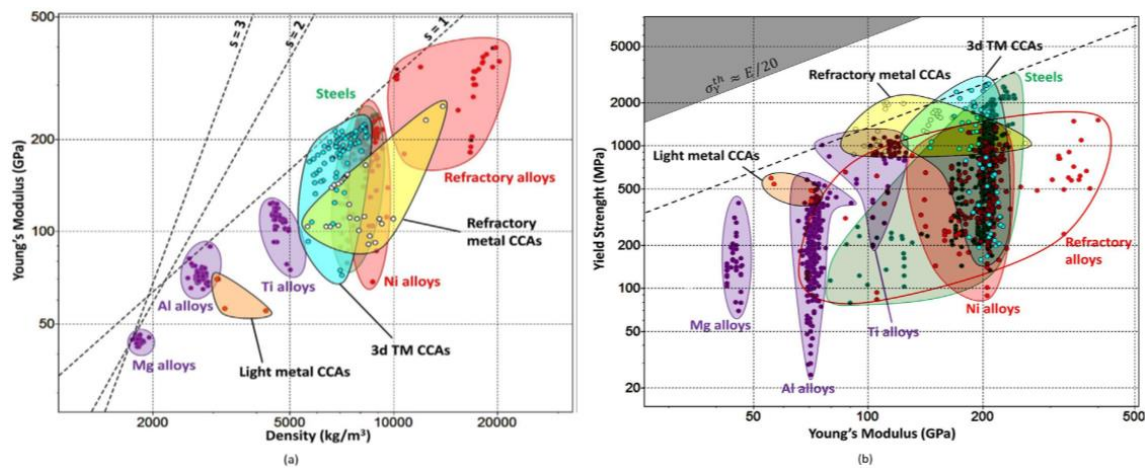


Figure 1-11 – Gorsse et al. charts for: a) materials property space for room temperature Young's modulus vs density of conventional metal alloys and CCAs. The dashed lines give performance indices for uniaxial tension (slope, $s = 1$), beam bending ($s = 2$) and panel bending ($s = 3$). It displays data for about 1220 commercial and 115 multi-principle element alloys. b) Room temperature yield strength plotted against Young's modulus for conventional metal alloys and CCAs. The contour (dashed line) shows the ratio of the yield strength over the Young's modulus. From ^[47].

According to Gorsse et al. ^[47], the best 3d transition metal CCA is equivalent to the best commercial alloys (Al alloys, steels, Ni alloys, refractory alloys), but inferior to the best commercial structural alloys in beam and panel bending, especially Mg-based, Al-based and Ti-based alloys. As for specific Young's modulus, 3d transition metal CCAs are better than conventional alloys when applying a temperature, as shown in Figure 1-11(a) ^[47].

The specific alloy classes of the 3d transition metal CCAs are shown in detail in Figure 1-12. Comparisons between 3d transition metal CCAs, stainless steels and commercial Ni alloys is suggested by overlap of common elements in these alloy families. Commercial stainless steels all have Fe, Cr and Ni as major elements. The figure illustrates that the 3d transition metal CCAs with the highest specific yield strengths all have Cr, Fe and Ni as major elements, all but one have Al, and all but one have Co ^[47].

2.5.1. Compositional effect

Murty ^[49] concludes that increasing configurational entropy due to the increasing number of alloying elements may not be sufficient to stabilize the MPEAs into single solid solution phases. The type of the alloying element is rather critical in determining the phase stability. Otto et al. ^[50], replaced the individual elements in the single-phase CoCrFeMnNi by elements with the same room temperature crystal structure and similar size and electronegativity. Their results showed that, except for the base CoCrFeMnNi alloy, all the other alloys have revealed the presence of multiple phases ^[50]. As a result, configurational entropy alone cannot be responsible for phase formation.

They illustrate, in Figure 1-14, the influence of principal element additions on the room temperature specific yield strength (part (a)) and yield strength vs. tensile ductility (part (b)). The 5-element CoCrFeMnNi alloy has the lowest density in its class of alloys and, as elements are progressively added to Ni, ductility increases ^[47], a behaviour caused (among other reasons) by nanotwinning ^[51].

2.5.2. Defects and strengthening mechanisms

In their review, George et al. ^[52] give a very good graphic explanation of how defects and strengthening mechanisms work in any given alloy, and specially in a HEA. The following extract is a citation of their review:

Metallic alloys contain defects that disrupt the regular 3D atomic structure of a perfect crystal. They can be classified as:

- Point defects (0D), for example, vacancies (Figure 1-15(a)), interstitial (atoms in the interstices of the crystal lattice) and substitutional (atoms that substitute on the host lattice) defects.
- Line defects (1D), for example, dislocations (Figure 1-15(b)).
- Interface defects (2D), for example, grain boundaries (which separate regions of different orientations in a polycrystalline material), twin boundaries (which separate regions that are mirror images of each other created by shear parallel to the twin planes, see Figure 1-15(c)), stacking faults (in which the normal stacking sequence of certain planes is disrupted), phase boundaries (which separate different phases in a material) and surfaces on which the solid is exposed to (often harsh) environments.
- Volume defects (3D), for example, precipitates, inclusions and voids.

As Figure 1-15 shows, in MPEAs it is difficult to distinguish between host atoms and substitutional solutes. Defects such as vacancies, stacking faults, twins and dislocations disrupt the local structure of a pure metal, whereas in a MPEA, they also disrupt the local chemistry.

As plasticity requires the movement of dislocations through the metal (Figure 1-15(d)), any obstruction to this motion strengthens the material. Many of the defects mentioned above can act as obstacles to dislocation motion, including alloying elements, vacancies (at relatively low temperatures), and/or twin, grain and phase boundaries. Some twin boundaries allow the partial dislocations to glide along their interfaces, thereby relieving some of the stresses built up by the dislocation pile-up and enhancing ductility.

Figure 1-15(d) shows schematically how dislocations are held up at precipitates and solutes, and grain and twin boundaries. In simple terms, the strengthening due to obstacles varies inversely with their spacing and directly with their ‘strength’, that is, the force required to break through. Thus, closely spaced, strong obstacles produce the most strengthening. Unlike in conventional metals, in which strengthening is usually accompanied by a loss of ductility and toughness, in some HEAs this compromise can be avoided, and an understanding of the reasons for this behaviour is critical for the mechanistic design of stronger and tougher materials. [52]

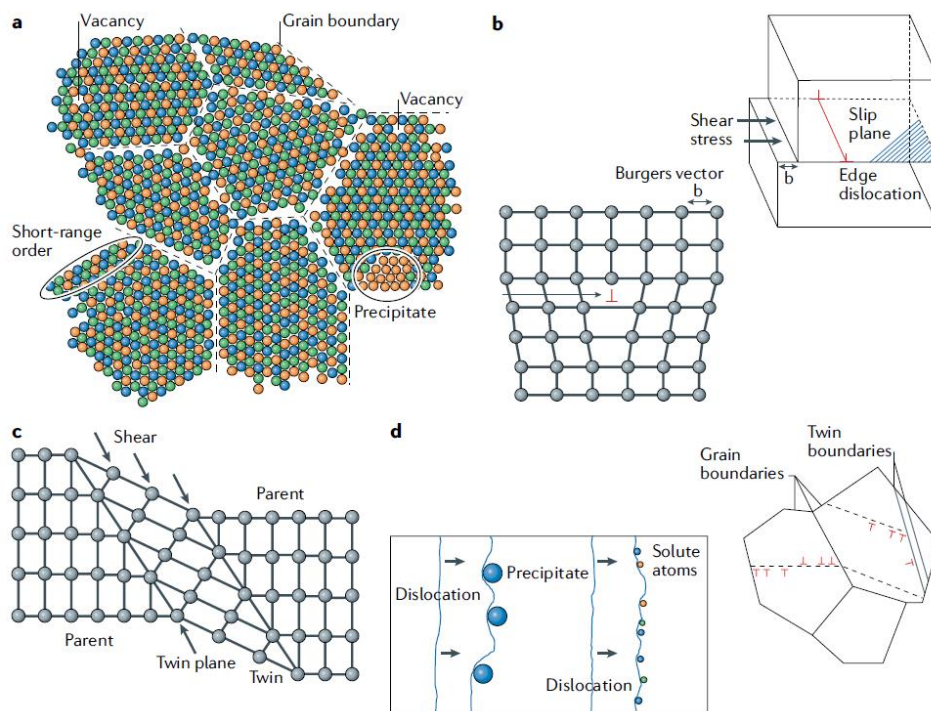


Figure 1-15 – Schematic representation of: a) different type of defects present in a crystal, b) a dislocation slip in a crystal, c) twinning, d) interaction of dislocations with obstacles (solute atoms and precipitates, grain and twin boundaries). From [52].

2.5.3. Deformation mechanisms

Fcc-structured MPEAs are known to be more ductile, displaying low strengths and high plasticity, whereas bcc-structured MPEAs show higher strengths and low plasticity [35,46,53]. Diao et al. [53] classify MPEAs in three categories, on the basis of crystallographic structure and mechanical behaviour: type I are HEAs that typically exist as solid solution fcc; type II HEAs comprise mixture of different phases, primarily a combination of bcc and fcc structures and, in very few cases, a mixture of fcc and hcp phases (this class of HEAs potentially exhibit a combination of high strength and enhanced ductility, depending on the variation in structures of the HEA [35]); and type III HEAs constitute mostly bcc-structured alloys typically suitable for refractory purposes.

With respect to the generic deformation behaviour, type I HEAs show characteristics similar to those observed in conventional fcc metals ^[19]. One of the extensively researched equiatomic HEA belonging to this category is the CoCrFeMnNi HEA, commonly referred to as the Cantor alloy ^[35]. As the Cantor alloy is the core of the present work, the next section will compile the deformation behaviour of fcc-structured MPEAs, or type I MPEAs.

Miracle and Senkov ^[12] compared the tensile properties of MPEA single-phase fcc solid solutions (with the exception of minority oxide, Cr-rich or Mn-rich second phase particles) and commercial alloys INCONEL® 600 (nominal composition Cr₁₈Fe₈Ni₇₄), 316 stainless steel (nominal composition Fe₇₀Cr₁₆Ni₁₀Mo₂Mn₂) and INCOLOY® 800 (nominal composition Cr₂₃Fe₄₂Ni₃₅). Their results are shown in Figure 1-16, where it is shown that yield (σ_y) and ultimate (σ_{uts}) strengths both decrease continuously with increasing temperature over the full range of temperatures. They also show that strength drops abruptly from 77 to 300 K, from 300 to 800 K it decreases slowly and then it drops again from 800 K to the maximum test temperature. The tensile ductility (ϵ) generally increases with decreasing temperature below 900 K, which is not unusual for solid solution austenitic alloys.

These assessments suggest that the mechanical behaviour of fcc HEAs is similar to standard engineering alloys. Therefore, these aspects will be described more carefully:

2.5.3.1. Yielding behaviour:

Pure fcc metals show practically no temperature dependence of yield strength between 500 and 77 K ^[54]. In contrast, the fcc Cantor alloy exhibits relatively strong temperature dependence of yield strength with almost a factor of four increase as the temperature is decreased from 500 to 77 K for the coarsest grain size material (Figure 1-17) ^[46].

2.5.3.2. Grain size effects:

Liu et al. ^[55] investigated the effect of grain refinement (Hall–Petch effect) by room-temperature Vickers micro-hardness measurements and found that the Hall–Petch slope of the Cantor alloy was higher than the upper bound of the Hall–Petch slopes of fcc metals ^[56]. This suggests a higher slip-transfer resistance at grain boundaries in this alloy ^[46].

Otto et al. ^[19] studied the Hall–Petch behaviour of the yield stress of the Cantor alloy as a function of temperature for grain sizes of ~4–155 μm , through tensile tests. They determined that the Hall–Petch slope of the Cantor alloy is 494 MPa $\mu\text{m}^{-1/2}$ at room temperature, which is higher than that of pure fcc metals (between 90–230 MPa $\mu\text{m}^{-1/2}$ ^[56]).

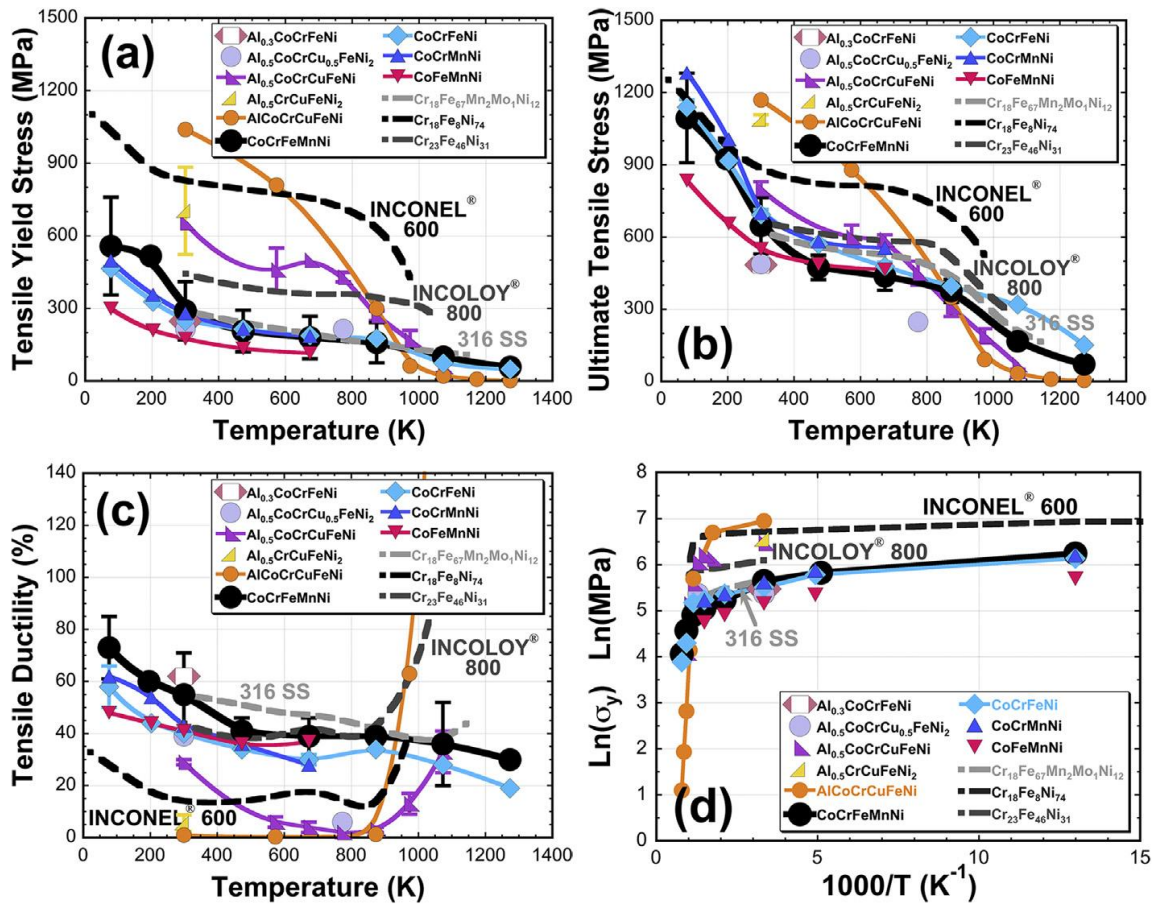


Figure 1-16 – Tensile data of 3d transition metal CCAs: a) yield strength, σ_y , b) ultimate strength, σ_u , and c) tensile ductility, ϵ , vs. temperature. d) Data are shown as $\ln(\sigma_y)$ vs $1000/T$ to illustrate the thermally activated nature of yield. Data for three commercial solid solution, austenitic alloys are shown for comparison: 316 stainless steel, INCONEL® 600 and INCOLOY® 800, with the concentrations in at.% indicated in the legend. From [12].

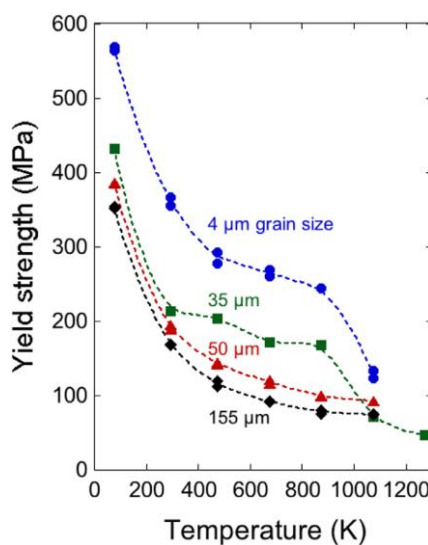


Figure 1-17 – Temperature and grain size dependence of the yield strength of the CoCrFeMnNi HEA. From [46].

2.5.3.3. Critical resolved shear stress:

Wu et al. [57] conducted compression and tensile tests where they concluded that there was no orientation dependence of the CRSS (meaning the Schmid law was valid), but a “smaller is stronger” size effect was seen with a power-law exponent near the lower bound for fcc metals indicative of a high friction stress [46,57]. Okamoto et al. [58] extrapolated the yield stress curves of small (1–10 μm) pillars to larger sizes (20–30 μm), and estimated a “bulk” CRSS of 33–43 MPa for the Cantor alloy, in agreement with the results of Otto et al. [19] for the polycrystalline yield stress divided by the Taylor factor.

2.5.3.4. Plastic deformation of polycrystalline alloys:

Otto et al. [19] plotted the representative engineering stress–strain curves of the CoCrFeMnNi alloy of 50 μm grain size, under tension at different temperatures. In their study, they found an augmentation of yield stress, flow stress and uniform elongation as the temperature decreases to liquid nitrogen temperature. The increase in ductility with lowering temperature (despite the increasing yield strength) is due to postponement of the onset of necking instability, which in turn is due to high, steady, work hardening that persists to higher strains at lower temperatures [46,59]. The early stage of plastic deformation in CoCrFeMnNi is characterized by planar slip of $1/2 \langle 110 \rangle$ dislocations on $\{111\}$ planes at temperatures in the range 77–873 K [19] (Figure 1-19). After performing deformation experiments, Okamoto et al. [58] cut foils parallel to the activated $\{111\}$ planes and examined them by transmission electron microscopy (TEM), and found long, smoothly curved dislocation with no discernible preferred orientation.

Otto et al. [19] also found extended pile-ups of the dislocations against grain boundaries in their experiments. Okamoto et al. [58] and Laplanche et al. [60] (Figure 1-18), both in 2016, also saw splitting of dislocations into $1/6 \langle 112 \rangle$ Shockley partials bounding stacking faults. Zhang et al. [61] performed *in situ* TEM straining experiments that suggested the mobility of perfect dislocations is low and their motion is extremely sluggish, and the partial dislocations move very quickly but are halted when they intersect a band of slow-moving perfect dislocations. George et al. [46] warn caution for these observations because the shear stress acting on the dislocations during *in situ* straining is not known and any apparent differences in mobility might be due to differences in the local stress, Schmid factor/ Peach-Koehler forces driving dislocation motion.

Smith et al. [62] performed high-resolution TEM observations on the Cantor alloy and showed that the separation between partial dislocations is highly variable (by a factor of two) at different points along the dislocation. Their calculations suggest that this may be due to variations in the local composition, affecting the local stacking fault energy and thus the partial separation. This will be further discussed in the stacking fault energy section.

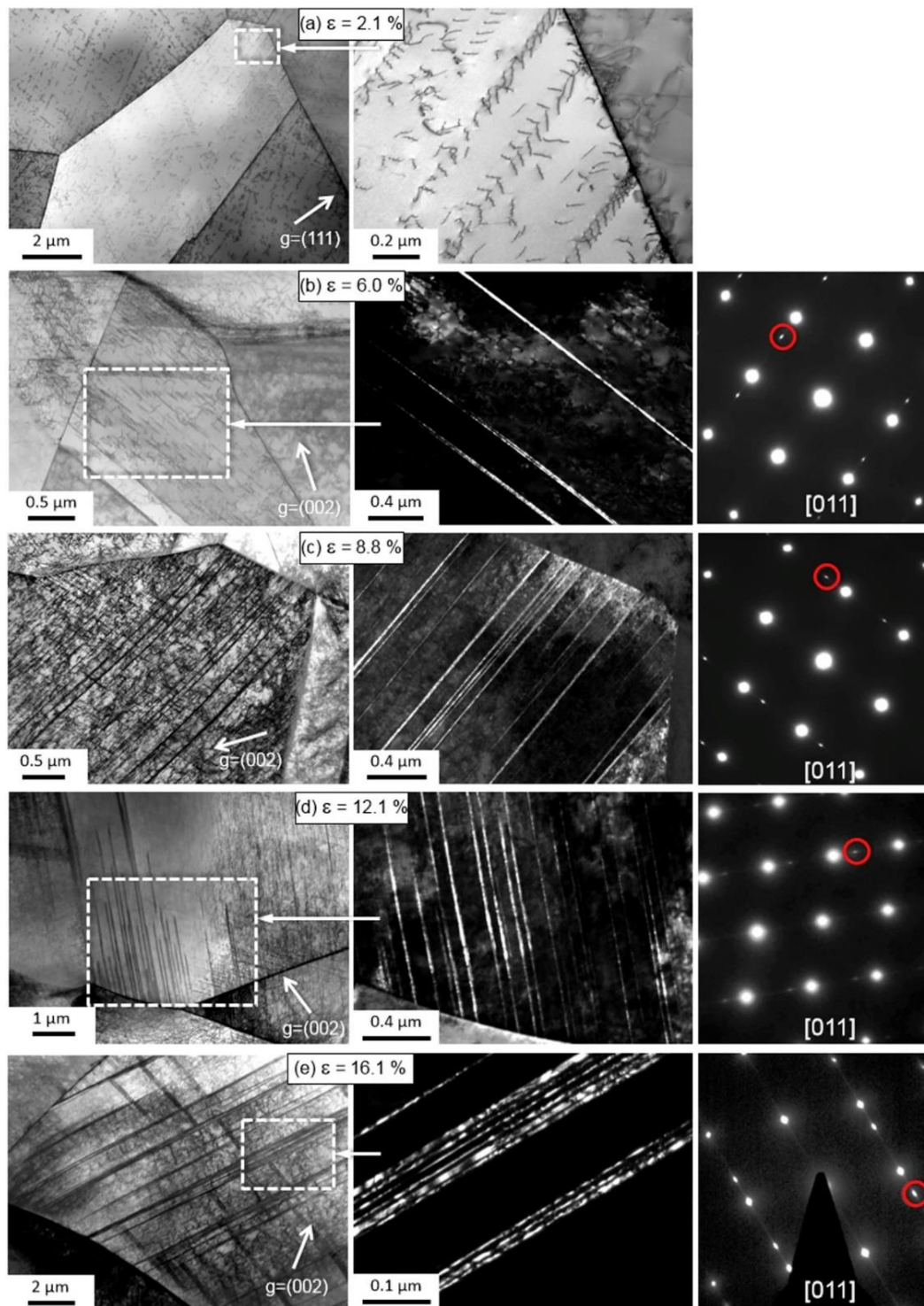


Figure 1-18 – TEM BF micrographs showing twin evolution with true tensile strain at 77 K. a) Both figures are bright field images. b)–e) Figures on the left are bright field images while those in the middle are dark field images with SAD patterns on the right showing diffraction spots from the twin and matrix. Diffraction spots circled in red in the SAD patterns were used to obtain the dark field images. The dashed rectangles in the left column delineate areas that are magnified in the middle column. From ^[60].

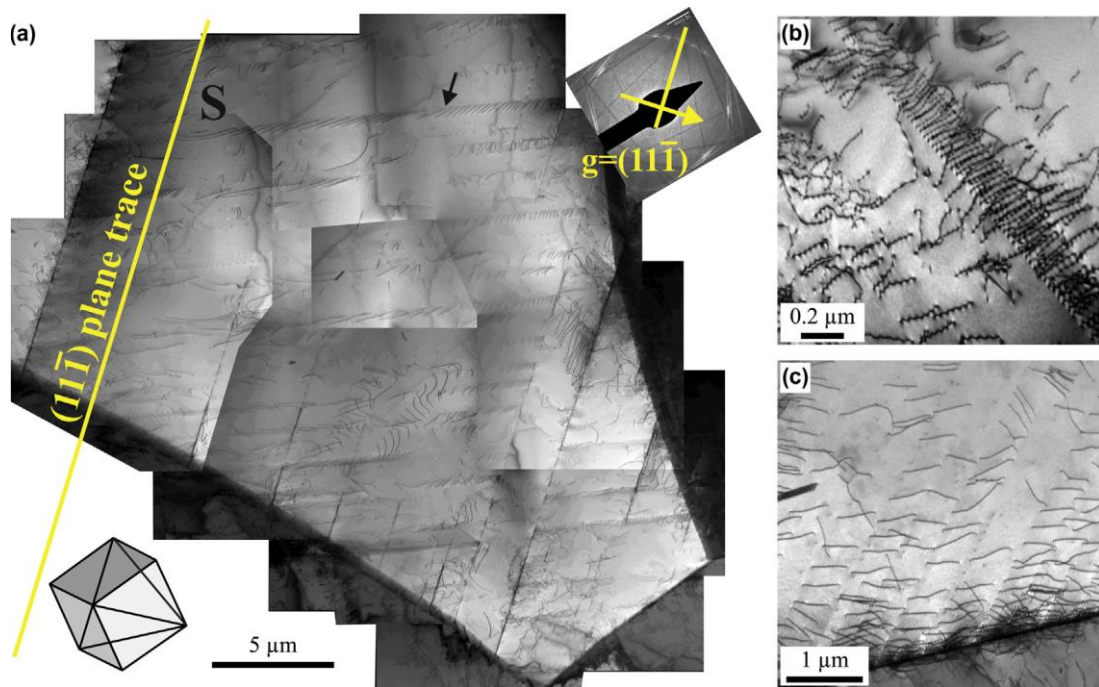


Figure 1-19 – Representative TEM BF micrographs from the gauge sections of interrupted tensile test specimens of the coarse-grained CoCrFeMnNi alloy (grain size 155 μm) after relatively small tensile strains: a) 1.7% at 873 K, b) 2.4% at 77 K and c) 2.1% at 293 K. From [19].

To conclude this subsection, the deformation and hardening of fcc alloys can be summarised in Figure 1-20.

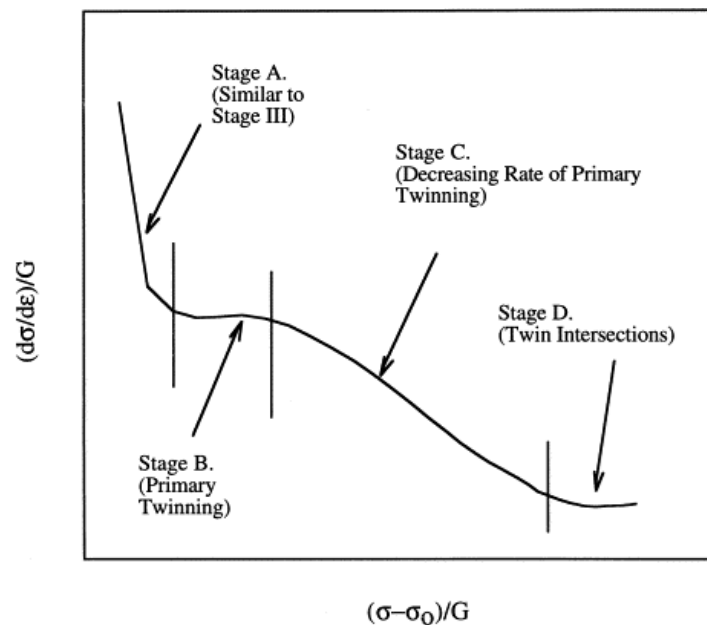


Figure 1-20 – Schematics of the four stage strain hardening response of an fcc alloy. From [63].

2.5.3.5. Twinning-induced plasticity (TWIP):

In metals that exhibit hardening only due to dislocation-dislocation interactions (Taylor hardening), the strain hardening rate generally decreases continuously until the Considère criterion is reached and necking instability sets in, followed by fracture [46].

The studies cited in the previous section [19,60] concluded that the dislocation substructure evolves from planar slip at small strains to cross-slipped tangled dislocations at intermediate strains and cell structures at high strains, similar to the microstructure evolution seen in most fcc metals [46]. Laplanche et al. [60] measured the increase in dislocation density with strain by TEM. Their results show the increase in dislocation density is the same at 77 K and at room temperature, consistent with the temperature-independent work hardening rate of fcc metals at low strains [46,64]. So if Taylor hardening is the only operative mechanism, the shear-modulus-normalized work hardening rate as a function of strain in Figure 1-21 should be identical at both 77 K and 293 K (since it depends only on the square-root of dislocation density and other constants that are independent of strain) [46]. However, these work hardening rates are different. Therefore, another mechanism must be operating at 77 K besides simple dislocation hardening: deformation-induced twinning, which, according to Laplanche et al. [60], appears sporadically, in some grains, after about 6% strain and consistently in all grains examined, after 9% strain. The nanoscale twins are of the normal kind seen in fcc metals [19] and contribute to hardening [46].

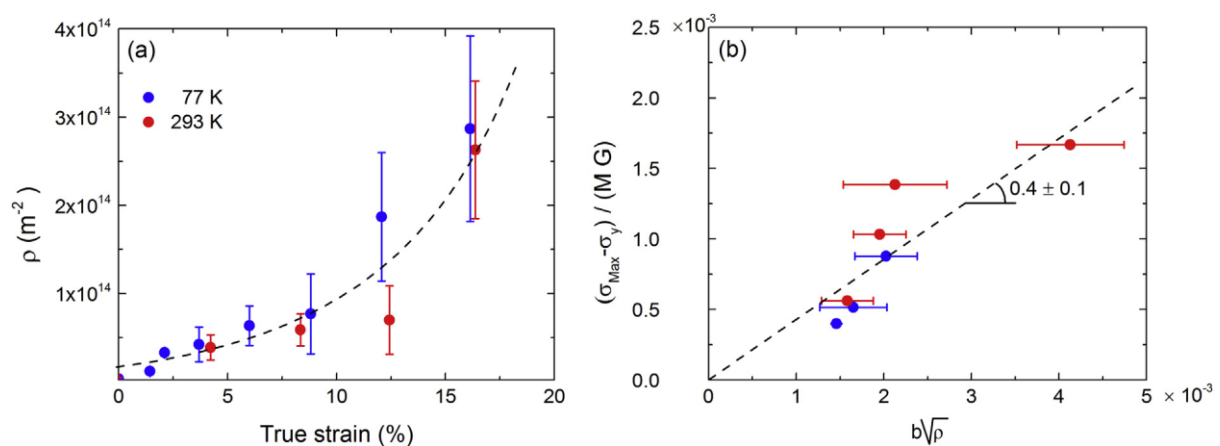


Figure 1-21 – a) Dislocation density ρ as a function of true strain. b) Taylor hardening plot showing linear dependence of the normalized work hardening $(\sigma_{\text{Max}} - \sigma_y) / (M \cdot G)$ as a function of $(b \cdot \rho^{1/2})$. From [60].

The Hall-Petch effect [65–68] can also take in effect the mechanical twins that contribute to strengthening but also divide the grains into smaller and smaller grains. Both Gali and George [59] and Otto et al. [19] conclude that deformation-induced twinning is responsible for high, constant work hardening that postpones the onset of necking instability to higher

strains ^[46]. Thus, the TWIP effect is able to increase both strength and ductility simultaneously ^[69]. Certain twin boundaries act as barriers to dislocation motion and others allow partial dislocations to glide along the twin-matrix interfaces ^[70], so that some of the accumulated stress is relieved and further deformation is facilitated ^[46].

2.5.3.6. Deformation in single-crystal MPEAs:

According to Kireeva et al. ^[71,72], and as in most fcc single crystals, the extent of the first stage is considerably reduced (sometimes to the point of extinction) when multiple slip systems are activated early on in the deformation process. Their TEM images showed considerable dislocation pile-ups in CoCrFeMnNi specimens that deformed mainly by single slip and dislocation tangles when multiple slip systems were activated, and twinning starting after applied strains of ~27% ^[71]. Abuzaid and Sehitoglu ^[73], however, found no twinning at room temperature in the same alloy (by EBSD or DIC techniques), even after applied strains of ~40% where the axial stresses reached ~720 MPa. This discrepancy indicates that higher resolution techniques are needed for twinning detection, or that parameters other than strain and temperature need to be consider.

Both research groups concluded that Schmid's law is valid and makes correct predictions for both slip and twinning ^[71-73]. Additionally, other authors seem to suggest that some dislocation plasticity is needed before twinning is activated ^[60,74].

The fundamental concepts of MPEAs have been discussed in this section, with a focus on solid solution, fcc, 3d transition metal alloys, as this is the family to which CoCrFeMnNi belongs. The next section will formally introduce the concepts of plastic deformation, always with the focus on the family of the studied alloy.

3. Plasticity in metals

As previously mentioned in section 1.1, plasticity in a metallic crystal is driven, at low and ambient temperatures, by two elementary mechanisms: slip and twinning. Both of these mechanisms depend on dislocations (a linear or one-dimensional defect around which some of the atoms are misaligned, represented graphically by the symbol \perp ^[75]), hence understanding the dislocation behaviour is critical to understand the plastic deformation of crystals. Very few techniques are able to capture their individual motion, and among them is in the *in situ* TEM straining experiments. This section will be dedicated to introduce the concepts needed to that end.

3.1. Dislocation slip

Figure 1-22 considers a dislocation, continuous within the crystal and bounds a region of slip. The definition of \vec{b} indicates that \vec{b} is invariant along the dislocation line, although the dislocation changes continuously from screw character at A to edge character at C in **Error! Reference source not found.**(b) and also in Figure 1-23. The dislocation line at B is between pure edge and pure screw character, called mixed, and its Burgers vector can be resolved into a screw component

$$\vec{b}_s = (\vec{b} \cdot \vec{\xi})\vec{\xi}$$

$$\vec{b}_e = \vec{\xi} \times (\vec{b} \times \vec{\xi})$$

Equation 1-6 – Equivalent Burgers circuit for a dislocation of screw (s) or edge (e) character.

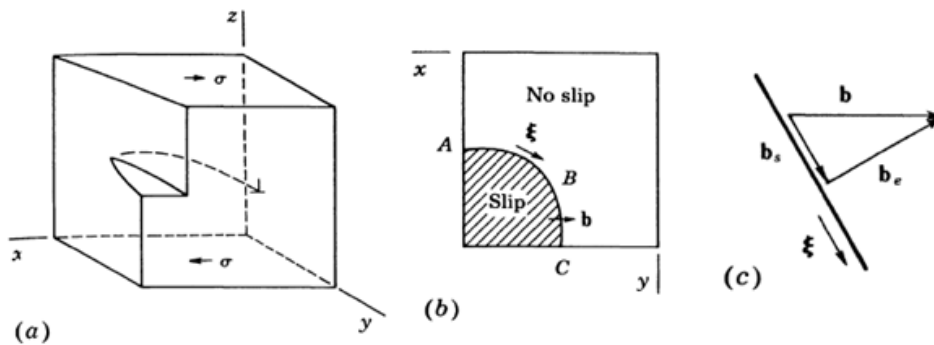


Figure 1-22 – a) Shear of a perfect crystal to form a mixed dislocation. b) Projection normal to the glide plane in a). c) Resolution of b) into components at point B. From [79].

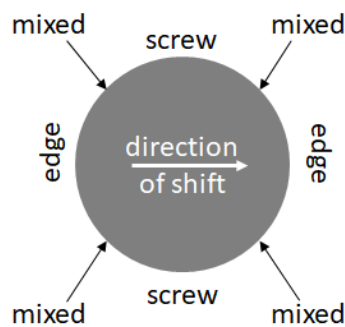


Figure 1-23. Dislocation loop. From [4].

If a dislocation is considered as a straight line, the motion of an edge dislocation by the displacement parallel to \vec{b} of the line parallel to $\vec{\xi}$ generates a plane over which glide displacement has taken place^[79]. This plane is called the glide plane and is defined by the plane normal given by $\vec{b} \times \vec{\xi}$. For a screw dislocation where \vec{b} is parallel to $\vec{\xi}$, $\vec{b} \times \vec{\xi} = 0$, and

the glide plane is indeterminate by the above definition ^[79]. Any plane for which \vec{b} is a zone axis is a possible glide plane for a screw dislocation.

Now, extending the glide-plane concept to curved dislocation lines (considered to be made up of straight pieces of differential length) results on the schematics shown in Figure 1-24. Since each edge piece is constrained to a given glide plane in conservative motion, a dislocation with part edge character is constrained to glide on a unique glide surface, composed of segments of planes for which \vec{b} is a zone axis ^[79]. On the other hand, pure screw segments can cross-slip from one glide plane \vec{m} to another \vec{n} , as shown in Figure 1-24(b), as long as the line of intersection $m \times n$ is parallel to \vec{b} .

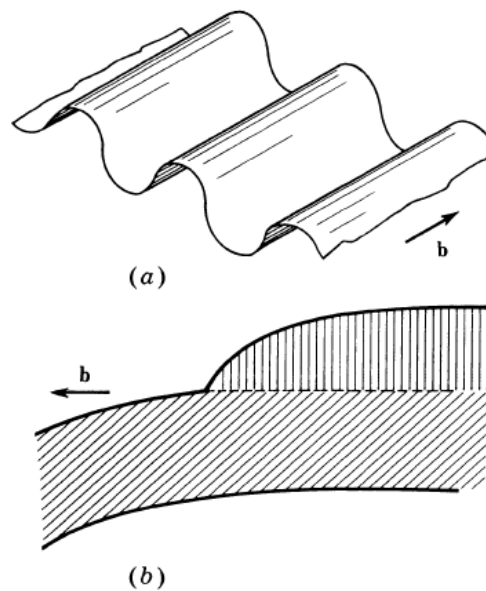


Figure 1-24 – a) Slip surface for an edge dislocation. b) Slip surface for a dislocation showing cross slip of a screw segment. From ^[79].

Slip of a dislocation along a slip plane occurs in response to shear stress on that plane ^[3]. In a tensile specimen of monocrystalline metal in which the tensile stress σ acts along an axis forming an angle ϕ with the normal to the slip plane and an angle λ with the slip direction, then the relation between σ and the resolved shear stress on the slip plane and in the slip direction, τ , is:

$$\sigma = \frac{\tau}{\cos \phi \cos \lambda}$$

Equation 1-7 – Schmid law.

Schmid ^[96] proposed in 1924 that slip in a single crystal is initiated when the resolved shear stress on a slip system reaches a critical value τ_c , which is a constant for a given material at a given temperature and is known as the critical resolved shear stress (CRSS). This result is called Schmid's law.

A shear stress acting on a dislocation is defined by the Peach-Koehler force ^[97]. A dislocation with line direction $\vec{\xi}$ that is under an external stress $\vec{\sigma}$ experiments

$$F = (\vec{\sigma} \cdot \vec{b}) \times \vec{\xi}$$

Equation 1-8 – Peach-Koehler force.

This equation relates the stress field in the material to an effective (energetic) force acting on a dislocation ^[98]. It has a glide and a climb component. For example, for an infinitely long edge dislocation along the z-direction, with the Burgers vector $\vec{b} = b_x \vec{e}_x$ and with the positive direction of the dislocation line vector out of the plane of figure ($\vec{\xi} = \vec{e}_z$), the dislocation force is $\vec{F} = \sigma_{xy} b_x \vec{e}_z - \sigma_{xx} b_x \vec{e}_y$, where σ_{xy} and σ_{xx} are the shear and normal stresses at the location of the dislocation, excluding the singular stresses from the dislocation itself. In this expression, the glide component of the dislocation force is $\vec{F}_{\text{glide}} = \sigma_{xy} b_x \vec{e}_z$, while $\vec{F}_{\text{climb}} = \sigma_{xx} b_x \vec{e}_y$ is the climb component ^[98].

3.2. Dislocations behaviour in crystals

The plasticity theory was developed to describe the behaviour of ductile metals. Metals in their usual form are polycrystalline aggregates (they are composed of large numbers of grains, each of which has the structure of a simple crystal). A crystal is a three-dimensional array of atoms forming a regular lattice ^[3]. The atoms vibrate around fixed points in the lattice but do not move away from them, being held more or less in place by the forces exerted by neighbouring atoms. The forces may be due to ionic, covalent, or metallic bonding.

The most common crystal structures in metals are the hexagonal close-packed (hcp), face-centred cubic (fcc) and body-centred cubic (bcc) (as seen in Figure 1-25).

Experiments show that plastic deformation is the result of slip on specific crystallographic planes, in response to shear stress along these planes. It is found that the slip planes are most often those that are parallel to the planes of closest packing ^[3], as the separation between such planes is the greatest and, therefore, slip between them is the easiest, since the resistance to slip as a result of interatomic forces decreases rapidly with interatomic distance. Within each slip plane there are in turn preferred slip directions, which once

more are those of the atomic rows with the greatest density, for the same reason. Together, a slip plane and a slip direction form a slip system.

- In hcp crystals (as zinc or magnesium), the planes of closest packing are those containing the hexagons and the slip directions in those planes are parallel to the diagonals.
- In body-centred cubic crystals there are six planes of closest packing and two slip directions in each, for a total of twelve primary slip systems.
- Face-centred cubic crystals have twelve primary slip systems: the close-packed planes are the four octahedral planes ($\{111\}$ type), and each contains three face diagonals as the closest-packed lines ($[110]$ types). As a result, fcc metals (such as aluminium, copper or gold), exhibit considerably more ductility than hcp metals.

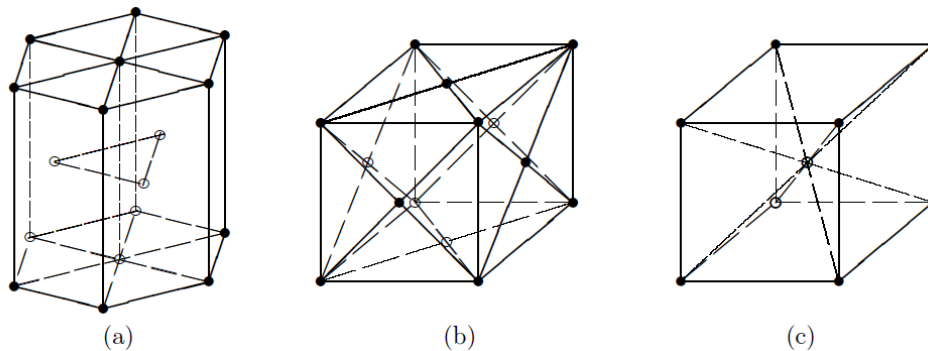


Figure 1-25 – Crystal structures: a) hexagonal close-packed (hcp); b) face-centred cubic (fcc); c) body-centred cubic (bcc). From ^[3].

The latter is the crystal form that is of interest for this work, as the crystalline lattice of CoCrFeMnNi at room and cryogenic temperatures is fcc. As stated in the previous sections, in fcc alloys slip systems are made of perfect $a/2[110]$ dislocations gliding on $\{111\}$ -type planes (Figure 1-26), as the smallest Burgers vectors possible in fcc crystals point along the various $[110]$ directions.

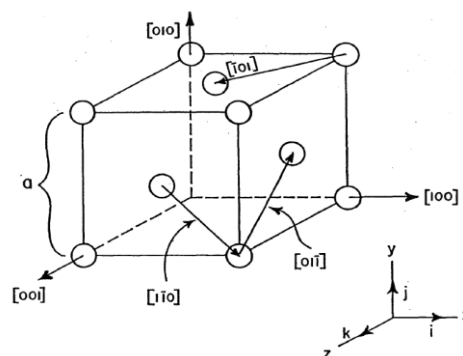


Figure 1-26 – Slip systems in fcc crystals. From ^[4].

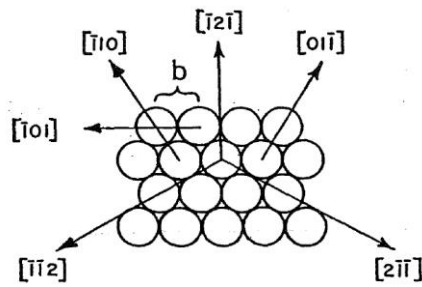


Figure 1-27 – The (111) plane in an fcc crystal. From [4].

Considering a as the lattice parameter of an fcc crystal, the length of the smallest Burgers vector possible for a perfect dislocation in this crystal structure is $a/\sqrt{2}$ [4]. This Burgers vector can be written as

$$\mathbf{b} = \frac{a}{2} [110]$$

Equation 1-9 – Burgers vector of a perfect dislocation in an fcc crystal.

where $[110]$ represents the vector $\vec{i} + \vec{j}$ (or its equivalent) [4].

Dislocations of the type $(a/2)[110]$ that lie on (111) planes may lower their energy by combining among themselves or by splitting into several new dislocations. Such a split creates a mobile imperfect (partial) dislocation, known as a Shockley dislocation [99]. Comparing with Figure 1-27 –, a dislocation line that lies along a $[1\bar{1}0]$ direction will have a Burgers vector pointing in a $[11\bar{2}]$ direction, equal to $a/\sqrt{6}$ in length [4]. Hence, the Burgers vector for a Shockley partial can be written as

$$\mathbf{b} = \frac{a}{6} [11\bar{2}]$$

Equation 1-10 – Burgers vector of a Shockley partial dislocation in an fcc crystal.

The most important reaction involving perfect and imperfect dislocations is the dissociation of a perfect dislocation into two Shockley dislocations [4]. For example, Figure 1-27 – shows that a perfect dislocation with a Burgers vector of $(a/2)[\bar{1}01]$ can split into two Shockley dislocations with the following Burgers vectors (Figure 1-28):

$$\frac{a}{2} [\bar{1}01] \rightarrow \frac{a}{6} [\bar{2}11] + \text{Stacking Fault} + \frac{a}{6} [\bar{1}\bar{1}2]$$

Equation 1-11 – Split of a perfect dislocation into two Shockley partials in an fcc crystal.

Both of these dislocations slip onto the (111) plane. The dissociation can occur with either a single or a double stacking fault. According to Anderson et al. [79], the Burgers circuit for a partial dislocation must start and end on the plane of the stacking fault.

All the possible combinations of slip systems are represented in Figure 1-29 – , which shows the “Thompson tetrahedron”, where all four {111} planes with their respective [110] and [112] type of vectors are represented.

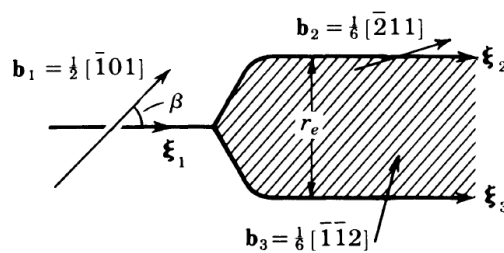


Figure 1-28 – Dissociation of a perfect dislocation into Shockley partials, with the stacking fault visible in between them. From [79].

3.3. Twinning

There are two different types of twinning: annealing and deformation. Annealing twinning occurs in the alloy grains during recrystallization processes, while deformation twinning appears once a sample of the alloy is subjected to external stress. This section will only describe deformation twinning (also called mechanical twinning), which is a particularly important deformation mechanism in crystals with only a limited number of slip systems [79].

Deformation twins formally correspond to rotation twins [79]. If one half of the crystal is rotated by π around an axis normal to the twin plane or around the shear direction in the twinning plane, it will join with the other half to form an unfaulted single crystal. The twin can be formed by shear, as seen in Figure 1-30. Because the deformation is a pure shear, the plane parallel to the large twin interface remains undistorted.

A deformation twin can be created by the motion of partial dislocations [4]. As an example, Figure 1-30 presents a Shockley dislocation of Burgers vector $(a/6)[112]$ that moves across each (111) close-packed plane contained in a section of an fcc crystal. The stacking sequence in this section would be changed from ABC to CBA (assuming that only single stacking faults are attached to the partial dislocations).

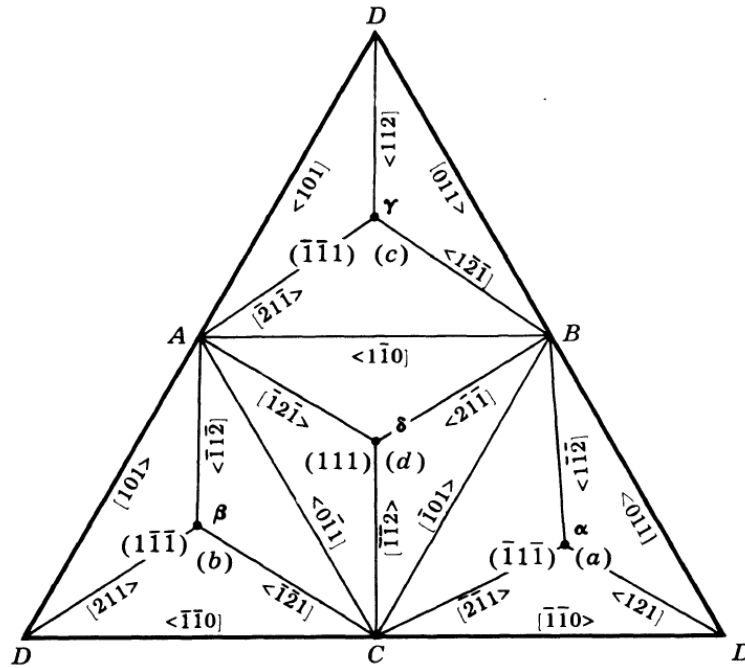


Figure 1-29 – A Thompson tetrahedron opened up at corner D. Notation example: (a) for glide plane, AB for Burgers vector of perfect dislocation, Aδ for Burgers vector of partial dislocation. The notation $[1\bar{1}0 >$ is used to indicate the sense of the direction. From [79].

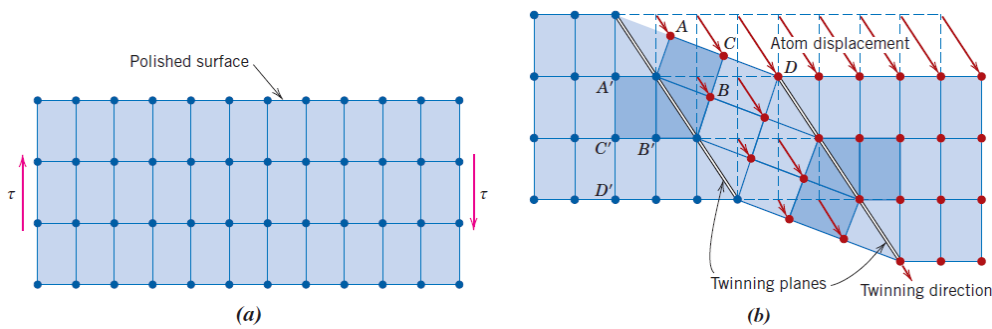


Figure 1-30 – Resulting twinning from an applied shear stress τ . a) Atom positions before twinning. b) After twinning; blue circles represent atoms that were not displaced, red circles depict displaced atoms. Atoms labelled with corresponding primed and unprimed letters (e.g., A' and A) reside in mirror-image positions across the twin boundary. From [75].

The affected region, called the twinned region, is a mirror image of the rest of the crystal. The stacking order after the occurrence of a fault is identical to the original one. This means that, as a result of twinning, the first plane that is “faulted”, as compared to the original stacking order, is the first plane beyond the twinning plane, and all other planes in the twinned region are “faulted” as well, with reference to the original stacking order. So the stacking fault can be regarded as one single layer of twinned material [101].

High strain rates, low stacking-fault energy and low temperatures facilitate deformation twinning (see ^[102]). While the stacking fault then is a very localized error, the twinning affects macroscopically large volumes. The removal of (part of) a closed-packed plane leads to an intrinsic stacking fault whereas the insertion of (part of) a closed-packed plane leads to an extrinsic stacking fault (see Figure 1-31), and one extrinsic fault is equivalent to two intrinsic faults in the stacking sequence.

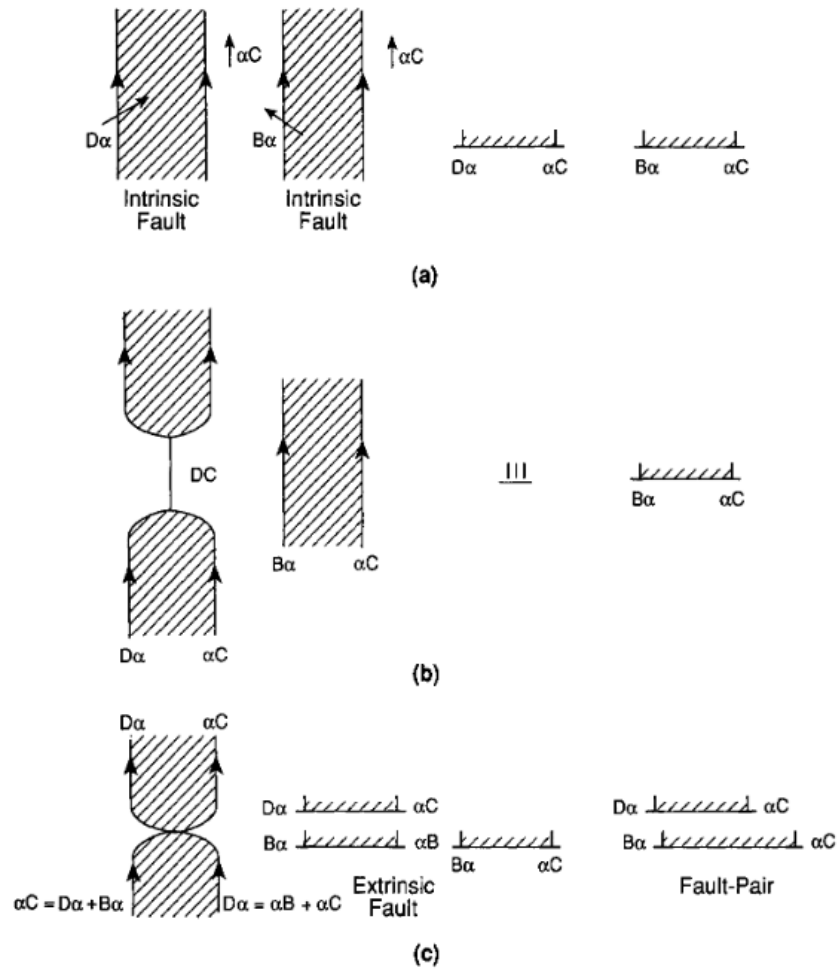


Figure 1-31 – Schematics of the formation of a fault pair in fcc crystals. From ^[102].

As a summary, so far, the previous sections presented: the MPEA world, its characteristics and properties, particularly the mechanicals, and introduced CoCrFeMnNi alloy as a solid solution that crystallises in the fcc form; also, the fundamental concepts of plasticity, with a focus on dislocation behaviour and twinning on fcc crystals. The next section will concentrate on CoCrFeMnNi alloy and its deformation mechanisms when subjected to external stress.

4. Cantor Alloy

4.1. Definition and microstructure

Cantor alloy is an equiatomic quinary alloy, composed of cobalt, chrome, iron, manganese and nickel. As already stated in section 1.2.4, it belongs to the 3d transition metal family and is a type I MPEA (fcc-structured).

Since its first report in 2004 [22], CoCrFeMnNi, also known as Cantor alloy, has been one of the most studied MPEAs due to it being a prototypical single-phase disordered solid solution (SS) alloy, which contributing to its popularity, according to Miracle and Senkov [12]. This popularity is evidenced by the many publications that either study or mention it, counting over 15 000 results for “Cantor alloy” on Google Scholar – up to July 2021 (Figure 1-32).

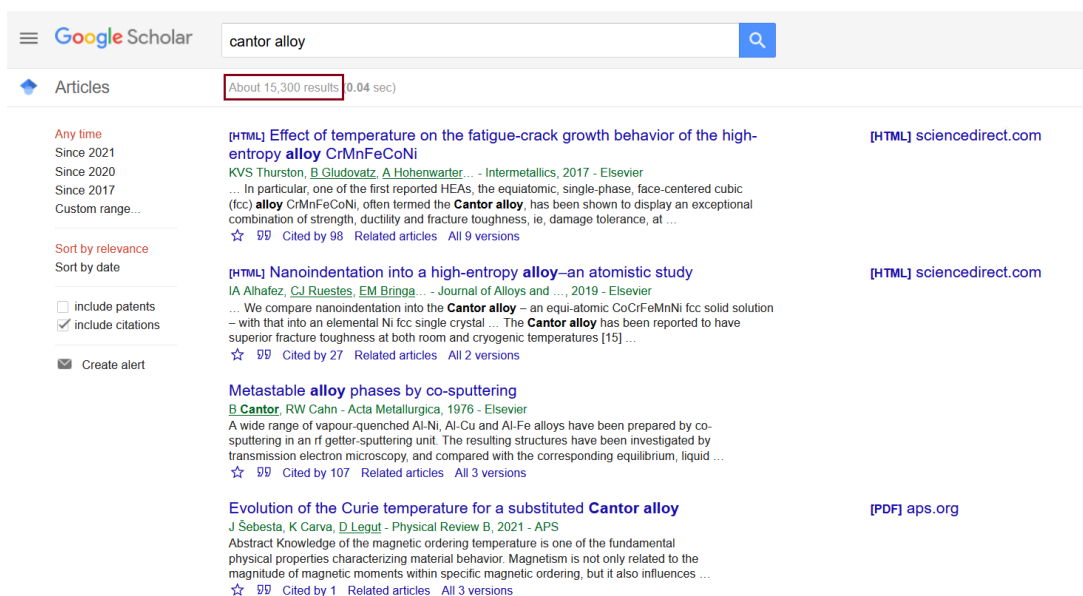


Figure 1-32 – Screen capture of “Cantor alloy” search on Google Scholar at the time of this study.

XRD, SEM, TEM, EBSD and atom-probe tomography experiments have been conducted extensively to examine CoCrFeMnNi microstructure [52]. The results show that the alloy is a single-phase, fcc, solid solution with no indication, so far, of clustering or short-range ordering (SRO). George et al. [52] clarify that if such local ordering were experimentally proven to exist, density functional theory (DFT) calculations suggest that it would have a profound effect on critical properties (stacking-fault energy and dislocation mobility).

It was reported by Otto et al. [103] that SRO decomposes into metallic (bcc-Cr) and intermetallic (L1₀-NiMn and B2-FeCo) phases below about 800°C. Nonetheless, after heat treatments above 800 °C, the metastable fcc SS state is reported to be retained at room

temperature at “normal” cooling rates [52]. After deformation processing and recrystallization, Laplanche et al. [60] report that the crystallographic texture is weak and close to random. At very low temperatures, below about 50 K, computations based on DFT show that the fcc structure of the Cantor alloy becomes unstable and transforms to the hcp structure [52].

The microstructure and, hence, the mechanical properties of Cantor alloy depend on the local atomic distribution in the fcc lattice. Murty et al. [14] described it as follows (also see Figure 1-5):

- a) There is a very large number of different local atomic environments or configurations with, for example, different A atoms surrounded by a wide range of different distributions of the other A, B, C, D and E atoms.
- b) There are significant local atomic distortions and lattice strains, caused by the different sizes of the different atoms and their varied local atomic environments.

Cantor published a review that comprises the current understanding of his alloy and its derivatives [104]. In it, he describes the local atomic distribution by considering a general lattice with a single atom at each lattice point with n_1 first near neighbours. The cluster size of each atom together with its n_1 first near neighbours is $n_1 + 1$ atoms (cluster: N_1). Cantor continues to explain that if there are $n_1 + 1$ atoms in a multicomponent equiatomic single-phase material with c components, the number of clusters is given by the law of permutations with repetition:

$$N_1 = c^{n_1+1}$$

And extending the cluster size to include the second near neighbours, the number of different clusters N_2 of $n_2 + n_1 + 1$ atoms is given by:

$$N_2 = c^{n_2+n_1+1}$$

Each atom in a single-phase fcc material has $n_1 = 12$ first and $n_2 = 6$ second near neighbours (refer to Cantor [104] for the references on these affirmations and calculations). For the Cantor alloy (5 components), there is a total of more than a billion different local atomic environments including first near neighbours only; and there is a total of almost twenty trillion local atomic environments including first and second near neighbours (the latter number is probably more relevant, since first and second near neighbour atomic interactions are both usually significant in fcc materials) [104]. This means that a piece of the alloy sufficiently large to include all possible local atomic configurations out to second near neighbours and to fully represent the alloy and its properties must have a linear

dimension equivalent to 2.7×10^4 adjacent clusters or be approximately 27 μm in size (Cantor considers cluster dimension as 1 nm ^[104]).

That is, individual grains smaller than 27 μm can be expected to have properties that deviate from the mean CoCrFeMnNi, and a sample of the alloy with a grain size below 27 μm will have properties that vary from grain to grain. According to Cantor, this is a very different situation than what is found in conventional materials (of either a single component or a single main component with one or more dilute alloying additions) ^[104]. The large number of different local atomic environments in multicomponent single-phase fcc SS is expected to play an important role in properties that depend strongly on local atomic interactions or dislocation slip and plastic flow.

4.2. Mechanical properties of Cantor alloy

Several reports on the behaviour of this alloy have been published. Gali and George ^[59] experimentally showed that strength has a strong temperature dependence below 473 K, which weakens at elevated temperatures up to 1273 K, and a modest strain-rate dependence at low homologous temperatures. In their review, George et al. ^[52] highlight that the alloy strength and ductility both increase with decreasing temperature (down to the cryogenic range), with ultimate strengths above 1 GPa and 60% elongations at 77 K. They also remark high ductility, caused by the delay in necking as the work-hardening rate is inversely proportional to temperature.

Otto et al. ^[19] showed representative engineering stress-strain curves for CoCrFeMnNi samples of different grain sizes (fine grain samples = 4.4 μm , coarse grain samples = 155 μm) at six different temperatures (tensile tests performed at engineering strain rate of 10^{-3} s^{-1} , at 77 K, 293 K, 473 K, 673 K, 873 K and 1073 K). These curves are found in Figure 1-33. The engineering strain in these curves is the ratio of cross-head displacement to the initial specimen gauge length (12.7 mm). They obtained the highest values of yield strength, ultimate tensile strength and elongation to fracture at liquid nitrogen temperature (77 K), and found that an increase in temperature results in a monotonic decrease in both the yield and ultimate tensile strengths.

They ^[19] also quantified (Figure 1-34) the temperature and grain size dependencies of the 0.2% offset yield strength σ_y , ultimate tensile strength σ_{uts} and elongation to fracture ϵ_f , finding that the strengths and the ductility show strong temperature dependencies, with their maxima also occurring at 77 K, and that for all grain sizes, σ_y and σ_u decrease monotonically with increasing temperature.

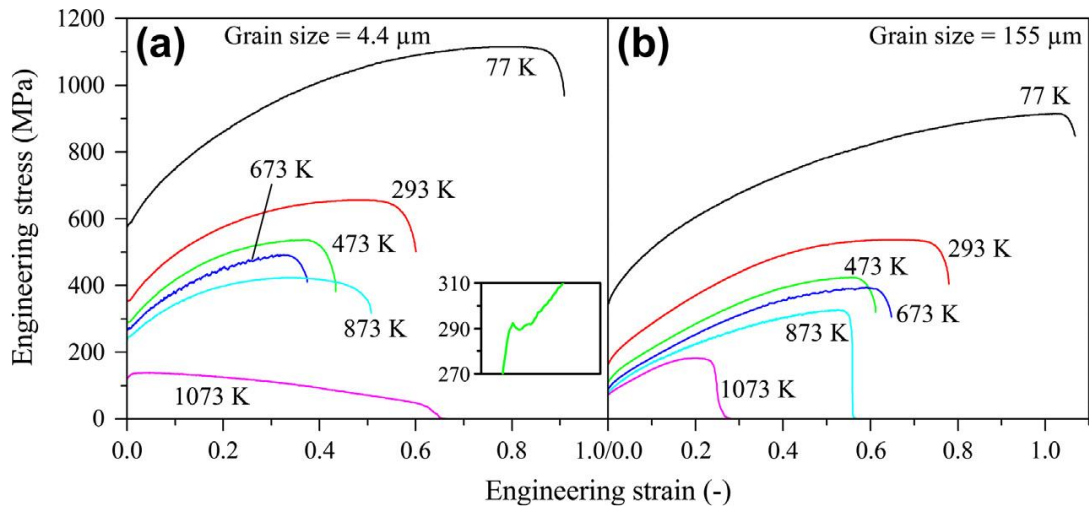


Figure 1-33 – Representative engineering stress–strain curves of the CoCrFeMnNi alloy at the six testing temperatures for the: a) fine-grained and b) coarse-grained. The inset in a) shows a small load drop after yielding for a fine-grained sample that was tested at 473 K. From [19].

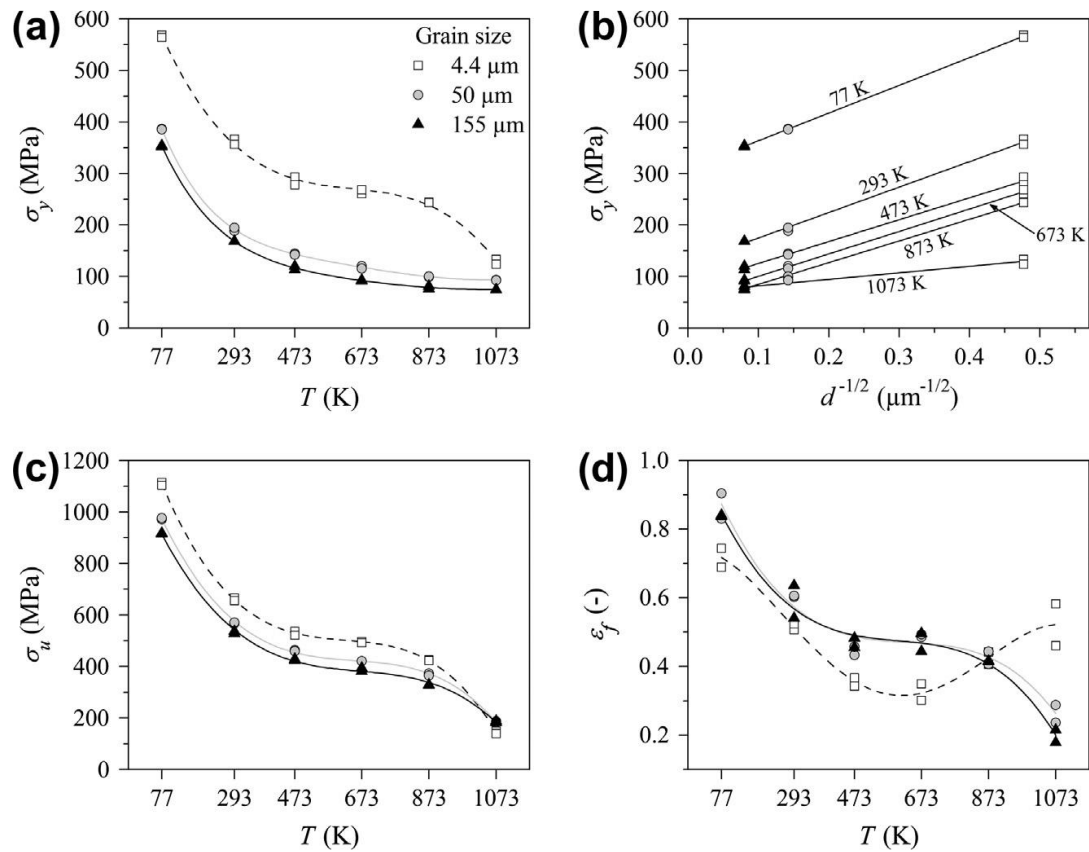


Figure 1-34 – Temperature and grain size dependence of: a) - b) 0.2% offset yield stress (σ_y), c) ultimate tensile strength (σ_{uts}), and d) elongation to fracture (ϵ_f). From [19].

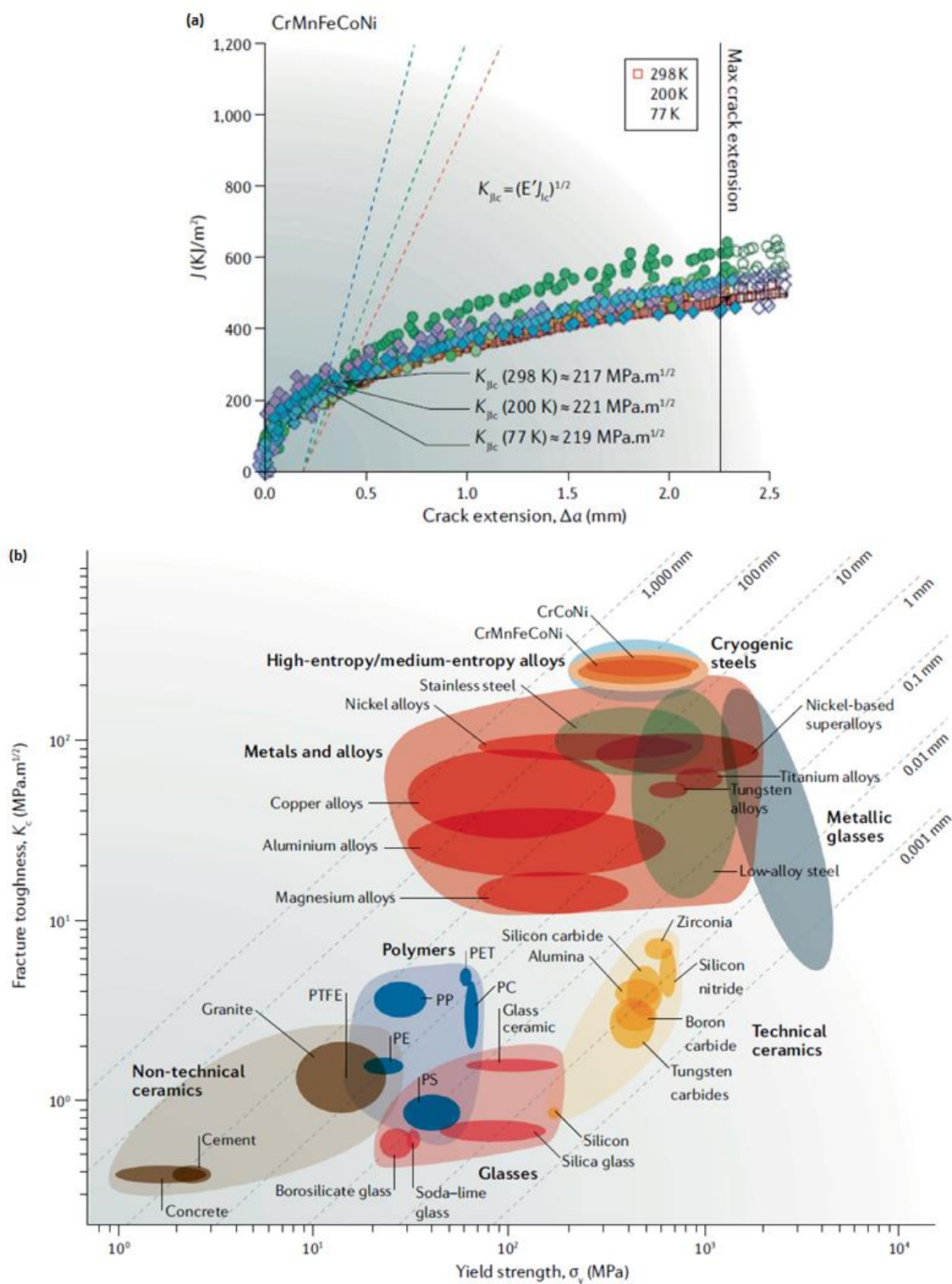


Figure 1-35 – Damage-tolerant properties of the Cantor CoCrFeMnNi alloy. a) Fracture toughness, crack resistance curves. b) Ashby plot of strength versus fracture toughness showing that CoCrNi-based, medium-entropy and high-entropy alloys are among the most damage-tolerant materials on record. From [52].

In their review, George et al. [52] summarise CoCrFeMnNi mechanical properties, and conclude (as Gludovatz et al. [51] also did) that it exhibits exceptional strength, ductility

and fracture toughness (Figure 1-35). Its crack-initiation toughness (K_{JIC}) is $\sim 220 \text{ MPa} \cdot \text{m}^{1/2}$, roughly independent of temperature from room temperature down to 77 K, whereas its crack-growth toughness goes above $\sim 300 \text{ MPa} \cdot \text{m}^{1/2}$ (increasing resistance to cracking as the crack length increases).

George et al. [52] conclude that, even though an increase in strength and ductility with decreasing temperature is seen in other fcc alloys (as in austenitic stainless steels), the uniqueness of Cantor alloy resides on its holding of high toughness at cryogenic temperatures (contrary to most materials that become more brittle as the temperature is decreased).

4.2.1. Dislocation behaviour of Cantor alloy

During a tensile test, dislocation slip is the main deformation mechanism. At room temperature, slip occurs by planar glide of $1/2 \langle 110 \rangle$ perfect dislocations on $\{111\}$ planes [19,58,60]. These perfect dislocations split into $1/6 \langle 112 \rangle$ Shockley partial dislocations, which, according to Okamoto et al. [58], bound a stacking fault with average splitting distances ranging from $\sim 3.5 - 4.5 \text{ nm}$ for the edge orientation to $\sim 5 - 8 \text{ nm}$ for the screw orientation, yielding a stacking fault energy of $30 \pm 5 \text{ mJ} \cdot \text{m}^{-2}$. Otto et al. [19] conclude that the relatively large partial separations (especially when normalized by the Burgers vector) imply that cross slip is difficult in this alloy, which is consistent with the planar slip and long dislocation pile-ups they observed at grain boundaries.

At lower magnifications, the dislocations are long and smoothly curved on the $\{111\}$ planes without any preferred line direction, implying similar mobilities of edge and screw segments [52,58]. Zhang et al. [61] performed *in situ* TEM straining experiments that suggest that the Shockley partials are more mobile than the perfect (undissociated) ones, which are very sluggish. Nevertheless, George et al. [52] caution against drawing conclusions on dislocation mobility from *in situ* observations, as no information regarding the locally resolved shear stress acting on the moving dislocations was available at the time of their review (2019).

Laplanche et al. [60] studied the microstructure evolution of CoCrFeMnNi at different temperatures and concluded that it is distinctly different when the straining is carried out at cryogenic temperatures. At 77 K, the distribution of dislocations and their density evolution with strain is initially similar to that at room temperature, as shown in Figure 1-36. They [60] showed in this figure (with same magnification and contrast conditions, $\vec{g} = (111)$, and similar true strain levels) that the microstructural evolution is associated with the formation of dislocation pile-ups. At around 20% strain, larger strains result in higher dislocation densities and eventually to their reorganization into cell structures. They

measured dislocation densities after deformation at 293 K and 77 K up to 20% strain using TEM. They showed the change in dislocation density ρ as a function of strain in Figure 1-21 (see Figure 1-18 in section 2.5.3.4).

According to the Taylor hardening model, the increase in shear stress ($\Delta\tau$) due to forest dislocation interactions is given by:

$$\Delta\tau = \frac{\Delta\sigma}{M} = \alpha\mu b\rho^{1/2}$$

Equation 1-12 – Shear stress in Taylor hardening model.

where $\Delta\sigma$ is the corresponding increase in the tensile stress, M is the Taylor factor (3.06), α is a constant, μ is the shear modulus (85 GPa at 77 K and 80 GPa 293 K) ^[105,106], b is the magnitude of the Burgers vector (0.254 nm at 77 K and 0.255 nm at 293 K) ^[106], and ρ is the dislocation density ^[60].

Zhang et al. ^[61] performed *in situ* TEM straining experiments to study the damage tolerance of this alloy and correlated it to dislocation behaviour, through the examination of the microstructural evolution next to a crack. They identified multiple deformation mechanisms activated at different stages of deformation, initiating by the motion of the Shockley partials and the corresponding formation of SFs. When they increased the applied stress, perfect dislocations started to move (albeit with difficulty) in localized bands containing arrays of many closely packed dislocations. These bands act as strong barriers for partial dislocation motion, which creates an outstanding strengthening effect.

Ding et al. ^[107] also performed *in situ* TEM straining experiments and found coherent twin boundaries that act as barriers for perfect dislocations but also offer them a glide path at 77K (Figure 1-37). They found that perfect glide of dislocations generated plastic strains without causing twin boundary migration, and also cross-slip at the beginning of plastic deformation (Figure 1-38). The cross-slip activity facilitated the interaction between dislocation in the primary and secondary slip systems.

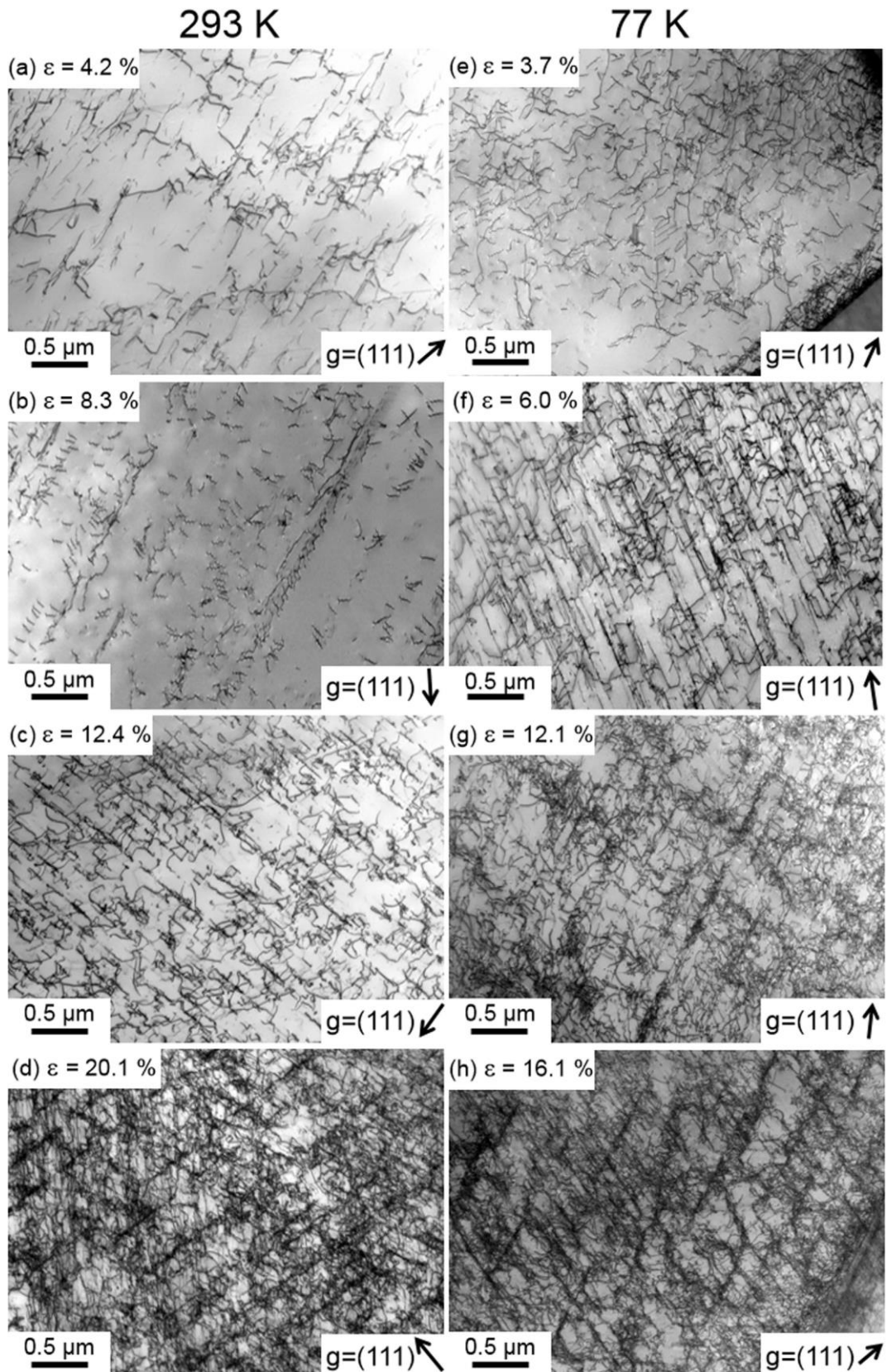


Figure 1-36 – TEM micrographs showing the evolution of dislocation structure with increasing true tensile strain at (a-d) 293 K and (e-h) 77 K. From ^[60].

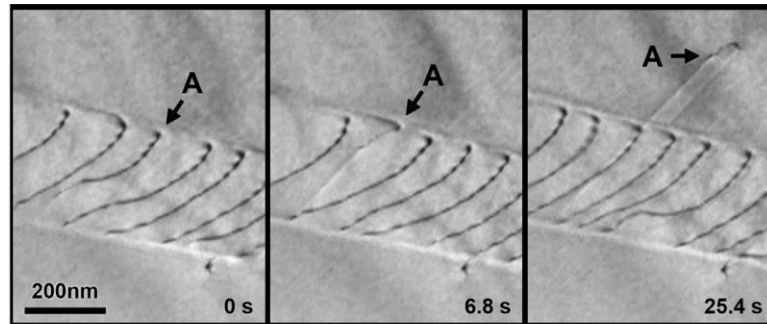


Figure 1-37 – Dislocation behaviour at 93K. “Dislocation A” cross-slips onto a secondary slip plane when its motion becomes impeded in the primary slip plane. From [107].

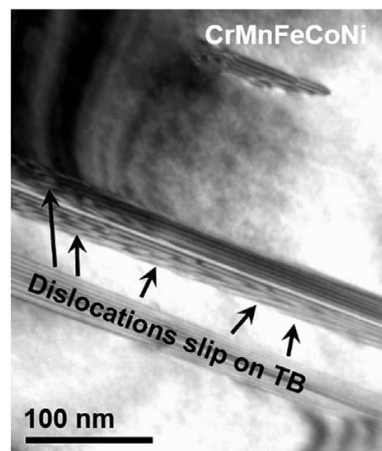


Figure 1-38 – Glide of full dislocations on twin boundaries at 93 K. From [107].

4.2.2. Mechanical twinning

Mechanical twinning is a competing deformation process to dislocation slip. The nucleation of mechanical twinning is assisted by stress concentrations to overcome the critical resolved shear stress for twinning, $\tau^{\text{CRSS-twin}}$ [53], which, according to Venables' theory, is [53,102,108]

$$\tau^{\text{CRSS-twin}} = \frac{\gamma b}{b_1(nb - b_1)}$$

Equation 1-13 – Venables' CRSS for twinning.

where γ is the SFE, b is the Burgers vector of the unit dislocation, b_1 is the Burgers vector of the Shockley partial dislocation, and n is the stress-concentration factor (which explains why twins were observed in some areas of the same crystal while in others, a high dislocation density was found). According to Meyers et al. [109], a low SFE is a necessary condition for the activation of mechanical twinning. Diao et al. [53] compared SFE values of

different alloys/elements, emphasising the ones where twinning activation is easier (Figure 1-39).

The resulting morphology of mechanical twins have thicknesses ranging from a few tens of nanometres to a few micrometres ^[19,51,53,60]. The crystallographic structure of faulted twin boundaries is characterized by a $\Sigma 3$ orientation difference, compared to the matrix.

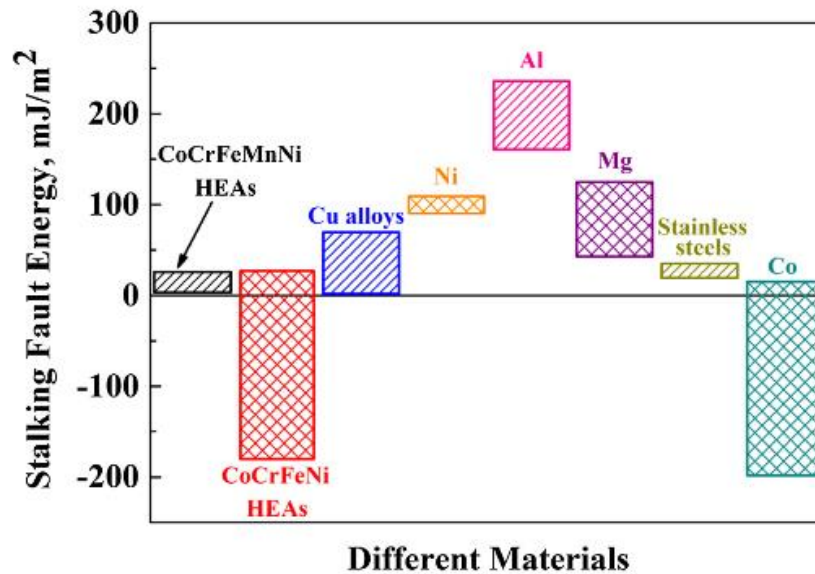


Figure 1-39 – Low stacking fault energy (SFE) of HEAs, compared with other conventional alloys, which is a necessary condition for the activation of mechanical twins. From ^[53].

In their study of 2016, Laplanche et al. ^[60] concluded that dislocation hardening only is not sufficient to attain the observed work hardening rate and thus that twinning is needed to explain the increased strength-ductility combination as temperature decreases. Therefore, they suggest that the microstructural evolution is similar at 77 K and 293 K, and that for strains below ~7.4%, there is only dislocation plasticity and the dislocation density increases similarly at the two temperatures, and after this strain twinning is activated as an additional deformation mode.

Based on an average of 10 tests at each 77K and 293 K, Laplanche et al. ^[60] found that the engineering yield strength σ_y increased from 265 ± 10 MPa to 460 ± 30 MPa and σ_{uts} increased from 600 ± 40 MPa to 1060 ± 70 MPa when the temperature decreased. Along with this gain of strength, they also found the tensile ductility also increased by ~50% when the temperature dropped to 77 K.

Their reported results can be found in Figure 1-40. Panel (c) shows the true strain hardening rate normalized by the shear modulus $((d\sigma/d\varepsilon)/\mu)$ as a function of the true strain. There, the strain hardening rate shows a monotonic decay with increasing strain at 293 K, diverging from the strain hardening rate at 77 K, which reveals three distinguishable stages: first, a continuous decrease in the strain hardening rate from $\sim\mu/20$ to $\sim\mu/30$ at $\sim 10\%$ true strain (similar to what is observed at 293 K); then, at larger strains (10-35%), the strain hardening rate remains almost constant around $\mu/30$; and finally, the strain hardening rate decreases until rupture at $\sim 44\%$.

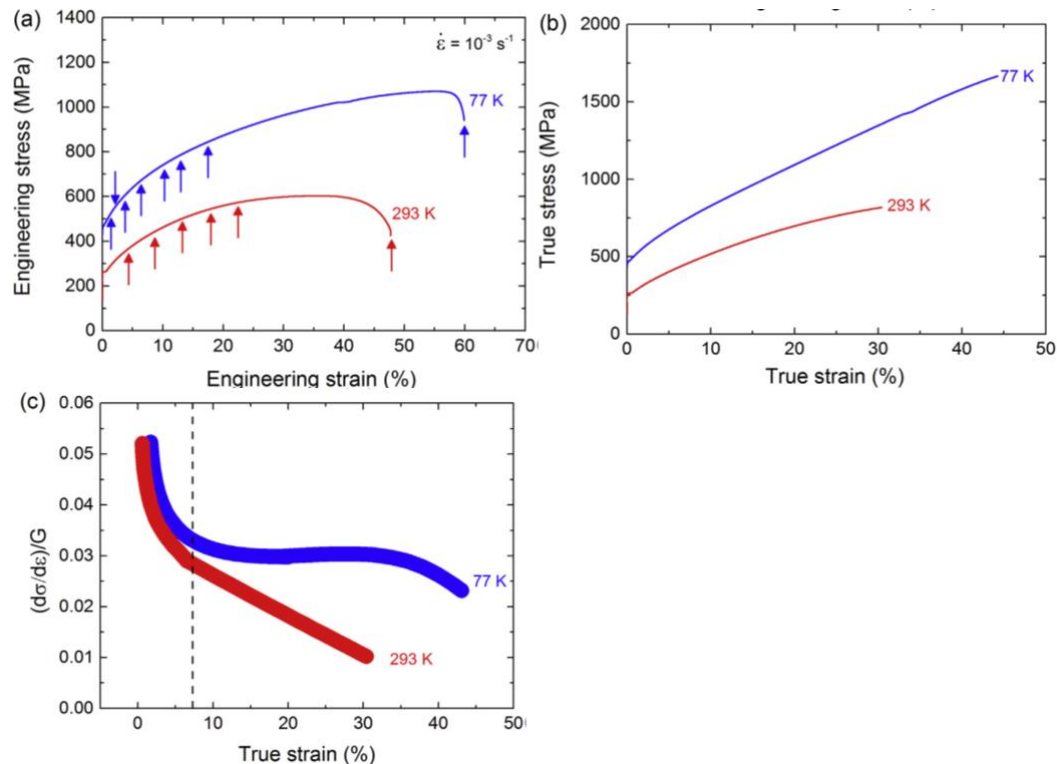


Figure 1-40 – Representative: a) engineering and b) true stress-strain curves of tensile tests at 77 K and 293 K. The arrows in a) indicate the strains at which several additional tensile tests were interrupted to study the evolution of microstructure. c) True strain hardening rate normalized by the shear modulus as a function of true strain. From [60].

Based on this, Laplanche et al. [60] conclude that, at 77 K, the true strain at which twins can be consistently observed is between 6.0% and 8.8%, or $7.4 \pm 1.4\%$, and they refer to this value as the “twinning stress” $\sigma_{tw} = 720 \pm 30$ MPa at 77 K, which, according to them, is the critical stress where twinning should be observed. This twinning stress is characteristic of a given material and grain size, hence, twinning should be observed also at room temperature as long as the stress in the tensile specimens reaches this value. However, George et al. [52] caution against this result, as the polycrystalline material investigated by the Laplanche team had a relatively small grain size of $17 \mu\text{m}$ and, according to Meyers et al. [110], the predisposition to twinning is enhanced as the grain size is increased.

They ^[60] then strained their specimens to 22.3% at room temperature to reach the critical twinning stress of ~ 720 MPa, and found no twins on a 680 MPa strained specimen, but did on an 820 MPa strained specimen. Their reasoning for this discrepancy is that at 293 K, there is much lower yield strength as a result of which higher strains are required to reach the twinning stress by work hardening. This result is in agreement with the one from Otto et al. ^[19]. Their conclusion ^[60] is that twinning shear makes a relatively small contribution to the total tensile strain because of the relatively low volume fraction of twins, however, it contributes significantly to strain hardening because of the extra boundaries introduced during twinning (dynamic Hall-Petch effect).

Ding et al. ^[107] performed *in situ* TEM straining experiments, finding twinning formation and growth that indicates it serves as an important deformation mechanism at cryogenic temperatures. In contrast, they rarely observed twinning at room temperature during their *in situ* TEM straining.

In contrast to the previously mentioned studies, Kireeva et al. ^[71] deformed [111]-oriented crystals at room temperature, observing twinning at a strain of 5%, which developed simultaneously with dislocation slip in several systems. When the applied strain was increased to 27%, the twinning density also increased (see Figure 1-41 (a)-(b)). They determined the thickness of the twins to be 15–25 nm. They also deformed [123]-oriented crystals, and observed partial dislocations and stacking fault formation at a strain of 10%, and twinning at a strain of 27% (Figure 1-42).

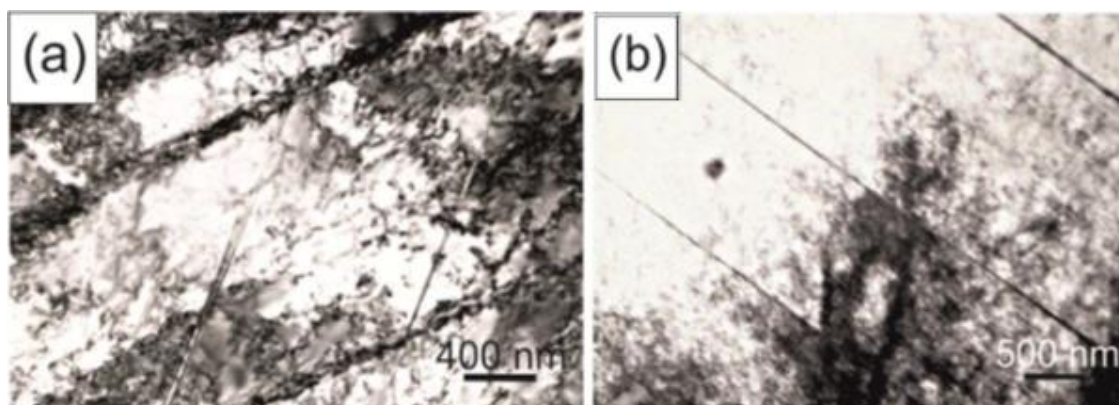


Figure 1-41 – Twinning in the [111]- oriented crystals of the CoCrFeMnNi HEA under tension at RT after the application of various tensile strain levels: a) bright field TEM image after a strain of $\epsilon = 5\%$; b) bright-field image after $\epsilon=27\%$. From ^[71].

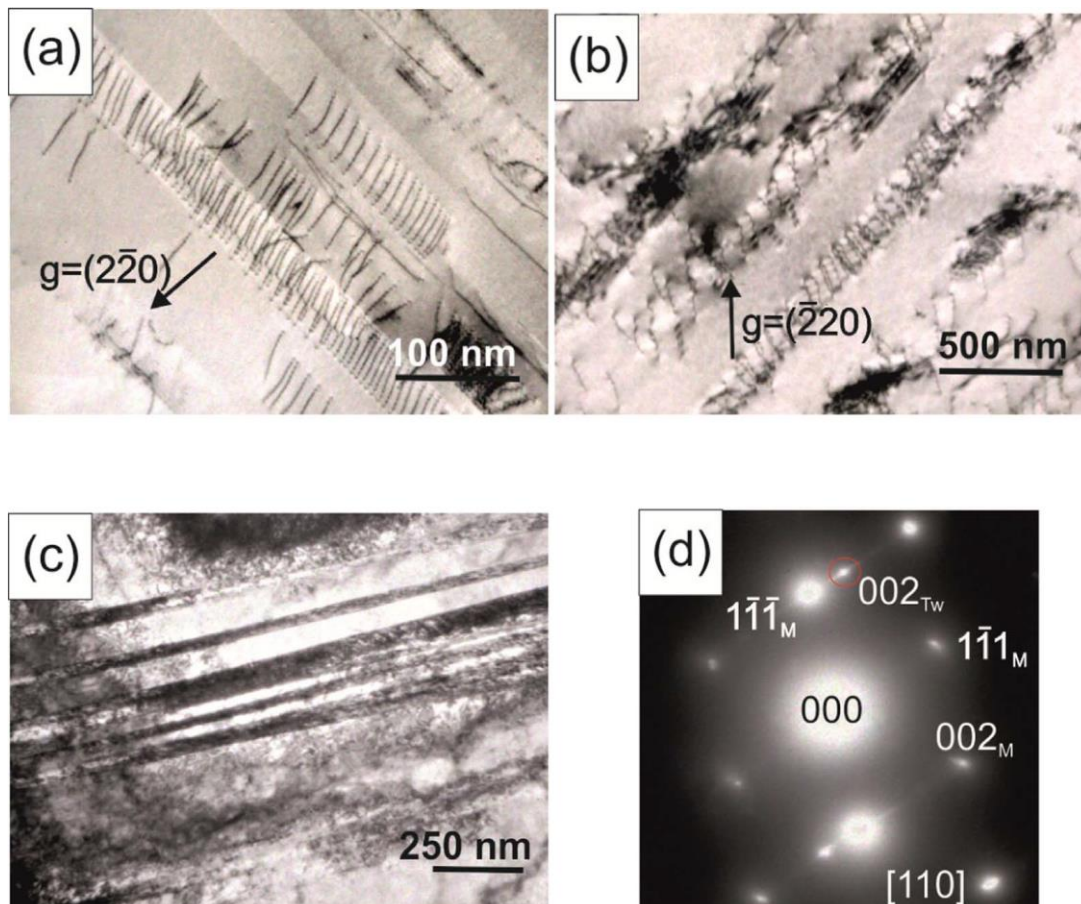


Figure 1-42 – Dislocation structure in the [123]- oriented crystals of the CoCrFeMnNi HEA under tension at RT after the application of various tensile strain levels: the bright field TEM images after the strain of: a) $\epsilon = 5\%$; b) $\epsilon = 10\%$; c) $\epsilon = 27\%$; and d) the corresponding diffraction pattern for the image in c), indicating that the inclined long features are deformation twins. From ^[71].

They ^[71] showed that in tensile deformation at RT, the CRSS for slip in single crystals of CoCrFeMnNi does not depend on the crystal orientation and that the Schmid law is satisfied. However, the dislocation structure of the single crystals deformed does. This orientation dependence of the dislocation structure in the early stages of deformation is dictated by the number of slip systems activated. In accordance to their previous work^[111], they observed twinning at both room temperature and 77 K.

Assuming that the twin boundaries act like grain boundaries, that is, as barriers to dislocation motion, the decrease in twin spacing with strain is indicative of a dynamic Hall–Petch effect that provides hardening to counteract the softening due to dislocation recovery processes ^[52]. This additional strengthening mechanism maintains a constant work-hardening rate at strains at which dislocation hardening fades away. George et al. ^[52] reviewed many TEM studies of samples taken from interrupted mechanical tests, and found that at 77 K and 293 K the corresponding tensile stresses were ~ 720 MPa, indicative

of a temperature-independent twinning stress, similar to what has been seen in many other materials, according to Meyers et al. [110].

4.2.3. Stacking fault energy and short range order in CoCrFeMnNi

As already stated, twins usually hinder dislocation motion and induce strengthening, but multiple twinning systems can also enhance ductility, for example, in twinning-induced plasticity (TWIP) steels or CoCrFeMnNi, which have low stacking fault energies and, therefore, relatively large separations between the Shockley partials [62,70].

Several simulation studies (DFT-based Monte Carlo, *ab initio* modelling, molecular dynamics simulation) [70,111–114] have been made to predict the degree of local chemical order influences in the SFE in CoCrFeMnNi and its derivate (“medium-entropy”, three element alloys, i.e. CoCrNi, etc. – see Figure 1-43), and also the twinning energy, the energy difference between the fcc and hcp phases (which governs the TRIP and TWIP effects) and the formation energy for point defects, all of which are parameters that are known to markedly affect the strength and deformation of CoCrNi-based HEAs [52].

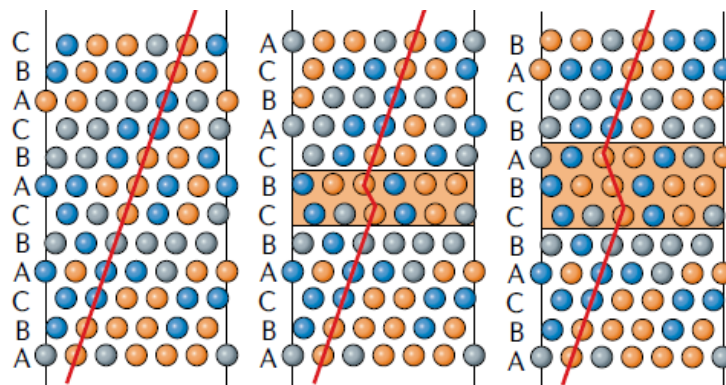


Figure 1-43 – Role of local chemical ordering on the stacking fault energy calculated by DFT for solid-solution CoCrNi alloys. Side view of atomic configurations in an originally fcc structure (left), with intrinsic stacking faults (middle) and extrinsic stacking faults (right). The orange shade indicates the stacking fault (ABC represent close-packed (111) planes). From [114].

Zaddach et al. [115] measured the SFE for CoCrFeMnNi by X-ray diffraction and obtained a value between 18.3 - 27.3 mJ/m². Huang et al. [112] quantified it at room temperature by experimental measurement and by *ab initio* calculations (using a supercell of nine fcc (111) layers with one intrinsic SF), and obtained a value of ~21 mJ/m². They also studied the SFE temperature dependency (Figure 1-44), suggesting that CoCrFeMnNi is more likely to deform by twinning with decreasing temperature. Zhao et al. [113] also calculated this temperature dependency, finding a dependent coefficient $d\gamma/dT = 0.11$ mJ/m²/K.

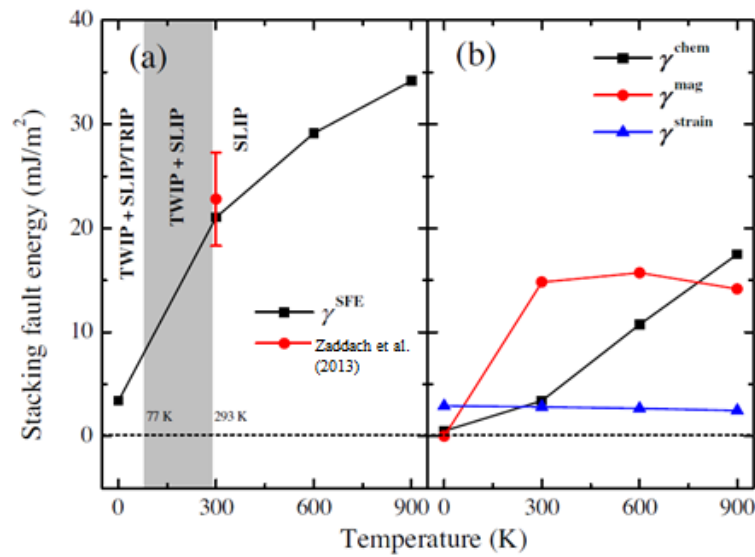


Figure 1-44 – Theoretical SFE of CoCrFeMnNi high entropy alloy. a) Total SFE $\gamma^{SFE} = \gamma^{chem} + \gamma^{mag} + \gamma^{strain}$. b) Individual contribution: chemical part γ^{chem} , magnetic part γ^{mag} and strain part γ^{strain} . From [112].

Smith et al. [62] performed high-resolution TEM observations on the Cantor alloy and showed that the separation between partial dislocations is highly variable (by a factor of two) at different points along the dislocation. Their calculations suggest that this may be due to variations in the local composition, affecting the local stacking fault energy and thus the partial separation (Figure 1-45).

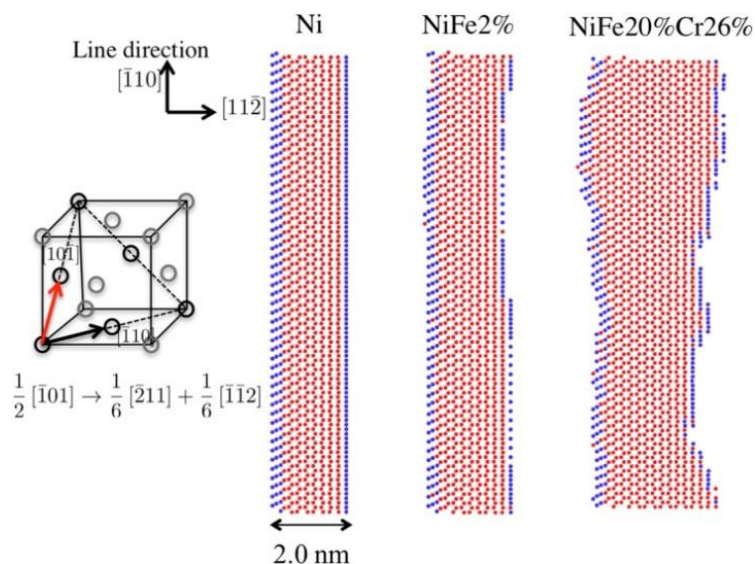


Figure 1-45. Variations in dissociation distance of a mixed $\frac{1}{2} [\bar{1}0\bar{1}]$ dislocation in concentrated Ni-20 at%Fe- 26 at%Cr compared to pure Ni and dilute Ni-2at%Fe alloy. The dislocations are created in bulk geometry with periodic boundary conditions in the line direction. Blue atoms belong to the partial dislocations, while red atoms comprise the stacking fault region between the partials. The dissociation distance varies along the dislocation line in the concentrated alloy. From [62].

Huang et al. [112] calculated the stacking fault energy as a function of temperature for the Cantor alloy, concluding it abruptly decreases to $\sim 3.4 \text{ mJ m}^{-2}$ at 0 K. As lower stacking fault energies enhance twinability [116,117], these calculations are consistent with the experimental observation that the Cantor alloy tends to twin more readily as the temperature is decreased [46].

The role of local chemical order in HEAs remains an open issue because few experiments have confirmed it experimentally [52]. One study, by Zhang et al. [118], used extended X-ray adsorption fine structure on CoCrNi and suggested that Cr atoms display a preference to bonding to Ni and Co atoms rather than other Cr atoms, which, according to George et al. [52], is consistent with DFT-based Monte Carlo predictions. However, more experimental confirmation is needed to affirm that such local chemical order actually exists in apparently random HEA solid solutions.

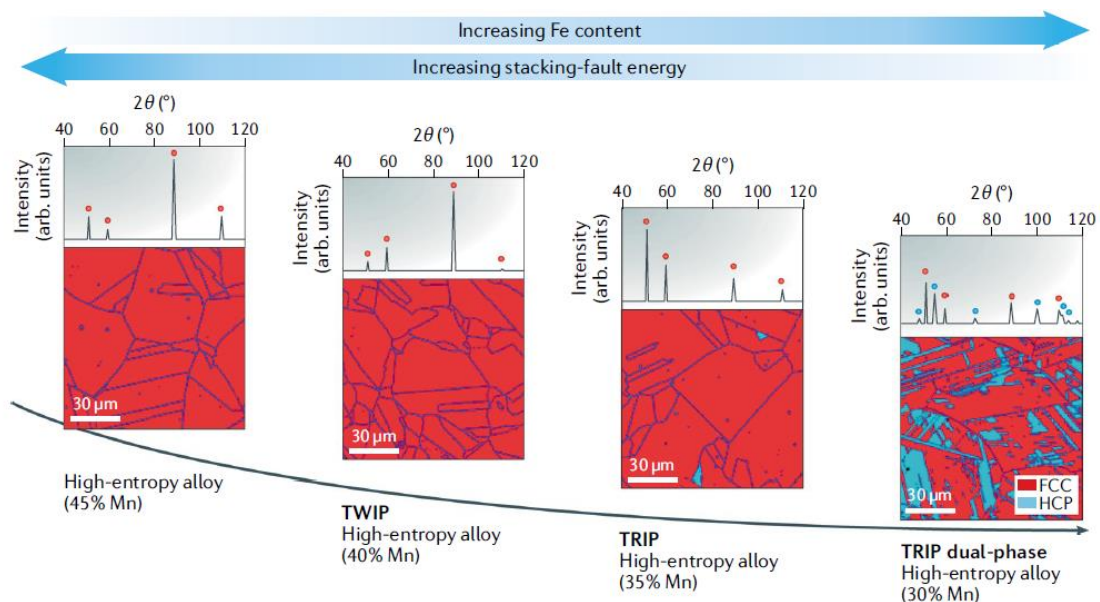


Figure 1-46 – Tuning the SFE and the phases in a set of non-equimolar derivatives of the Cantor alloy. The phase fractions (red: fcc, blue: hcp) for the alloy system $\text{Fe}_{80-x}\text{Mn}_x\text{Co}_{10}\text{Cr}_{10}$ change as a function of Mn content. The associated dominant phases are indicated. The spectra above the microstructure images show X-ray diffraction signals in which the peaks identify the respective phase fractions probed over millimetre-sized sample regions. From [52,119].

Li et al. [119,120] performed experiments on a set of Cantor-related HEAs with composition $\text{Fe}_{80-x}\text{Mn}_x\text{Co}_{10}\text{Cr}_{10}$, where the Mn content was varied between $x = 30 \text{ at.}\%$ and $45 \text{ at.}\%$. Figure 1-46 shows the evolution of SFE with Fe content, where Li et al. found that the Mn-rich alloy (45 at.%) deforms by the development of complex dislocation patterns, the 40 at.% Mn is a TWIP alloy and the 35 at.% Mn is a TRIP alloy, reflecting the influence of the reduction in SFE with decreasing Mn content. The 30 at.% Mn variant is an alloy consisting

initially of two HEA phases (fcc and hcp). The fcc phase is metastable, so it partially transforms into hcp martensite upon loading ^[120]. The alloys consisting of two such (metastable) HEA phases are characterized by a near-zero SFE ^[52].

5. Motivations: MuDiLingo project

This work is inscribed into the MuDiLingo project: A Multiscale Dislocation Language for Data-Driven Materials Science ^[121], where *in situ* TEM straining experiments on CoCrFeMnNi were performed and video sequences extracted from them are used by the MuDiLingo team at Forschungszentrum Jülich in Germany to perform deep learning segmentation, 3D reconstruction, simulations and analysis to create a “dislocation database” using machine learning.

6. References

- [1] J. A. Newell, *Essentials of Modern Materials Science and Engineering*, Wiley Global Education, USA, **2008**.
- [2] R. E. Hummel, *Understanding Materials Science: History, Properties, Applications*, Springer Science & Business Media, Verlag, New York, USA, **2004**.
- [3] J. Lubliner, *Plasticity Theory*, Dover Publications, Mineola, New York, USA, **2008**.
- [4] J. Weertman, J. R. Weertman, *Elementary Dislocation Theory*, The Macmillan Company, New York, USA, **1971**.
- [5] M. F. Ashby, *Acta metall.* **1972**, *20*, 887–897.
- [6] H. J. Frost, M. F. Ashby, *A Second Report on Deformation-Mechanism Maps*, Division Of Engineering And Applied Physics, Harvard University, Cambridge, Massachusetts, USA, **1973**.
- [7] M. E. Kassner, K. Smith, *J. Mater. Res. Technol.* **2014**, *3*, 280–288.
- [8] S. Praveen, H. S. Kim, *Adv. Eng. Mater.* **2018**, *20*, 1700645.
- [9] J. W. Yeh, *Ann. Chim. Sci. Mat.* **2006**, *31*, 633–648.
- [10] J. W. Yeh, S. K. Chen, S. J. Lin, J. Y. Gan, T. S. Chin, T. T. Shun, C. H. Tsau, S. Y. Chang, *Adv. Eng. Mater.* **2004**, *6*, 299–303.
- [11] J. W. Yeh, Y. L. Chen, S. J. Lin, S. K. Chen, *Mater. Sci. Forum* **2007**, *560*, 1–9.
- [12] D. B. Miracle, O. N. Senkov, *Acta mat.* **2017**, *122*, 448–511.
- [13] B. S. Murty, J. W. Yeh, S. Ranganathan, P. P. Bhattacharjee, *High-Entropy Alloys*, Elsevier, **2019**.

- [14] B. S. Murty, J. W. Yeh, S. Ranganathan, P. P. Bhattacharjee, in *High-Entropy Alloys*, Elsevier, **2019**, pp. 13–30.
- [15] F. R. de Boer, W. C. M. Mattens, R. Boom, A. R. Miedema, A. K. Niessen, in *Cohesion and Structure*, North-Holland, **1988**, p. 758.
- [16] A. Takeuchi, A. Inoue, *Mater. Trans. JIM* **2000**, *41*, 1372–1378.
- [17] A. Takeuchi, A. Inoue, *Mater. Trans.* **2005**, *46*, 2817–2829.
- [18] J. W. Yeh, *JOM* **2013**, *65*, 1759–1771.
- [19] F. Otto, A. Dlouhý, Ch. Somsen, H. Bei, G. Eggeler, E. P. George, *Acta Materialia* **2013**, *61*, 5743–5755.
- [20] D. B. Miracle, J. D. Miller, O. N. Senkov, C. Woodward, M. D. Uchic, J. Tiley, *Entropy* **2014**, *16*, 494–525.
- [21] A. Cottrell, *An Introduction to Metallurgy*, The Institute Of Materials, London, England, **1975**.
- [22] B. Cantor, I. T. H. Chang, P. Knight, A. J. B. Vincent, *Mater. Sci. Eng. A* **2004**, *375–377*, 213–218.
- [23] B. S. Murty, J. W. Yeh, S. Ranganathan, P. P. Bhattacharjee, in *High-Entropy Alloys*, Elsevier, **2019**, pp. 1–12.
- [24] C. Y. Hsu, J. W. Yeh, S. K. Chen, T. T. Shun, *Metall Mater Trans A* **2004**, *35*, 1465–1469.
- [25] B. Fultz, *Prog. Mater. Sci* **2010**, *55*, 247–352.
- [26] R. A. Swalin, J. Arents, *J. Electrochem. Soc.* **1962**, *109*, 308C.
- [27] Y. N. Osetsky, L. K. Béland, A. V. Barashev, Y. Zhang, *Curr. Opin. Solid State Mater. Sci.* **2018**, *22*, 65–74.
- [28] K.-Y. Tsai, M.-H. Tsai, J.-W. Yeh, *Acta Materialia* **2013**, *61*, 4887–4897.
- [29] E. J. Pickering, N. G. Jones, *International Materials Reviews* **2016**, *61*, 183–202.
- [30] D. Rohrberg, K.-H. Spitzer, L. Dörrer, A. J. Kulińska, G. Borchardt, A. Fraczkiewicz, T. Markus, M. H. G. Jacobs, R. Schmid-Fetzer, *Metall. Mater. Trans. A* **2014**, *45*, 269–279.
- [31] J. Dąbrowa, W. Kucza, G. Cieślak, T. Kulik, M. Danielewski, J.-W. Yeh, *J. Alloys Compd* **2016**, *674*, 455–462.
- [32] A. Paul, *Scr. Mater.* **2017**, *135*, 153–157.
- [33] W. Kucza, J. Dąbrowa, G. Cieślak, K. Berent, T. Kulik, M. Danielewski, *J. Alloys Compd.* **2018**, *731*, 920–928.
- [34] S. Ranganathan, *Curr. Sci.* **2003**, *85*, 1404–1406.

- [35] I. Basu, V. Ocelík, J. Th. M. De Hosson, *J. Mater. Res.* **2018**, *33*, 3055–3076.
- [36] M.-H. Tsai, J.-W. Yeh, *Mater. Res. Lett.* **2014**, *2*, 107–123.
- [37] J. R. Davis, Ed. , *Metals Handbook Desk Edition, 2nd Ed.*, ASM International, **1998**.
- [38] A. D. McNaught, A. Wilkinson, **1997**.
- [39] H.-P. Chou, Y.-S. Chang, S.-K. Chen, J.-W. Yeh, *Mater. Sci. Eng. B* **2009**, *163*, 184–189.
- [40] C.-L. Lu, S.-Y. Lu, J.-W. Yeh, W.-K. Hsu, *J Appl Crystallogr* **2013**, *46*, 736–739.
- [41] M. H. Tsai, *Entropy* **2013**, *15*, 5338–5345.
- [42] K. Zhang, Z. Fu, *Intermetallics* **2012**, *28*, 34–39.
- [43] T. T. Zuo, R. B. Li, X. J. Ren, Y. Zhang, *J. Magn. Magn. Mater* **2014**, *371*, 60–68.
- [44] Y.-F. Kao, S.-K. Chen, T.-J. Chen, P.-C. Chu, J.-W. Yeh, S.-J. Lin, *J. Alloys Compd* **2011**, *509*, 1607–1614.
- [45] S. Singh, N. Wanderka, K. Kiefer, K. Siemensmeyer, J. Banhart, *Ultramicroscopy* **2011**, *111*, 619–622.
- [46] E. P. George, W. A. Curtin, C. C. Tasan, *Acta mat.* **2020**, *188*, 435–474.
- [47] S. Gorsse, D. B. Miracle, O. N. Senkov, *Acta mat.* **2017**, *135*, 177–187.
- [48] M. F. Ashby, D. Cebon, *Le Journal de Physique IV* **1993**, *3*, C7-1.
- [49] B. S. Murty, J. W. Yeh, S. Ranganathan, P. P. Bhattacharjee, in *High-Entropy Alloys*, Elsevier, **2019**, pp. 31–50.
- [50] F. Otto, Y. Yang, H. Bei, E. P. George, *Acta mat.* **2013**, *61*, 2628–2638.
- [51] B. Gludovatz, A. Hohenwarter, D. Catoor, E. H. Chang, E. P. George, R. O. Ritchie, *Science* **2014**, *345*, 1153–1158.
- [52] E. P. George, D. Raabe, R. O. Ritchie, *Nat. Rev. Mater.* **2019**, *4*, 515–534.
- [53] H. Y. Diao, R. Feng, K. A. Dahmen, P. K. Liaw, *Curr. Opin. Solid State Mater. Sci.* **2017**, *21*, 252–266.
- [54] P. F. Koshelev, *Strength Mater.* **1971**, *3*, 286–291.
- [55] W. H. Liu, Y. Wu, J. Y. He, T. G. Nieh, Z. P. Lu, *Scr. Mater.* **2013**, *68*, 526–529.
- [56] Z. C. Cordero, B. E. Knight, C. A. Schuh, *Int. Mater. Rev.* **2016**, *61*, 495–512.
- [57] Z. Wu, Y. F. Gao, H. Bei, *Scr. Mater.* **2015**, *109*, 108–112.
- [58] N. L. Okamoto, S. Fujimoto, Y. Kambara, M. Kawamura, Z. M. T. Chen, H. Matsunoshita, K. Tanaka, H. Inui, E. P. George, *Sci Rep* **2016**, *6*, 35863.
- [59] A. Gali, E. P. George, *Intermetallics* **2013**, *39*, 74–78.

- [60] G. Laplanche, A. Kostka, O. M. Horst, G. Eggeler, E. P. George, *Acta Materialia* **2016**, *118*, 152–163.
- [61] Z. Zhang, M. M. Mao, J. Wang, B. Gludovatz, Z. Zhang, S. X. Mao, E. P. George, Q. Yu, R. O. Ritchie, *Nature Communications* **2015**, *6*, DOI 10.1038/ncomms10143.
- [62] T. M. Smith, M. S. Hooshmand, B. D. Esser, F. Otto, D. W. McComb, E. P. George, M. Ghazisaeidi, M. J. Mills, *Acta Materialia* **2016**, *110*, 352–363.
- [63] E. El-Danaf, S. R. Kalidindi, R. D. Doherty, *Int. J. Plast.* **2001**, *17*, 1245–1265.
- [64] R. W. K. Honeycomb, P. Paufler, *The Plastic Deformation of Metals*, Edward Arnold, London, England, **1984**.
- [65] E. O. Hall, *Proc. Phys. Soc. B* **1951**, *64*, 747–753.
- [66] R. W. Armstrong, *Metall. Mater. Trans. B* **1970**, *1*, 1169–1176.
- [67] I. Karaman, H. Sehitoglu, A. J. Beaudoin, Y. I. Chumlyakov, H. J. Maier, C. N. Tomé, *Acta mat.* **2000**, *48*, 2031–2047.
- [68] O. Bouaziz, N. Guelton, *Mater. Sci. Eng. A* **2001**, *319–321*, 246–249.
- [69] B. C. De Cooman, Y. Estrin, S. K. Kim, *Acta Materialia* **2018**, *142*, 283–362.
- [70] Z. Zhang, H. Sheng, Z. Wang, B. Gludovatz, Z. Zhang, E. P. George, Q. Yu, S. X. Mao, R. O. Ritchie, *Nat Commun* **2017**, *8*, 14390.
- [71] I. V. Kireeva, Y. I. Chumlyakov, Z. V. Pobedennaya, I. V. Kuksgausen, I. Karaman, *Materials Science & Engineering A* **2017**, *705*, 176–181.
- [72] I. V. Kireeva, Y. I. Chumlyakov, Z. V. Pobedennaya, A. V. Vyrodova, I. Karaman, *Materials Science & Engineering A* **2018**, *713*, 253–259.
- [73] W. Abuzaid, H. Sehitoglu, *Materials Characterization* **2017**, *129*, 288–299.
- [74] B. Gludovatz, E. P. George, R. O. Ritchie, *JOM* **2015**, *67*, 2262–2270.
- [75] W. D. Callister, D. G. Rethwisch, *Materials Science and Engineering: An Introduction*, Wiley, **2018**.
- [76] J. A. Ewin, W. Rosenhain, *Royal Society* **1900**, *65*, DOI <https://doi.org/10.1098/rspl.1899.0004>.
- [77] V. Volterra, *Ann. Sci. École Norm. Sup.* **1907**, *24*, 401–517.
- [78] A. E. H. Love, *A Treatise on the Mathematical Theory of Elasticity*, Cambridge University Press, New York, USA, **2013**.
- [79] P. M. Anderson, J. P. Hirth, J. Lothe, *Theory of Dislocations*, Cambridge University Press, New York, USA, **2017**.
- [80] J. Frenkel, *Z. Physik* **1926**, *37*, 572–609.

- [81] J. K. Mackenzie, **1949**.
- [82] A. Kelly, *Strong Solids*, Oxford University Press, **1973**.
- [83] S. S. Brenner, in *Growth and Perfection of Crystals*, by R. H. Doremus et Al., Wiley, New York, USA, **1958**, p. 3.
- [84] R. F. Tinder, J. Washburn, *Acta metall.* **1964**, *12*, 129–137.
- [85] R. F. Tinder, Metallurgical Soc. Amer. Inst. Mining Metall. Petrol Eng. INC 420 Commonwealth DR ..., **1964**, p. 94.
- [86] G. Masing, M. Polanyi, in *Ergebnisse der exakten naturwissenschaften*, Springer, Berlin, Heidelberg, **1923**, pp. 177–245.
- [87] L. Prandtl, *ZAMM* **1928**, *8*, 85–106.
- [88] U. Dehlinger, *Ann. Phys.* **1929**, *2*, 749.
- [89] E. Orowan, *Z. Physik* **1934**, *89*, 634–659.
- [90] M. Polanyi, *Z. Physik* **1934**, *89*, 660–664.
- [91] G. I. Taylor, *Proceedings of the Royal Society of London. Series A, Containing Papers of a Mathematical and Physical Character* **1934**, *145*, 362–387.
- [92] J. Burgers, *Proc. Acad. Science* **1939**, *42*, 293–378.
- [93] P. B. Hirsch, R. W. Horne, M. J. Whelan, *Philos. Mag.* **1956**, *1*, 677–684.
- [94] F. C. Frank, *London, Edinburgh Dublin Philos. Mag. J. Sci.* **1951**, *42*, 809–819.
- [95] B. A. Bilby, R. Bullough, E. Smith, J. M. Whittaker, *Proc. R. Soc. A: Math. Phys. Eng. Sci.* **1955**, *231*, 263–273.
- [96] E. Schmid, Delft, **1924**, pp. 342–353.
- [97] M. Peach, J. S. Koehler, *Phys. Rev.* **1950**, *80*, 436–439.
- [98] V. A. Lubarda, *J. Mater. Res. Technol.* **2019**, *8*, 1550–1565.
- [99] R. D. Heidenreich, W. Shockley, *Proc. Phys. Soc.* **1948**, *57*.
- [100] H. Huang, X. li, Z. Dong, W. Li, S. Huang, D. Meng, X. Lai, T. Liu, S. Zhu, L. Vitos, *Acta mat.* **2018**, *149*, DOI 10.1016/j.actamat.2018.02.037.
- [101] E. J. Mittemeijer, *Fundamentals of Materials Science*, Springer Berlin Heidelberg, Berlin, Heidelberg, **2011**.
- [102] J. W. Christian, S. Mahajan, *Prog. Mater. Sci* **1995**, *39*, 1–157.
- [103] F. Otto, A. Dlouhý, K. G. Pradeep, M. Kuběnová, D. Raabe, G. Eggeler, E. P. George, *Acta mat.* **2016**, *112*, 40–52.
- [104] B. Cantor, *Prog. Mater. Sci* **2021**, *120*, 100754.

- [105] A. Haglund, M. Koehler, D. Catoor, E. P. George, V. Keppens, *Intermetallics* **2015**, *58*, 62–64.
- [106] G. Laplanche, P. Gadaud, O. Horst, F. Otto, G. Eggeler, E. P. George, *Journal of Alloys and Compounds* **2015**, *623*, 348–353.
- [107] Q. Ding, X. Fu, D. Chen, H. Bei, B. Gludovatz, J. Li, Z. Zhang, E. P. George, Q. Yu, T. Zhu, R. O. Ritchie, *Mater. Today* **2019**, *25*, 21–27.
- [108] J. A. Venables, *Philos. Mag.* **1961**, *6*, 379–396.
- [109] M. A. Meyers, A. Mishra, D. J. Benson, *Progress in Materials Science* **2006**, *51*, 427–556.
- [110] M. A. Meyers, O. Vöhringer, V. A. Lubarda, *Acta Materialia* **2001**, *49*, 4025–4039.
- [111] I. V. Kireeva, Y. Chumlyakov, Z. Pobedennaya, D. Kuksgauzen, I. Karaman, H. Sehitoglu, Tomsk, Russia, **2016**, p. 020090.
- [112] S. Huang, W. Li, S. Lu, F. Tian, J. Shen, E. Holmström, L. Vitos, *Scripta Materialia* **2015**, *108*, 44–47.
- [113] S. Zhao, G. M. Stocks, Y. Zhang, *Acta mat.* **2017**, *134*, 334–345.
- [114] J. Ding, Q. Yu, M. Asta, R. O. Ritchie, *Proc. Natl. Acad. Sci. USA* **2018**, *115*, 8919.
- [115] A. J. Zaddach, C. Niu, C. C. Koch, D. L. Irving, *JOM* **2013**, *65*, 1780–1789.
- [116] N. Bernstein, E. B. Tadmor, *Phys. Rev. B* **2004**, *69*, 094116.
- [117] E. B. Tadmor, N. Bernstein, *J. Mech. Phys. Solids* **2004**, *52*, 2507–2519.
- [118] F. X. Zhang, S. Zhao, K. Jin, H. Xue, G. Velisa, H. Bei, R. Huang, J. Y. P. Ko, D. C. Pagan, J. C. Neumeier, W. J. Weber, Y. Zhang, *Phys. Rev. Lett.* **2017**, *118*, 205501.
- [119] Z. Li, C. C. Tasan, H. Springer, B. Gault, D. Raabe, *Sci Rep* **2017**, *7*, 40704.
- [120] Z. Li, K. G. Pradeep, Y. Deng, D. Raabe, C. C. Tasan, *Nature* **2016**, *534*, 227–230.
- [121] ERC, “A Multiscale Dislocation Language for Data-Driven Materials Science,” can be found under <https://cordis.europa.eu/project/id/759419>, **2021**.

Chapter 2

EXPERIMENTAL METHODOLOGY AND RESULTS

This chapter will introduce the experimental techniques used in this research work, *in situ* TEM straining tests, to analyse the dislocation movement in different CoCrFeMnNi specimens. To be able to fully understand the technique, section 2 of this chapter will focus on the principles of image formation and electronic diffraction on a TEM, keys to comprehend and analyse the behaviour of dislocations in further chapters.

1. Specimens

Three types of CoCrFeMnNi specimens were used in the *in situ* TEM straining experiments:

Table 2-1 – Type of Specimens.

Specimen	Co %	Cr %	Fe %	Mn %	Ni %
35/I2-Head	20	20	20	20	20
X1	20	20	20	20	20
1484Recuit ^[1]	20	15	26	17	22

The ingots were prepared via two different methods, both resulting in a homogeneous single phase microstructure, with large grains ($\approx 50 \mu\text{m}$) ^[2]:

- 35/I2-Head ingots were produced by arc melting and drop casting under a pure Ar atmosphere (8.4×10^{-4} Pa) from raw materials of at least 99.9% purity. The Mn weight loss during arc melting was compensated by adding 1 g (for a 475 g ingot). The arc-melted buttons were flipped and remelted five times for homogenization, and then drop casted in rectangular Cu moulds to be solution-annealed 48 h at 1200°C. After this process, they were cold-rolled from 12.7 mm to 4 mm thick slabs and annealed 1 h at 900°C. These specimens were manufactured at ORNL (Oak Ridge National Laboratory) in Tennessee, USA and provided by Antonin Dlouhy, from the Institute of Physics of Materials in Brno, CZ. For a detailed process on the specimens' processing, please refer to ^[3].
- Both X1 and 1484Recuit ingots were prepared from pure metals pellets or powders of at least 99,9% purity. They were processed by hot forging (2 h at 1060°C under vacuum, to

a diameter of 12 mm with the total section reduction of about 40%) and partially by cold rolling (section reduction ~90%) to refine the microstructure. They were provided by Anna Frackiewicz, MINES Saint-Étienne in France. For a detailed process on the specimens' processing, please refer to [4].

The ingots of each type were first cut into rectangular specimens of 3 x 1.5 mm, with a thickness varying from 500 to 800 nm, using electro-discharge machining [2]. Then, specimens were mechanically thinned down with SiC paper in the region of 30 μm . The rectangular specimens were, as a final step, electropolished in a Struers Tenupol twin-jet polishing unit using a 10% Perchloric acid-90% Ethanol electrolyte to create electron-transparent regions around a central hole, typically 50-500 nm thick [2]. The electron transparency depends both on the voltage of the TEM, on the average atomic number of the chemical species contained in the specimen (the larger, the less transparent) and for crystalline materials, of the diffraction vector employed to form images (Ref: Williams & Carter or Edington). For the Cantor alloy studied in this thesis, regions up to 800 nm thick could be monitored under specific diffraction conditions (see below). Also, dislocations were characterized in zones not thinner than 100 nm to ensure sufficient line length. The preparation process was carried out by the Specimen Preparation Service at CEMES-CNRS laboratory. The detailed process can be found on [5]. The final specimen is glued onto a Cu grid using ethyl 2-cyanoacrylate glue (Figure 2-1).

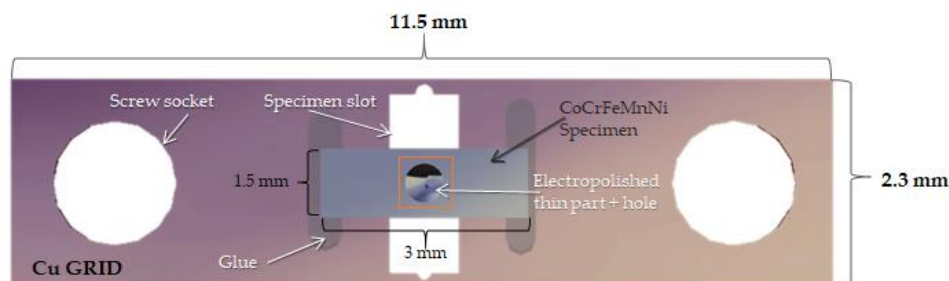


Figure 2-1 – Model of a specimen glued to a Cu grid. The orange frame shows the electro-thinned area of the specimen with the pierced hole.

2. Experimental procedure

2.1. Set-up

Once the specimen is glued onto the Cu grid, it is then fixed to the uniaxial straining holder (α tilt) used for the in situ TEM straining experiments by means of two screws. The holder used is a commercial Gatan holder, model 671, cooled by liquid N_2 , operating from about 100°C (empty N_2 reservoir and resistance heating) down to cryogenic (full N_2 reservoir) temperatures (Figure 2-2) driven by an outside controller connected to the thermocouple attached to the sample jaws. The holder, once filled with N_2 , is capable of stabilizing at a

temperature of around 100 K within 30 minutes, when a good vacuum is reached in the reservoir shell [2]. The straining mechanism consists of a fixed and a mobile jaw, the latter of which is displaced by a motorised controller with a single push-button operation that starts or stops the elongation process, at rates from 10 nm/s up to 1 $\mu\text{m/s}$.

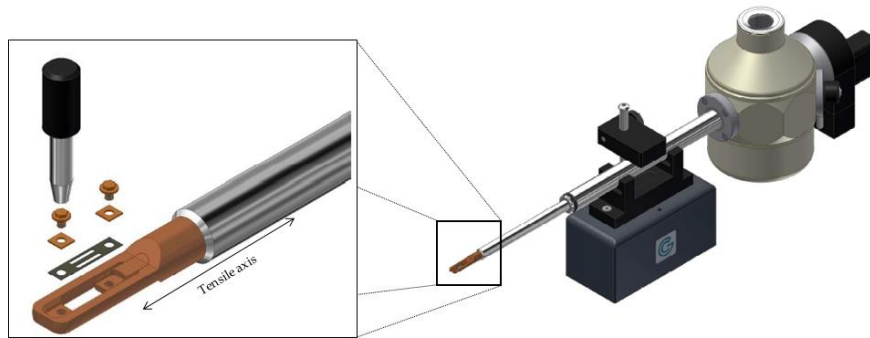


Figure 2-2 – Gatan LN₂ holder with specimen set up. Images property of Gatan®. Insert showing the specimen area, tensile grid and both screws to attach it.

Once the specimen is loaded onto the holder, the holder is inserted into the TEM. The *in situ* tensile experiments were carried out on a LaB₆ JEOL 2010 TEM operating at 200 KeV. Depending on the desired temperature for a specific experiment, the holder's reservoir is filled or not with liquid N₂. Temperature stabilization needs between a few minutes to about half hour before starting the straining depending how cold one wants to go. Once it reaches thermal equilibrium due to heat transfer by conduction between the holder and the specimen, straining may begin.

During *in situ* experiments, short strain pulses (on the order of 10^{-3} s^{-1}) are applied, separated by longer periods where the dislocation movements are observed. In average, the strain rate of the *in situ* experiments are in the order of 10^{-4} to 10^{-5} s^{-1} [2]. The maximum applied stress in the sample corresponds to the region where the hole rim is parallel to the straining axis [6], as the hole introduces a stress concentration. Also, in the zones with pre-existing fractures on the hole rim, there is more tendency to trigger the deformation in response to stress application [7].

Figure 2-3 shows a specimen, electropolished to obtain a thin area where a hole was pierced following the preparation method already presented. Part (c) of the figure shows the hole rim around which several different grains can be distinguished (delimited by white dashed lines). Each grain has its own crystal orientation, which can be determined during the *in situ* TEM straining test following the procedure that will be explained in section 2.4.

As it can be seen in the image, the size of each grain varies from a few to several tens of microns. There are many more grains present in a specimen, however during an *in situ* TEM straining experiment there is only access to the electron transparent areas of the specimen, that means, only the grains in the thinned part of the specimen around the hole. This leaves only a few grains where plastic deformation can be witnessed. Of these grains, only the ones neighbouring the hole and perpendicular to the straining axis will have a stress concentration large enough to trigger plastic deformation, further reducing the areas where slip systems will activate.

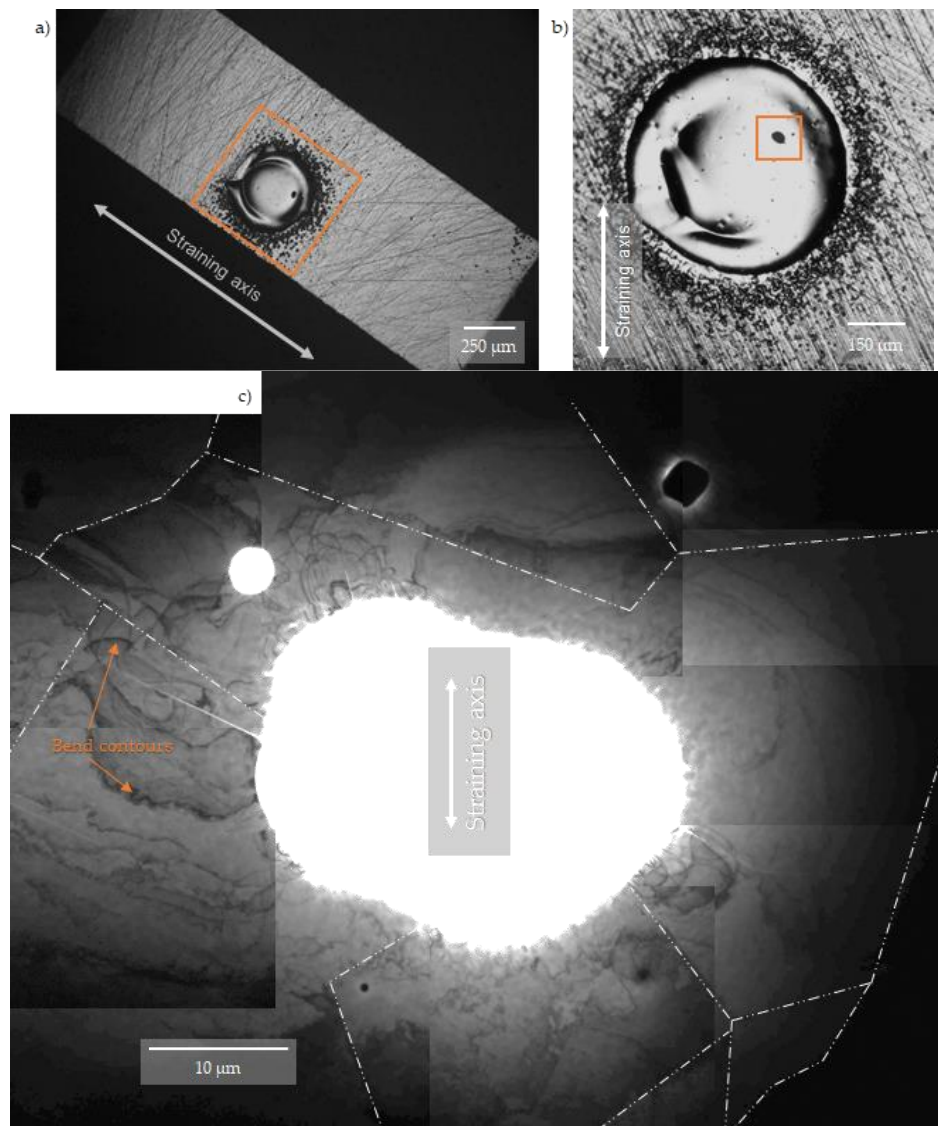


Figure 2-3 – a) Optical microscope image of a specimen; the orange frame indicates the electropolished thinned area and the hole. b) Optical microscope image at a higher magnification showing the highlighted area from the previous part. The second orange frame indicates the hole around which deformation will be witnessed. c) Composed TEM image of the electropolished hole, showing several grains around it (white dashed lines), identified because of the difference in contrast between areas when tilting; orange arrows signal examples of bend contours. All images indicate the corresponding direction of the straining axis on the experiment.

To better target the grains where deformation can be witnessed, the crystal orientation must be known in order to identify the possible slip planes and their directions. Also, calculating the Schmid factors for each slip plane/Burgers vector combination is a good indicator of which slip systems are more susceptible to activate under tensile deformation ^[6]. This will be explained in detail in the next sections.

The strain pulses will not trigger plastic deformation right away, but after a certain elongation in μm has occurred. When straining, the specimen will first drift until self-alignment with the tensile axis, because of the mechanical clearance between elements. Once the specimen is aligned and in place, actual deformation will start when pulsing. Bend contours (part (c) of Figure 2-3) movement indicates elastic deformation is taking place (bend contours are not line defects in the crystal, they occur when a set of diffraction planes is not parallel everywhere ^[8]; they are not fixed on a specific position but will move when tilting – when straining, they will move with no tilting). Once stabilization is reached, bend contours will stop moving. This indicates that the onset of plasticity is close and dislocation movement may occur anytime then.

Once dislocations start to move, the dynamic observation is recorded in MPEG2 video format using a Megaview III camera from Soft Imaging System (now EMSIS) and stored on hard drives ^[2]. This is also valid for the recording of micrographs and diffraction patterns (DP) obtained from electronic diffraction (see section 2.2.). The images and DPs are analysed, as well as the video files, studied frame by frame, with the representative sequences and images extracted from them.

The DPs are the basis for image formation in a TEM. Both of these concepts will be explained in the next sections.

2.2. Electronic diffraction

In TEM, a beam of electrons is accelerated through a thin specimen. On the exit side of the crystalline specimen, several diffracted beams are present in addition to the transmitted beam, and these are focused by the objective lens to form a spot pattern in its back focal plane (Figure 2-4). When a beam of electrons is incident on the top surface of a thin crystalline specimen, specific diffracted beams emerge at the bottom exit surface ^[9]. Each individual atom in the crystal scatters the incident beam, however the scattered wavelets will only be in phase in particular crystallographic directions.

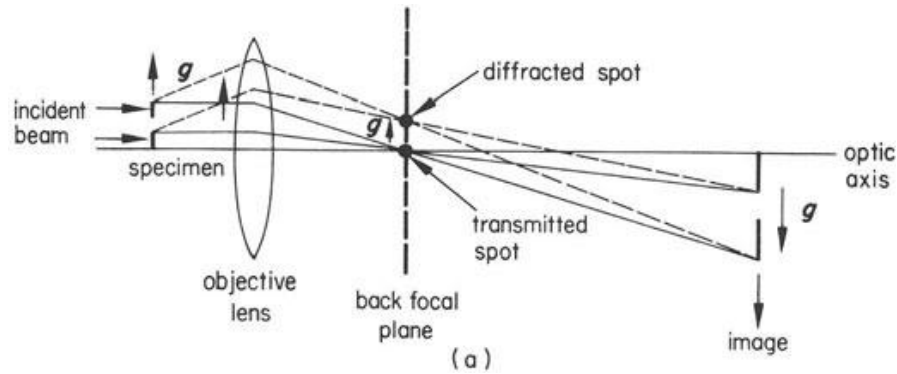


Figure 2-4 – The formation of a focused diffraction pattern in the back focal plane of the objective lens. From [9].

Figure 2-5 shows an example of an incident beam direction B of $[100]$ in an aluminium fcc single-crystal specimen. The transmitted beam is marked T and the arrangement of diffracted beams D around the transmitted beam is characteristic of the four-fold symmetry of the $[100]$ cube axis of aluminium [9].

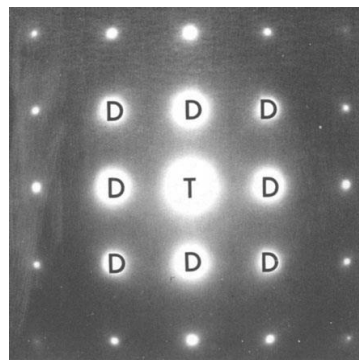


Figure 2-5 – A typical spot pattern from an aluminium fcc single crystal specimen oriented along a specific zone axis. Here, incident beam direction $B = [100]$. T , transmitted spot; D , diffracted spot. From [9].

When a suitably focused beam of electrons passes through a crystal, diffraction will occur if the three Laue conditions are simultaneously fulfilled:

$$\begin{cases} a(\cos \alpha_1 - \cos \alpha_2) = n_1 \lambda \\ b(\cos \beta_1 - \cos \beta_2) = n_2 \lambda \\ c(\cos \gamma_1 - \cos \gamma_2) = n_3 \lambda \end{cases}$$

Equation 2-1 – Laue conditions.

where a , b and c are the crystal lattice parameters and n_1 , n_2 and n_3 are the Laue orders of diffraction. The cosines of the angles define the directions of the incident and diffracted beams [10].

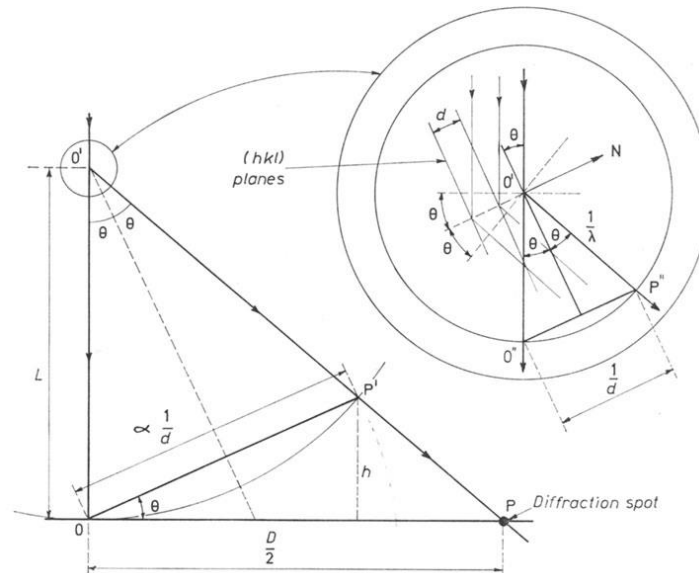


Figure 2-6 – The basic geometry of diffraction. For electron diffraction the angle θ is small and P' very near to P . From [10].

The combined conditions for diffraction are more generally represented by the Bragg Law, which may be said to contain the Laue conditions. Figure 2-6 shows a circular inset where a parallel beam of electron waves enters a crystal with an angle of incidence θ with a set of crystallographic planes of interplanar spacing d and Miller indices hkl [10]. Diffraction occurs when the ray paths via successive planes in the system differ from each other by an exact number of wavelengths. The diffracted ray then leaves the plane at an angle θ (or 2θ with the incident beam), following the Bragg law:

$$n\lambda = 2d \sin \theta$$

Equation 2-2 – Bragg law.

From Equation 2-2, when $n = 1$ (for a better explanation on why n is considered as equal to the unity, please refer to [11]), an alternative form of the equation can be construed:

$$\frac{1}{d} = 2 \left(\frac{1}{\lambda} \right) \sin \theta$$

Equation 2-3 – Alternative Bragg law.

The inset in Figure 2-6 shows a sphere of radius $1/\lambda$ with its centre at O' , intersecting the direct beam at O'' and the diffracted beam at P'' . The distance $O''P''$ is $2 \sin \theta / \lambda$ which is equal to $1/\lambda$. The direction of $O''P''$ is parallel to $O'N$, which is perpendicular to (hkl) . This insert presents the construction of the “sphere of reflection” or “Ewald sphere” [10].

Figure 2-7 describes diffraction in terms of the Bragg law for a TEM specimen of thickness between $1000 - 3000 \text{ \AA}$. Considering the case when the incident beam is made up of plane waves in phase and oriented at an angle θ relative to two hkl crystal planes I and II [9], and assuming the two waves are reflected by these crystal planes at an angle θ , two situations may occur:

- The two waves may be in phase (Figure 2-7), and reinforcement will occur and a strong reflected beam will be present.
- The waves may be out of phase: they will interfere and there will be either zero or a very weak reflected beam.

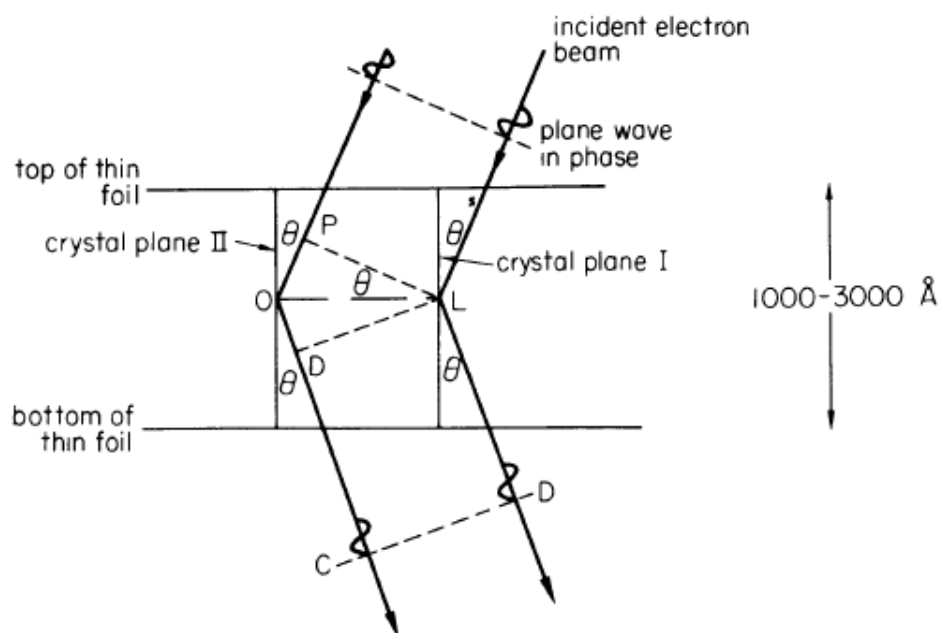


Figure 2-7 – Reflection at the Bragg angle θ from crystal planes in a thin foil electron microscope specimen. From [9].

The scattering vector \vec{K} (the vector resulting from incident and diffracted waves considered from the scattering of only two atoms), scattering at the Bragg angle θ in a TEM is

$$|\vec{K}| = \frac{2 \sin \theta}{\lambda}$$

Equation 2-4 – Scattering vector.

From Equation 2-3 and Equation 2-4, the conclusion can be drawn that

$$|\vec{K}| = \frac{1}{d} = \vec{g}$$

Equation 2-5 – Scattering vector in a TEM.

Bragg's Law gives a very useful physical picture of the diffraction process because the diffracting planes appear to behave as mirrors for the incident electron beam ^[11]. Therefore, the diffracted beams, or the spots in the DP, are often called "reflections" and the vector \vec{g} is called the diffraction vector (also called reciprocal lattice vector).

2.2.1. Reciprocal lattice

The single-crystal electron diffraction spot pattern is similar to a network of points that are at distances proportional to $1/d$ or \vec{g} (the reciprocal lattice vector) from the centre of the diffraction pattern (O in Figure 2-6) ^[10]. The line joining O to any point is also parallel to the normal to the diffracting plane and so represents the vector \vec{g} on a proper scale. The array of points therefore determines vectors from the origin O and, because it is a regular network, it is regarded as a layer of a reciprocal lattice. The reciprocal lattice is a regular three-dimensional pattern of points which is related to the 3D crystal lattice by the condition that the vector distances in the former, \vec{g}_{hkl} , are perpendicular to (hkl) planes in the space lattice and have lengths g_{hkl} inversely proportional to the corresponding interplanar spacing d_{hkl} .

The reciprocal lattice is important because it may be used as a tool to simplify considerably the interpretation of electron diffraction patterns. The reciprocal lattice derives directly from the Laue conditions described in Equation 2-1, because their solution is

$$\frac{\vec{P}}{\lambda} = h\vec{a}^* + k\vec{b}^* + l\vec{c}^*$$

Equation 2-6 – Reciprocal Lattice.

where \vec{a}^* , \vec{b}^* and \vec{c}^* are vectors defined such that $\vec{a} \cdot \vec{a}^* = \vec{b} \cdot \vec{b}^* = \vec{c} \cdot \vec{c}^* = 1$, and $\vec{a}^* \cdot \vec{b} = \vec{b}^* \cdot \vec{a} = \vec{a}^* \cdot \vec{c} = \vec{c}^* \cdot \vec{a} = \vec{b}^* \cdot \vec{c} = \vec{c}^* \cdot \vec{b} = 0$.

The conditions $\vec{a} \cdot \vec{a}^* = 1$ and $\vec{a}^* \cdot \vec{b} = 0$ mean that \vec{a}^* is perpendicular to \vec{b} and \vec{c} and, by a similar argument, \vec{b}^* is perpendicular to \vec{a} and \vec{c} while \vec{c}^* is perpendicular to \vec{a} and \vec{b} . For

crystal structures with orthogonal axes (as a cubic crystal structure), the axes of the reciprocal lattice coincide with the crystal lattice. The relations $\vec{a}^* \cdot \vec{a} = 1, \dots$, define the magnitudes of the vectors as $|\vec{a}^*| = 1/|\vec{a}|$, which is the origin of the term reciprocal lattice [9]. The reciprocal lattice has the following properties:

- The vector \vec{g}_{hkl} to the point (hkl) of the reciprocal lattice is normal to the plane (hkl) of the crystal lattice.
- The magnitude of \vec{g}_{hkl} is $1/d_{hkl}$, where d_{hkl} is the interplanar spacing of the family of (hkl) planes.

These two properties define the reciprocal lattice as an array of points, each one corresponding to a particular (hkl) plane and defined by a corresponding vector. Figure 2-8 shows this relationship between planes in the real lattice and points in the reciprocal lattice for a cubic crystal structure. Each point is labelled with the particular (hkl) indices of the corresponding reflecting plane [9]. Figure 2-8(c) shows that a point (hkl) in the reciprocal space is defined by $h\vec{a}^*$ along the x axis, $k\vec{b}^*$ along the y axis and $l\vec{c}^*$ along the z axis, giving

$$\vec{g}_{hkl} = h\vec{a}^* + k\vec{b}^* + l\vec{c}^*$$

Equation 2-7 – Reciprocal lattice vector.

The reciprocal lattice of a primitive cubic cell with lattice constant a is a primitive cubic, where the lattice constant of the reciprocal unit cell is $1/a$ [12]. The reciprocal lattice of a fcc lattice can be deduced by considering that any fundamental vector of the primitive trigonal unit cell of the bcc lattice is normal to two fundamental vectors of the primitive trigonal unit cell of the fcc lattice (see Figure 2-9 and Figure 2-10).

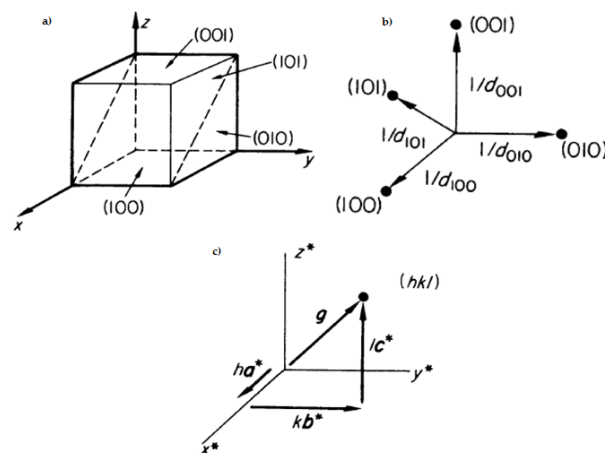


Figure 2-8 – The relationship between: a) crystal planes, b) equivalent reciprocal lattice points and c) the geometric description of Equation 2-7. From [9].

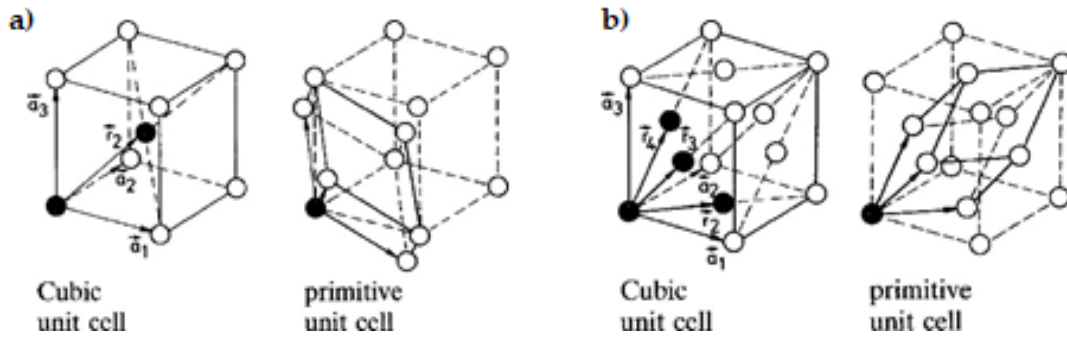


Figure 2-9 – Unit cells for: a) bcc crystal structures and b) fcc crystal structures. Adapted from [12].

Not every reciprocal lattice point can be observed as predicted by Equation 2-7 when the fundamental vectors of a non-primitive unit cell are used, some will disappear [12]. In the reciprocal lattice of the non-primitive fcc structure (Figure 2-10(b)), the reciprocal lattice points 200, 220, etc., are allowed, but 100, 210, etc., are “forbidden”. The reasons for this depend on the zero rules ($F = 0$) of the structure amplitude F .

Figure 2-11 shows the zero rules for a fcc crystal. Based on this, from this time forth, whenever the plane families [100], [110] or [112] are mentioned for fcc structures, this manuscript is in fact referring to plane families [200], [220] or [224], respectively.

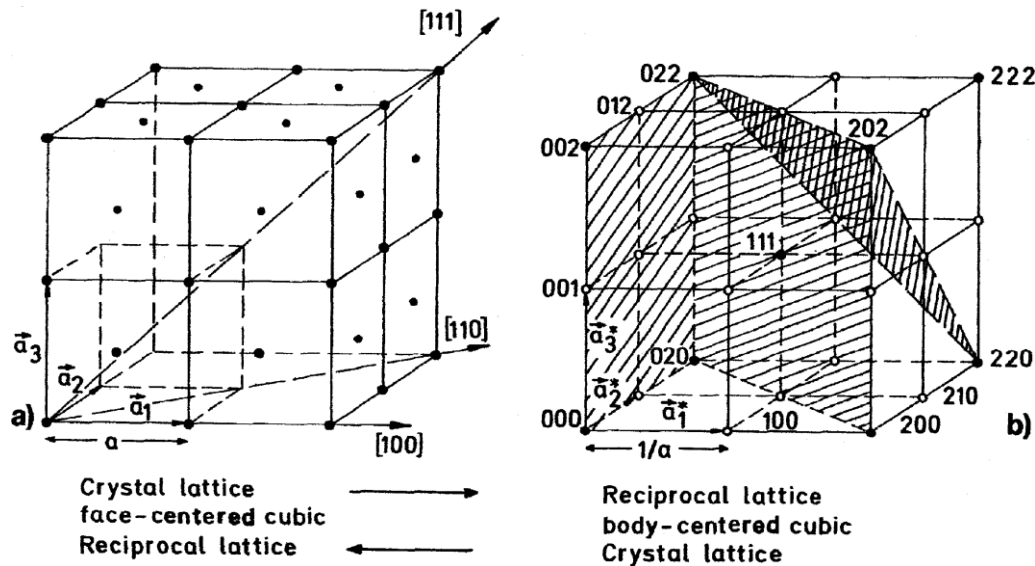


Figure 2-10 – bcc crystal (b) as the reciprocal lattice of a fcc lattice (a) and vice versa. Only the full circles in b) are reciprocal-lattice points. The open circles are forbidden by the extinction rules for the structure amplitude F . From [12].

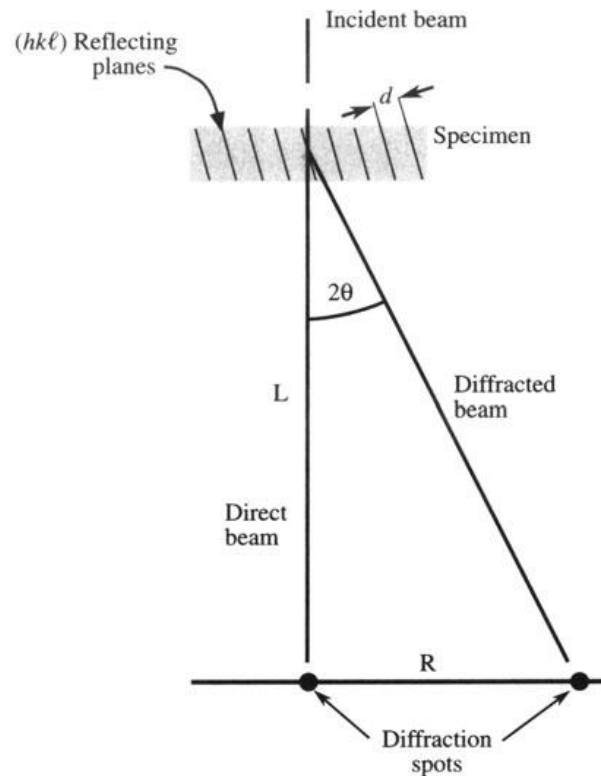


Figure 2-12 – The relationship between the spacing R of diffraction maxima and the camera length, L . Increased magnification corresponds to effectively increasing L , although in practice this is accomplished with lenses. From ^[13].

From Figure 2-12, it can be seen that the camera length in the TEM is a calculated value rather than a physical distance ^[13]. If electrons are scattered through an angle 2θ at the specimen, the separation of the direct and diffracted beams as measured on the screen (R) is determined by L as

$$\frac{R}{L} = \tan 2\theta \sim 2\theta$$

Equation 2-8 – Camera length in TEM.

And from Equation 2-2 (also $\sim 2\theta$), Equation 2-8 can be rewritten as

$$Rd = \lambda L$$

Equation 2-9 – Relationship between Equation 2-2 and Equation 2-8.

Consequently, knowing the interplanar spacing (d) of the specimen and the camera constant (λL) of the microscope can give the value of R , the spacing between diffraction spots in a specific DP. The camera constant depends on the model of the TEM, on the accelerating voltage and on the projected lens excitation. For the conditions used in this work (a JEOL 2010 TEM operating at 200 KeV and $L = 80$ cm), the spacing between diffraction spots for the closest DP spot distances for the Cantor alloy (fcc structure, lattice parameter $a = 3.597\text{\AA}$ at 300K [14]) is shown in Table 2-2. Note that these values are only valid for printed DPs of 6×8 cm dimension.

Table 2-2 – Spacing between diffraction spots for a fcc crystal, following the previously specified conditions.

hkl plane	R (cm)
111	~ 0.67
200	~ 0.77
220	~ 1.10
311	~ 1.29

Thus, indexing DPs depends on two parameters (exemplified in Figure 2-13):

- The distance R from the diffracted spot to the transmitted beam (centre spot), characteristic of the interplanar spacing d_{hkl} of the reflecting plane.
- The angles between lines drawn from the centre spot to diffracted spots ($h_1k_1l_1$), ($h_2k_2l_2$) – the angles between the planes (only if more than one \vec{g} is visible in the DP). Table 2-3 summarizes the relationship between these angles.

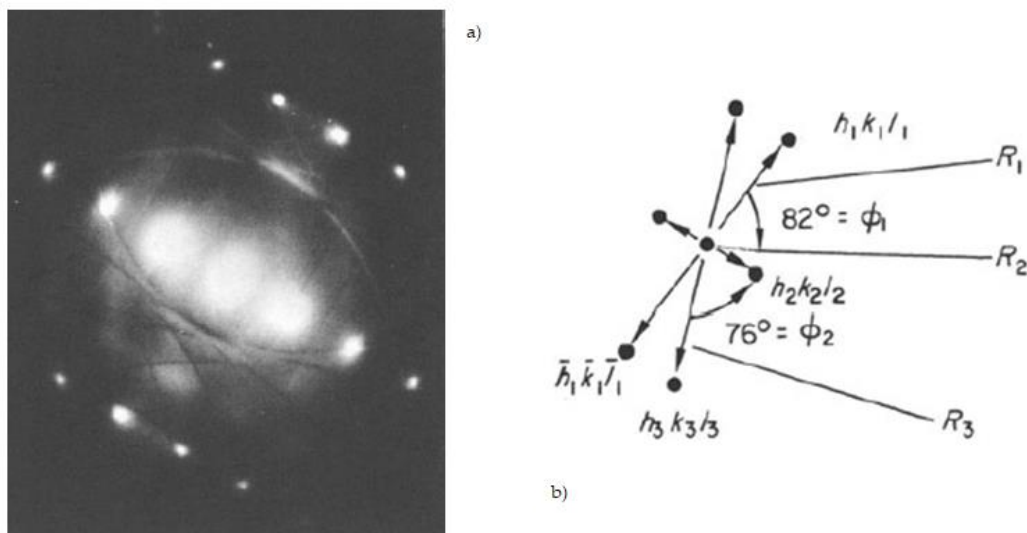


Figure 2-13 - a) A diffraction pattern from a single crystal of aluminium, indexed as shown in b). From [9].

Table 2-3 – Angles between selected hkl planes. Adapted from [9].

$h_1k_1l_1$	$h_2k_2l_2$	Angles between planes				
111	111	0°	70° 32'			
	200	54° 44'				
	220	35° 16'	90°			
	311	29° 30'	58° 31'	79° 59'		
	422	19° 28'	61° 52'	90°		
200	200	0°	90°			
	220	45°	90°			
	311	25° 14'	72° 27'			
	422	35° 16'	65° 54'			
220	220	0°	60°	90°		
	311	31° 29'	64° 46'	90°		
	422	30°	54° 44'	73° 16'	90°	
422	422	0°	33° 33'	48° 11'	60°	
	311	10° 10'	42° 24'	60° 30'	75° 45'	90°

2.3. Imaging in a TEM

Section 2.2. sets the basis of electronic diffraction, which are the foundation for image formation in TEM. Once a DP, obtained through selection area diffraction, is projected onto the screen and indexed, this DP, and more specifically its bright central spot (containing direct electrons and some scattered electrons [13]), can be used to form two types of image: bright field (BF) and dark field (DF) images. Figure 2-14(a) shows the formation of a BF image, if the direct beam is selected, and (b) shows that, if scattered electrons of any form are selected, the image formed is a DF image.

If the DP changes, the image will also change. Henceforth, it is critical to relate the DP to the image [13] by indicating the direction of the \vec{g} in the image.

The ideal condition to image dislocations in TEM depends, evidently, on the direction of \vec{g} , but also on its nature, that is, on its Burgers vector \vec{b} . This leads to the conclusion that the image of a dislocation depends on the term $\vec{g} \cdot \vec{b}$ (see [15]), where the result can be either zero or an integer for a perfect dislocation, and zero, a fraction or an integer for a partial dislocation.

For perfect or partial dislocations with $\vec{g} \cdot \vec{b} = 1, 2, \dots$, the image is a dark line in BF or a white line in DF. For partial dislocations with fractional values of $\vec{g} \cdot \vec{b}$, the contrast is complicated [15]. However, the most useful feature of dislocation images is their invisibility in BF and DF images happening at $\vec{g} \cdot \vec{b} = 0$. This situation, where the crystal behaves as if

the dislocation were not present ^[15], is known as the “invisibility criterion” and has been one of the first criterion to determine the Burgers vector ^[16].

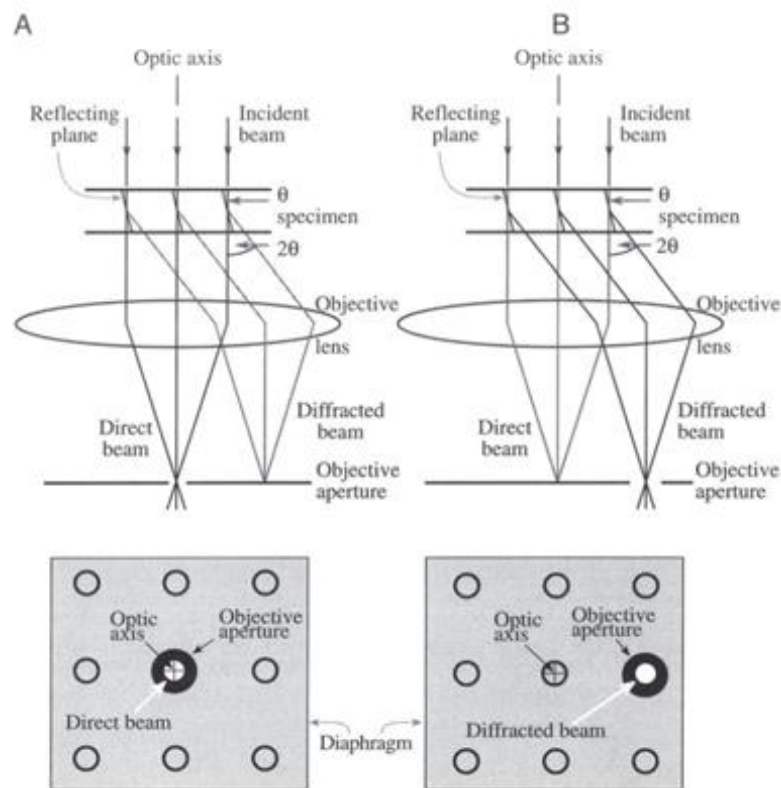


Figure 2-14 – Ray diagrams showing how: (a) a BF image formed from the direct beam, and (b) a displaced-aperture DF image formed with a specific off-axis scattered beam. From ^[13].

2.4. Crystal orientation determination

Diffraction patterns can help determine the direction of the electron beam and also the complete orientation of that region of the specimen illuminated by the beam ^[17], once a DP is obtained and indexed (\vec{g}_1), it can be used in conjunction with (ideally) at least two other (\vec{g}_2 and \vec{g}_3) ^[12,17] of the same crystal to access its orientation with respect to a specific axis. A knowledge of the exact orientation of crystals is important for investigating lattice defects ^[12] and plasticity mechanisms.

A method for representing the crystal orientation is the stereographic projection. The stereographic projection is a very ancient geometrical technique, that originated in the second century A.D. in the work of the Alexandrian astronomer Claudius Ptolemy who used it as a means of representing the stars on the heavenly sphere ^[18]. The stereographic projection was first applied to crystallography in the work of F. E. Neumann ^[19,20] and was further developed by W. H. Miller ^[21].

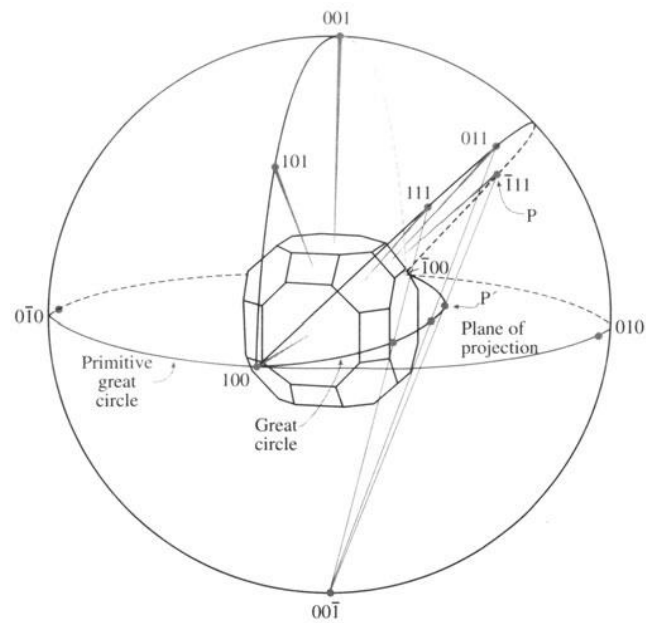


Figure 2-15 – The stereographic projection, where the crystal is at the centre of the sphere. From [17].

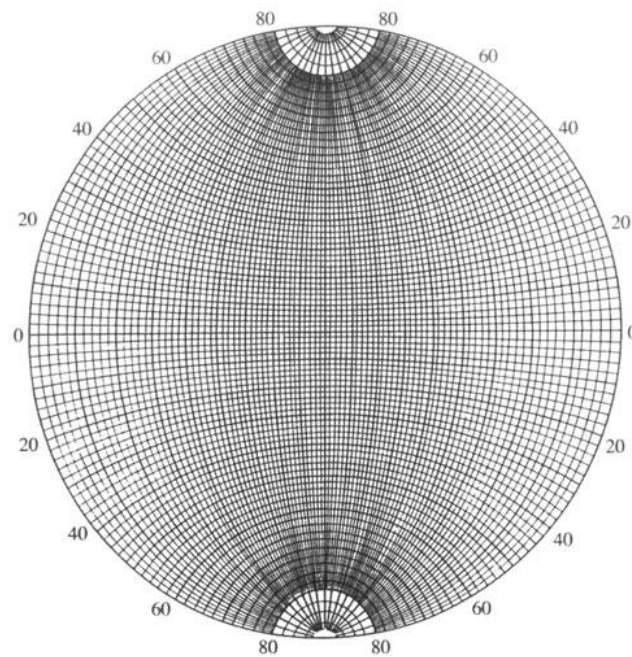


Figure 2-16 – The Wulff net, where each meridian is 2° apart, so the net covers 180° . From [17].

The geometry of the stereographic projection may be described as follows: the crystal is imagined to be at the centre of a sphere (Figure 2-15); the normals to the crystal faces are imagined to radiate out from the centre and to intersect the sphere in an array of points. Each point on the sphere therefore represents a crystal face or plane (and is labelled with the appropriate Miller index). The (angular) distance between two points is equal to the

angle between the corresponding planes (lines of longitude are called great circles which pass through the north and south poles, the angular distances between the poles being 180° ; lines of latitude are called small circles and represent different angular distances from the north and south poles, the largest of which is the equator at 90° from the north and south poles, and is also called primitive great circle or parallel of latitude) ^[18].

Representing the normal to any (hkl) plane in the stereographic projection is made easy by using the net devised by G. V. Wulff ^[22] (Figure 2-16), where the equator line represents 0° and the north and south poles represent 90° .

The coordinates needed to construct this 2D graphic representation of a crystal can be obtained as follows:

- As already mentioned, two to three \vec{g} are needed (indexed from their respective DPs). They will be positioned onto the Wulff net using their latitude and longitude coordinates.
- The latitude is obtained from the tilt at which the \vec{g} was imaged. When the tilt is positive, the position of the \vec{g} will be on the east pole and when it is negative, on the west pole of the net.
- The longitude is obtained from measuring the angle between a line drawn from the centre spot to diffracted spots and the straining axis (vertical in all the JEOL 2010 TEM images and DPs). This angle will be referred as α from now on. This α angle is positioned onto the net from the north pole down.
- To confirm the \vec{g} s are correctly positioned, the angles between them must coincide with the angles reported in Table 2-3.
- Once the \vec{g} s are confirmed to be in the correct coordinates, the rest of the (hkl) plane normals can be added to complete the stereographic projection (the main (hkl) planes reported are {111}, {001} and {110} plane families).

A stereographic projection constructed following these steps will give the orientation of a crystal at 0° of tilt. The straining axis will be parallel to its central vertical line. Each stereographic projection will be related to a set of specific Euler angles ($\varphi_1, \varphi, \varphi_2$) (for more information on this topic, please refer to ^[23]).

An example of a crystal orientation determination will be given using specimen 35/I2-Head10 (Figure 2-17), where the presence of a fissure in the grain identified as G1 makes this the more likely place where dislocation movement will start. However, for the purpose of this example (crystal orientation determination), G2 will be the focus.

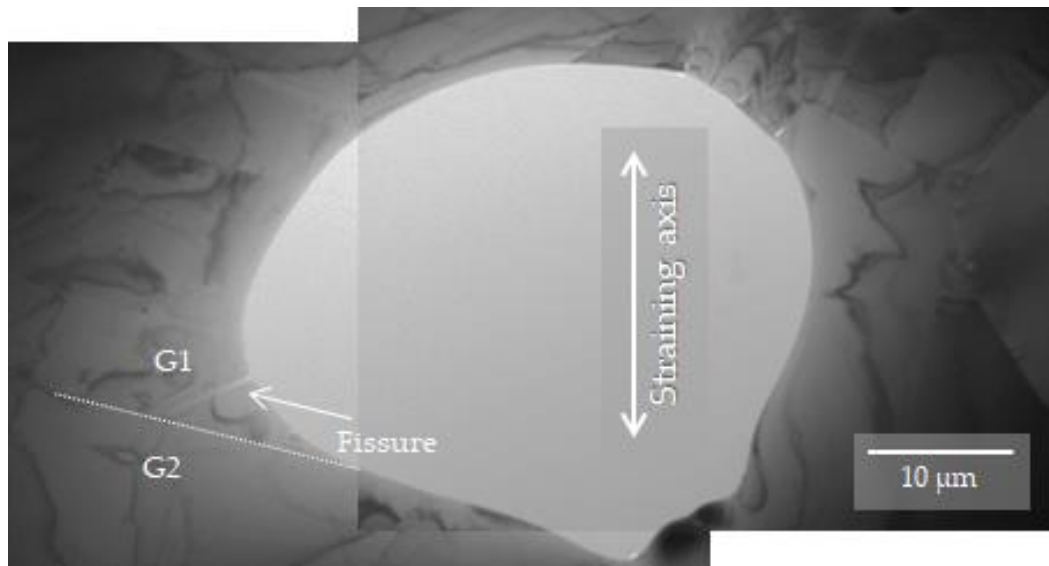


Figure 2-17 – TEM image of Specimen 35/I2-Head10, strained at $T = 293$ K. The hole rim shows the presence of several grains of different crystal orientations, specially signalling the left side, where grains G1 and G2 are separated by a grain boundary (white dashed line). A fissure is already present in G1. The straining axis direction is indicated by the white arrow.

First, as per the steps previously indicated, at least two DP are obtained at different \vec{g} (presented in Figure 2-18). The tilt at which they were taken is noted (latitude) and the angle between the diffraction spots and the straining axis is calculated (longitude). The distance between the spots is measured to determine the type of plane.

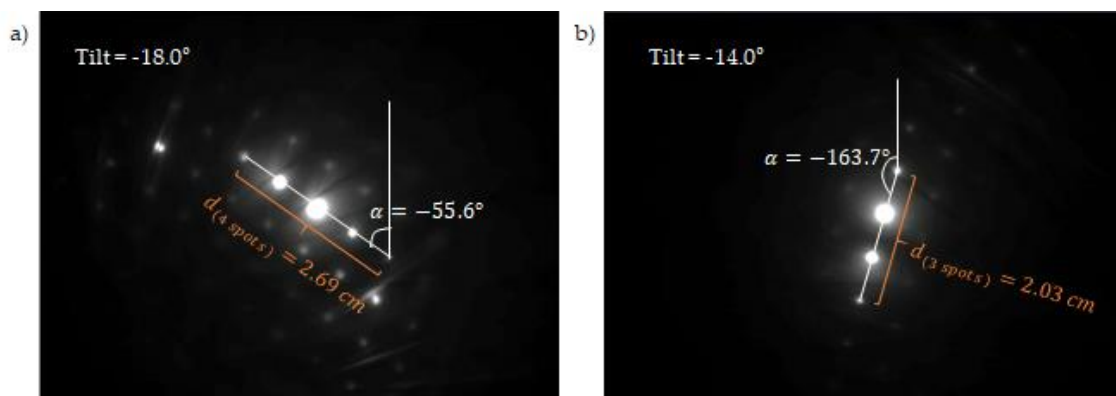


Figure 2-18 – DPs of specimen 35/I2-Head10 taken at: a) -18.0° of tilt and b) -14.0° of tilt. In orange, the distance measured between visible spots. In white, the measured angle between the spots and the straining axis.

From the figure, the type of plane can be determined using the values from Table 2-2. The analysis of both DPs can be found in Table 2-4. These are the values that will be used to

construct the stereographic projection, which will be possible with the aid of Stereoproj, a software part of the Pycotem package ^[24,25].

Table 2-4 – DP analysis from specimen 35/I2-Head10.

Image	Plane Determination				Position	
	Distance (cm)	Spots	R (cm)	Plane type	Tilt	α
a)	2.69	4	0.67	{111}	-18.0°	-55.6°
b)	2.03	3	0.67	{111}	-14.0°	-163.7°

Stereoproj (Figure 2-19) presents an empty Wulff net and input parameters (plane type, tilt and inclination α , or Euler angles if known) to be completed by the user. The “Crystal parameter” section is filled out automatically when selecting the type of crystal (fcc in the case for CoCrFeMnNi). The “Axis / Rotation” section is the most relevant for entering the values obtained from DPs:

- g-vector: the type of plane.
- Tilt (α, β, z): the tilt at which the DP was taken. As the holder used for this study is a single-tilt holder, the values of β and z are zero.
- Inclination: the measured inclination angle.

One diffraction pattern is chosen to be entered. The second DP will be used to verify that all planes are in the correct position, by rotating the projection along the chosen g (Figure 2-20). Once both \vec{g} are in their correct placement, the poles/planes can be added to obtain the final stereographic projection and its corresponding Euler angles (Figure 2-21).

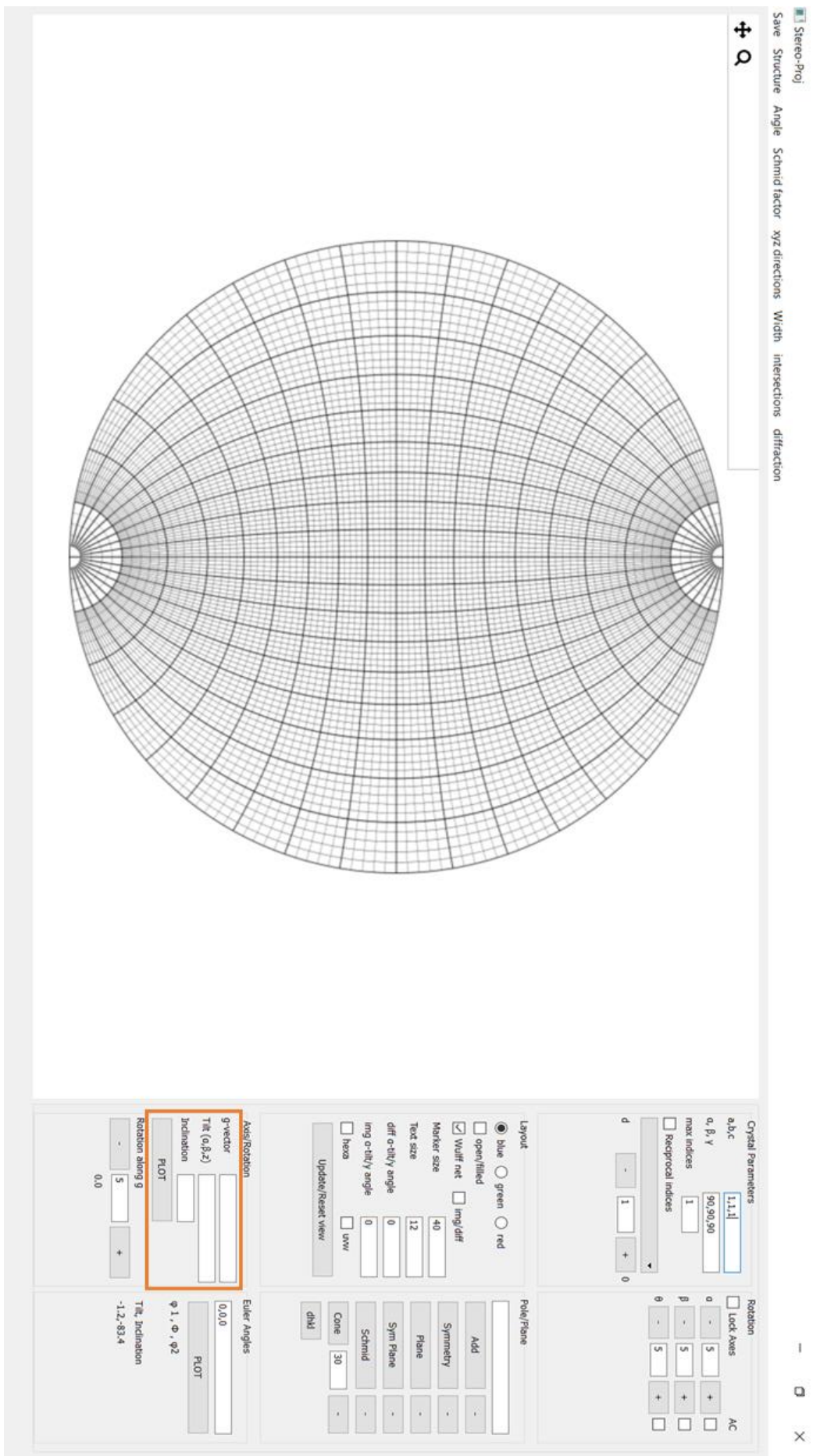


Figure 2-19 – Stereoproj interface. The orange frame highlights the input parameters the user must fill in order to start the construction from a set of DPs.

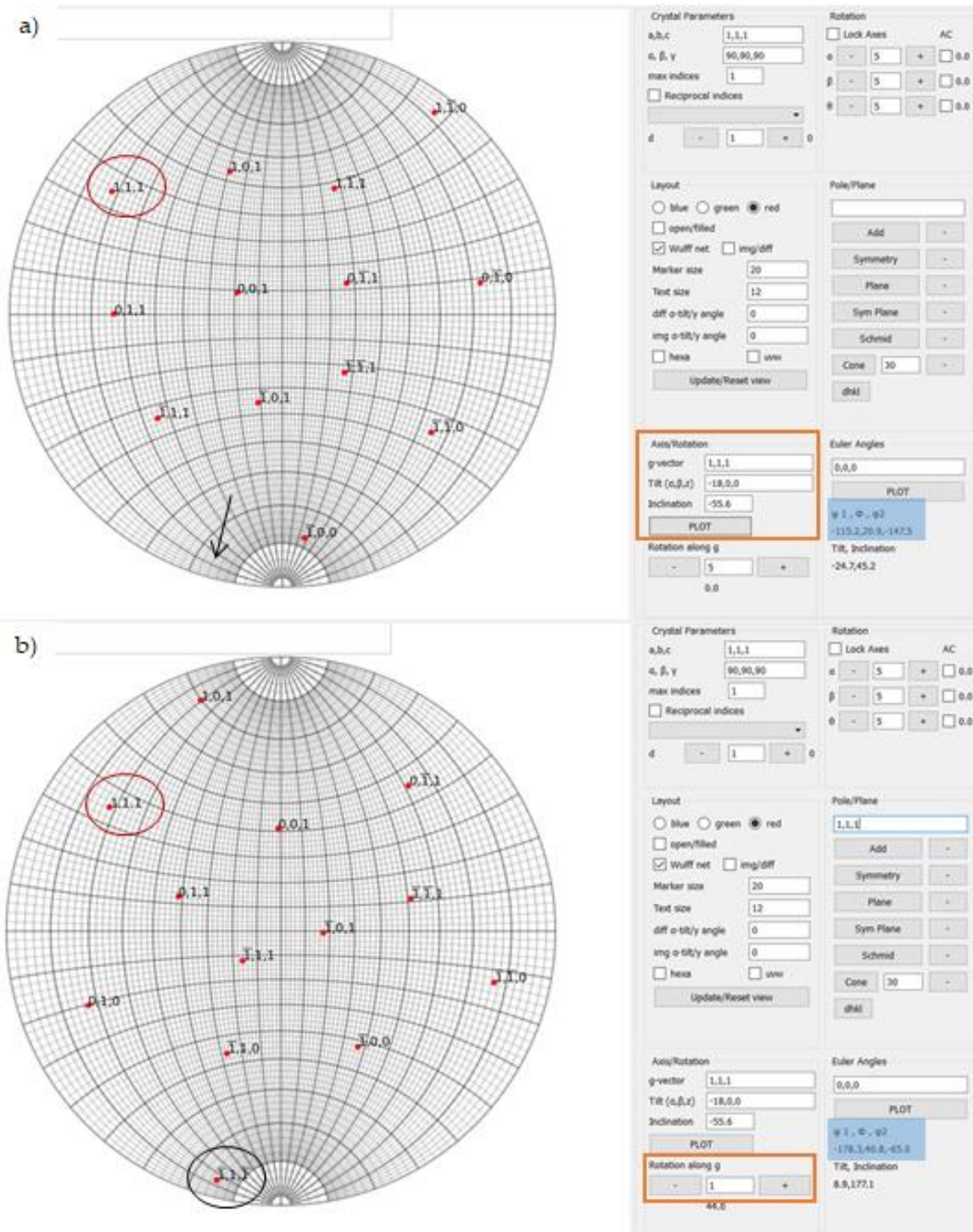


Figure 2-20 – a) The values for the first DP are entered (orange frame) as pole (111) (red circle). Note that no other pole corresponds to the calculated position for the second DP (black arrow). b) After rotating around $g = (111)$ 44° (orange frame), pole $(\bar{1}\bar{1}\bar{1})$ (black circle) falls into the place previously marked by the black arrow. Note that the Euler angles (blue frames) change when rotating along g .

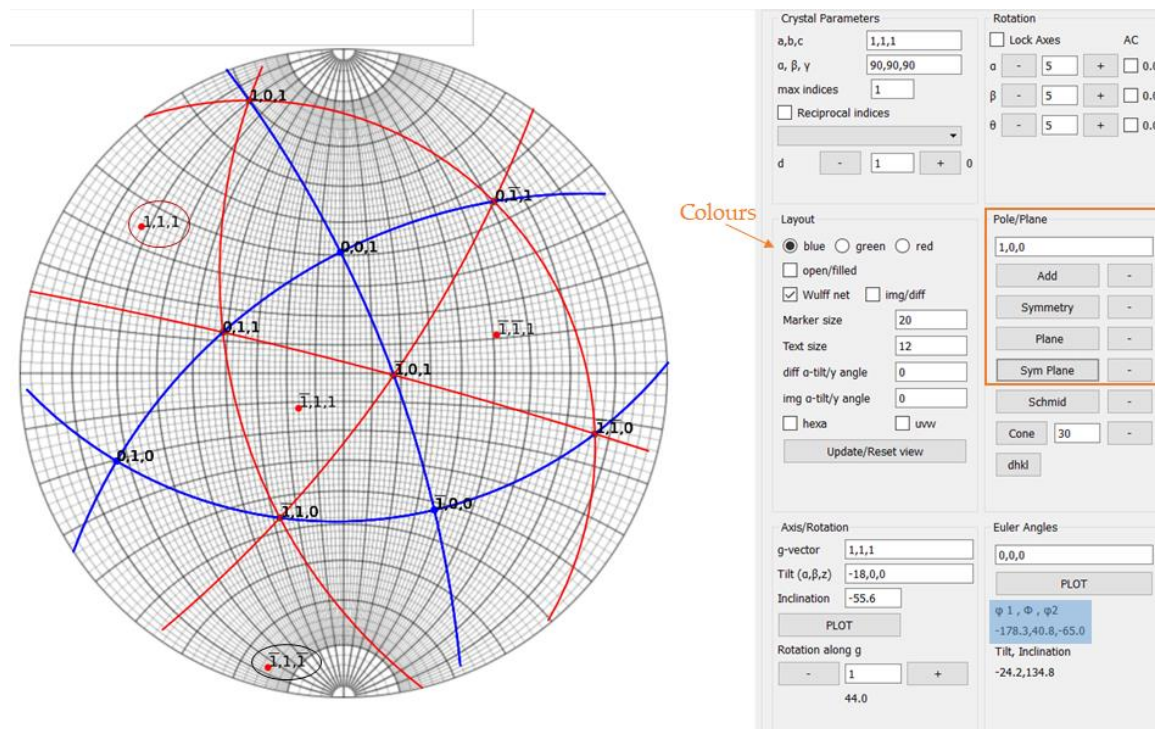


Figure 2-21 – Final stereographic projection for G2 of specimen 35/12-Head10. Orange frame: user enters the family of planes to plot, changing the colours using the options on the Layout section (indicated by orange arrow); Red circle: first DP; black circle: second DP; blue frame: final Euler angles.

3. Direct results from *in situ* TEM straining experiments

Now that the theoretical basis of TEM manipulations are explained, this section will focus on applying these concepts to interpret the *in situ* TEM straining experiments.

3.1. Indexing dislocations

Finding the invisibility criterion to index dislocations can be done either in conventional TEM imaging or during *in situ* TEM straining experiments. Independently of the experiment, the technique is the same and the steps to follow are identical:

- Identify the dislocations to study and their habitat grain.
- Determine the orientation of said grain, following the steps of section 2.4.
- Once the grain's orientation is known, determine the slip plane of the dislocation. The slip traces created after dislocations moving are parallel to the slip plane; superposing the slip trace over the grain's stereographic projection allows for the determination of the slip plane.
- Obtain (preferably and when the conditions allow it) two $\vec{g} \cdot \vec{b} = 0$ conditions.

Because, for screw dislocations, $\vec{g} \cdot \vec{b} = \|\vec{g}\| \|\vec{b}\| \cos 90 = 0$, \vec{b} can be said to be the plane normal positioned 90° away from \vec{g} . This can be precisely determined following Table 2-3. These steps are exemplified next.

In an *in situ* TEM straining experiment, once the yield stress is attained (as explained in section 2.1.), dislocations will start to move in the most favourably oriented grain of the specimen. Once spotted, the orientation of the grain is determined and the stereographic projection is constructed following the process previously presented in section 2.4. (also see ^[25]). Continuing with the example of specimen 35/I2-Head10, strained at $T = 293$ K, perfect dislocations were seen moving in G2 forming a pile-up (Figure 2-22).

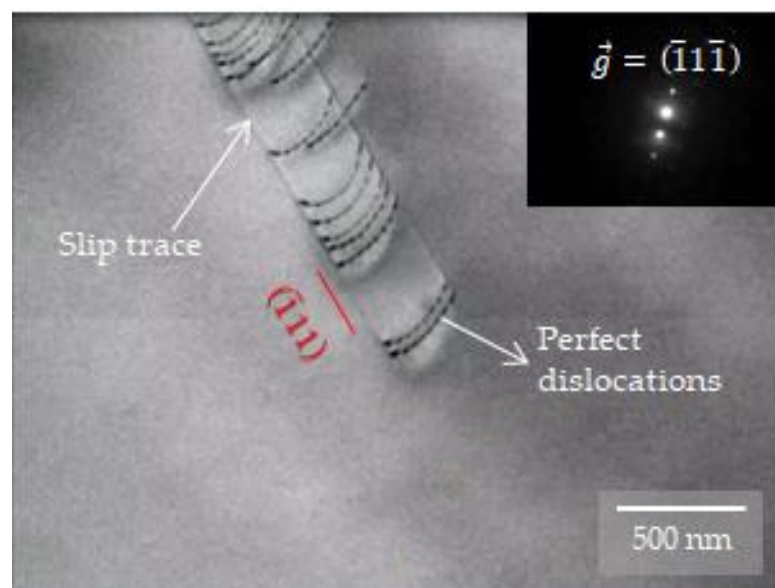


Figure 2-22 – Specimen 35/I2-Head10, G2. A pile-up of perfect dislocations, where its slip traces are clearly visible, glides on plane $(\bar{1}1\bar{1})$ (in red). Insert: corresponding diffraction pattern of the image.

Once the dislocations are identified and the grain's orientation is known, the slip traces help determine that the glide plane of this pile-up is on $(\bar{1}1\bar{1})$, as it corresponds to the normal of the same plane, as seen on Figure 2-21. Now, $\vec{g} \cdot \vec{b} = 0$ conditions are identified (Figure 2-23 (a)-(b)). Part (c) of the figure presents again the stereographic projection, now showing in black both vectors that fulfil the invisibility criterion, and 90° away from each the Burgers vector can be identified as $\vec{b} = [0\bar{1}1]$.

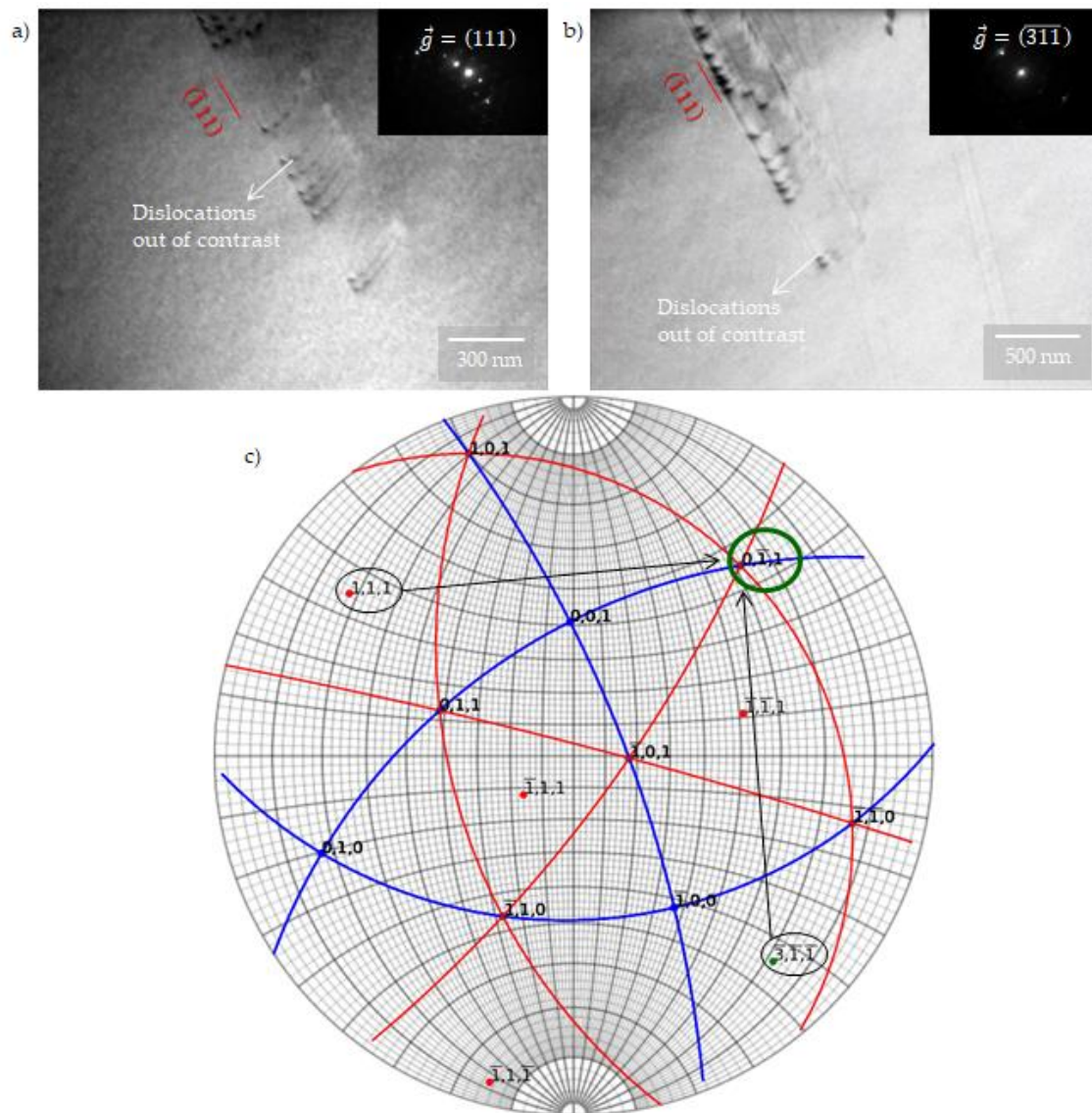


Figure 2-23 – Same specimen and pile-up as before. a) and b) show two conditions where dislocations are out of contrast. c) Both \vec{g} from the previous parts (in black circles) indicate the Burgers vector (green circle).

From the previous figures, the slip system for the pile-up is then indexed as $(\bar{1}\bar{1}1)[0\bar{1}1]$.

The case for partial dislocations is more complicated. However, the same principle can be used to determine their slip system and index them. As a reminder,

$$\frac{a}{2}[110] \rightarrow \frac{a}{6}[211] + \text{SF} + \frac{a}{6}[\bar{1}2\bar{1}]$$

From Table 2-3, the likely \vec{g} s to fulfil the invisibility criterion for partial dislocations (of $[11\bar{2}]$ type Burgers vector) are $\{111\}$, $\{110\}$ or $\{113\}$ types. This case will be presented in detail in the next chapter.

3.2. Observation of stacking faults vs. twinning

The definition of these mechanisms was already presented in Chapter 1 (section 3.1.7), but it is important to the identification of stacking faults (SFs) and twinning in TEM. A stacking fault is an error in the sequence of atom layers of the closest packed plane (Figure 2-24) and, in low stacking-fault energy materials, they can be seen as “extended dislocation” – a stacking fault bounded by partial dislocations.

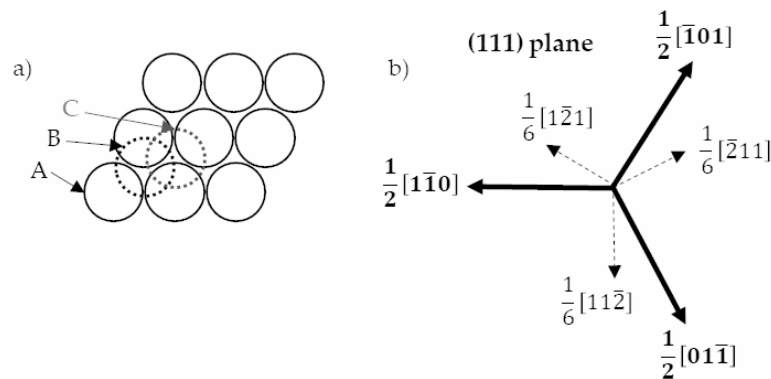


Figure 2-24 – a) Projection normal to the (111) plane showing the three types of stacking positions A, B and C. b) fcc possible Burgers vectors and their Shockley partials in a (111) plane. Adapted from [26].

The split of a perfect dislocation on a (111) plane into two partial dislocations is energetically favourable because the energy of a line defect is proportional to the square of the Burgers vector magnitude¹. Considering a perfect dislocation dissociating into two Shockley partials with $\vec{b}_p = 1/6 \langle 11\bar{2} \rangle$, this direction is no longer in the closest packed direction; the two resulting Burgers vectors are now at 60° with respect to one another and, in order to complete a perfect dislocation, they repel each other. As the partial dislocations repel, a stacking fault is created in between. The stacking fault has a higher energy than that of the perfect crystal, thus it attracts the partial dislocations together again.

¹ This is called the Frank criterion [27], which states that the energy of a dislocation is proportional to b^2 , and that in order for a dislocation \vec{b} to dissociate into two dislocations \vec{b}_1 and \vec{b}_2 while being energetically stable, the following must occur:

$$b^2 > b_1^2 + b_2^2$$

SFs can be intrinsic (formed when a layer of the atoms is removed from the normal sequence – from ABCABC... to ABC|BC...) or extrinsic (formed by the addition of a layer of atoms to the normal sequence – from ABCABC... to ABCAB|A|C...) [26]. Note from part (a) of the previous figure that three layers are shifted by $1/3 \langle 111 \rangle$ (which is the value of the displacement vector \vec{R}_f) along the plane normal, forming a repeat pattern with periodicity $\langle 111 \rangle$ [28]. This means that removing a [111] plane when displacing the stacking in the direction of \vec{R}_f , as shown in Figure 2-25, produces an intrinsic SF [29].

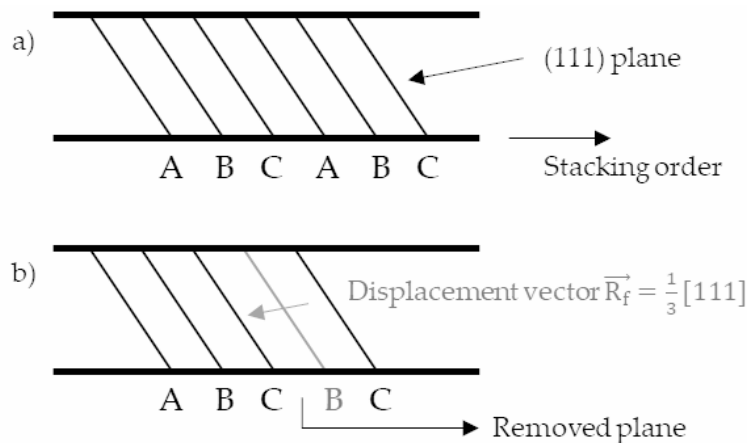


Figure 2-25 – Intrinsic stacking fault formation. a) Perfect crystal. b) SF present with its associated displacement vector. Adapted from [29].

The SF contrast is observed in TEM as fringes (Figure 2-26). The superposition of two intrinsic SFs generates a stacking similar to the one originated by an extrinsic SF, and there is a displacement vector \vec{R}_f opposite to the intrinsic fault direction. Superposing three SFs leads to a displacement vector $\vec{R}_f = [111]$, meaning that the stacking contrast corresponds to that of a perfect crystal [29]. Superposing a supplementary fault, the associated \vec{R}_f will lead to a contrast corresponding to just one SF.

Twinning can be thus defined as an overlap of three SFs (shifting every layer above a pre-selected (111) plane from ABCABC... to CBACBA... [28]). The creation of a mechanical twinning is done by the movement of multiple partial dislocations with the same Burgers vector on adjacent (111) planes. This occurs in three stages, according to Vergnol and Grilhe [30]:

1. The development of an initial large stacking fault.
2. The nucleation of a micro-twin by superposition of extended faults in the neighbouring planes.
3. The extension of this nucleus by propagation of the twin boundary through the strained material.

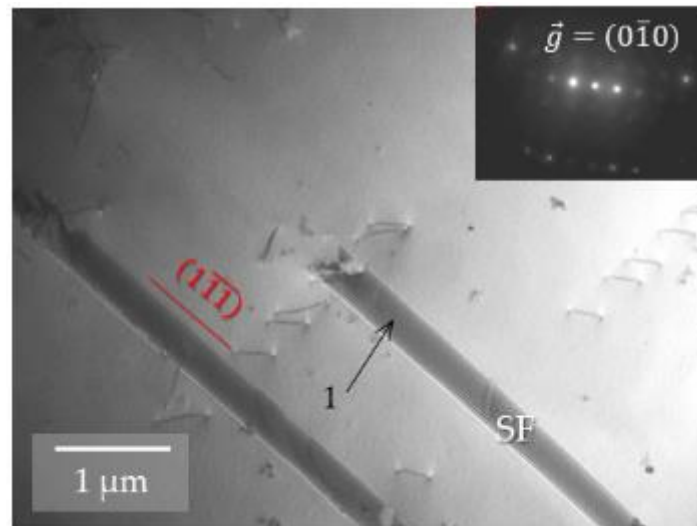


Figure 2-26 – Specimen 35/I2-HeadB, strained at $T = 100$ K. The SFs present show contrast type 1 (one SF, no superposition).

Because the Burgers vectors of the partial dislocations are the same, the extremities of the overlapping SFs are not exactly in the same place, thus a sequence of contrasts associated with the increase of SFs can be seen in TEM, as seen in the next figure:

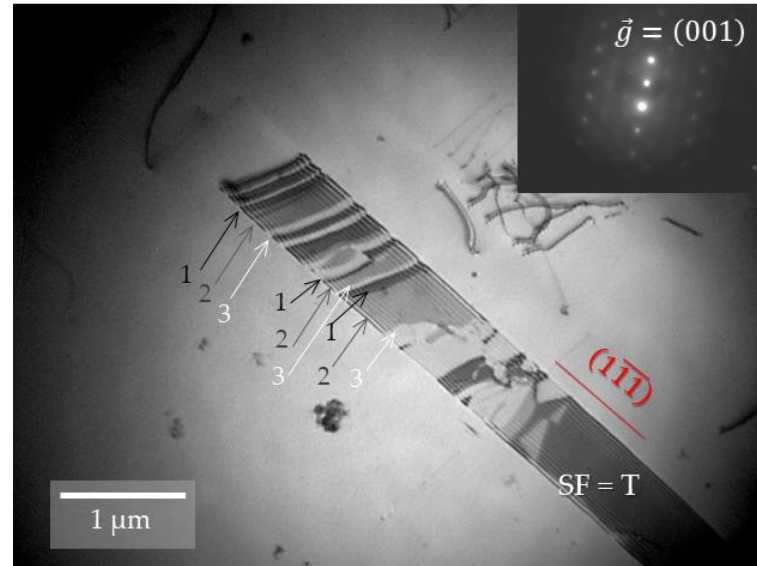


Figure 2-27 – Specimen 35/I2-HeadB, strained at $T = 100$ K. The superposition of partial dislocations leads to twinning, as evidenced by the contrast shift (1-2-3).

The greatest probability for twinning occurrence corresponds with the strain conditions which induces extrinsic faults in the crystal ^[30].

3.3. Thickness determination

When imaging crystal defects, for example, in the observation of dislocation structure and *in situ* experiments, the question arises whether such thin foils are representative of the bulk material ^[12]. The main effect is due to the close presence of surfaces that are dislocation sinks. This has been rationalized through the notion of "image forces" that simplify the calculation of the stress exerted by a surface on a given dislocation ^[31].

Electropolished samples exhibit varying thicknesses from a few tens of nm at the very edges of the central hole to several microns when moving away from it. Electron transparency depends on several factors including atomic numbers of atoms composing the sample, acceleration voltage and beam intensity as well as the diffraction vector used during imaging. Observations reported in this work address thicknesses ranging from 100 to ~ 700 nm, mainly depending on the location of plastic events, that are difficult to forecast. Above ~ 800 - 1000 nm, the signal/ratio becomes too weak to capture useful dynamical sequences of dislocation movements.

Although many ways exist to calculate a given specimen thickness (convergent beam electron diffraction (CBED), electron energy loss spectrometry (EELS) – see below), this study opted for a trace analysis method, which consists on determining the projected width of an activated glide plane, directly accessible through slip traces, that are profusely created during straining experiments. A more complex way is to determine the direction of intersection of the habit plane of the defect (in this case, dislocations) and the angle between the habit plane and the foil normal ^[9].

An explanation on the technique is given by Delmas et al. ^[32], which is, in turn, derived from Kelly ^[33]:

The absence of through-thickness defects such as twin boundaries or stacking fault ribbons makes the foil thickness measurement by conventional TEM very difficult. So, an original method based on the TEM *in situ* straining technique has been developed. Samples are strained in the TEM to cause dislocation motions. The occurrence of slip traces at the surfaces of the specimen induced by the dislocation motions allows the accurate calculation of the foil thickness. Indeed, by measuring the apparent distance between two slip traces on the images and taking into account imaging conditions, thickness of the foil can be deduced using simple trigonometric relationships. The relation between the apparent distance between slip traces and the thickness is given by the following relation:

$$t = d_{\text{app}} \frac{\sin(\theta)}{\cos(\theta - |\beta|)}$$

Equation 2-10 – Thickness of a TEM foil in relation with the active slip traces.

where θ represents the angle between the slip plane and the specimen plane and β is the tilting angle of the sample in the TEM. [33]

To exemplify this calculation, still micrographs from the *in situ* TEM straining of a specimen of CoCrFeMnNi named 35/I2-Head22 (strained at 96 K) were taken. The indexation of the pile-up of perfect dislocations (showed in Figure 2-24(a)) was made as explained in the previous section. There are two active slip systems in this area: $(\bar{1}\bar{1}1)[\bar{1}10]$, the primary system with a Schmid factor of 0.46, and $(\bar{1}11)[0\bar{1}1]$, the secondary system with a Schmid factor of 0.32. This example will concentrate on the primary slip system (insert of part (a) of the figure).

Figure 2-24 (b) shows the trigonometric relationships between the apparent width (d_{app}) of the slip traces, which exist in the image plane – a projection of the specimen, the tilting angle ($+27.0^\circ$ for the image in (a)), and the thickness of the specimen. In this case,

$$d_{\text{app}} = 291 \text{ nm}$$

$$\theta = 50^\circ$$

$$\beta = 27^\circ$$

$$\Rightarrow t = 291 \text{ nm} \frac{\sin(50^\circ)}{\cos(23^\circ)} = 240 \text{ nm}$$

It is important to note that this measure (and all measures of its type) is local. It can only attest of the thickness of the specimen in the area of the micrograph, on the slip system used for the measure.

To confirm the relevance of the result, the same sample was studied using the EELS – EFTEM technique (the experiment was performed at CEMES-CNRS by Cécile Marcelot, in a Hitachi I2TEM microscope operating at 300 KeV). The same area of study was, unfortunately, not identified when performing the EELS – EFTEM measure; however, an area next to the hole rim was used in its place. The results are shown in Figure 2-29. The maximum thickness obtained by this technique is $t = 114 \text{ nm}$.

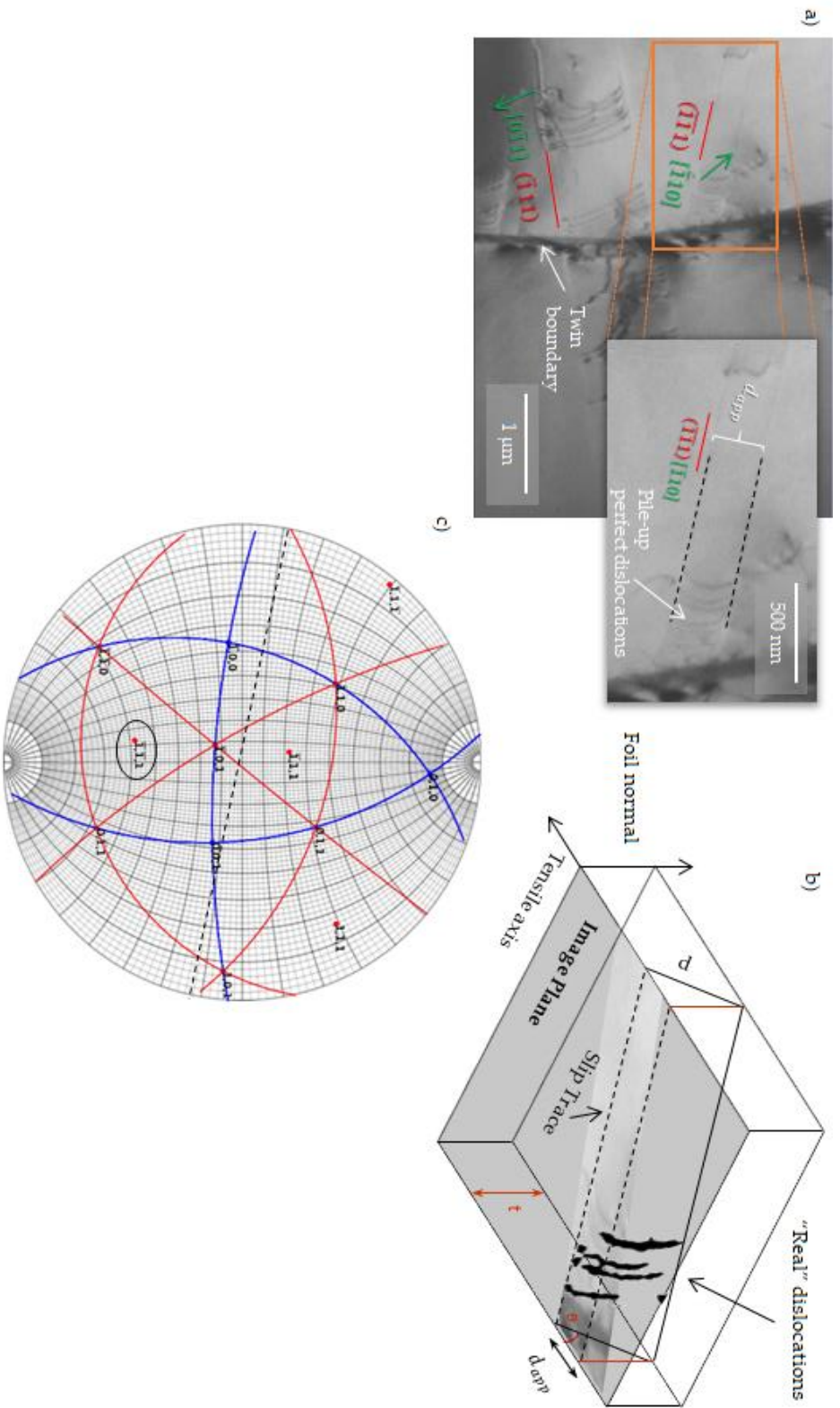


Figure 2-28 – Specimen 35/12-Head22, strained at $T = 96$ K. Two slip systems are active (in red) and their Burgers vectors direction are indicated (in green). The primary slip system (highlighted in the orange frame) is piled against a twin boundary; the insert magnifies the highlighted area, showing the pile-up and its apparent width (in white) and its slip traces (in black). b) Trigonometric construction of the image in the projection plane (same as in (a)), showing the pile-up, d_{app} , d , θ and t . c) Corresponding stereographic projection, showing the primary plane (111) (black circle) corresponding perfectly to the slip traces of (a) (black dashed line).

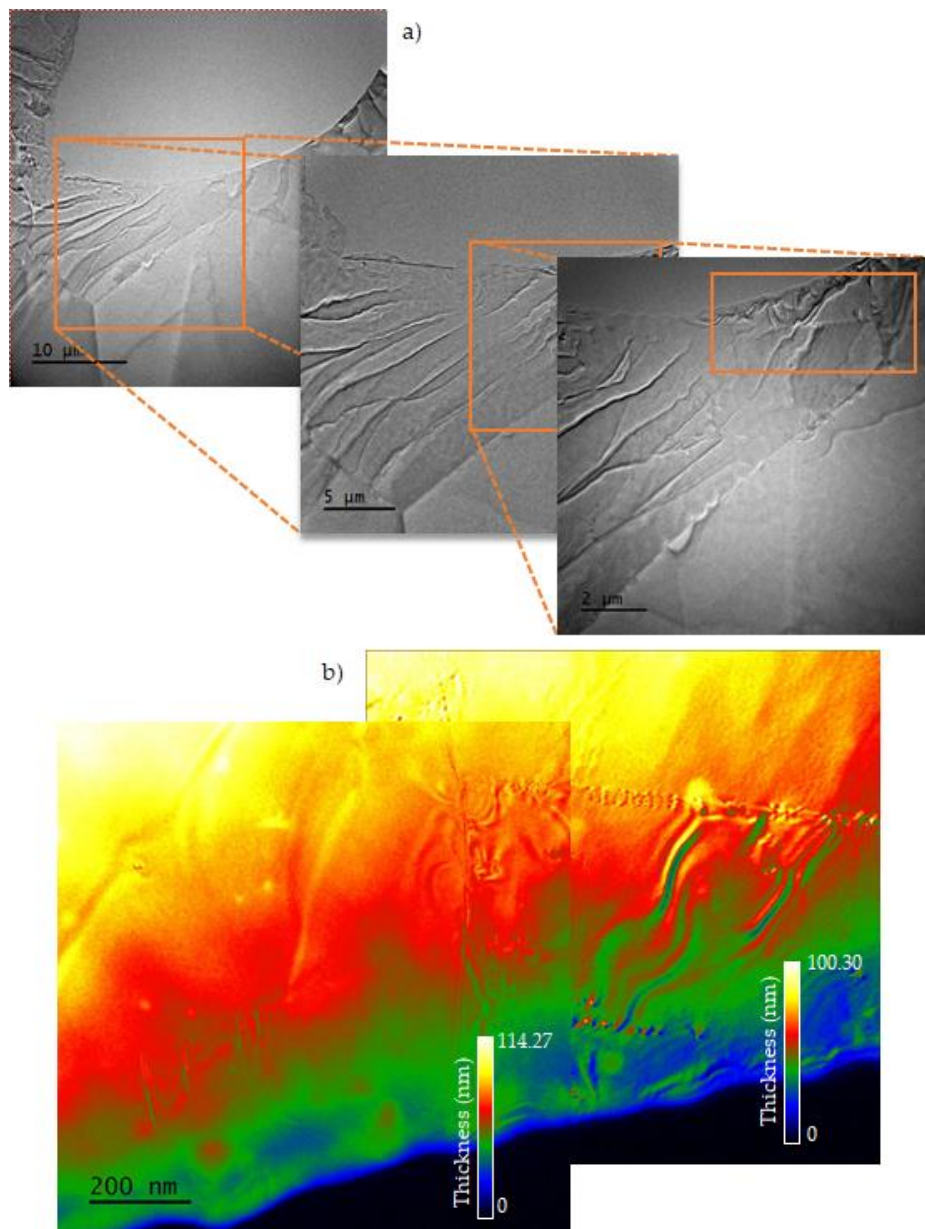


Figure 2-29 – Same specimen as the previous figure, in another area of the hole rim. a) TEM micrograph for the selection of the area for the analysis, where each insert shows increasing magnification over the area. b) Thickness cartography of the selected area (180° rotation). The thickness can be calculated with the help of the colour legend.

There is a discrepancy on the measured thickness because, as evidenced from the last figure, the thickness map can only be taken in an area very close to the hole rim, as EELS cannot be performed on thick samples.

A cross-section including the same area of the EELS – EFTEM scan was taken to measure its thickness. This was done in a Thermo Fisher HELIOS FIB-SEM, after Pt coating both faces of the specimen over the selected area (Figure 2-30). A cross-section of the area was

lifted-out and welded onto a TEM grid. This cross-section was measured, and the results are shown in Figure 2-30. In the 1/8th of the cross-section, the measured thickness does correspond to the EELS measurement of about 120 nm. The figure permits to appreciate the typical wedge shape of an electropolished sample.

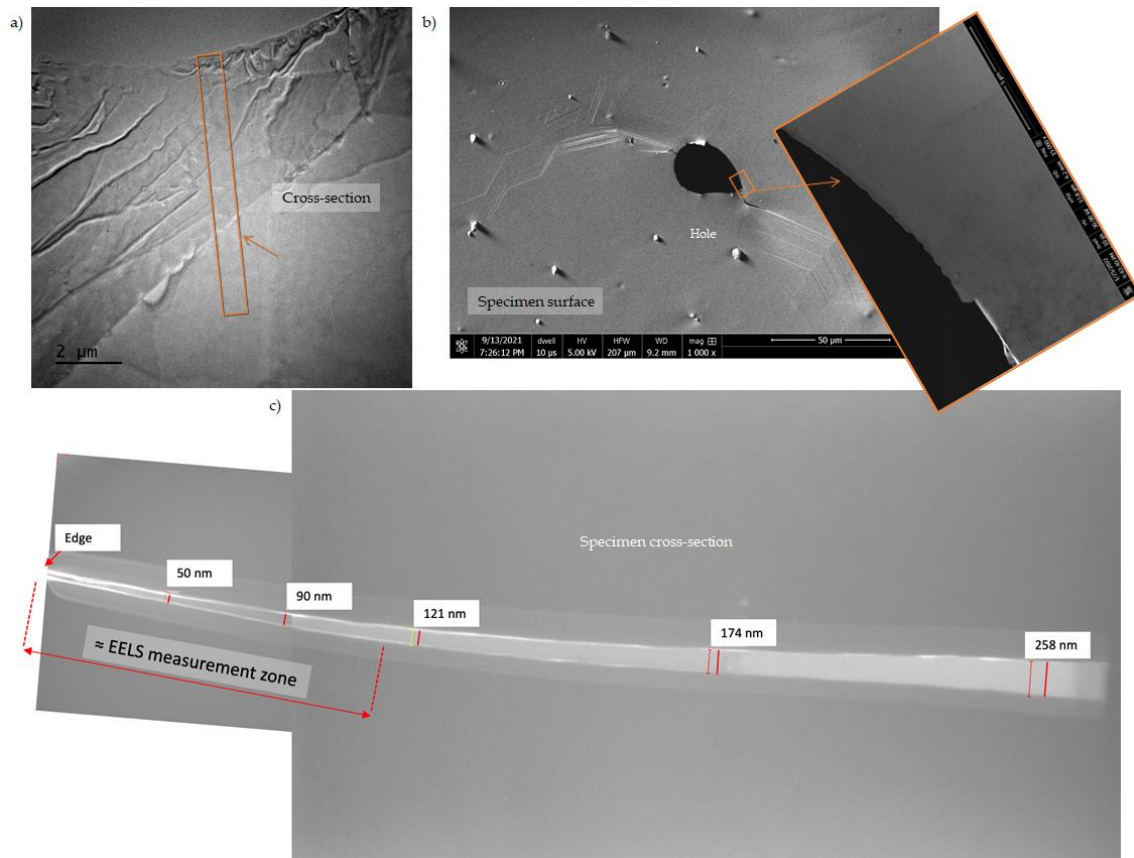


Figure 2-30 – Same specimen as before. a) Same TEM micrograph, indicating the section to be lift-out for the cross-section (in orange). b) FIB-SEM image of the specimen, showing the hole and, in the orange frame and insert, the same area to perform the cross-section. c) Measured thickness values (red lines) along the cross-section.

To sum up, calculating the local thickness of a specimen with the aid of the apparent width of a slip plane gives a reliable measure.

4. Conclusions

This chapter introduced the specimens and the technique used in this study. The theoretical bases were given and the different parameters that can be determined from *in situ* TEM straining experiments were introduced.

This chapter explained how to:

- Identify dislocations in TEM (perfect – undissociated and dissociated into Shockley partials, and twinning).
- Index those dislocations to know their slip system (glide plane and Burgers vector).
- Obtain the crystallographic orientation of a studied grain (though the diffraction patterns obtained from the *in situ* experiment).
- Calculate the local thickness of the specimen (and, by extension, other projected measurements) from the projected TEM image.

The next chapter will expand on these methods to analyse the behaviour of dislocations in the CoCrFeMnNi alloy at RT and LN₂T.

5. Bibliography

- [1] A. Fraczkiewicz, *Alliage métallique, pièce métallique et procédé d'obtention*, **2016**, FR1459567.
- [2] D. Oliveros, A. Fraczkiewicz, A. Dlouhy, C. Zhang, H. Song, S. Sandfeld, M. Legros, *Mat. Chem. Phys.* **2021**, 272, 124955.
- [3] O. Schneeweiss, M. Friák, M. Dudová, D. Holec, M. Šob, D. Kriegner, V. Holý, P. Beran, E. P. George, J. Neugebauer, A. Dlouhý, *Phys. Rev. B* **2017**, 96, 13.
- [4] M. Mroz, Design and Structural Optimization of a High Entropy Alloy (HEA) of the CoCrFeMnNi Family with High Mechanical Resistance., Université de Lyon, **2018**.
- [5] D. Oliveros, M. Legros, D. Lamirault, *In Situ TEM Tensile Specimen Preparation*, **2019**.
- [6] A. Coujou, Ph. Lours, N. A. Roy, D. Caillard, N. Clement, *Acta metall. mater.* **1990**, 38, 825–837.
- [7] A. Rajabzadeh, Etude Expérimentale et Théorique de La Migration de Joints de Grains, Couplée à Un Cisaillement, Université Toulouse III Paul Sabatier, **2013**.
- [8] D. B. Williams, C. B. Carter, in *Transmission Electron Microscopy*, Springer US, Boston, MA, **2009**, pp. 407–417.
- [9] J. W. Edington, *Electron Diffraction in the Electron Microscope*, Macmillan Education UK, London, **1975**.
- [10] K. W. Andrews, D. J. Dyson, S. R. Keown, *Interpretation of Electron Diffraction Patterns*, Springer US, Boston, MA, **1967**.
- [11] D. B. Williams, C. B. Carter, in *Transmission Electron Microscopy: A Textbook for Materials Science* (Eds.: D.B. Williams, C.B. Carter), Springer US, Boston, MA, **1996**, pp. 177–189.
- [12] L. Reimer, H. Kohl, *Transmission Electron Microscopy: Physics of Image Formation*, Springer, New York, NY, **2008**.

- [13] D. B. Williams, C. B. Carter, in *Transmission Electron Microscopy: A Textbook for Materials Science* (Eds.: D.B. Williams, C.B. Carter), Springer US, Boston, MA, **1996**, pp. 131–153.
- [14] L. R. Owen, E. J. Pickering, H. Y. Playford, H. J. Stone, M. G. Tucker, N. G. Jones, *Acta Materialia* **2017**, *122*, 11–18.
- [15] J. W. Edington, *Interpretation of Transmission Electron Micrographs*, Macmillan Education UK, London, **1975**.
- [16] A. Howie, M. J. Whelan, N. F. Mott, *Proc. R. Soc. Lond. A* **1962**, *267*, 206–230.
- [17] D. B. Williams, C. B. Carter, in *Transmission Electron Microscopy: A Textbook for Materials Science* (Eds.: D.B. Williams, C.B. Carter), Springer US, Boston, MA, **1996**, pp. 265–287.
- [18] C. Hammond, *The Basics of Crystallography and Diffraction*, Oxford University Press, Oxford, New York, **2016**.
- [19] F. E. Neumann, *Beiträge zur Krystallonomie*, ES Mittler, **1823**.
- [20] F. E. Neumann, *Das Krystall-System des Albites und der ihm verwandten Gattungen*, **1830**.
- [21] W. H. Miller, *A Treatise on Crystallography*, Deighton, London, England, **1839**.
- [22] G. Wulff, *Z. Kristallogr. – Cryst. Mater.* **1909**, *46*, 261–265.
- [23] F. Mompiou, *Pycotem n.d.*
- [24] F. Mompiou, R. Xie, *JMI* **2021**, *282*, 84–97.
- [25] D. Oliveros, M. Legros, *In Situ TEM Straining Test*, **2019**.
- [26] J. P. Hirth, J. Lothe, *Theory of Dislocations*, Wiley, New York, **1982**.
- [27] F. C. Frank, *Physica* **1949**, *15*, 131–133.
- [28] W. Cai, V. V. Bulatov, J. Chang, J. Li, S. Yip, in *Dislocations in Solids*, Elsevier, **2004**, pp. 1–80.
- [29] M. Chassagne, Interactions dislocations / macles par simulations à l'échelle atomique en microscopie électronique a transmission in-situ, Institut Polytechnique de Grenoble, **2010**.
- [30] J. F. M. Vergnol, J. R. Grilhe, *J. Phys. France* **1984**, *45*, 1479–1490.
- [31] W. Ye, A. Ougazzaden, M. Cherkaoui, *Int. J. Solids. Struct.* **2013**, *50*, 4341–4348.
- [32] F. Delmas, M. J. Casanove, P. Lours, A. Couret, A. Coujou, *Mater. Sci. Eng. A* **2004**, *373*, 80–89.
- [33] P. M. Kelly, *Phys. Stat. Sol. (a)* **1975**, *32*, 529–532.

Chapter 3

PLASTICITY MECHANISMS IN THE CoCrFeMnNi ALLOY

In situ TEM straining experiments were performed on CoCrFeMnNi specimens (as described in Chapter 2), and the activation of plasticity mechanisms and the behaviour of dislocations were observed in real time. This chapter presents the results and conclusions of these observations.

As already stated in section 4 of Chapter 1, dislocations in CoCrFeMnNi are understood to behave as follows (according to, among others, ^[1-3]):

- Slip is initiated by planar glide of $1/2 \langle 110 \rangle$ perfect dislocations on $\{111\}$ planes that can split into $1/6 \langle 112 \rangle$ Shockley partials.
- In order for twinning to occur, a critical stress " σ_{tw} " (or "twinning stress") must be reached, according to Laplanche et al. ^[3].
- Twinning is observed at low temperatures (77 K) above the critical stress, only after planar glide of perfect dislocations.
- Little to no twinning is observed at room temperature (refer to ^[3,4]). An exception is the study done by Kireeva et al. ^[5], where they did observe twinning at room temperature, at a much lower strain than the previously mentioned study by Laplanche et al.
- Cross slip is difficult in this alloy, according to Otto et al. ^[1].

Different techniques were used to reach the previous conclusions on the plasticity mechanisms for CoCrFeMnNi, together with, however, very few *in situ* TEM tensile experiments (i.e., ^[6,7]). The aim of this work was to carry out this type of straining experiment to understand how the plasticity mechanisms are triggered by means of direct observation of dislocations on non-pre-oriented grains of CoCrFeMnNi polycrystalline specimens at both room and liquid nitrogen temperatures, and comparing them to the existing assumptions from the literature, and to use the dislocations as probes to obtain the relevant physical data through data-mining and analysis (in the context of the MuDiLingo project ^[8]), on the attempt to close the bridge between experimental observations and modelling / simulation of dislocation behaviour in CoCrFeMnNi alloy.

This chapter will start by discussing the critical resolved shear stress in the alloy, followed by the comparison of the behaviour of dislocations and the mechanisms activated at both temperatures.

1. Critical resolved shear stress (CRSS) calculation

When performing an *in situ* TEM straining experiment, the exact applied stress is not known (as explained in Chapter 2). However, the CRSS can be locally measured using the curvature radius of a dislocation loop, using the following equation:

$$R = \frac{\mu b}{\tau}$$

Equation 3-1 – Curvature of a dislocation loop.

where R is the curvature radius, μ is the elastic modulus, b is the Burgers vector and τ is the CRSS. Please refer to Appendix 2 and 3 for the deduction of this equation and for the theoretical basis of the CRSS calculation.

To calculate the exact shape of the dislocation loop and thus the values of R and, by extension, of τ , Douin et al. ^[9] developed the software DISDI.

In its documentation, Douin ^[10] explains that DISDI is a software that calculates the self-energy, the line tension and the conditions of stability (Wulff plot) of a dislocation in an anisotropic crystal as a function of its orientation in a given plane, and the shape of the dislocation under a given shear stress (for perfect or two-fold dissociated dislocations). Knowing the fault energy, DISDI can also calculate the dissociation width; or, on the contrary, knowing the dissociation distance in a given orientation, it allows to calculate the fault energy of the crystal.

To calculate the value of τ , DISDI ask to input (as shown in Figure 3-1) the lattice parameter of the crystal (in nm), as well as the elastic constants C_{11} , C_{12} and C_{44} (in Pa); then the information of the dislocation to be used to locally measure the CRSS value (type of dislocation, Burgers vector, slip plane).

The first input in DISDI is the crystal parameters of CoCrFeMnNi. Owen et al. ^[11] give the value of the lattice parameter calculated using neutron diffraction patterns (because the alloy crystallises in fcc form, there are no other lattice parameters to be entered); and

Teramoto et al. [12] determined the monocrystalline elastic constants experimentally using ultrasound resonance spectroscopy, assuming a paramagnetic state (which, according to Schneeweiss et al. [13], is the magnetic state of CoCrFeMnNi between 93 K and 300 K). These values are listed in Table 3-1.

Table 3-1 – Lattice parameter and elastic constants for CoCrFeMnNi.

a (nm)	c₁₁ (Pa)	c₁₂ (Pa)¹	c₄₄ (Pa)
0.3597 [11]	2.026x10 ¹¹ [12]	1.166x10 ¹¹ [12]	1.382x10 ¹¹ [12]

For the dislocation input, the first step is to choose a slip system with a dislocation isolated or with a large separation from the other dislocations in the pile-up. Once this chosen system is indexed (the slip plane, the Burger's vector and the dislocation line direction are known), the values are entered on the "Dislocation" section.

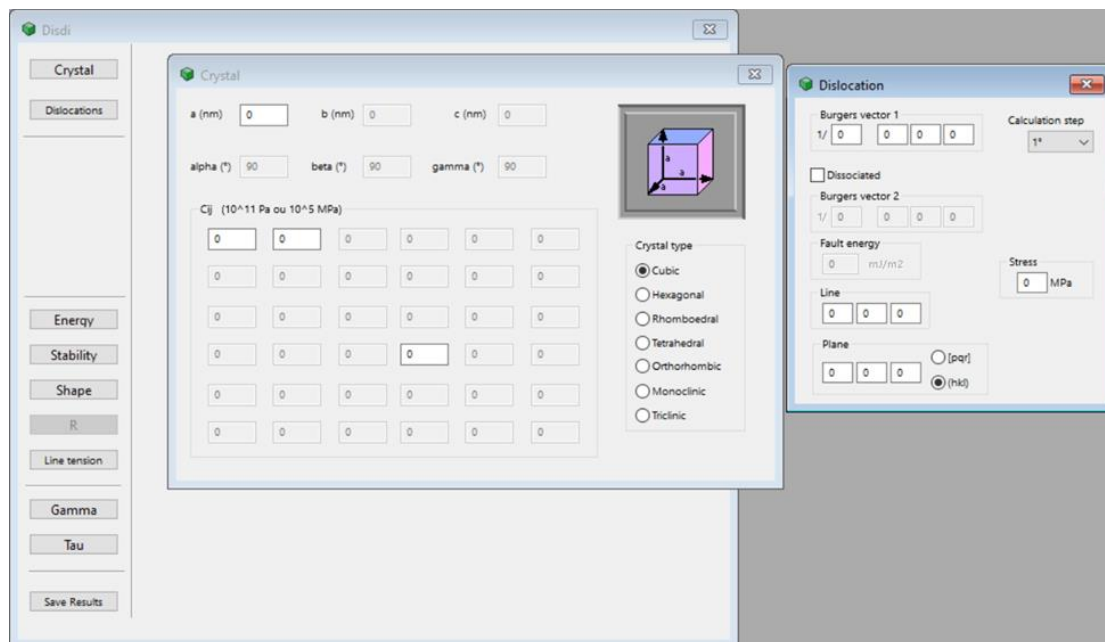


Figure 3-1 – DISDI's interface: the "crystal" section, where the crystal parameters are entered (lattice parameter and elastic constants), and the "dislocation" section, where the information of the slip system is entered.

To exemplify this, an isolated perfect dislocation in the middle of a pile-up was chosen, from specimen 35/I2-Head13 (see Figure 3-2 and Supplementary Video 1 in Appendix 1), strained at room temperature ($T = 293$ K).

¹ As the elastic constant of C_{12} is not directly related to the physical deformation, Teramoto et al. [12] experimentally defined and determined an alternative independent elastic constant, C' , defined as $(C_{11}-C_{12})/2$. The value of C_{12} is thus obtained from C' .

First, the dislocation was indexed using $\vec{g} \cdot \vec{b} = 0$ conditions, and it is determined to glide on the slip system $(\bar{1}\bar{1}1)[0\bar{1}1]$, with a Schmid factor $m = 0.46$.

DISDI can then provide the shape of the dislocation loop, its energy and line tension (in J/m) and its stability. The software is also able to calculate the values of τ (in MPa) for the chosen dislocation. To do this, the user is asked to input the values of τ_{\min} , τ_{\max} , a chosen step for the calculation, and the electron beam direction.

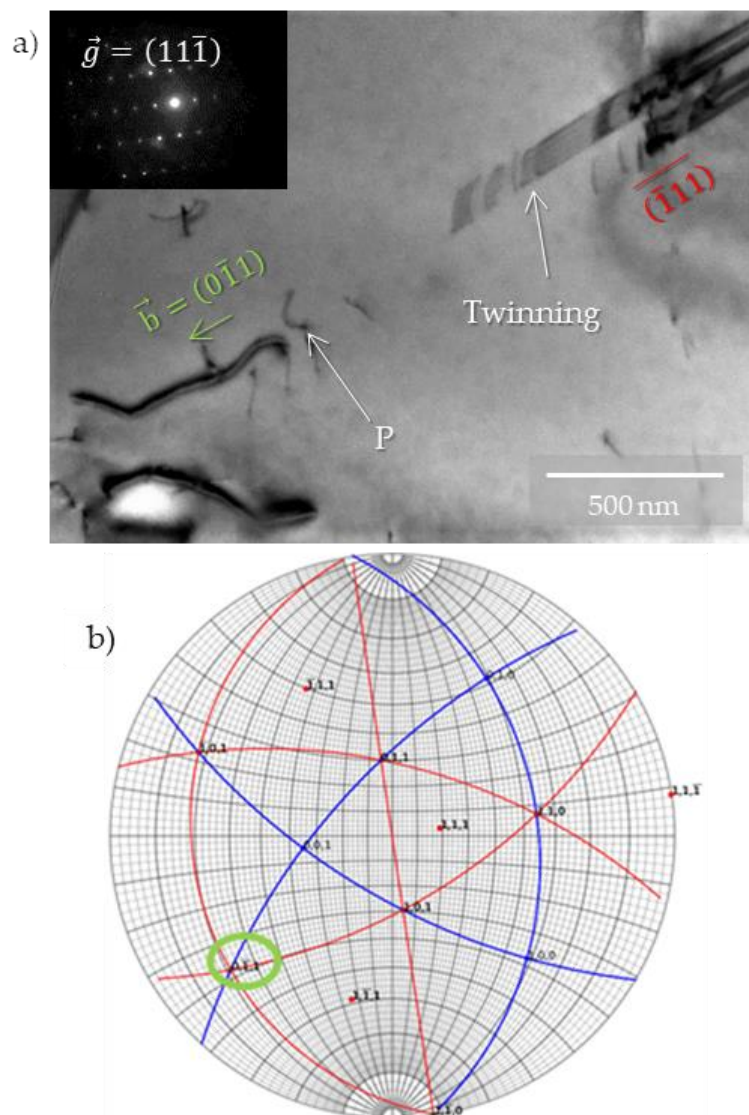


Figure 3-2 – 35/I2-Head13 specimen, strained at $T = 293$ K. The tensile axis is parallel to the vertical axis on the image. a) At the head of the pile-up there are perfect dislocations nearing and crossing over an obstacle. The “isolated” perfect dislocation is identified as “P”. Following P, there are dissociated dislocations forming twinning (“T”), as evidenced by the stacking faults. In red, the slip plane; in green, the Burgers vector direction. The insert shows the diffraction pattern for the image ($\vec{g} = (11\bar{1})$). b) The stereographic projection showing the orientation of the grain. In green, the Burgers vector for P.

To obtain the beam direction (z axis on the specimen plane), a simple manipulation on the Stereoproj software (from Pycotem [14]) is needed, after entering the Euler angles for the grain of the chosen dislocation (see Figure 3-3). Knowing this information and the magnification of the image (thus, the apparent width of the slip plane), DISDI provides the resulting calculations of the locally measured CRSS for the inputted parameters, to then be fitted (by the user) by superposing the calculated loop onto the dislocation on the image (see Figure 3-4).

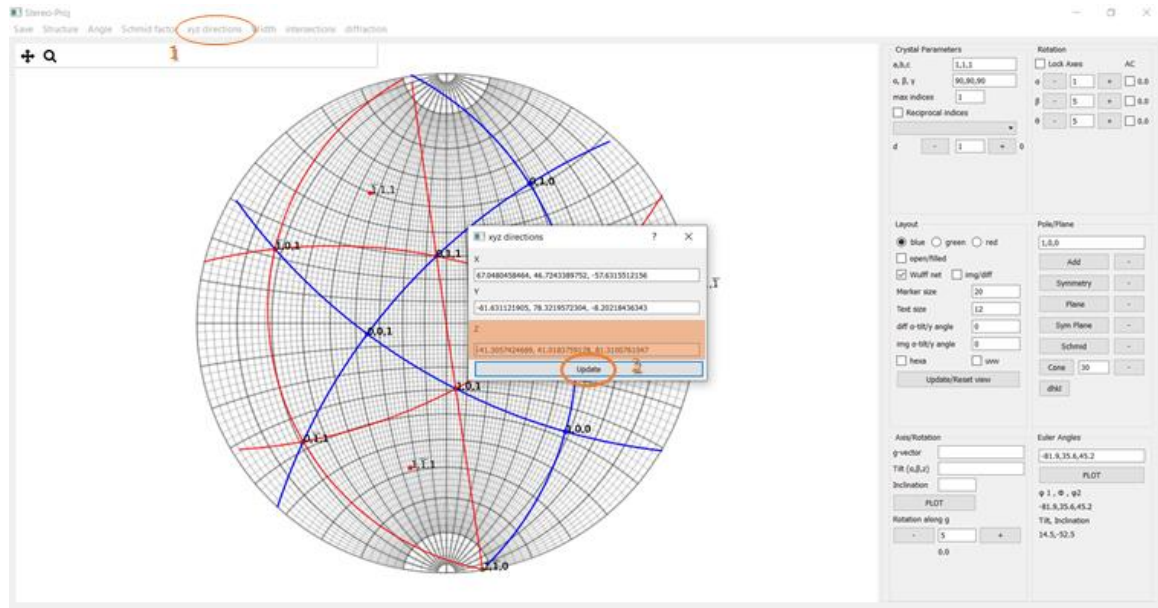


Figure 3-3 – Stereoproj screen capture showing the stereographic projection of Head13 and the steps to obtain the beam direction: 1- Click on “xyz directions”. 2- Click on “Update”. The “z” direction is the electron beam’s plane direction.

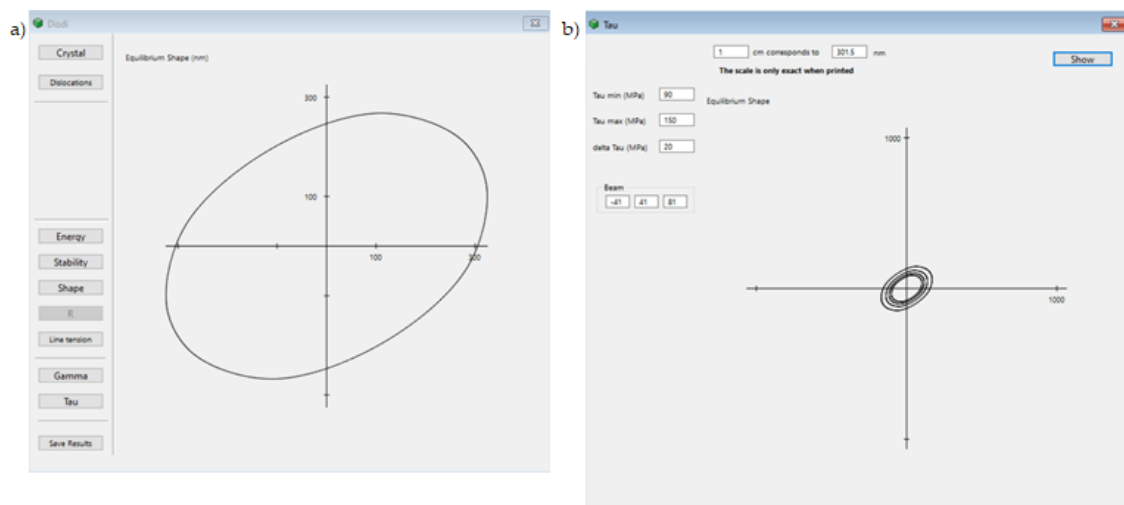


Figure 3-4 – DISDI screen capture of: a) shape of the dislocation loop in equilibrium, b) proposed CRSS values for the dislocation “P” ($\tau_{min} = 90, \tau_{max} = 150, \Delta\tau = 20$). The scales on the axis are in nm.

In the case of specimen 35/I2-Head13, 1 cm corresponds to 301 nm for a figure of 8 cm of width. This is the value entered on DISDI to obtain the CRSS “ellipses”. Once the correct “ellipse” is chosen (the one that fits the dislocation shape in the figure better – see Figure 3-5), the locally measured CRSS for the dislocation is known, in this case: $\tau = 210$ MPa.

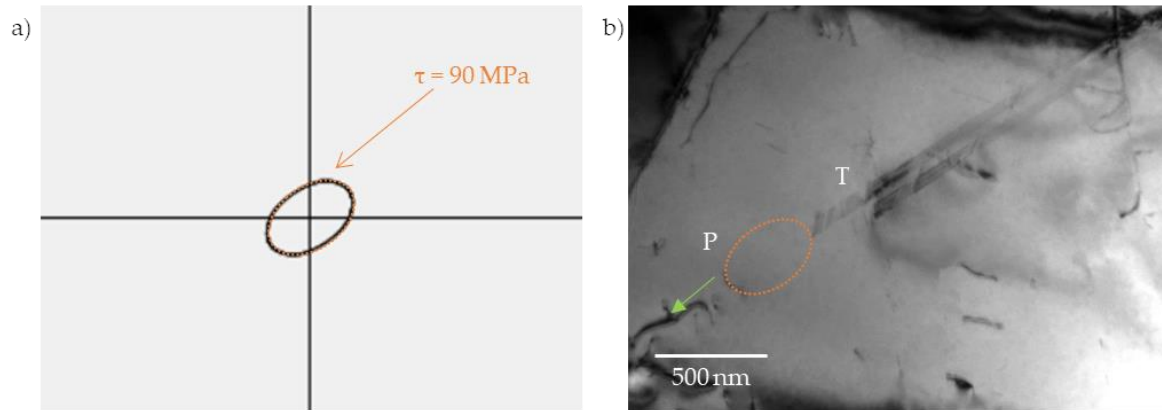


Figure 3-5 – a) Excerpt from DISDI’s calculation for $\tau = 90$ MPa. a) Same Head13 figure as before, with the proposed loop fitted onto it (in orange). Note that the direction of the loop follows the direction of the Burgers vector (in green).

From the Schmid Law, the locally measured strength σ_{exp} can be calculated:

$$\tau = \sigma_{\text{exp}} m$$

Equation 3-2 – Schmid law.

where m is the Schmid factor for the active slip system. For 35/I2-Head13, the values are:

Table 3-2 – Head13 locally measured stresses.

Schmid factor m	τ (MPa)	σ_{exp} (MPa)
0.46	90 ± 3	194 ± 7

The errors of these results come from the measurement of the dislocation loop radius, which, in turn, will affect the selection of the fitted loop in DISDI. The measurement error is in the order of ± 0.1 cm (when measuring on a printed TEM image of 6 x 8 cm), which is then converted to nm depending on the magnification at which the image was taken. There is also the appreciation error when selecting the better fitted ellipse; this error is in the order of ± 2 MPa (the minimum value to appreciate the ellipses’ differences – meaning a slightly bigger and a slightly smaller ellipse). The dispersion of these error gives the error value presented in the tables for τ and σ values.

Following this calculation process, the CRSS values for an array of 24 isolated but active dislocations from different specimens were measured, both at room and at liquid nitrogen temperatures. These results are presented in Table 3-3 and Table 3-4, respectively.

Table 3-3 – Locally measured τ and σ for an array of dislocations on specimens strained at $T = 293\text{K}$.

	Specimen	Slip system	Schmid factor m	τ (MPa)	σ_{exp} (MPa)
1	35/I2-Head13	$(\bar{1}11)[0\bar{1}1]$	0.46	90 ± 3	194 ± 7
2	35/I2-Head14	$(1\bar{1}1)[\bar{1}01]$	0.27	140 ± 3	518 ± 11
3	35/I2-Head14	$(1\bar{1}1)[011]$	0.46	70 ± 3	153 ± 6
4	35/I2-Head14	$(\bar{1}11)[101]$	0.45	170 ± 3	379 ± 7
5	35/I2-Head15	$(1\bar{1}\bar{1})[101]$	0.33	40 ± 2	121 ± 7
6	35/I2-Head24	$(\bar{1}\bar{1}1)[\bar{1}0\bar{1}]$	0.44	60 ± 2	137 ± 6
7	35/I2-Head24	$(111)[0\bar{1}1]$	0.22	30 ± 3	137 ± 12
8	35/I2-Head30	$(\bar{1}\bar{1}1)[1\bar{1}0]$	0.34	80 ± 2	236 ± 7
9	35/I2-Head30	$(111)[1\bar{1}0]$	0.14	50 ± 2	353 ± 18
10	35/I2-Head43B	$(\bar{1}11)[101]$	0.27	40 ± 2	151 ± 9
11	X1-21	$(\bar{1}11)[0\bar{1}1]$	0.38	26 ± 2	69 ± 6
Averages				72 ± 2	222 ± 9

Table 3-4– Locally measured τ and σ for an array of dislocations on specimens strained at cryogenic temperatures.

	Specimen	Slip system	Schmid factor m	T (K)	τ (MPa)	σ_{exp} (MPa)
1	35/I2-Head22	$(\bar{1}\bar{1}1)[011]$	0.40	96	90 ± 3	226 ± 7
2	35/I2-Head22	$(\bar{1}11)[0\bar{1}1]$	0.32	96	150 ± 2	467 ± 7
3	35/I2-Head28	$(\bar{1}\bar{1}1)[1\bar{1}0]$	0.11	103	70 ± 3	660 ± 32
4	35/I2-Head28	$(\bar{1}11)[0\bar{1}1]$	0.46	103	120 ± 3	261 ± 6
5	35/I2-Head28	$(\bar{1}\bar{1}1)[\bar{1}10]$	0.36	103	62 ± 2	173 ± 7
6	35/I2-Head28	$(\bar{1}11)[\bar{1}10]$	0.46	103	135 ± 3	293 ± 6
7	35/I2-Head29	$(\bar{1}\bar{1}1)[1\bar{1}0]$	0.41	104	160 ± 3	388 ± 7
8	35/I2-Head29	$(1\bar{1}1)[\bar{1}01]$	0.46	104	55 ± 3	120 ± 6
9	35/I2-Head29	$(111)[0\bar{1}1]$	0.06	104	28 ± 2	452 ± 39
10	X1-21	$(\bar{1}11)[\bar{1}10]$	0.48	102	39 ± 2	82 ± 5
11	X1-21	$(\bar{1}11)[0\bar{1}1]$	0.38	102	30 ± 2	79 ± 6
Averages					85 ± 3	291 ± 12

The averages calculated in the tables show that the (locally measured) strength at RT is (222 ± 9) MPa and at LN₂T is (291 ± 12) MPa. These results are in accord with the tendency that Cantor alloy is stronger when lowering the temperature. Because of the large array of slip systems measured, the dispersion of values is also large. According to the radius and

shape of each dislocation measured, τ values change, leading to conclude that the direction of the slip system (its orientation) plays an important role on the strength of the specimen.

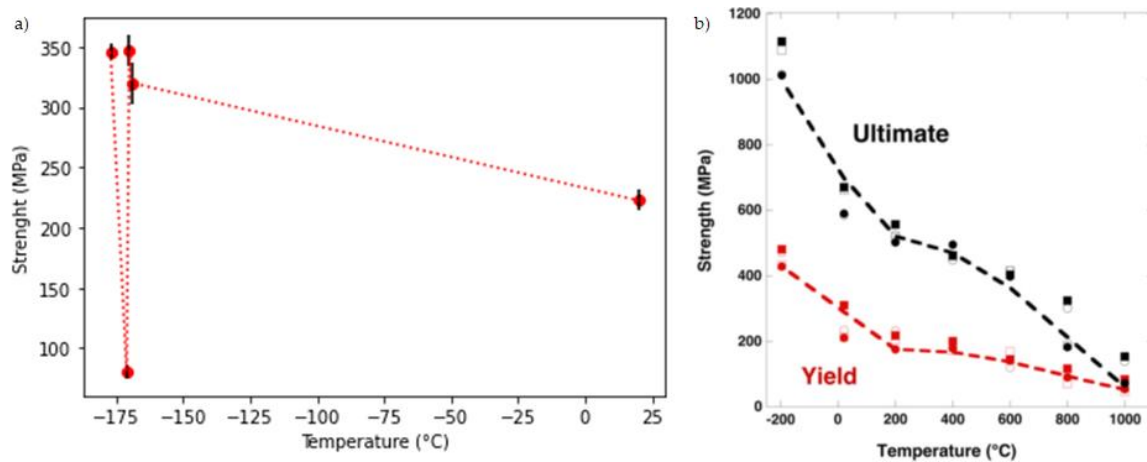


Figure 3-6 – Tensile strength vs. temperature for CoCrFeMnNi alloys. a) Experimentally calculated in this study, for rectangular specimens of 3 x 1 mm. In red, the position of the averages for each tested temperature; in black, their respective error bars. b) Results from Gali and George ^[15], for dog-bone shaped specimens of gage sections of 10 x 2.5 x 0.63 mm strained in a tensile essay machine.

From the plot on part (a) of the figure, it is clear that there is a tendency for the decrease of strength with increasing temperature. The only exception is given by the specimen tested at 102 K (-171 °C). This can be due to the measurement being taken at low deformation or to the fact that it is not the same specimen type (X1 vs. 35/I2-Head).

Comparing these results to the ones described in the literature (for example, the *ex situ* tensile tests performed by Gali and George ^[15]), the conclusion can be made that *in situ* tensile essays on CoCrFeMnNi are analogous to macroscopic tensile essays (see Figure 3-6), therefore

$$\sigma_{\text{exp}} \approx \sigma_y$$

(σ_{UTS} was not measured experimentally as specimens were never strained to rupture during the *in situ* tensile experiments). It is important to mention that Figure 3-6(a) was constructed using the average σ_{exp} for each temperature range measured (96, 102, 103, 104 and 293 K) and that T was converted from K to °C to facilitate the comparison to part (b) of the figure.

2. Dislocation behaviour: comparing the same specimen at two temperatures

Sections 3 and 4 will explain in detail the differences in mechanisms and dislocation behaviour for CoCrFeMnNi specimens strained at room and at cryogenic temperatures. These differences, however, depend also on other factors, such as crystal orientation, thickness of the specimen ^[16], etc., making a direct comparison difficult.

To overcome this difficulty, a specimen was selected to be strained at cryogenic and then at room temperature, consecutively. The order of the temperature is not random: an *in situ* TEM tensile experiment using the configuration already explained in Chapter 2, at room temperature, needs an elongation between 550-650 μm to trigger plastic deformation, whereas at cryogenic temperature it is triggered between 10-50 μm , due to the thermal compression of the straining holder (and, thus, of the specimen + grid configuration). Knowing this, the choice was made to strain the specimen first at cryogenic temperature, stopping the experiment several minutes after plastic deformation is reached (after activation of plasticity mechanisms), waiting for the specimen to reach room temperature and then strain it again.

The goal of this experiment was to identify if dislocation behaviour is the same at both temperature regimes, and if the same mechanisms are activated. For this purpose, the specimen X1-21 was selected (see Figure 3-7).

It is worth noting that when talking about “elongation”, this work is making reference to the difference of the displacement value given by the specimen holder controller at the observation of the mechanism’s activation vs. the value given at the onset of plasticity.

2.1. Mechanism activation

Straining started at 102 K. At the 14 minutes’ mark, the plastic regime was reached by the activation of planar slip of a pair of perfect dislocations in grain 1, gliding in the system (111)[0 $\bar{1}$ 1], with a Schmid factor $m = 0.40$ (Figure 3-8(a-b)). This system was not further developed once the dislocations reached the specimen surface.

Around 7 minutes and 2 μm of elongation later (21 minutes’ mark), another system is activated in grain 2, also a pair of perfect dislocations followed by 6 other perfect dislocations. Next to this pile-up, a parallel one is also activated, however with a different contrast. $\vec{g} \cdot \vec{b} = 0$ conditions confirm they are not the same system (Figure 3-8(c-d)). System 1 is ($\bar{1}$ 11)[0 $\bar{1}$ 1], $m = 0.38$; system 2 is ($\bar{1}$ 11)[$\bar{1}$ 10], $m = 0.48$. Both systems seem to

be activated at the same time. Both these systems continue to move to the top right until they encounter the grain boundary ①-② that acts as a barrier.

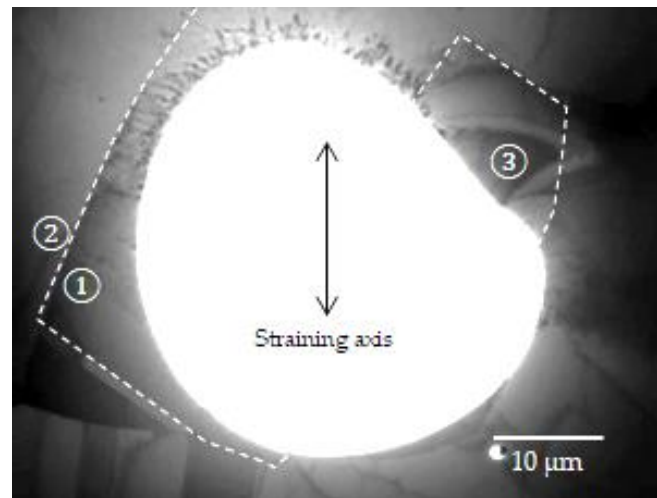


Figure 3-7 – Low magnification image of specimen X1-21. The electropolished hole is in the center of the image. Around it, the areas where deformation occurred: grains 1, 2 and 3 (delimited by white dashed lines). The straining axis is indicated by the black arrow (this direction will be the same for all subsequent images in this section).

At the 43 minutes' mark and 7 μm of elongation, dislocations activated in grain 3 (Figure 3-8(e-f)). They did so by planar glide of perfect dislocations, moving on the system $(\bar{1}\bar{1}1)[10\bar{1}]$, $m = 0.22$. These dislocations moved slower than the previous systems in grains 1 and 2, and did not move at all when changing temperatures.

The tensile test was stopped after an elongation of 9 μm , so as to not deform irreversibly the specimen in order to strain it again at room temperature. The test was restarted at $T = 293\text{ K}$ once the specimen reached this temperature.

The first system to continue gliding was $(\bar{1}\bar{1}1)[0\bar{1}1]$ in grain 2 (called previously system 1), with a pair of perfect dislocations always heading the pile-ups. At the same time mark, it is worth noting the activation of a third system in this grain (Figure 3-9(a-b)): $(\bar{1}\bar{1}1)[1\bar{1}0]$, $m = 0.29$. These will become the most active slip systems in the specimen at RT. Grain 3 showed no further movement during the room temperature straining.

After an elongation of 11 μm , systems 2 and 3 of grain 2 continue to move, forming pile-ups against the same grain boundary (Figure 3-9(c-d)). Neither of these systems managed to transmit dislocations across this grain boundary during the straining experiment.

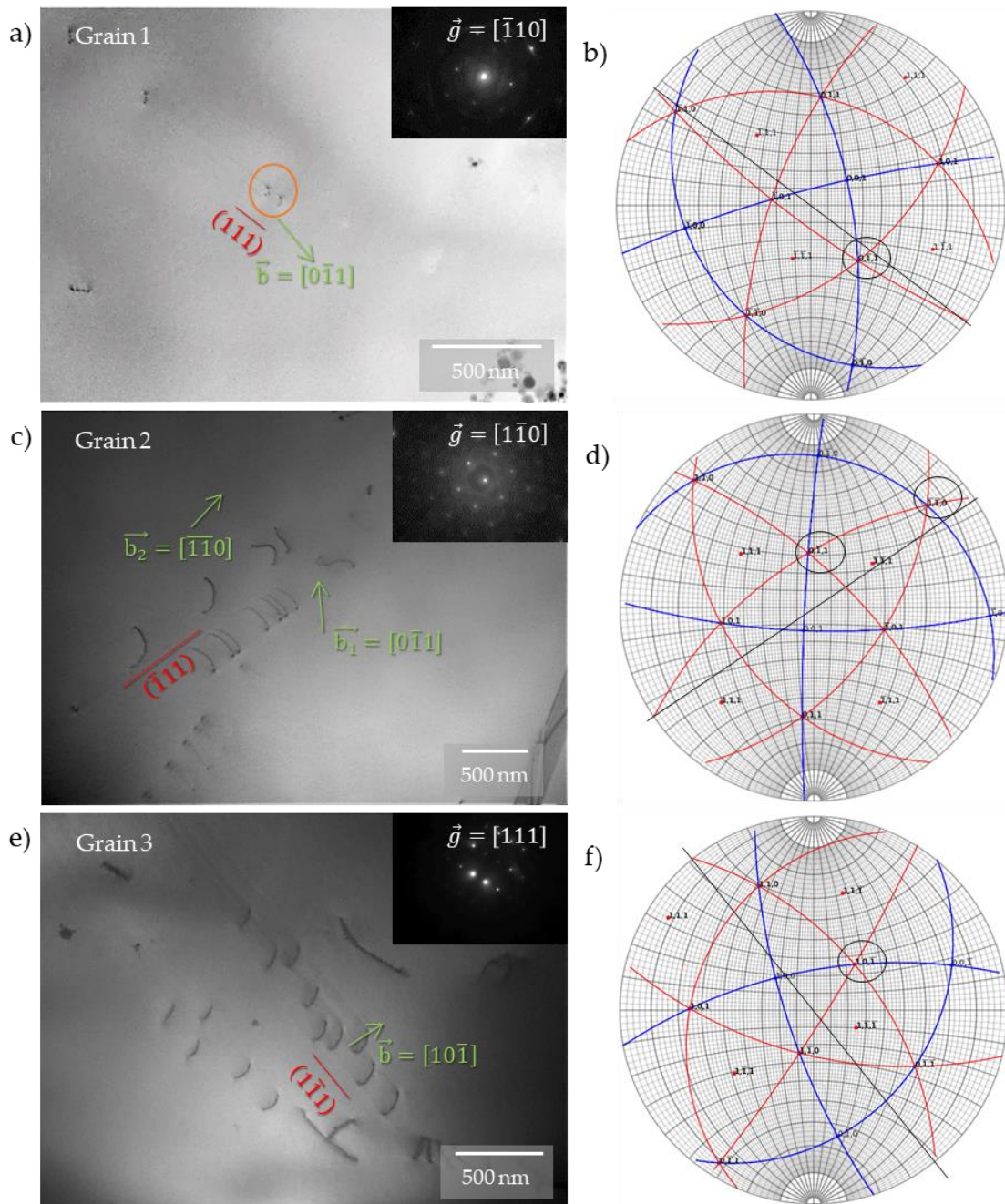


Figure 3-8 – Specimen X1-21 strained at $T = 102$ K. The tensile axis is parallel to the vertical axis on the image. a) Plastic regime is reached in grain 1 with the movement of a pair of perfect dislocations (orange circle); insert: corresponding diffraction pattern. b) Stereographic projection for grain 1. c) Two active systems of perfect dislocations in grain 2, same plane but different Burgers vectors; insert: corresponding diffraction pattern. d) Stereographic projection for grain 2. e) Perfect dislocations gliding in grain 3; insert: corresponding diffraction pattern. f) Stereographic projection for grain 3. Note: each micrograph signals the gliding plane in red and the Burgers vector directions in green; they are also indicated in each corresponding stereographic projection.

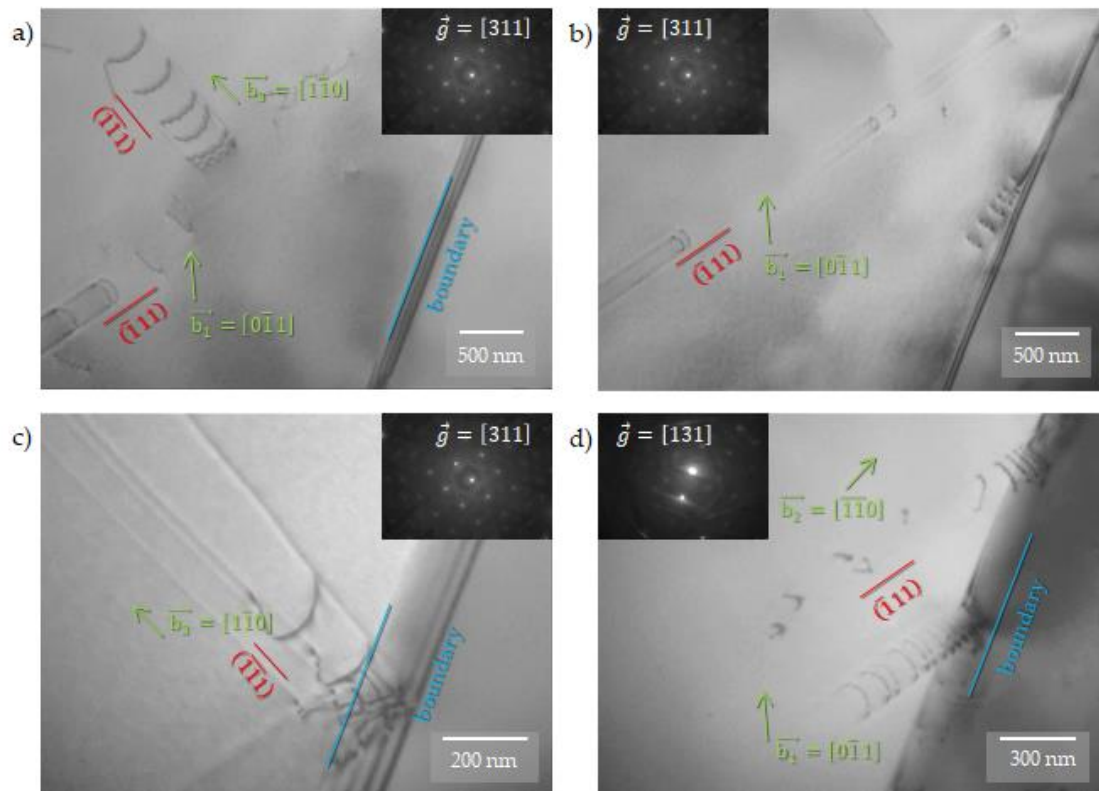


Figure 3-9 - Specimen X1-21 strained at $T = 293$ K. The tensile axis is parallel to the vertical axis on the image. All the micrographs correspond to grain 2: a) Activation of existing slip systems as well as a third one; insert: corresponding diffraction pattern. b) Slip system 1, showing perfect dislocations moving in pairs when leading the pile-up; insert: corresponding diffraction pattern. c) Slip system 3 piled-up against the grain boundary in blue; insert: corresponding diffraction pattern. d) Slip systems 1 and 2 piled-up against the grain boundary; insert: corresponding diffraction pattern. Note: each micrograph signals the gliding plane in red and the Burgers vector directions in green, as well as the grain boundary in blue.

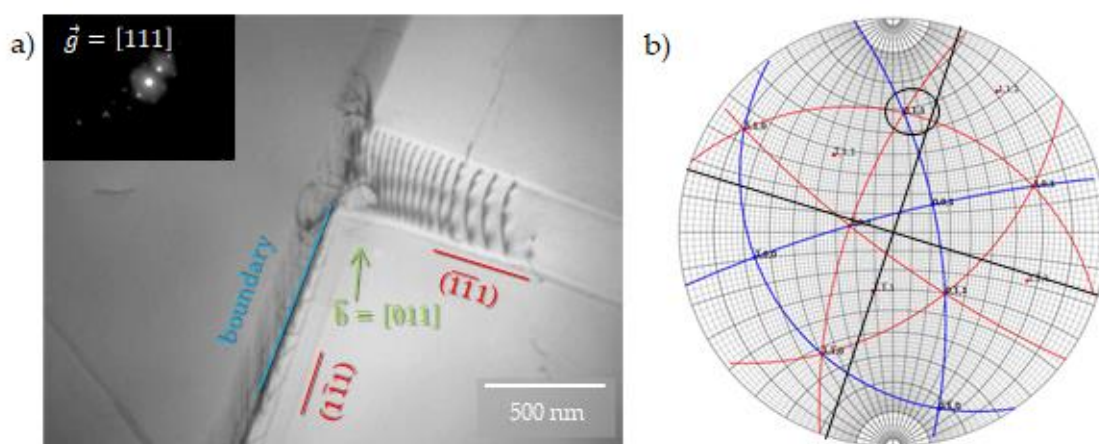


Figure 3-10 – Same specimen strained at $T = 293$ K. The tensile axis is parallel to the vertical axis on the image. a) Grain 1; slip system $(\bar{1}\bar{1}1)$ activated and piling-up against the grain boundary (in blue), getting blocked and then cross-slipping to slip system $(1\bar{1}1)$; insert: corresponding diffraction pattern. b) Stereographic projection of grain 1, clearly showing both slip systems and their shared Burgers vector.

At the 59 minutes' mark and 29 μm of elongation, the activation of supplementary slip systems is noted in grain 1. They are $(\bar{1}\bar{1}1)[011]$, with a Schmid factor $m = 0.43$, and $(1\bar{1}1)[011]$, $m = 0.26$. The first of them will develop, by the end of the experiment, a crack in prolongation of its direction; they both share the same Burgers vector, and as dislocations from the first system get blocked against the grain boundary, they eventually cross-slip to the second (as evidenced in Figure 3-10).

By the end of the *in situ* tensile experiment, several cracks had developed: a large one in grain 1, and two on the right side of the hole, both above and below grain 3 (Figure 3-11). Slip traces evidence that grains 1 and 2 were the zones with the maximum stress concentration.

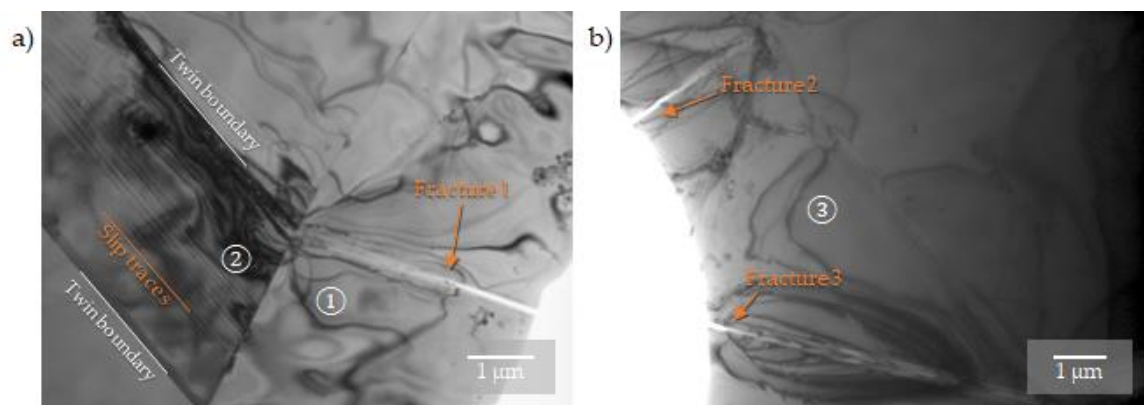


Figure 3-11 – Same specimen after the *in situ* TEM tensile experiment. The tensile axis is parallel to the vertical axis on the image. a) Left side of the hole, showing grains 1 and 2, the fissure in grain 1 and the slip traces evidencing deformation in grain 2. b) Right side of the hole, showing the fissures on the top and the bottom of grain 3.

In general, dislocation behaviour and plasticity mechanisms did not differ with the variation of temperature (meaning that the activation of mechanisms, such as twinning, does not depend on temperature but on an alternative parameter). There were, however, certain differences that will be developed next.

2.2. Critical Resolved Shear Stress

Among all the slip systems activated on the specimen X1-21, only one remained active at both test temperatures: $(\bar{1}\bar{1}1)[0\bar{1}1]$ in grain 2 (Figure 3-8(c) and Figure 3-9(a-b)). The results were given on Table 3-3 and Table 3-4, and they are summarised on Table 3-5.

These measurements (although locally obtained for a single slip system in a single grain) are in line with the trend of values from the literature (see for example Gludovatz et al.

^[17]), and in complete accordance with the values compiled by George et al. ^[18]. They show, as expected, an increase of resistance when the temperature decreases ^[15].

Table 3-5 – CRSS calculation for specimen X1-21.

Slip system	Schmid factor m	Temperature (K)	τ (MPa)	σ (MPa)
$(\bar{1}11)[0\bar{1}1]$	0.38	102	30 ± 2	79 ± 6
		293	26 ± 2	69 ± 6

2.3. Dislocation movement

Dislocation motion in CoCrFeMnNi alloy has been described as “jerky”, which is confirmed by the observations during *in situ* TEM straining. Under the influence of a certain τ , dislocations move forward, not smoothly, but in what appears to be “jumps”.

These jerky movements appear to be constant in time and jump size, leading to correlate them to the local atomic landscape (chemical fluctuations) of the slip system. They are, however, longer or shorter depending on the straining temperature. A more thorough analysis on the jerky motions of dislocations at both temperature ranges will be presented in the next chapter.

3. Dislocation behaviour at room temperature

3.1. Planar glide of perfect dislocations

Dislocations glide in $\{111\}$ type planes, and their slip system is easily indexed following the procedure indicated in Chapter 2, section 3.1.

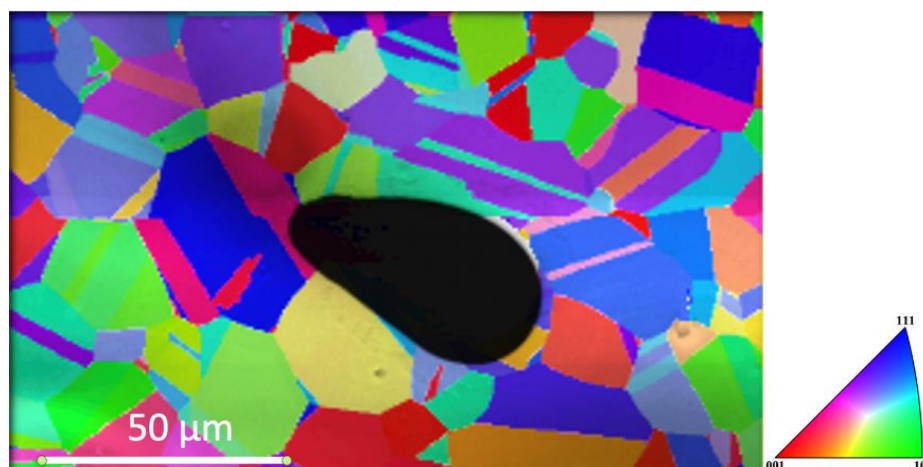


Figure 3-12 – EBSD cartography of a specimen, showing the different grains (of different orientations) in colours, around the hole (black). Tensile direction is vertical. Right: inverse pole figure plotted along z (direction perpendicular to the foil).

A typical TEM specimen can have around 2 – 3 different grains (see Figure 3-12) in the immediate area around its hole, in the thinner parts that are electron-transparent. Once straining starts, the primary slip plane is activated after a certain deformation (the experimental configuration does not allow the measure of the applied strain).

Figure 3-13 (and Supplementary Video 2) shows specimen 35/I2-Head14 at the start of straining and the activation of the primary slip system of a grain by the moving of a perfect dislocation (a-b). The slip system is $(1\bar{1}1)[\bar{1}01]$. The determination of the Burgers vector was possible because of $\vec{g} \cdot \vec{b} = 0$ conditions found during the experiment. The Schmid factor for this active slip system is $m = 0.27$, which is not the highest on this grain.

Shortly after the movement of the first dislocation, the slip system continues to be active and perfect dislocations start to move in pairs. Part (c) of the figure evidences this, as well as a secondary slip system that was activated (after a further elongation of 20 μm). This secondary slip system is $(\bar{1}11)[0\bar{1}1]$, with a Schmid factor $m = 0.36$. Thus, a more favourable energetic path was found for deformation in this grain.

Before continuing with the analysis of the 35/I2-Head14 experiment, it is worth noting that the phenomenon seen in part (c) of the figure, where perfect dislocations start moving in pairs before forming a pile-up, is a recurring one (also seen in Figure 3-8(a) and in Figure 2-22 of Chapter 2). This will be addressed more thoroughly in the next chapter.

The pair of dislocations presented in Figure 3-13(d), gliding on the primary slip system, shows clear dissociation and, after a further time lapse, also do the ones from the secondary slip system. Dissociation of perfect dislocations is a common occurrence during the *in situ* TEM tensile experiments in CoCrFeMnNi alloy.

3.1.1. Dissociation of perfect dislocations and SFE determination

To accurately measure the dissociation distance and the stacking fault energy, three dislocations under low stress were chosen, belonging to specimen 35/I2-Head10, strained at RT. Two of these dislocations glided on parallel planes of slip system $(111)[10\bar{1}]$ in grain 1 ($\vec{b}_L = [11\bar{2}]$ and $\vec{b}_T = [2\bar{1}1]$), and the third one glided on slip system $(\bar{1}\bar{1}\bar{1})[\bar{1}01]$ in grain 2 ($\vec{b}_L = [1\bar{1}\bar{2}]$ and $\vec{b}_T = [\bar{2}\bar{1}1]$). The dissociation distance was measured in different segments of each dislocation, corresponding to different ψ angles (the dislocation character, measured as the angle between the Burgers vector and the dislocation line), as shown in Figure 3-14.

Figure 3-13 – Specimen 35/12-Head14, strained at $T = 293$ K. The tensile axis is parallel to the vertical axis on the image and on the stereographic projection. a) An area of the specimen where deformation is expected to occur. b) The first dislocation moving, a perfect dislocation (circled in black) gliding on plane (111) (in red); insert: corresponding diffraction pattern. c) A pair of dislocations gliding on system (111)[101] (black), and the secondary slip system (111)[011] (grey) (slip planes are showed in red, Burgers vector directions in green). d) Stereographic projection of the grain showing the Burgers vector for the primary slip system (black), and for the secondary slip system (grey).

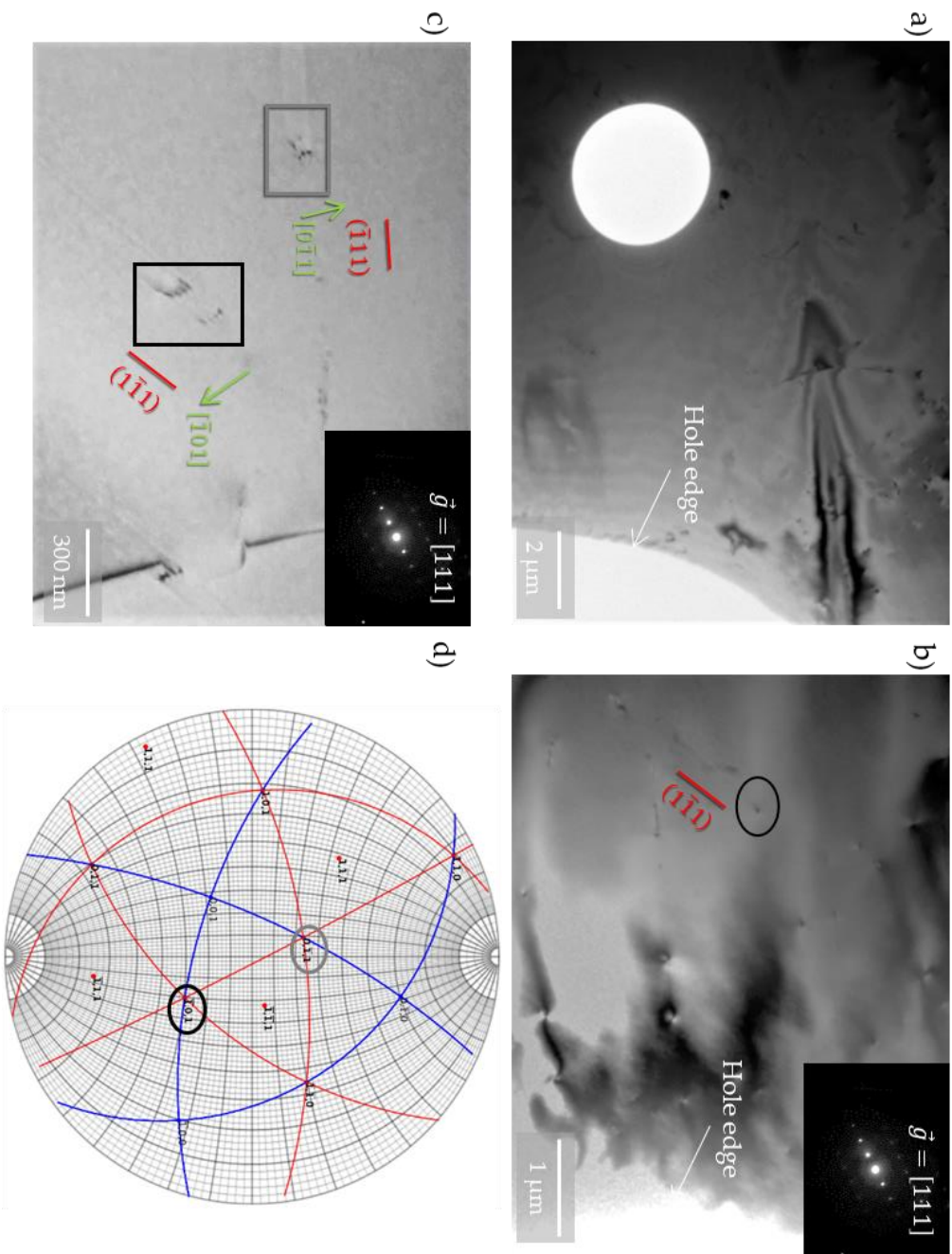


Figure 1-28 in Chapter 1 illustrates the dissociation of a perfect dislocation into two Shockley partials and an enclosed stacking fault. Applying the Frank criterion to this circuit, the elastic strain energy in a crystal is reduced by the dissociation of a perfect dislocation into partials. The interaction between the partials is such that they repel one another by a force that varies as $1/r$ ^[19], where r is the separation between partials.

The formation of the fault between the partials produces an increase in energy γr per unit length. At the equilibrium separation r_e , the force γ is equal and opposite to the elastic force, and so the equilibrium condition is

$$r_e = \frac{\mu b_p^2 (2 - \nu)}{8\pi\gamma (1 - \nu)} \left(1 - \frac{2\nu \cos(2\psi)}{2 - \nu} \right)$$

Equation 3-3 – Equilibrium separation distance of two Shockley partials.

where b_p is the magnitude of the Burgers vector of the partial dislocations, μ is the shear modulus, ν is the Poisson's ratio, ψ is the angle between the Burgers vector and the dislocation line (the character of the dislocation), and γ is the stacking fault energy ^[20].

From this equation, the isotropic value for the SFE can be determined as

$$\gamma = \frac{\mu b_p^2 (2 - \nu)}{8\pi r_e (1 - \nu)} \left(1 - \frac{2\nu \cos(2\theta)}{2 - \nu} \right)$$

Equation 3-4 – Isotropic stacking fault energy depending on the dislocation dissociation distance.

The dissociation distances are estimated taking into account that the measured values are projections: the distance r_p is a projection of the real distance r (see section 3.3 of Chapter 2 for the schematics of this calculation), and the dislocation line l_p is also a projection of l (see part (d)) of Figure 3-14 for the schematics of this manipulation). Knowing the dissociation distances, the isotropic SFE values for the dislocations presented in the image above can be locally calculated (using μ and ν from ^[21], and b using the lattice parameter from ^[11]). Using DISDI, these values can also be determined considering the elastic tensor (and the same input values used in Chapter 2). These values are expressed in Table 3-6.

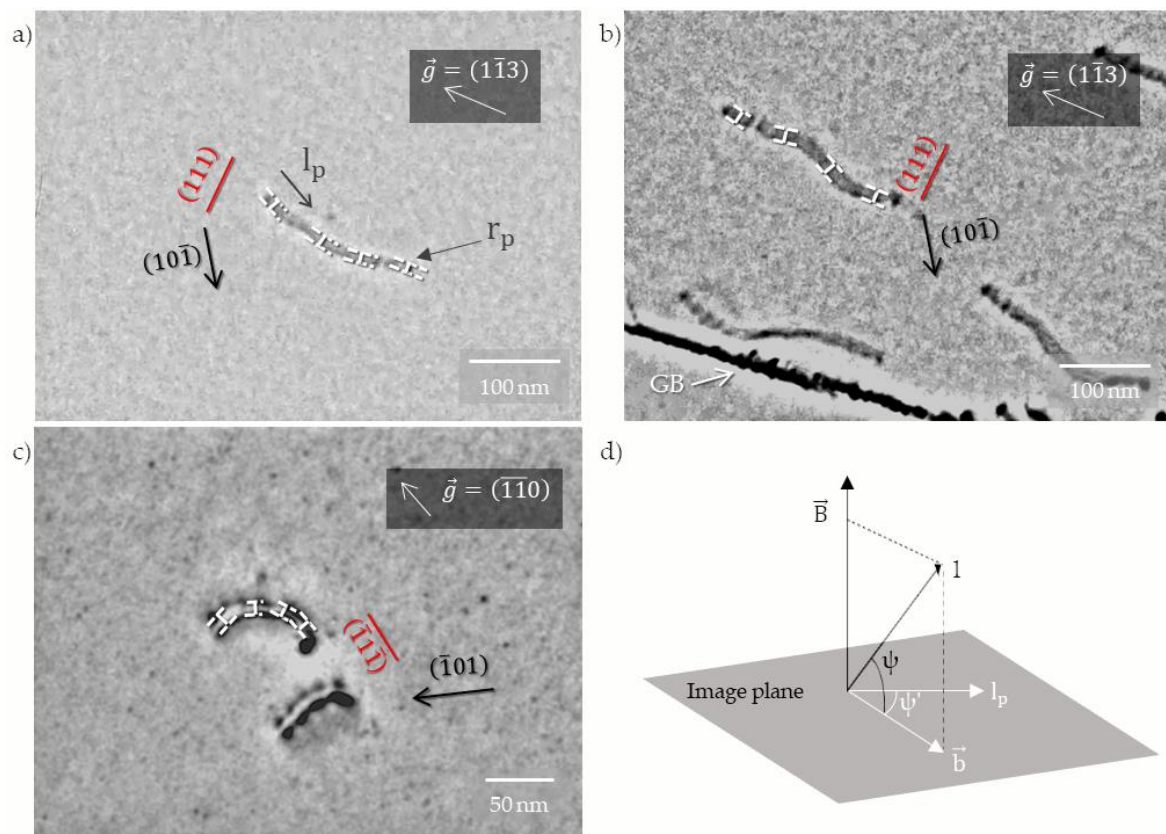


Figure 3-14 – Specimen 35/I2-Head10, strained at $T = 293$ K. In red, the slip plane; in black, the Burgers vector. \vec{g} are indicated by dark grey highlights. The segments where the dissociation distances were measured are shown using white lines. a) Dislocation 1, showing the projected dissociation distance measured (r_p) and the projected dislocation line (l_p). b) Dislocation 2, same grain and slip system. White arrow indicates the GB. c) Dislocation 3, different grain and slip system. d) Schematics showing the relationship between l_p and l (dislocation line), with respect to the Burgers vector and the beam direction (\vec{B}), to calculate ψ .

Figure 3-15 presents the plotted values of the dissociation distance with respect to the dislocation character, comparing them to the calculated value of SFE by Okamoto et al. ^[2] (30 mJ/m^2) and to the average of the experimentally calculated SFE ($\sim 11 \text{ mJ/m}^2$). This difference of almost half the value is a result of the difference between the partial separation (5.7 nm for Okamoto et al. vs. 19 nm for this work). The measurements in bright field TEM are also less precise than in dark field, that were not carried out here. Overall, the γ values obtained in this study using Equation 3-4 and using DISDI are consistent between them. The values obtained are more in accordance with Zaddach et al. ^[22] ($18.3 - 27.3 \text{ mJ/m}^2$ obtained by X-ray diffraction).

Table 3-6 - Dissociation values and locally measured γ_{SFE} at T = 293 K.

	r (nm)	ψ (°)	Δr (nm)	$\gamma_{SFE}^{iso-exp}$ (mJ/m ²)	γ_{SFE}^{DISDI} (mJ/m ²)	$\Delta\gamma_{SFE}^{iso-exp}$	$\Delta\gamma_{SFE}^{DISDI}$
Dislocation 1	16 ± 1	63 ± 1	15	12 ± 1	11	14	15
	16 ± 1	77 ± 1		13 ± 1	13		
	15 ± 1	78 ± 1		14 ± 1	18		
	13 ± 1	89 ± 1		16 ± 1	19		
Dislocation 2	19 ± 1	63 ± 1	19	10 ± 1	9	11	12
	18 ± 1	77 ± 1		11 ± 1	12		
	20 ± 1	78 ± 1		10 ± 1	13		
	19 ± 1	89 ± 1		11 ± 1	14		
Dislocation 3	24 ± 1	0 ± 1	22	5 ± 1	8	8	10
	22 ± 1	45 ± 1		7 ± 1	6		
	19 ± 1	78 ± 1		11 ± 1	10		
	21 ± 1	81 ± 1		10 ± 1	14		
			19			11	12

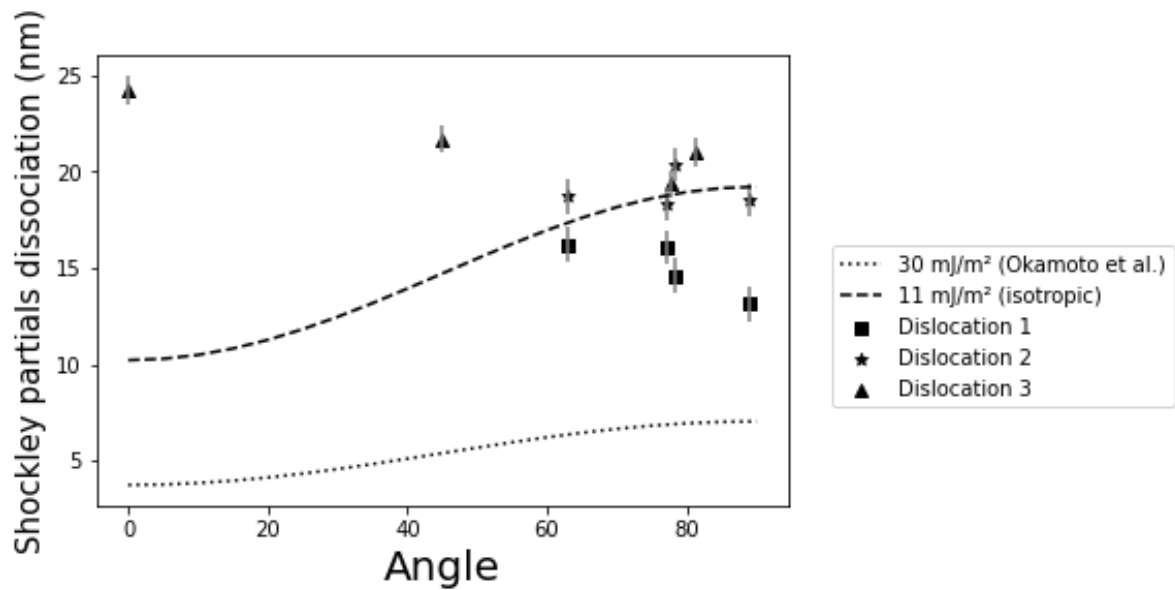


Figure 3-15 – Measured dissociation distance between Shockley partials vs. dislocation character, including SFE values (experimentally calculated and Okamoto et al. [2]). Error bars are shown in grey.

The resulting values of γ vary along the dislocation line for each dislocation measured. This leads to concluding that the local landscape of the grain / slip system configuration plays an important role on the stacking fault energy. Atomic model calculations have been

conducted on this subject: Shih et al. [23] point out that the SFE is likely to be affected by local atomic configuration, and Smith et al. [24] also observed in their models a local variation of stacking fault width along the dislocation lines in CoCrFeMnNi, proving the importance of local effects in HEAs.

3.1.2. Cross-slip

Dislocations can only move conservatively on glide planes simultaneously containing the Burgers vector and line direction. In principle, a screw dislocation can glide conservatively on any $\{111\}$ plane containing its Burgers vector \vec{b} . Nonetheless, the glide motion of the screw dislocation is not entirely confined on one $\{111\}$ plane, because there is another $\{111\}$ plane on which the screw dislocation can also glide with the same \vec{b} [25]. The event in which a part of screw-oriented segment of a dislocation starts to move on a different $\{111\}$ plane is called cross-slip.

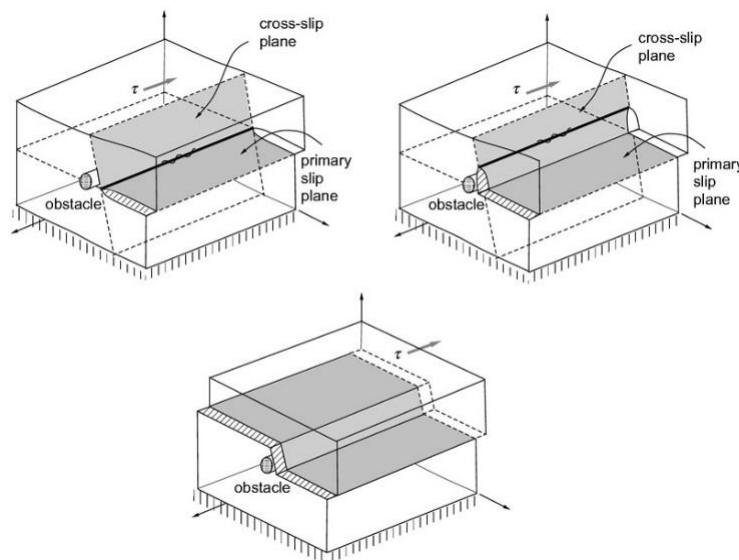


Figure 3-16 – Double cross-slip process to avoid an obstacle. From [25].

Cross slip occurs when the local stresses push a dislocation into a plane which is different from the original plane of slipping [26], to allow it to overcome an obstacle, for instance (see schematics on Figure 3-16). Unforced cross-slip is believed to be a rare event in low SFE fcc crystals and requires the assistance of thermal fluctuations, obstacles and local stress in the CoCrFeMnNi alloy. In this study, out of 19 grains strained at room temperature, around 30% of them presented activation of cross-slip, mostly on identified obstacles.

One example of dislocations cross-slipping to overcome an obstacle occurred during the straining of specimen 35/I2-Head15, where a pile-up of perfect dislocations gliding on plane (111) encountered a twin boundary lying on plane $(\bar{1}\bar{1}\bar{1})$ (see Figure 3-17). Because

there is only one common \vec{b} to both these planes, the Burgers vector is determined to be $\vec{b} = [110]$.

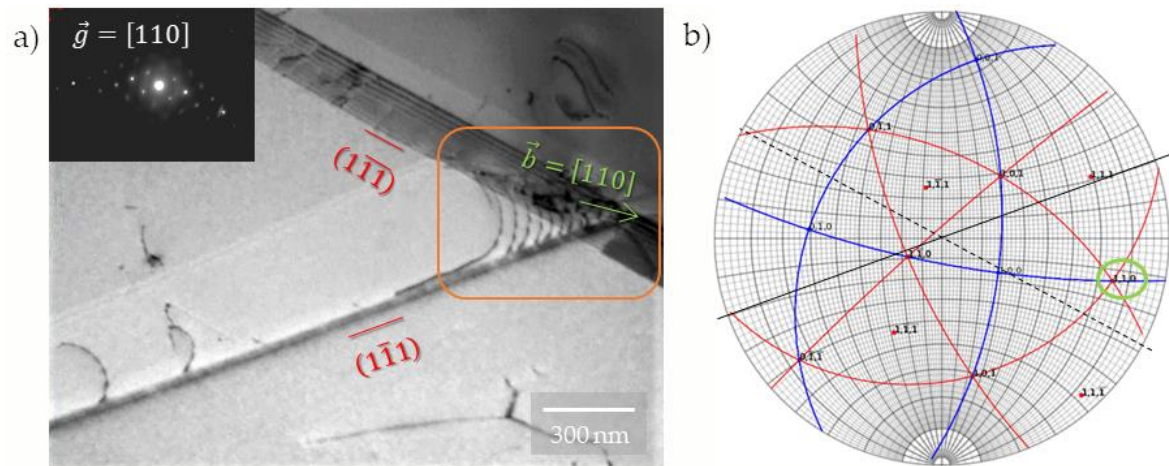


Figure 3-17 – Specimen 35/I2-Head15, strained at $T=293$ K. a) The orange frame emphasizes dislocations moving on slip plane $(1\bar{1}\bar{1})$ that encounter a twin boundary with the direction of plane $(1\bar{1}\bar{1})$ and cross-slip into it. Their Burgers vector is $\vec{b} = [110]$, as it is the only common \vec{b} for these two planes. Slip planes in red, Burgers vector and its direction in green; insert: corresponding diffraction pattern. b) Corresponding stereographic projection and orientation. The solid black line shows the primary slip plane, while the dashed black line shows the cross-slip / twin plane. In green, the Burgers vector.

Dislocations gliding on the primary slip system $(1\bar{1}\bar{1})[110]$ have a Schmid factor $m = 0.10$. Dislocations cross-slipping to system $(1\bar{1}\bar{1})[110]$ have a Schmid factor $m = 0.17$. Although neither of these systems have a very high Schmid factor, the one for the cross-slipped plane is higher than the original. The geometric criterion (see ^[27]) is not very high and, when increasing strain, dislocations do transmit across the grain boundary (although their new slip system in the new grain has a Schmid factor of 0.17, not different than the cross-slip system). This leads to the conclusion that for dislocations on the primary system it is energetically similar to cross-slip or to transmit across the twin boundary, and they eventually do both.

The fact that low Schmid factor slip systems are activated is not uncommon as the alloy, even in the annealed state, contains many remaining dislocations. These remnant dislocations can be activated even if their Schmid factor is not maximum. ^[28]

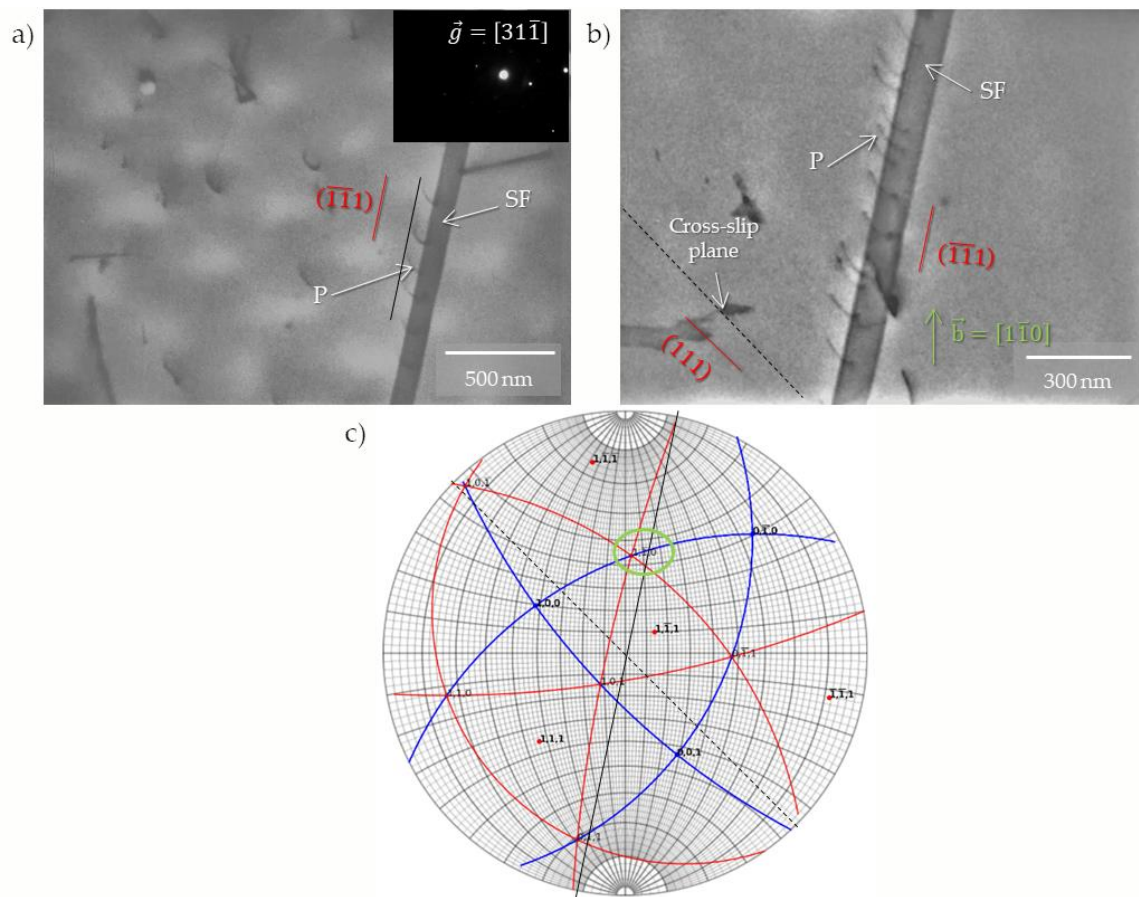


Figure 3-18 – Specimen 35/I2-Head24, strained at $T=293$ K. a) Perfect dislocations gliding on plane $(\bar{1}\bar{1}1)$ (shown in red and marked with black solid line), identified as “P”. Parallel plane shows SF contrast; insert: corresponding diffraction pattern for both images. b) Same slip system of perfect dislocations “P”, after a time lapse. The slip traces of the cross-slipped dislocation can be seen appearing, corresponding to slip plane (111) (black dashed line). The Burgers vector corresponding to these two planes is $\vec{b} = [1\bar{1}0]$, the only common \vec{b} . Slip planes in red, Burgers vector and its direction in green. c) Corresponding stereographic projection and orientation showing the primary slip plane (solid black line), the cross-slip plane (dashed black line), and the common Burgers vector (in green).

Specimen 35/I2-Head24 showed another example of cross-slip, this time intra-granular. Dislocations can be seen gliding on plane $(\bar{1}\bar{1}1)$, next to a parallel darker slip trace, as it is shown in Figure 3-18(a). After a 42 minutes’ time lapse, dislocations on this plane cross-slip into plane (111) (part (b) of figure and Supplementary Video 3). The cross-slip is out of camera, however visible appearing slip traces indicate that it occurred and in which plane it happened. The only common Burgers vector for these two planes is $\vec{b} = [1\bar{1}0]$ (part (c) of figure). Calculating the Schmid factors for both systems gives as result the following: $m = 0.15$ for primary slip system $(\bar{1}\bar{1}1)[1\bar{1}0]$, and $m = 0.40$ for cross-slip system $(111)[1\bar{1}0]$. This indicates that the cross-slip plane is more favourable to the dislocation movement than the first one.

Specimen 35/I2-Head12, shown in Figure 3-19 (and in Supplementary Video 4) gives another example. This specimen showed large dissociation of Shockley partials.

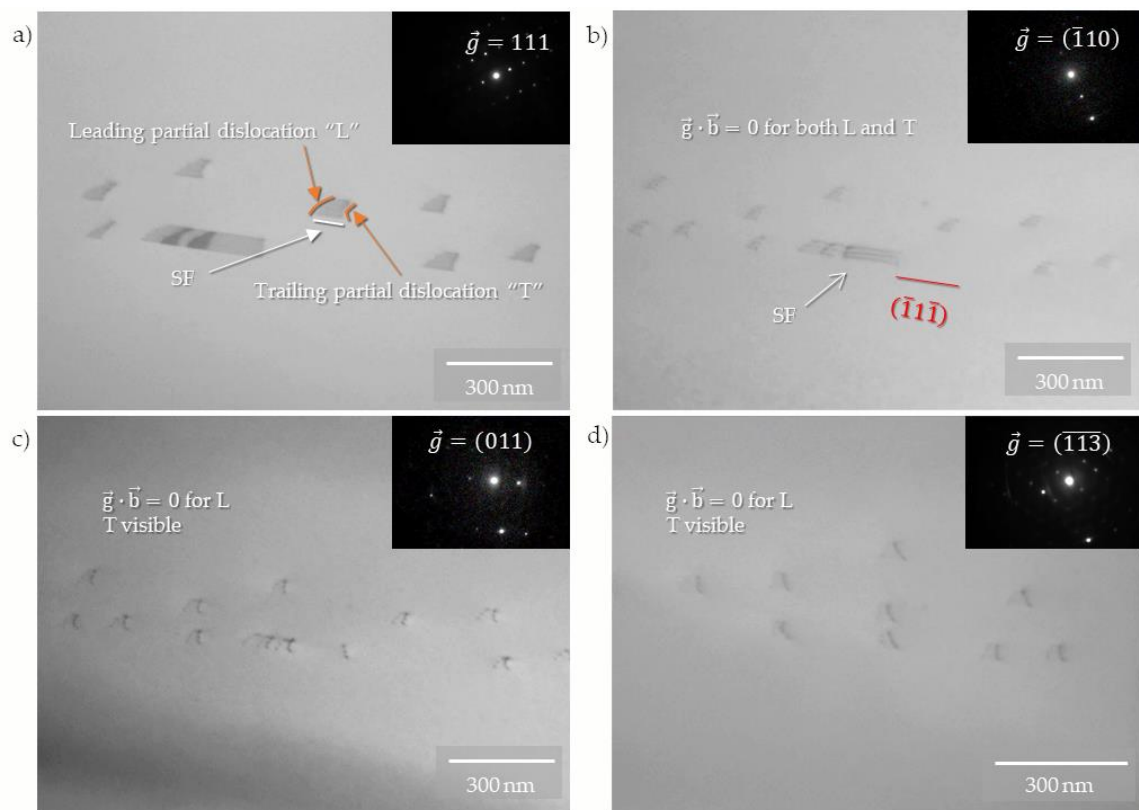


Figure 3-19 – Specimen 35/I2-Head12 strained at $T = 293$ K. a) High magnification of a set of partial dislocations (leading “L” and trailing “T” in orange), clearly showing the stacking fault in between them, in white; insert: corresponding diffraction pattern. b) In red, the slip plane where dislocations glide, $(\bar{1}\bar{1}\bar{1})$. The stacking fault SF is clearly visible, while both L and T are invisible; insert: corresponding diffraction pattern. c) and d) $\vec{g} \cdot \vec{b} = 0$ condition for L, while T is visible and SF invisible; insert: corresponding diffraction patterns.

Leading dislocation L and trailing dislocation T are both Shockley partials of the $1/6\langle 112 \rangle$ type. Two $\vec{g} \cdot \vec{b} = 0$ conditions in the *in situ* experiment allowed for the indexation of L (see Figure 3-19 (c) and (d)), identifying it as the partial dislocation on system $(\bar{1}\bar{1}\bar{1})[21\bar{1}]$ (for this purpose, see also the corresponding stereographic projection in Figure 3-20). Part (b) of the figure, however, shows a $\vec{g} \cdot \vec{b} = 0$ condition for both L and T, meaning this condition extinguishes the full Burgers vector $[10\bar{1}]$. Calculating the Schmid factor for all possible systems will permit the indexation of T, and also confirms the indexation of L as having the highest Schmid factor for the grain. T is then determined to be the partial dislocation on system $(\bar{1}\bar{1}\bar{1})[1\bar{1}\bar{2}]$. All values are reflected on Table 3-7.

Table 3-7 – Schmid factor calculation for specimen 35/I2-Head12.

In Grey shadow, the Schmid factor for the leading partial dislocation (coincidentally, the highest); in Green shadow, the Schmid factor for the trailing partial dislocation (the second highest). This table only shows the calculation for the two planes that showed dislocation activity during the *in situ* experiment.

Slip system		Schmid factor m
Plane	\vec{b}	
$\bar{1}\bar{1}\bar{1}$	$2\bar{1}\bar{1}$	0.38
	$\bar{1}\bar{1}\bar{2}$	0.26
	$12\bar{1}$	0.12
	$10\bar{1}$	0.37
111	$10\bar{1}$	0.17
	$\bar{1}\bar{2}\bar{1}$	0.34
	$11\bar{2}$	0.02
	$2\bar{1}\bar{1}$	0.32

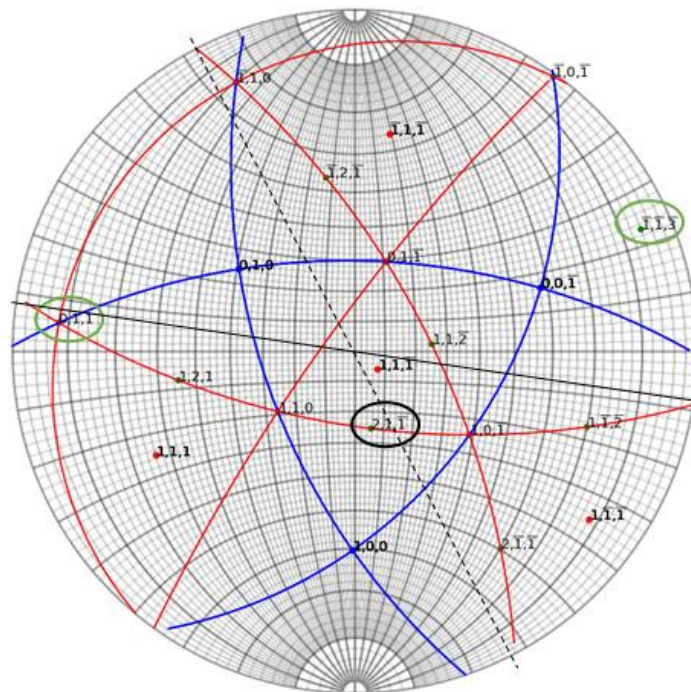


Figure 3-20 – Corresponding stereographic projection for specimen 35/I2-Head12, showing the glide plane (solid black line) and the two image vectors that fulfil the extinction conditions for L in green, and the L Burgers vector in black. The dashed black line shows the cross-slip plane.

After further deformation at $T = 293$ K of this specimen, the dissociation of the partial dislocations leads to the activation of another mechanism: twinning (evidenced by the contrast of the stacking faults in Figure 3-22(a)). See section 3.2 of Chapter 2 for more information on this subject). A secondary slip plane is detected, also with twinning activation (Figure 3-22(b)). From its slip traces and the stereographic projection of Figure 3-20, this secondary slip plane is identified as (111). Parts (c) and (d) show that

dislocations, by an unknown reason, cross-slip between these two planes. The orange frames on these two images show an example region where this occurred.

In fcc metals, screw dislocations can cross-slip from one (111) type plane to another, as long as the Burgers vector is common to both slip planes. When a perfect dislocation is dissociated into two Shockley partials on a (111) type plane, these dislocations can only glide on the plane that contains them both (meaning they cannot cross-slip as no other (111) type plane will be common to them) ^[25]. However, the case of specimen 35/I2-Head12 appear to show cross-slip of dissociated dislocations. Upon further analysis of the experiment, it is clear that Shockley partials encounter obstacles strong enough to facilitate the activation of cross-slip; they, however, first recombine into a perfect dislocation at these obstacles to be able to cross-slip to a different plane that contains their $1/2[110]$ Burgers vector. The Friedel-Escaig mechanism has been proposed to explain this.

In the Friedel-Escaig mechanism ^[29–32], the two partial dislocations constrict to a point, recombining to form a perfect screw dislocation on their original glide plane, and then re-dissociate on the cross-slip plane creating two different partial dislocations. Shear stresses then may drive the dislocation to extend and move onto the cross-slip plane (Figure 3-21). In particular, Escaig has shown that the process depends mainly on the ratio of the width of splitting under stress on the primary and the cross slip planes. This causes the process to be orientation dependent ^[26]. Caillard and Martin ^[26] studied experimentally this mechanism and confirmed it for fcc alloys. It has also been confirmed by atomic simulations ^[33].

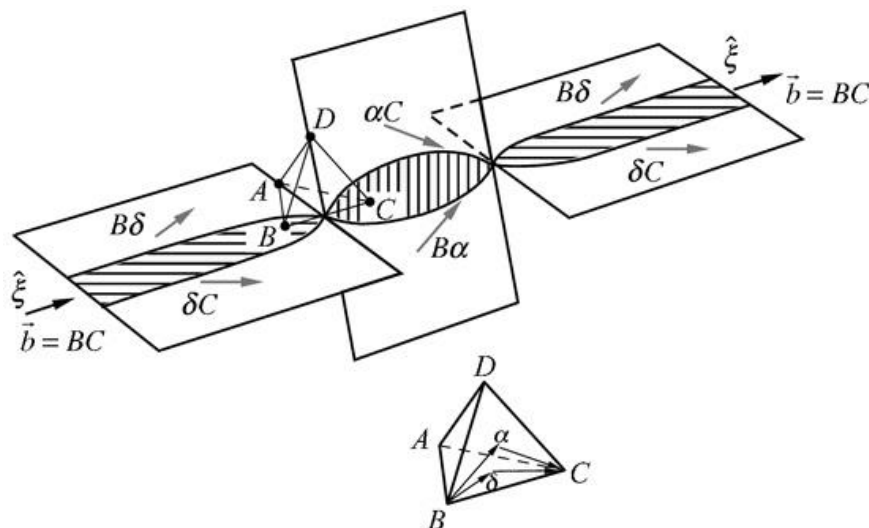


Figure 3-21 – The Friedel–Escaig mechanism of cross-slip. From ^[25].

As already presented on Figure 3-19(c), there is a confirmed Burgers vector for a perfect dislocation, $[10\bar{1}]$, which is, coincidentally, both the only vector onto which L and T can recombine and the only common \vec{b} for planes $(\bar{1}1\bar{1})$ and (111) (according to the geometry presented on Figure 3-20).

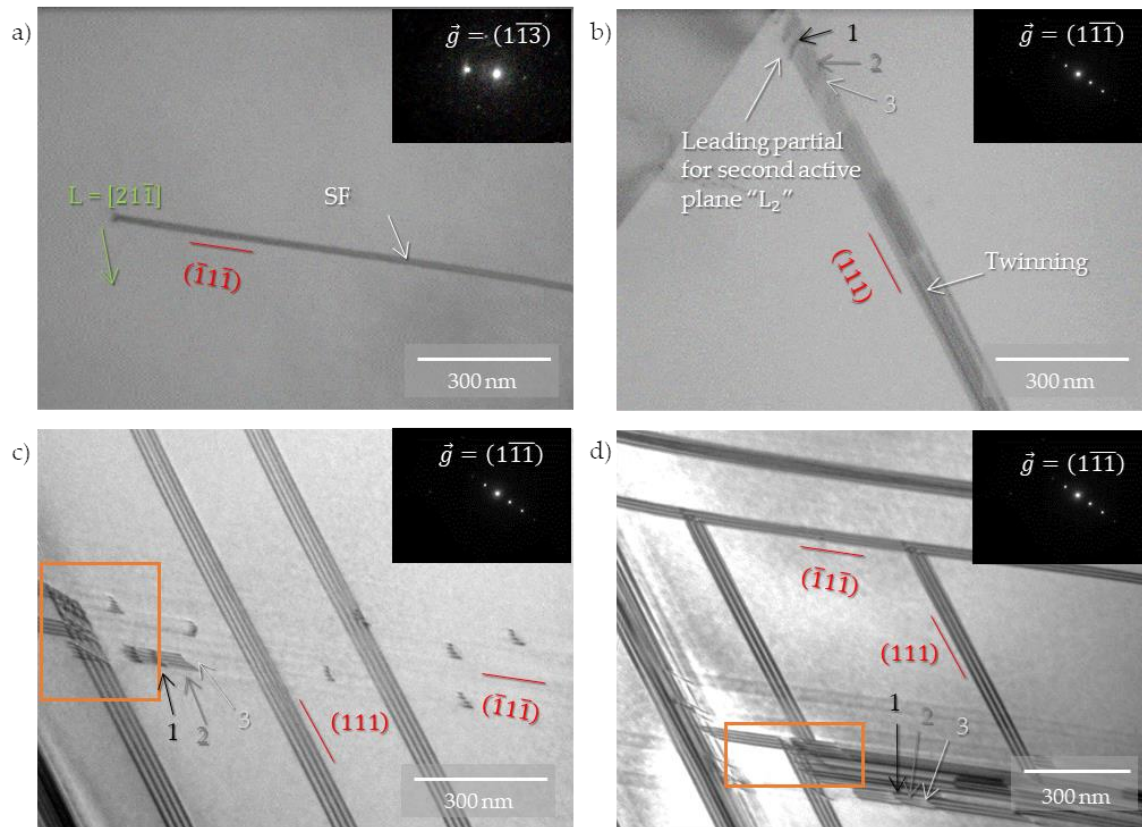


Figure 3-22 – Same specimen as before. a) Same slip system as before, $(\bar{1}1\bar{1})[21\bar{1}]$. In red, the slip plane, in green, the leading Burgers vector and its direction; insert: corresponding diffraction pattern. b) A secondary slip system, (111) , in red. This secondary slip system shows evidence of twinning by the contrast changes of the SF (indicated by 1, 2, 3 markers); insert: corresponding diffraction pattern. c) Planes $(\bar{1}1\bar{1})$ and (111) , where twinning is an active mechanism (indicated by 1, 2, 3 markers). The interaction of dislocations between these two active slip systems is highlighted with the orange frame, showing confirmation of cross-slip between them; insert: corresponding diffraction pattern. d) Same as before, the orange frame highlights the same area as the previous one, after further deformation. Cross-slip can be detected at almost each intersection of the two slip planes; insert: corresponding diffraction pattern.

To summarise, the process can be explained as follows: dislocations glide in plane $(\bar{1}1\bar{1})$ in the form of largely dissociated Shockley partials, which create intrinsic SFs (see Appendix 4 for the SF characterization) that lead to twinning formation, either by intrinsic SF + nucleation of Frank sessile dislocations or by intrinsic SF + stair-rod sessile dislocations ^[34]. The leading dislocation is L ($\vec{b}_L = [21\bar{1}]$) and the trailing is T ($\vec{b}_T = [11\bar{2}]$). A moment is reached, assisted by thermal fluctuation and, possibly, local stress ^[35], where they encounter an obstacle (which could be an out of contrast sessile

dislocation), and they recombine onto a perfect dislocation “P” ($\vec{b} = [10\bar{1}]$). This perfect dislocation has a Schmid factor comparable to that of L, so it is energetically possible for this to occur. They then cross-slip from plane $(\bar{1}\bar{1}\bar{1})$ to plane (111) through P. Once in their new plane, they dissociate again into two new Shockley partials. As no $\vec{g} \cdot \vec{b} = 0$ conditions were found for the secondary slip plane, the assumption on their nature has to be made based on their Schmid factors (Table 3-7). The secondary system leading partial dislocation “L₂” is then either $[\bar{1}\bar{2}\bar{1}]$ or $[2\bar{1}\bar{1}]$, as they have the highest (and similar) Schmid factors for their habitat plane; however, according to the Thompson tetrahedron, the assumption can be made that it is $[2\bar{1}\bar{1}]$. This entire process is compatible with dissociation and recombination expected from the Thompson tetrahedron (Figure 3-23).

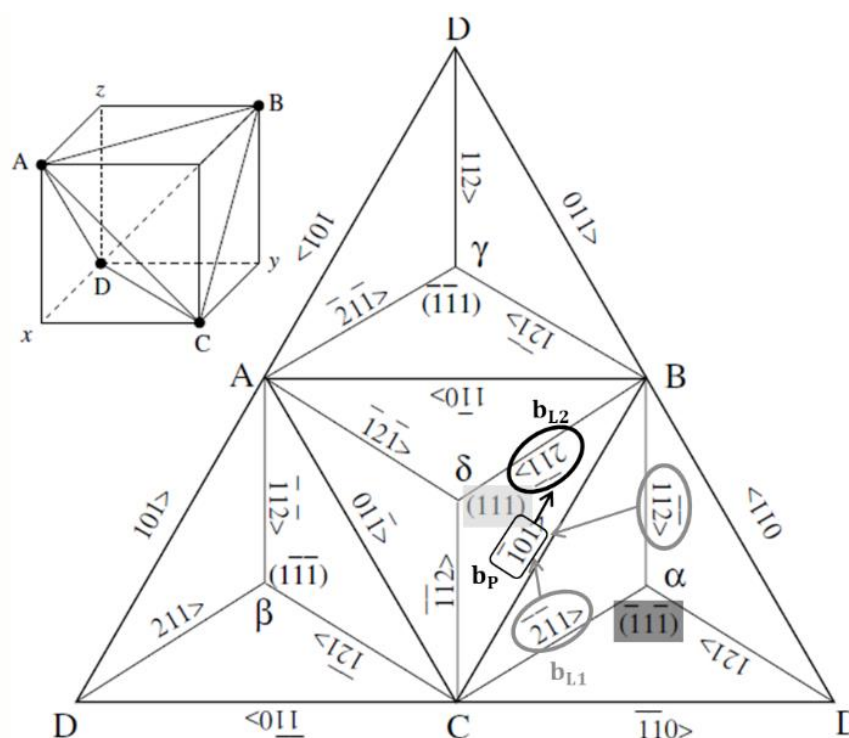


Figure 3-23 – The Thompson tetrahedron, showing in dark grey the primary slip system with the dissociated dislocation, the recombined perfect dislocation in black rectangle, and the secondary slip system and potential leading partial dislocation after redissociation in black.

The Friedel-Escaig mechanism taking place on this specimen was also present in another specimen, 35/I2-Head26, also strained at $T = 293$ K. Figure 3-24 shows the sequence over a time-lapse t , where largely dissociated Shockley partials bounding large SFs in plane $(\bar{1}\bar{1}\bar{1})$ are active. They encounter a twin boundary laying parallel to plane $(\bar{1}\bar{1}\bar{1})$, which blocks their path (part (a) of figure). Part (b) shows that, after a time lapse $t = 571$ s, at least one partial dislocation recombines into a perfect dislocation, cross-slips into plane (111) to dissociate again. The only common perfect Burgers vector to both $(\bar{1}\bar{1}\bar{1})$ and (111) is $\vec{b} = [0\bar{1}\bar{1}]$. Because no $\vec{g} \cdot \vec{b} = 0$ conditions were found in the experiment for neither slip

system, the nature of the Shockley partials must rely entirely on the Schmid factor calculation, presented in Table 3-8.

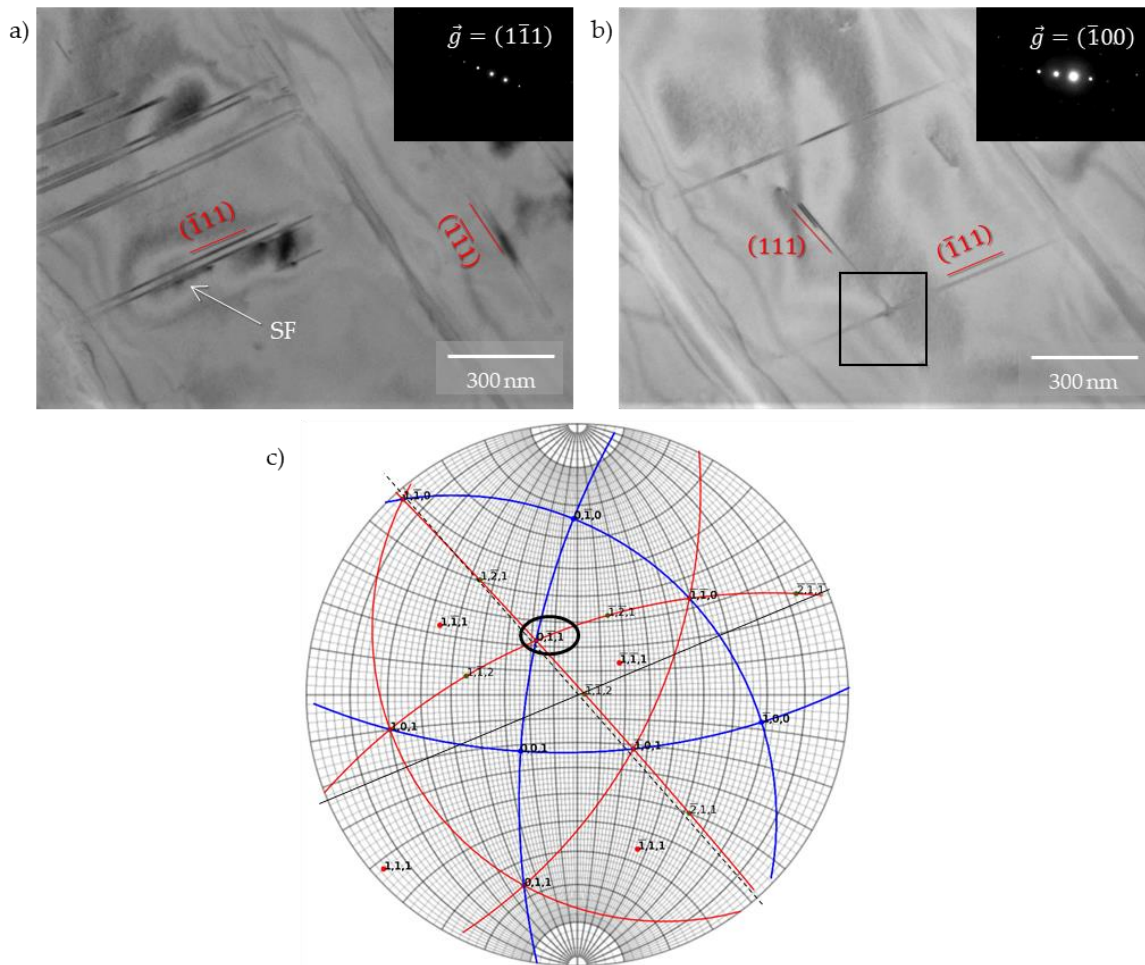


Figure 3-24 – Specimen 35/I2-Head26 strained at $T = 293$ K. a) Largely dissociated Shockley partials gliding in plane $(\bar{1}11)$. SF is indicated by white arrow. There is also a twin boundary that is parallel to plane $(\bar{1}11)$. Both are identified in red; insert: corresponding diffraction pattern. b)

After $t = 571$ s, a dislocation can be seen cross-slipping from plane $(\bar{1}11)$ to plane (111) (black frame); insert: corresponding diffraction pattern. c) Corresponding stereographic projection and orientation. The solid black line shows the primary slip plane $(\bar{1}11)$, the dashed black line corresponds to the cross-slip plane (111) , while the black circle marks the common Burgers vector, $\vec{b} = [0\bar{1}1]$.

These results allow to infer that the leading partial dislocation for the primary slip system is $(\bar{1}11)[\bar{1}\bar{2}1]$ (which has the highest Schmid factor for this system). Because the perfect dislocation $[0\bar{1}1]$ has a smaller Schmid factor in the secondary slip system than in the primary, dislocations dissociate again to find the most energetically favourable path, that is $(111)[\bar{1}\bar{2}1]$.

Table 3-8 – Schmid factor calculation for specimen 35/I2-Head26.

In Grey shadow, the Schmid factor for the perfect dislocation common to both slip planes. In Green shadow, the Schmid factor for the highest partial dislocation on each slip system. This table only shows the calculation for the two planes that showed dislocation activity during the *in situ* experiment.

Slip system		Schmid factor m
Plane	\vec{b}	
$\bar{1}11$	$0\bar{1}1$	0.32
	$1\bar{1}2$	0.10
	$\bar{1}2\bar{1}$	0.45
	$\bar{2}1\bar{1}$	0.35
111	$0\bar{1}1$	0.25
	$\bar{1}2\bar{1}$	0.43
	$1\bar{1}2$	0.01
	$\bar{2}1\bar{1}$	0.42

3.2. Twinning

Specimen 35/I2-Head12 already introduced the fact that twinning can, and does, occur when straining at RT, regardless of the deformation or strain applied.

Another example of twinning at RT comes from specimen 35/I2-Head13 (already presented when discussing CRSS in Chapter 2), to show that twinning is not related to cross-slip when straining at RT (as the previous example). Figure 3-25 presents the specimen at start of plastic deformation. Dislocations can be first seen moving in the form of an isolated perfect dislocation (“P”), gliding on plane ($\bar{1}11$), followed by twinning in the same plane. This happens under a pre-existing crack tip in the specimen parallel to plane ($1\bar{1}1$) (part (a) of figure). Parts (b) and (c) exhibit the leading (“L”) and trailing (“T”) partial dislocations that conform the twinning, and the $\vec{g} \cdot \vec{b} = 0$ condition for L. This allows for the indexation of L as ($\bar{1}11$)[$1\bar{1}2$], with a Schmid factor $m = 0.49$.

As previously explained in Chapter 2, P was indexed using $\vec{g} \cdot \vec{b} = 0$ conditions, and it is determined to glide on the slip system ($\bar{1}11$)[$0\bar{1}1$], with a Schmid factor $m = 0.46$ (part (d) of figure). The presence of pinning points (obstacles) that may help the dissociation of perfect dislocations into Shockley partials and the fact that the Schmid factor for L is higher than the one for P (and thus more energetically favourable), allow for a configuration favourable to twinning to dominate the slip.

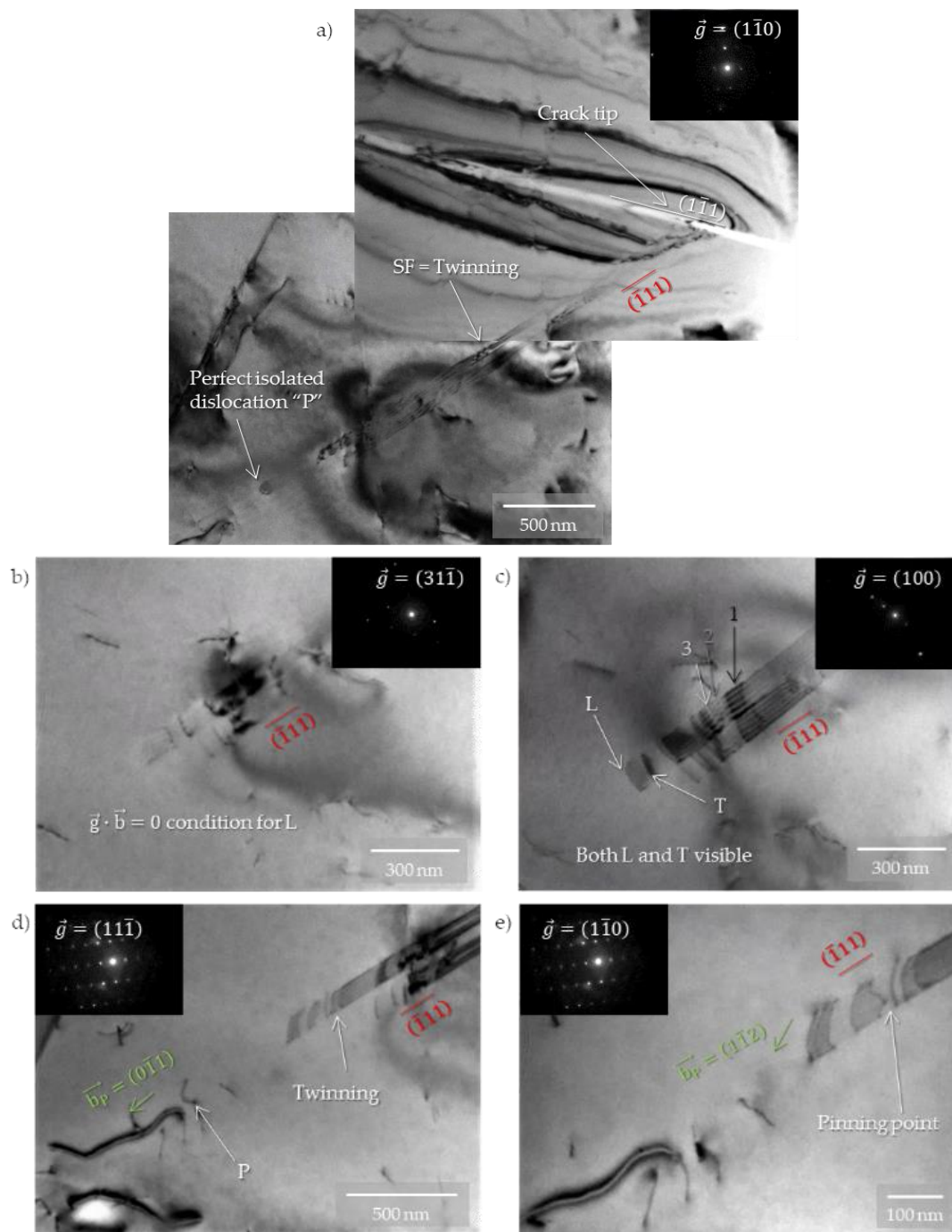


Figure 3-25 – Specimen 35/I2-Head13 strained at $T = 293$ K. a) Deformation was activated under a crack tip parallel to plane $(\bar{1}\bar{1}1)$ (in white), on plane $(\bar{1}\bar{1}1)$ (in red), by means of twinning (evidenced by the SF traces and 1, 2, 3 alternating contrast). A single isolated perfect dislocation “P” is seen heading the twin. b) $\vec{g} \cdot \vec{b} = 0$ condition for the leading partial dislocation “L” in the twinning. c) Both the leading “L” and the trailing “T” partial dislocations are visible, the SF in between them with the 1, 2, 3 alternating contrast evidences twinning. d) Dislocation P (its Burgers vector in green), followed by twinning. e) Dissociation is highlighted when increasing magnification, and it is distorted when a trailing dislocation is pinned by an obstacle (identified by the white arrow); the Burgers vector of the partial dislocation L is shown in green. All images show inserts of the corresponding diffraction patterns, and slip plane is identified in red.

When SFE is low, and considering the Frank criterion, the split of dislocations is easy. In fcc structures, mechanical twins originate in regions of high stress concentration (as, for example, in the head of a piled up group of dislocations) [36]. This high stress concentration region, which also comprises multiple pinning points, assists the uneven dissociation of dislocations. This could mean that there are local atomic clusters interacting as solutes with the dislocations, magnifying dissociation and, thus, helping twinning nucleation.

The *in situ* TEM experiments presented thus far show there is no dependence on a critical stress or on temperature to activate twinning. However, what is clear is that an applied shear stress is able to split the asymmetric dissociation of perfect dislocations, even at or just before the onset of plastic deformation [28].

Figure 3-26 reproduces the variation of the Peach-Kohler shear stress acting on both partial dislocations \vec{b}_{p1} and \vec{b}_{p2} that compose a perfect dislocation \vec{b} for the slip system with the highest Schmid factor. The stress difference τ'_d between the shear acting on the edge component of each partial dislocation (σ_{yz}^1 and σ_{yz}^2) will favour the constriction of dislocation b when positive or its dissociation when negative. This Escaig stress is then plotted in a standard stereographic triangle for the most favourable slip system. When the crystal is loaded in tension, τ'_d reaches the strongest positive values (red zone) near the 001 orientation. In the blue region, τ'_d is negative and the applied stress tends to increase the splitting [37,38]. In compression, the inverse would occur.

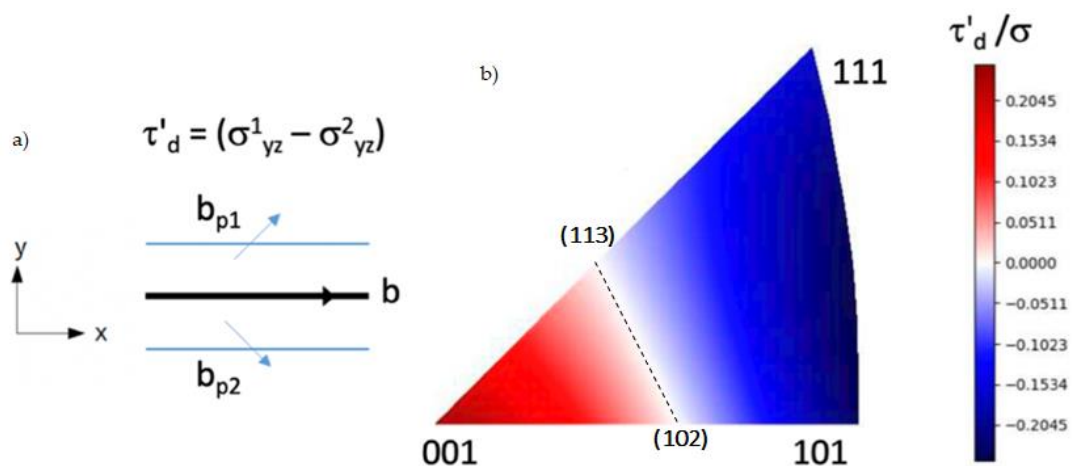


Figure 3-26 – Escaig split of two partial dislocations in function of the straining direction in tension. a) b_{p1} and b_{p2} ($a/6[112]$ type) compose a perfect dislocation b ($a/2[110]$ type) split in the (xy) plane. τ'_d is the difference between the Peach Kohler stresses acting on the edge components of b_{p1} and b_{p2} . b) Sign and amplitude of τ'_d in function of the direction of the applied stress in the standard stereographic triangle. Figure made by Frédéric Mompiau, from [28]. The dotted line shows the orientation limit where partial experience equal stress (directions (113) to (102)).

Considering this, an analysis of the grains strained at RT (where the primary slip system was activated) was made and each crystallographic orientation was plotted in a standard stereographic triangle (please consider that there may be slight variations on position because the straining axis has a tendency to align parallel to the edges of the hole in the thinnest areas; therefore, in a given experiment where several grains are stressed at once, grain orientations are collected where the actual tensile axis is within $\pm 15^\circ$ of the macroscopic one).

The standard stereographic triangle was built from the Euler angles of each studied grain, with respect to the straining axis, using the ATEX software ^[39]. The result is shown in Figure 3-27 (each dot corresponds to the straining axis of the strained grain): blue dots represent the orientations where twinning was activated, and red dots where there was only perfect glide active; the grey dots represent grains where only secondary slip systems were active. The specimen identification of each dot on the figure is given on Table 3-9.

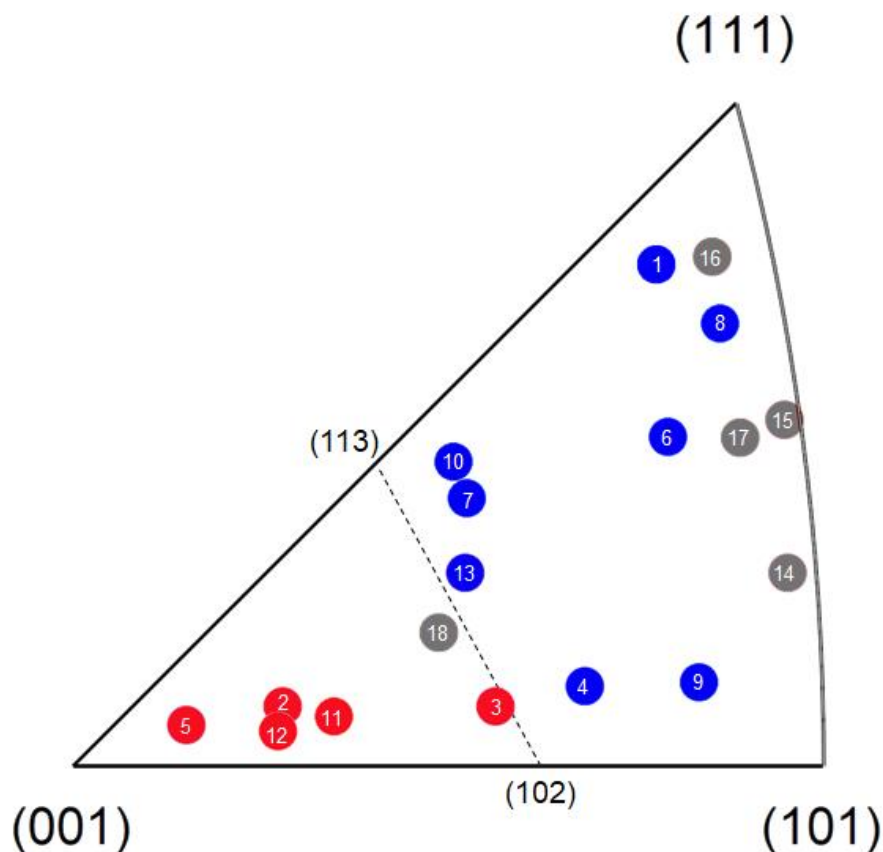


Figure 3-27 – Orientation dependence of micro-twinning (blue dots) vs. perfect dislocation glide (red dots) in a standard triangle at room temperature. Adapted from ^[28]. The limit is given by the dotted line (directions (113) to (102)). Grey dots show the grains where systems other than the primary were activated.

Table 3-9 – Specimens used to construct the room temperature standard triangle in Figure 3-27.

	Specimen	Grain	Euler Angles			Mechanism
			φ_1	φ	φ_2	
1	1484Recuit1	LS 1	29.7	126.9	84.2	Twinning
2	1484Recuit1	LS 3	84.2	39.7	107.7	Perfect glide
3	35/I2-Head1	LS1	157.6	75.4	140.6	Perfect glide
4	35/I2-Head4	RS 1	84.9	65.4	150.5	Twinning
5	35/I2-Head8	LS 1	-101.5	38.8	-173.6	Perfect glide
6	35/I2-Head12	LS 1	163.2	37.0	-92.2	Twinning
7	35/I2-Head12	LS 2	-71.3	120.6	34.8	Twinning
8	35/I2-Head12	RS 2	29.1	51.6	13.8	Twinning
9	35/I2-Head13	LS 2	-81.9	35.6	45.2	Twinning
10	35/I2-Head14	LS 1	-54.8	32.9	-145.0	Twinning
11	35/I2-Head15	RS 1	169.2	77.2	120.0	Perfect glide
12	35/I2-Head26	LS 1	94.4	29.1	-106.8	Perfect glide
13	35/I2-Head26	RS 2	73.0	43.6	167.8	Perfect glide
14	35/I2-Head10	LS 1	-138.5	72.4	34.0	Perfect glide
15	35/I2-Head10	LS 2	-179.8	41.3	-65.0	Perfect glide
16	35/I2-Head10	RS 1	-46.6	74.4	-52.8	Perfect glide
17	35/I2-Head24	LS 1	-152.7	53.2	-66.9	Twinning
18	35/I2-Head26	RS 1	-45.0	33.1	-138.7	Twinning

(LS refers to the left side of the specimen's hole; RS refers to the right side).

Specimen 35/I2-Head12, which exemplifies the Escaig split the best, is represented by dot number 7. This specific orientation is close to the limit line where partial dislocations experience equal stress; this could be the reason why the dissociation decreases when reverting the applied stress (as seen in Supplementary Video 4). However, the tendency to twin is greater due to the crystal orientation of this grain, thus leading to twinning formation on the two slip systems activated.

Dot 9 (Figure 3-25) twins, and dot 11 (Figure 3-17) does not, which also confirm the orientation dependency to micro-twin or not. Other specimens shown thus far, however, do not correlate in this dependency (see grey dots on the figure – for example, dots 14 to 16, corresponding to specimen 35/I2-Head10 from Figure 3-14, where only planar glide was active). This is due to the fact that the slip systems active in those grains do not correspond to the primary systems or to the ones with the highest Schmid factors. This leads to conclude that the orientation dependency can only be accurately determined when considering the primary slip systems alone (when the highest Schmid factor system of the grain is activated – not always the case, depending on the presence of cracks or obstacles impeding or favouring the activation of a given system during straining). A notable example of the opposite is given by dot 17 (specimen 35/I2-Head24 of Figure 3-18), where SFs were developed along with planar glide, yet none on the primary slip system, thus giving an unclear conclusion on its orientation dependency for the activation of mechanisms.

As stated in Oliveros et al. [28], after conclusions made on thin foil effects on dislocations [36,40–42], it can be argued that working in a thin foil favours the splitting of dislocations, as image forces act in opposite direction on opposite surfaces [43], thus, nucleation of partial dislocations can also be favoured compared to perfect ones in thin foils [44]. Both effects will influence the behaviour of dislocations only in very thin foils (30-50 nm and below), which is far from the experimental conditions of this study (as already stated in Chapter 2).

4. At cryogenic temperatures

4.1. Planar glide of perfect dislocations

There is no noticeable difference in the behaviour of perfect dislocations at cryogenic temperature versus their behaviour at room temperature. However, three remarks can be made on this subject:

1. Dislocations also have the tendency to move in pairs (of perfect ones) when activating a slip system in a "virgin" region (glide planes that haven't seen plastic deformation yet). The occurrence of this phenomenon is higher than at RT. This will be further discussed in the next chapter.
2. Perfect dislocations also dissociate, as they do at RT, however with larger dissociation distances. This allows for the experimental calculation of the SFE values, as presented in the next subsection.
3. Perfect dislocations encounter more obstacles ("pinning points") than their counterparts at RT – or these pinning points affect the dislocation lines more. These obstacles are invisible in the TEM observations; thus their nature cannot be determined. Their influence on dislocation movement, however, is visible, and the

conclusion can be made that they are stronger at low temperatures than at RT. This will be further discussed in the next chapter.

4.1.1. Dissociation of perfect dislocations and SFE determination

The same procedure was used to determine experimentally the value of SFE, measuring the dissociation distance between Shockley partials and calculating γ using Equation 3-4 and DISDI. The corresponding measurements and results are presented in the next Figure and Table. A compendium of these results is presented in the graph of Figure 3-29.

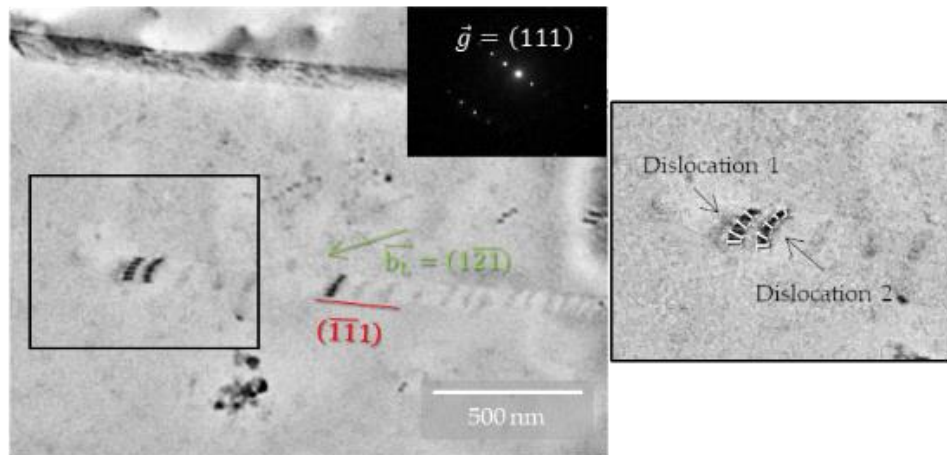


Figure 3-28 – Specimen 35/I2-Head29, strained at T = 104 K. In red, the slip plane; in green, the leading partial’s Burgers vector; insert: corresponding diffraction pattern. Two dissociated dislocations are used to measure the separation distances; they are highlighted in black. The inserted frame shows the same dislocations at 1.5x. The segments where the dissociation distances were measured are shown using white lines.

Table 3-10 – Dissociation values and locally measured γ_{SFE} at T = 104 K.

	r (nm)	ψ (°)	Δr (nm)	$\gamma_{SFE}^{iso-exp}$ (mJ/m²)	γ_{SFE}^{DISDI} (mJ/m²)	$\Delta \gamma_{SFE}^{iso-exp}$	$\Delta \gamma_{SFE}^{DISDI}$
Dislocation 1	55 ± 4	30 ± 1	61	3 ± 1	3	3	3
	59 ± 4	34 ± 1		3 ± 1	2		
	65 ± 4	42 ± 1		3 ± 1	4		
	67 ± 4	60 ± 1		3 ± 1	3		
Dislocation 2	33 ± 4	0 ± 1	51	4 ± 1	6	3	4
	48 ± 4	30 ± 1		3 ± 1	3		
	52 ± 4	34 ± 1		3 ± 1	3		
	53 ± 4	42 ± 1		3 ± 1	5		
	67 ± 4	60 ± 1		3 ± 1	5		
			56			3	3

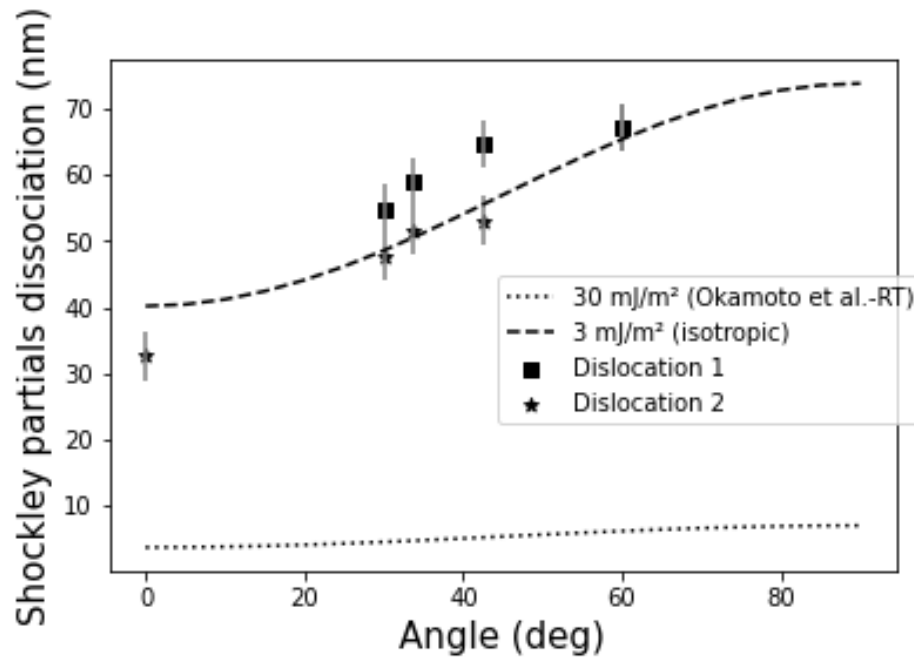


Figure 3-29 – Measured dissociation distance between Shockley partials vs. dislocation character at LN₂T, including SFE values (experimentally calculated and Okamoto et al. [2] at room temperature).

The ab initio calculations by Huang et al. [45] predict ~ 3.4 mJ/m² at 0 K.

4.1.2. Cross-slip

Even though the SFE is lower, perfect dislocations still cross-slip when strained at cryogenic temperatures, either intra-granular or onto twin boundaries, when encountering strong obstacles. Specimen 35/I2-HeadB, strained at $T = 100$ K, shows a grain (G1) where a pile-up of perfect dislocations (with a Burgers vector $\vec{b}_p = [101]$) glides in the $(\bar{1}\bar{1}\bar{1})$ plane. This pile-up of perfect dislocations is followed by Shockley partial dislocations, which, as evidenced by the "1, 2, 3"-type contrast in their wake (contrast generated by the presence of 1, 2 and 3 superimposed SFs), can be attributed to twinning (Figure 3-30).

The primary slip system activates in the direction of the main crack tip that opened during straining. The Schmid factor for system $(\bar{1}\bar{1}\bar{1})[101]$ is $m = 0.33$. Although high, it is not the highest for this grain. The highest is for system $(\bar{1}\bar{1}\bar{1})[10\bar{1}]$ ($m = 0.46$). Because the Burgers vectors for these two systems are not the same, there must be a mechanism besides cross-slip that allows dislocations to find a better energetic configuration. The crack then bifurcates probably after encountering a GB or a twin, opening a second one in the direction of plane $(\bar{1}\bar{1}\bar{1})$, thus allowing for the activation of the most energetically favourable system. This will become the secondary slip system (Figure 3-31).

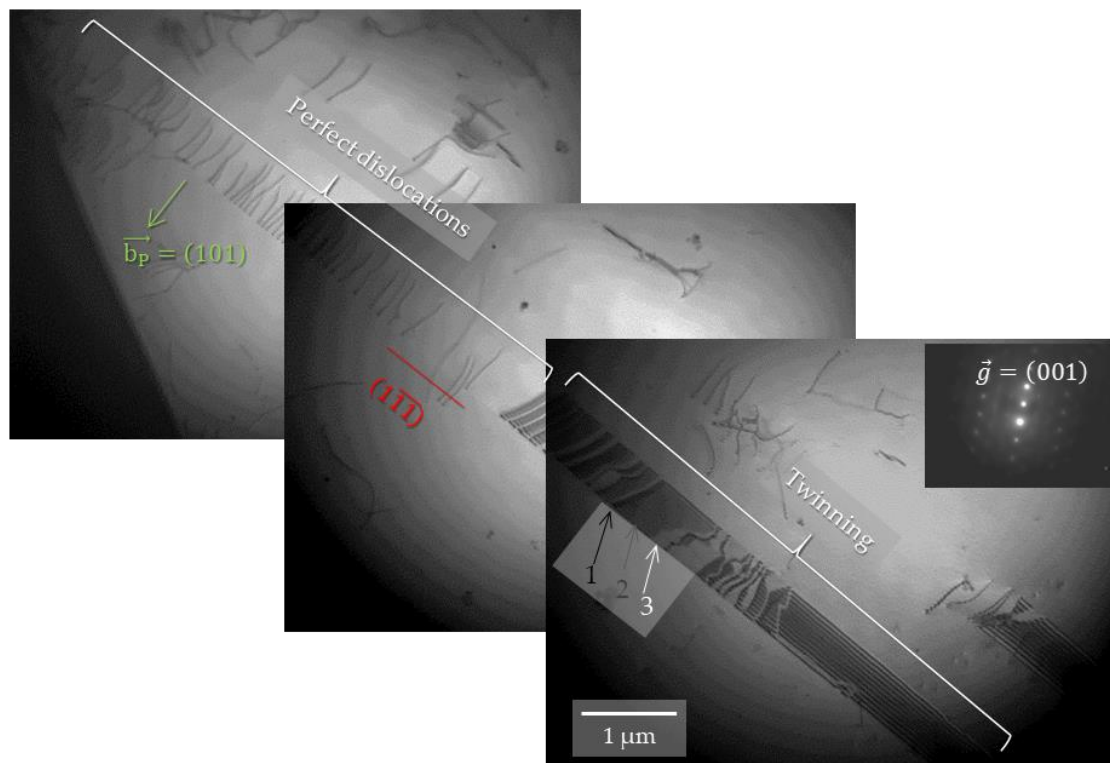


Figure 3-30 – Specimen 35/I2-HeadB, strained at $T = 100$ K. The image shows a pile-up of perfect dislocations ($\vec{b}_p = [101]$, in green) being followed by partial dislocations activating twinning (notice the “1, 2, 3”-type SF contrasts), gliding in plane $(\bar{1}\bar{1}\bar{1})$ (in red). Insert: corresponding diffraction pattern.

The secondary crack emits a pile-up on the secondary slip system direction. This pile-up then encounters a boundary to its left. Dislocations transmit across this boundary, into a second grain (G2 – a twin grain). It is there, on G2, that cross-slips occurs. The path of dislocations starting from slip system $(\bar{1}\bar{1}\bar{1})[10\bar{1}]$ is shown in Figure 3-32.

Once dislocations are in G2, they glide in plane $(\bar{1}\bar{1}\bar{1})$ (Figure 3-33(a)). These perfect dislocations encounter the twin boundary 2, which lies along $(\bar{1}\bar{1}\bar{1})$. Supplementary Video 5 shows that the majority of dislocations seem to disappear on the twin boundary while a few are transmitted to the grain to their left. By changing imaging conditions, it is now clear that the “disappearing” dislocations are, in fact, cross-slipping onto the twin boundary (parts (b) and (c) of the figure).

The only common Burgers vector to these two planes is $\vec{b} = [101]$. This means that dislocations glide on system $(\bar{1}\bar{1}\bar{1})[101]$ ($m = 0.25$) and cross-slip onto system $(\bar{1}\bar{1}\bar{1})[101]$ ($m = 0.32$), which is a better energetic path for them.

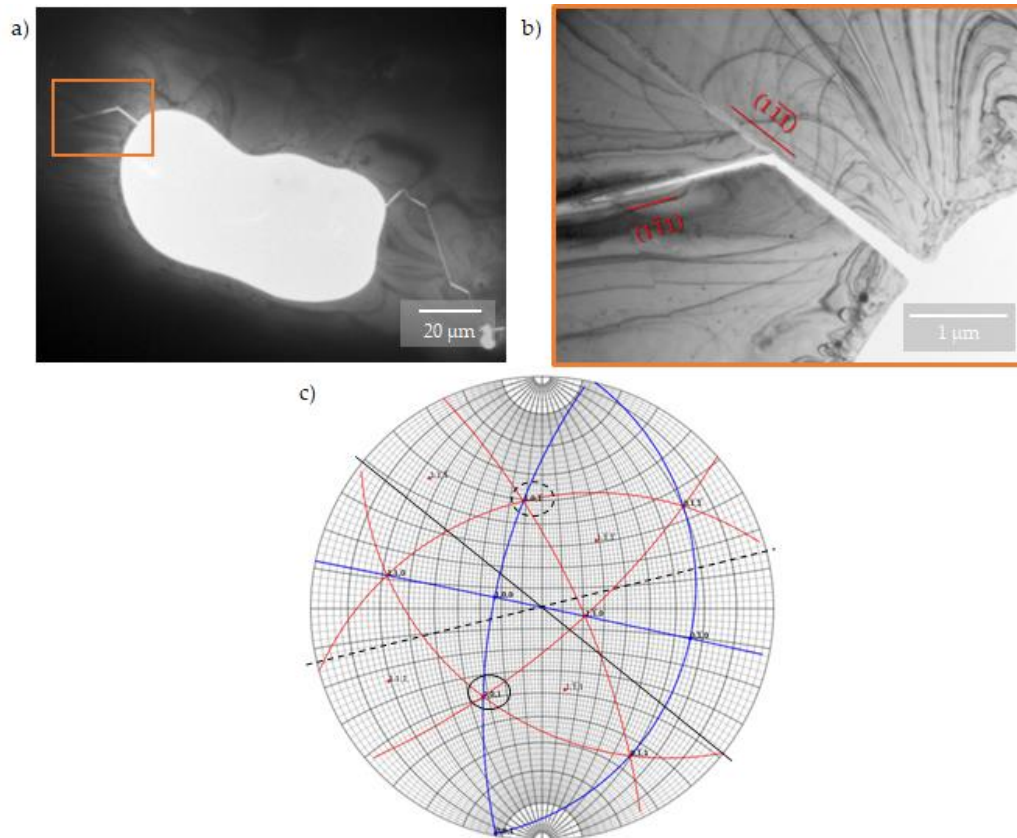


Figure 3-31 – Same specimen. a) After deformation, the bifurcation of the crack is visible on the left side of the hole. The orange frame highlights the deformation area. b) Magnification of the area in the orange frame, corresponding to G1, showing (in red) the bifurcation of the crack with their planes (directions). The primary in the $(1\bar{1}\bar{1})$ direction, and the secondary in the $(1\bar{1}\bar{1})$ direction. c) Corresponding stereographic projection showing the primary (solid black lines) and the secondary (dashed black lines) slip systems.

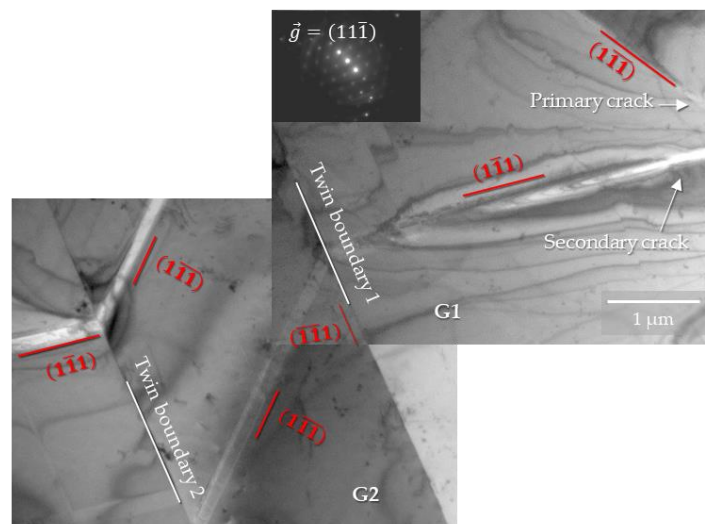


Figure 3-32 – Same specimen. Top right: G1, containing both cracks and primary and secondary slip planes (in red), the latest of which transmits to G2 across twin boundary 1. Bottom left: G2, where visible slip traces on plane $(1\bar{1}\bar{1})$, in red, evidence the transmission of dislocations until pile-up encounters twin boundary 2. Insert: corresponding diffraction pattern.

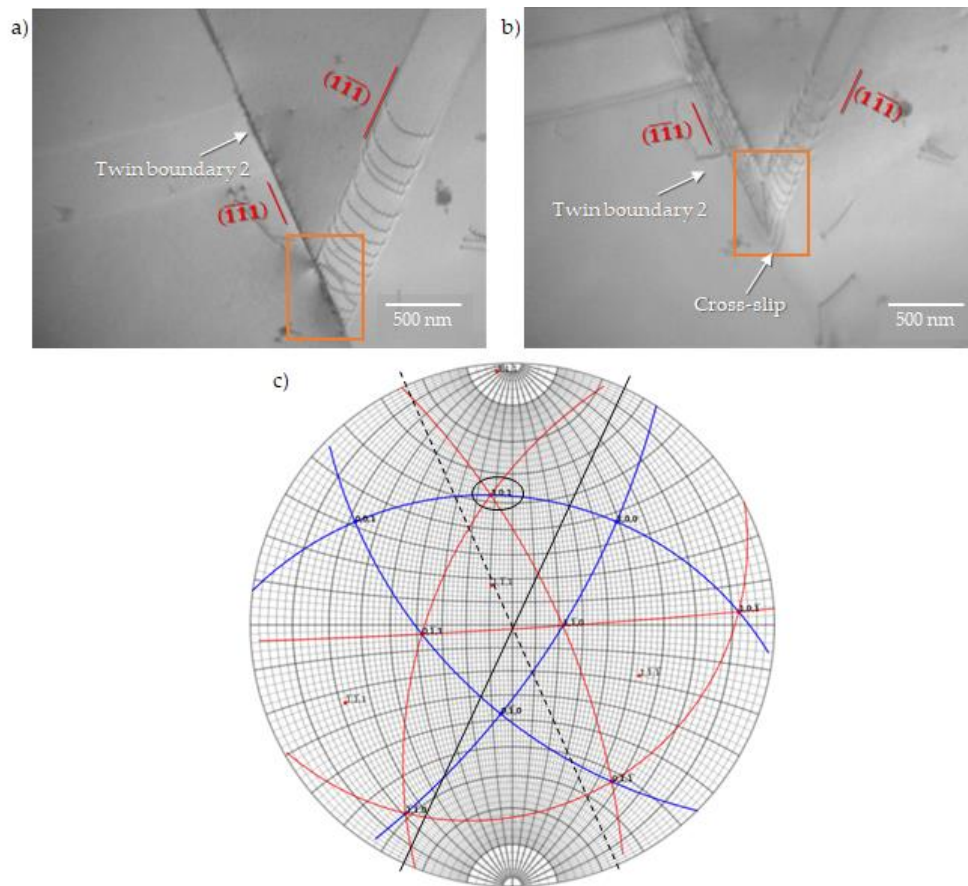


Figure 3-33 – In red, the slip planes; the orange frames show the area where dislocations cross-slip. a) Perfect dislocations gliding in plane $(1\bar{1}\bar{1})$ and disappearing on the twin boundary $(\bar{1}\bar{1}\bar{1})$. b) By changing imaging conditions, dislocations are revealed to be cross-slipping into the twin boundary. c) Stereographic projection: slip plane in solid black line, twin boundary / cross-slip plane in dashed black line, only common Burgers vector circled in black.

Another example is presented in Figure 3-34(a) from specimen 35/I2-Head28, strained at $T = 104$ K. In this specimen, the primary slip system is active in the form of perfect dislocations gliding on $(\bar{1}\bar{1}\bar{1})[011]$ (the Burgers vector was determined by $\vec{g} \cdot \vec{b} = 0$ conditions, it will be called \vec{b}_1), with a Schmid factor $m = 0.28$. They encounter a boundary on the bottom centre (not in camera vision). From this boundary, a secondary slip system is activated, gliding on $(\bar{1}\bar{1}\bar{1})[\bar{1}\bar{1}\bar{0}]$ (again, confirmed by $\vec{g} \cdot \vec{b} = 0$ conditions, it will be called \vec{b}_2), $m = 0.47$.

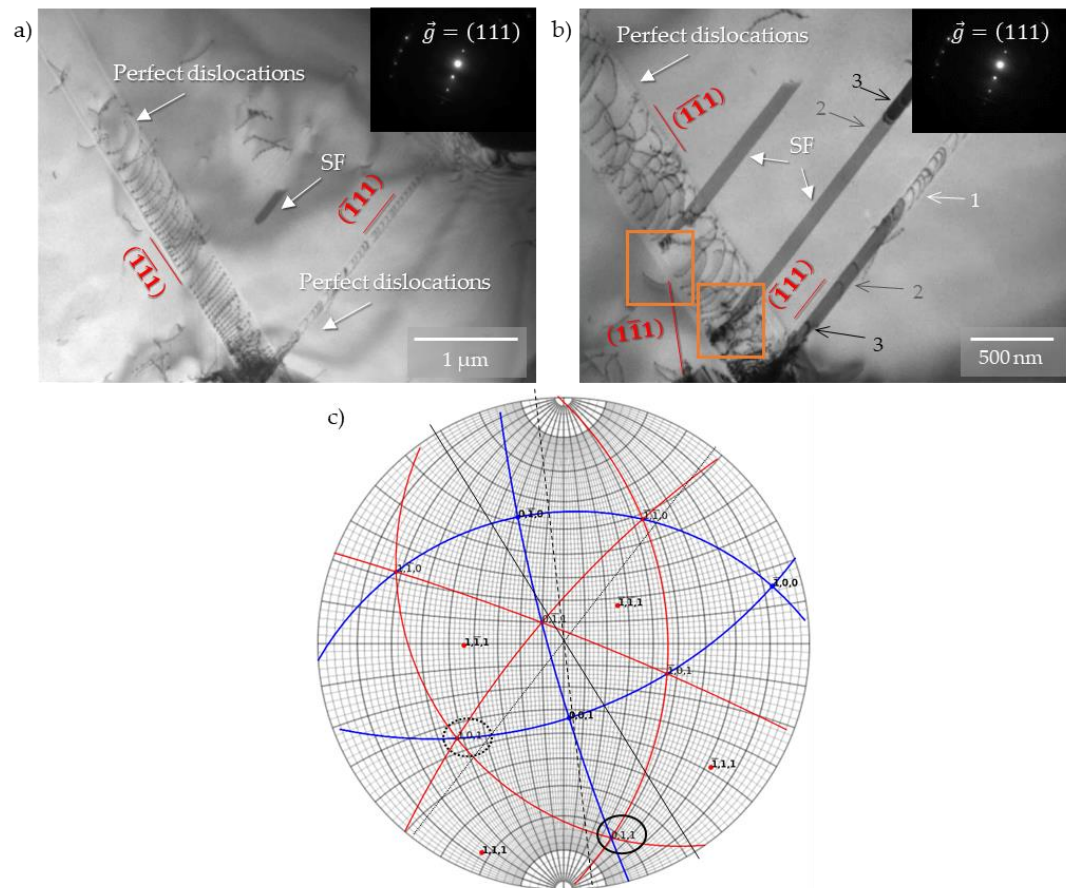


Figure 3-34 – Specimen 35/I2-Head28, strained at $T = 104$ K. a) A “big” pile-up of perfect dislocations glides on primary system $(\bar{1}\bar{1}1)[011]$. Next to it, two slip planes on $(\bar{1}11)$ can be seen, one of perfect dislocations and one where just SF is visible; insert: corresponding diffraction pattern. b) After additional straining, dislocations on the primary system get pinned by obstacle and become sessile. This causes dislocations to cross-slip to plane $(1\bar{1}1)$ (orange frames). SF become larger, leading eventually to twinning; insert: corresponding diffraction pattern. c) Corresponding stereographic projection. The solid black line shows the primary slip system, the dashed black line, the cross-slip plane, and the dotted black line, the SF / eventual twinning.

After more straining, dislocations from the primary slip system start to get “pinned” (see part (b) of the figure). This is caused by obstacles (sessile dislocations or atomic clusters acting as solutes) that hinder dislocation movement, making them sessile and facilitating for them to find a different path. They find it in the plane where their Burgers vector is common, that is, they cross-slip to plane $(1\bar{1}1)$. Slip system $(1\bar{1}1)[011]$ (part (c) of figure) has a Schmid factor $m = 0.01$. Even though this is not more energetically favourable – the opposite, even – the partial dislocations creating SF in plane $(\bar{1}11)$ glide into the primary slip system (orange frames in part (b) of the figure), acting as a strong barriers for the perfect dislocations on the primary system, preventing them from moving forward.

4.2. Twinning

Twinning is activated at cryogenic temperatures more easily than at RT (evidenced by the larger number of blue dots corresponding to twinning in strained grains, as seen in Figure 3-37 versus Figure 3-27). Both the examples presented in the previous section for cross-slip also show good examples of twinning.

Continuing with specimen 35/I2-Head28 from Figure 3-34(b), the image shows alternating contrast in the secondary slip system $(\bar{1}11)[\bar{1}\bar{1}0]$, which, as already explained, indicates twinning in the system, because the perfect dislocations on this system eventually dissociate. The two Shockley partials around \vec{b}_2 show the highest Schmid factors, allowing to conclude that the leading partial “L” is $[211]$ ($m = 0.4737$) and the trailing partial “T” is $[\bar{1}\bar{2}1]$ ($m = 0.33$). Even though the Schmid factors for the perfect dislocation 2 and for L are almost identical, perfect dislocations still dissociate. Energetically, it is convenient for this system to either slip or twin; however, obstacles (such as out of contrast sessile dislocations) must be present and favour twinning activation.

In this case, a proposed mechanism that can explain twinning formation is the Fujita-Mori model ^[46], which is based on a dislocation reaction first proposed by Cohen and Weertman ^[47]: two slip systems must be active in a crystal; the leading partial dislocation of a primary slip dislocation splits into a stair-rod dislocation (a sessile $1/6\langle 110 \rangle$ -type) and a twinning partial dislocation (a glissile $1/6\langle 112 \rangle$ -type) on the conjugate slip plane (Figure 3-35). Cohen and Weertman proposed that a perfect dislocation at the head of a pile-up in front of a strong barrier (as a Lomer-Cottrell lock or dislocation dipole), can dissociate into a sessile $1/3\langle 111 \rangle$ -type Frank dislocation and a $1/6\langle 112 \rangle$ -type partial dislocation ^[48]. The partial dislocation can glide away from the Frank dislocation on the conjugate slip plane trailing a wide stacking fault. The difference between both models is that in the CW model, additional partials have to be emitted for a twin to thicken, requiring a highly ordered arrangement of stacking faults to be produced by chance, whereas in the FM model, the cross-slip of the partial dislocations occurs in an orderly manner.

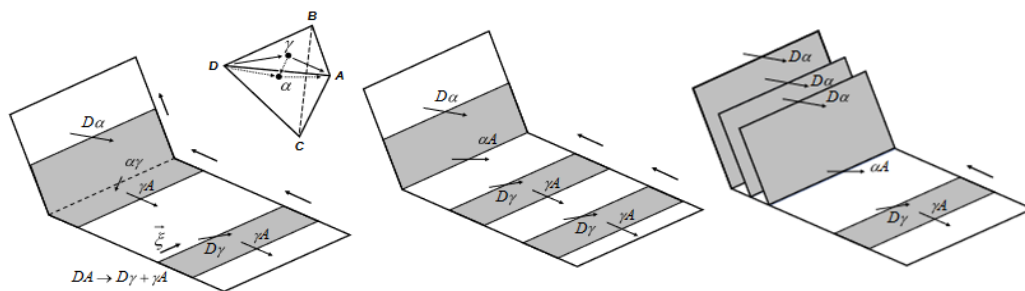


Figure 3-35 – Schematic representation of the Fujita-Mori stair-rod cross slip twinning mode. From ^[48].

As dislocation from the primary slip system in specimen 35/I2-Head28 cross-slip into the secondary slip system, dislocations pinned by obstacles can act as barriers, leading to the dissociation of $(\bar{1}11)[\bar{1}\bar{1}0]$ dislocations into a glissile $(\bar{1}11)[211]$ and a sessile partial dislocation, allowing for twinning to activate in this plane regardless of the small energetic difference from Schmid factors. This is also observed in specimen 35/I2-Head22, strained at $T = 100$ K (Figure 3-36), where perfect dislocations gliding in system $(\bar{1}11)[0\bar{1}1]$ ($m = 0.49$) encounter sessile dislocations that dissociate them into $(\bar{1}11)[\bar{1}\bar{2}1]$ ($m = 0.41$) and activating twinning. This observation reinforces the hypothesis that twinning may develop once a sufficient density of obstacles exist (strain hardening, leading to a sufficient amount of stress ^[3]) or if the existing obstacles are oriented conveniently to create the right reaction with incoming dislocations (through cross-slip for instance ^[49]).

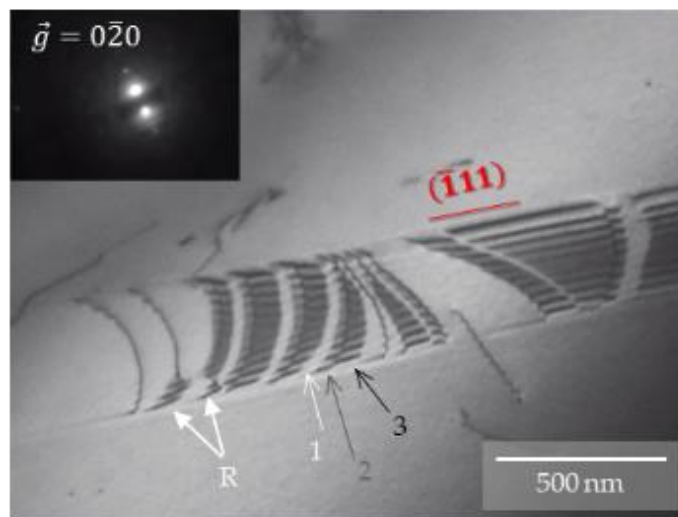


Figure 3-36 – Specimen 35/I2-Head22, strained at $T = 100$ K. Perfect dislocations encounter sessile dislocations that cause a (non-identified) reaction “R” and dissociate them, activating twinning (as evidenced by alternating 1, 2, 3 contrast).

Another possible explanation for twinning nucleation is the interaction of perfect dislocation with existing SFs. A study ^[50] performed on fcc Al alloys showed that full dislocation-SF interactions lead to the stress field of the two partial dislocations in the SF to impede the full dislocation motion, enhancing the strength of the alloy, and during plastic deformation, the presence of the stress field of the two partial dislocations in the SF may be able to entrap the full dislocations, resulting in dislocation storage. Another study, through the concurrent atomistic-continuum (CAC) method ^[51], showed that several possible scenarios can occur when a perfect dislocation encounters a SF (extrinsic in nature – ESF):

- the full dislocation dissociates into two Shockley partials adjacent to the first hcp plane, transforming the ESF into a three-layer twin,

- the full dislocation dissociates into two Shockley partials adjacent to the second hcp plane, transforming the ESF into an ISF.

Specimen 35/I2-HeadB (from Figure 3-30) also shows twinning activation following the dissociation of perfect dislocations on the primary slip system of G1, $(1\bar{1}\bar{1})[101]$ with $m = 0.33$. When dissociating, they do so onto a leading Shockley partial "L", $\vec{b}_L = [1\bar{1}\bar{2}]$ and $m = 0.40$, and a trailing Shockley partial "T", $\vec{b}_T = [21\bar{1}]$ and $m = 0.29$. The dissociated slip system for L has a higher Schmid factor than the one for perfect undissociated dislocations, which makes this the most energetically favourable system for G1, thus leading to twinning formation when enough L dislocations glide.

As for the specimens strained at RT, the crystallographic orientations of the grains strained at cryogenic temperatures were plotted into a standard triangle, to identify if there is an orientation dependency for twinning activation. The results are presented in the following figure, and the identification of each dot is given in Table 3-11.

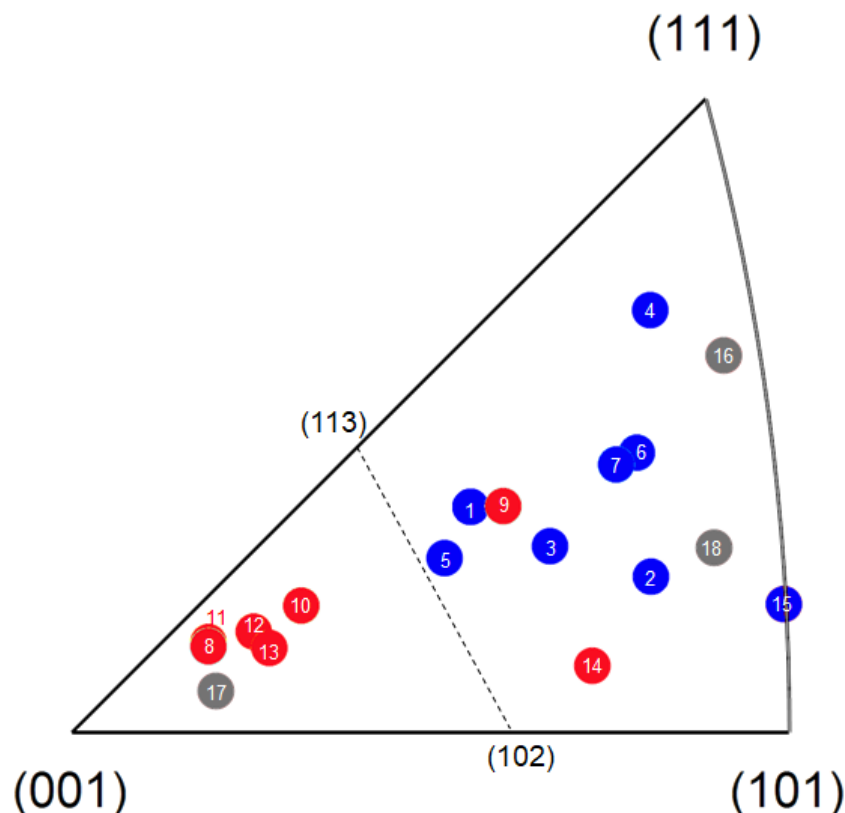


Figure 3-37 – Orientation dependence of micro-twinning (blue dots) vs perfect dislocation glide (red dots) in standard triangles at cryogenic temperatures. Adapted from [28]. The limit is given by the dotted line (directions (113) to (102)). Grey dots show the grains where systems other than the primary were activated.

Table 3-11 - Specimens used to construct the Cryogenic Temperature standard triangle in Figure 3-37.

	Specimen	T (K)	Grain	Euler Angles			Mechanism
				φ_1	φ	φ_2	
1	35/I2-Head17	100	RS 1	-175.5	25.6	-110.6	Twinning
2	35/I2-Head17	100	RS 2	154.4	60.6	-60.7	Twinning
3	35/I2-Head17	100	RS 3	-165.8	31.6	-119.8	Twinning
4	35/I2-Head23	97	RS 1	163.1	36.6	-99.7	Twinning
5	35/I2-Head22	96	LS 1	110.6	32.7	97	Twinning
6	35/I2-Head28	100	LS 1	8	35.6	-169.4	Twinning
7	35/I2-Head28	100	LS 3	4.9	34.2	-166.5	Twinning
8	35/I2-Head29	102	LS 1	97.9	45.4	165.4	Perfect glide
9	35/I2-Head29	102	RS 3	-24.7	69.9	115.6	Perfect glide
10	35/I2-Head29	102	RS 4	58.9	16.1	-134.7	Perfect glide
11	35/I2-HeadB	100	LS 1	-103.8	25.7	93.4	Perfect glide
12	35/I2-HeadB	100	LS 3	-11	81.8	114.7	Perfect glide
13	35/I2-Head22	96	RS 1	69.3	39.5	-68.1	Perfect glide
14	1484_Recuit4	113	RS 1	-106.5	14.4	-107.5	Perfect glide
15	35/I2-HeadB	100	LS 2	103.8	31.8	-146.9	Twinning
16	35/I2-Head22	96	LS 2	-121.4	44.6	160.6	Perfect glide
17	35/I2-Head28	100	LS 2	94.7	34.9	-103.4	Twinning
18	35/I2-Head29	102	LS 3	-17.1	11.2	148.5	Perfect glide

Same as with the RT standard triangle, at cryogenic temperature there is orientation dependency when the primary slip system (highest Schmid factor) is activated. For example, dot 15 (corresponding to Figure 3-30) corresponds to a twin grain with twinning activation, dot 7 (Figure 3-34) also corresponds to twinning activation, while dots 11, 12 (Figure 3-33) and 8 (Figure 3-28) all show perfect glide of dislocations.

However, as with the grains studied at RT, when a system other than the primary is activated, the reliability of the orientation dependency diminishes, as is the case with the grey dots in the figure (16, 17, 18). Another case is the one from dots 9 and 14, where there was no activation of micro-twinning yet the primary and highest Schmid factored systems

were activated. A reason for this discrepancy is that the initial density of dislocations is highly reduced in a TEM foil. If the dislocations of the most favourable systems, as predicted by the Schmid factor, are not initially present, some alternative ones (less favoured, but initially present) may be activated. Indeed, the stress needed to nucleate new dislocations is always prohibitive compared to the stress needed to propagate existing ones.

Nonetheless, the liquid nitrogen straining experiments performed in this study proved that twinning can occur at any given time mark or deformation, coupled with the fact that SFE is lower when temperature decreases. A few examples are:

- Specimen 35/I2-HeadB shows twinning at the same time as perfect glide activation, a few minutes after plastic deformation started.
- Specimen 35/I2-Head28 shows twinning at the end of the *in situ* straining experiment, after activation of several slip systems in different grains.
- Specimen 35/I2-Head17 (presented in Figure 3-38, deformed at $T = 100$ K, corresponding to dot 2 in the Figure 3-37) shows multiple largely dissociated dislocations where visible SF are present. These planes of dissociated dislocations (unfortunately, the nature of the partials could not be determined) lead to twinning. Twinning activation started after $1 \mu\text{m}$ of elongation, meaning it was activated even before planar glide.

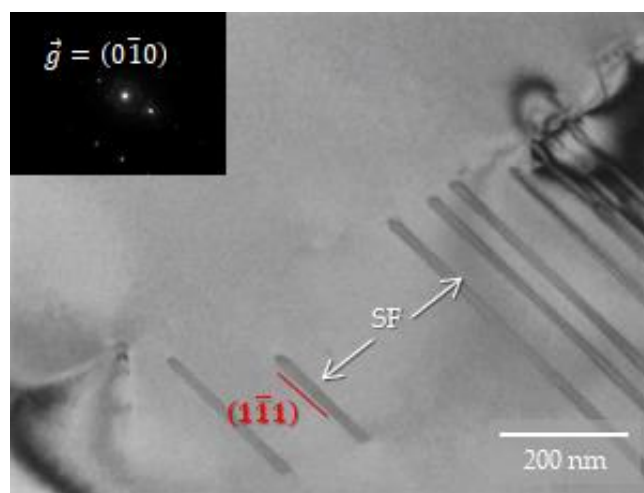


Figure 3-38 – Specimen 35/I2-Head17, strained at $T = 100$ K. There are at least 9 visible SFs on plane $(1\bar{1}1)$.

These examples were chosen to demonstrate the variability of twinning and the independence of their activation from stress, leading to conclude that, as it is the case for twinning at RT, its activation / nucleation depends mainly on the orientation of the crystal.

5. Conclusions

In situ TEM straining experiments were carried out at room and near liquid nitrogen temperature on an equimolar CoCrFeMnNi austenitic high entropy alloy. It was found that:

- CRSS can be locally measured using the radius of curvature of moving perfect dislocations. The experimentally calculated σ stress is comparable to the yield stress from *ex situ* tensile results, permitting to compare *in situ* local measurements to macroscopic results, and validating the trend that the resistance to plastic deformation in CoCrFeMnNi is higher when the temperature is lower.
- Planar glide in CoCrFeMnNi follows what is expected in a typical fcc metal: dislocations with $1/2[110]$ Burgers vector glide in $\{111\}$ plane, and dissociate asymmetrically in two Shockley partials of $1/6[112]$ type.
- The value of the dissociation change as a function of the crystal orientation, the applied stress, temperature, but also as a function of the local atomic arrangement. In average, this SFE is low, in the range of 8-15 mJ/m².
- The dissociation of perfect dislocation can therefore occur without obstacles provided the orientation is favourable. This leads to the development of extended stacking faults. These extended stacking faults serve as seeds to the expansion of mechanical twins.
- Despite this low SFE, cross-slip is frequently observed in this alloy. This seems to happen as a response to the activation of the Friedel-Escaig mechanism when dislocations are stopped on strong obstacles (GB, twins).
- *In situ* TEM experiments also allowed to observe twinning activation, at both temperatures, and independently of the strain applied. In average, we showed that twinning activation depends more on the grain orientation than on temperature or critical stresses.
- Twinning is however more frequent at low temperature and this could be the result of a lowering of the stacking fault energy and a more effective pinning of both partial dislocations, which will favour the slower speed of the trailing dislocation, favouring the extension of stacking faults that serve as seeds for twinning.
- This last point could be critical to explain the exceptional mechanical performances of such alloy at cryogenic temperatures. More experiments were undertaken to better characterize the type and strength of local pinning points in HEAs, especially at low T, and will be discussed in the next chapter.
- In all, the more noticeable difference between dislocation behaviour at RT and LN₂T is the variation of the “jump” distance when dislocations glide. This will be presented more thoroughly on the next chapter.

This study confirms the dislocation behaviour observed in the literature for CoCrFeMnNi alloy, as well as casting light on twinning activation, in particular. The next chapter will present more comprehensive analysis on the intrinsic factors that influence dislocation behaviour in this alloy (i.e., pinning points, atomic landscape, etc.), which will play an important role in understanding its behaviour and mechanical properties.

6. References

- [1] F. Otto, A. Dlouhý, Ch. Somsen, H. Bei, G. Eggeler, E. P. George, *Acta Materialia* **2013**, *61*, 5743–5755.
- [2] N. L. Okamoto, S. Fujimoto, Y. Kambara, M. Kawamura, Z. M. T. Chen, H. Matsunoshita, K. Tanaka, H. Inui, E. P. George, *Sci Rep* **2016**, *6*, 35863.
- [3] G. Laplanche, A. Kostka, O. M. Horst, G. Eggeler, E. P. George, *Acta Materialia* **2016**, *118*, 152–163.
- [4] Q. Ding, X. Fu, D. Chen, H. Bei, B. Gludovatz, J. Li, Z. Zhang, E. P. George, Q. Yu, T. Zhu, R. O. Ritchie, *Materials Today* **2019**, *25*, 21–27.
- [5] I. V. Kireeva, Y. I. Chumlyakov, Z. V. Pobedennaya, I. V. Kuksgausen, I. Karaman, *Materials Science & Engineering A* **2017**, *705*, 176–181.
- [6] S.-W. Kim, J. H. Kim, *Materials Science and Engineering: A* **2018**, *718*, 321–325.
- [7] S. Lee, M. J. Duarte, M. Feuerbacher, R. Soler, C. Kirchlechner, C. H. Liebscher, S. H. Oh, G. Dehm, *Materials Research Letters* **2020**, *8*, 216–224.
- [8] ERC, “A Multiscale Dislocation Language for Data-Driven Materials Science,” can be found under <https://cordis.europa.eu/project/id/759419>, **2021**.
- [9] J. Douin, P. Veyssi re, P. Beauchamp, *Philos. Mag. A* **1986**, *54*, 375–393.
- [10] J. Douin, **2020**.
- [11] L. R. Owen, E. J. Pickering, H. Y. Playford, H. J. Stone, M. G. Tucker, N. G. Jones, *Acta Materialia* **2017**, *122*, 11–18.
- [12] T. Teramoto, K. Yamada, R. Ito, K. Tanaka, *Journal of Alloys and Compounds* **2019**, *777*, 1313–1318.
- [13] O. Schneeweiss, M. Fri k, M. Dudov , D. Holec, M.  ob, D. Kriegner, V. Hol y, P. Beran, E. P. George, J. Neugebauer, A. Dlouh y, *Phys. Rev. B* **2017**, *96*, 13.
- [14] F. Mompou, R. Xie, *JMI* **2021**, *282*, 84–97.
- [15] A. Gali, E. P. George, *Intermetallics* **2013**, *39*, 74–78.
- [16] S. H. Oh, M. Legros, D. Kiener, G. Dehm, *Nature Mater* **2009**, *8*, 95–100.
- [17] B. Gludovatz, A. Hohenwarter, D. Catoor, E. H. Chang, E. P. George, R. O. Ritchie, *Science* **2014**, *345*, 1153–1158.
- [18] E. P. George, W. A. Curtin, C. C. Tasan, *Acta mat.* **2020**, *188*, 435–474.
- [19] F. R. N. Nabarro, *Advances in Physics* **1952**, *1*, 269–394.
- [20] J. P. Hirth, J. Lothe, *Theory of Dislocations*, Wiley, New York, **1982**.

- [21] A. Haglund, M. Koehler, D. Catoor, E. P. George, V. Keppens, *Intermetallics* **2015**, *58*, 62–64.
- [22] A. J. Zaddach, C. Niu, C. C. Koch, D. L. Irving, *JOM* **2013**, *65*, 1780–1789.
- [23] M. Shih, J. Miao, M. Mills, M. Ghazisaeidi, *Nat Commun* **2021**, *12*, 3590.
- [24] T. M. Smith, M. S. Hooshmand, B. D. Esser, F. Otto, D. W. McComb, E. P. George, M. Ghazisaeidi, M. J. Mills, *Acta Materialia* **2016**, *110*, 352–363.
- [25] W. Cai, W. D. Nix, *Imperfections in Crystalline Solids*, Cambridge University Press, Cambridge, **2016**.
- [26] D. Caillard, J. L. Martin, *J. Phys. France* **1989**, *50*, 2455–2473.
- [27] J. Kacher, B. P. Eftink, B. Cui, I. M. Robertson, *Current Opinion in Solid State and Materials Science* **2014**, *18*, 227–243.
- [28] D. Oliveros, A. Fraczkiewicz, A. Dlouhy, C. Zhang, H. Song, S. Sandfeld, M. Legros, *Mat. Chem. Phys.* **2021**, *272*, 124955.
- [29] J. Friedel, in *Les Dislocations*, Gauthier-Villars, Paris, **1956**.
- [30] J. Friedel, in *Dislocations and Mechanical Properties of Crystals*, Wiley, New York, USA, **1957**, p. 330.
- [31] B. Escaig, Doctoral thesis No A 382, Université d’Orsay, **1968**.
- [32] B. Escaig, *J. Phys. France* **1968**, *29*, 225–239.
- [33] T. Rasmussen, K. W. Jacobsen, T. Leffers, O. B. Pedersen, S. G. Srinivasan, H. Jónsson, *Phys. Rev. Lett.* **1997**, *79*, 3676–3679.
- [34] H. Idrissi, L. Ryelandt, M. Veron, D. Schryvers, P. J. Jacques, *Scripta Materialia* **2009**, *60*, 941–944.
- [35] W. Cai, V. V. Bulatov, J. Chang, J. Li, S. Yip, in *Dislocations in Solids*, Elsevier, **2004**, pp. 1–80.
- [36] J. Friedel, *Dislocations*, Pergamon Press, Great Britain, **1964**.
- [37] F. D. León-Cázares, C. M. F. Rae, *Crystals* **2020**, *10*, 445.
- [38] S. M. Copley, B. H. Kear, *Acta Metallurgica* **1968**, *16*, 227–231.
- [39] B. Beausir, J.-J. Fundenberger, *ATEX*, Université De Lorraine, Metz, France, **2017**.
- [40] M. Tang, W. Cai, G. Xu, V. V. Bulatov, *Modelling Simul. Mater. Sci. Eng.* **2006**, *14*, 1139–1151.
- [41] M. Verdier, M. Fivel, I. Groma, *Modelling Simul. Mater. Sci. Eng.* **1998**, *6*, 755–770.
- [42] G. Saada, *Microscopie électronique des lames minces cristallines*, Masson Paris, **1966**.

- [43] P. Veyssiere, *ISIJ International* **1991**, 31, 1028–1048.
- [44] S. H. Oh, D. Kiener, G. Dehm, M. Legros, P. Gruber, *Microscopy and Microanalysis* **2007**, 13, 278–279.
- [45] S. Huang, W. Li, S. Lu, F. Tian, J. Shen, E. Holmström, L. Vitos, *Scripta Materialia* **2015**, 108, 44–47.
- [46] H. Fujita, T. Mori, *Scripta Metallurgica* **1975**, 9, 631–636.
- [47] J. B. Cohen, J. Weertman, *Acta metall.* **1963**, 11, 996–998.
- [48] B. C. De Cooman, Y. Estrin, S. K. Kim, *Acta Materialia* **2018**, 142, 283–362.
- [49] J. Liu, C. Chen, Y. Xu, S. Wu, G. Wang, H. Wang, Y. Fang, L. Meng, *Scripta Materialia* **2017**, 137, 9–12.
- [50] Z. Yan, Y. Lin, *Mater. Sci. Eng. A* **2018**, 734, 224–228.
- [51] S. Xu, L. Xiong, Y. Chen, D. McDowell, *Crystals* **2017**, 7, 120.

Chapter 4

DISLOCATION MOVEMENT IN THE LOCAL ATOMIC LANDSCAPE

The last chapter focused on dislocation behaviour and plasticity mechanisms activated at room and cryogenic temperatures. This chapter will focus on the various factors that modify or regulate specifically the movement of dislocations in CoCrFeMnNi alloy, several of which were briefly mentioned in Chapter 3 – all directly related to the local atomic landscape, and observable during *in situ* TEM straining.

1. Dislocation movement

Under the influence of a certain τ , dislocations move forward. They do so, not with a smooth displacement, but in what has been defined as “jerky” or “sluggish” motion (which has suggested high lattice friction ^[1,2]). This jerky motion of dislocations is presented in this work as “jumps”. These jumps are evidenced during *in situ* TEM straining as dislocations moving forward, then pausing over a certain time, and then “jumping” into a new position.

To understand the significance of these jumps, an array of dislocations moving in pile-ups were chosen, both at RT and at LN₂T, and the distance of their jumps was calculated. Figures 1 and 2 present these dislocations. Their movement was tracked in time, and the figures present this in the following manner: the chosen dislocation is highlighted in black, each jump the dislocation makes is marked in hues of red (followed by yellow and green when pertinent).

Examples of the jumps are presented in Supplementary Video 6, and the results obtained from the time track movement in the figures is shown in Table 4-1.

Table 4-1 – Jump distances for dislocations in various systems at both Temperature ranges (calculated from Figure 4-1 and Figure 4-2). In grey shadow, calculations at RT; LN₂T in white.

Image	Sample	T (K)	Slip System	Dislocation identification	d (left/up) (nm)	d (right/down) (nm)	Δd (nm)	Δt (s)
4-2 (a)	X1_24	293	$(\bar{1}\bar{1}1)[0\bar{1}1]$	Dislocation 1: Last (upper pile-up)	34 ± 5	65 ± 5	49	73
					38 ± 5	55 ± 5	46	94
					53 ± 5	50 ± 5	52	45
					32 ± 5	32 ± 5	32	40
					19 ± 5	5 ± 5	12	25
					32 ± 5	66 ± 5	49	26
					37 ± 5	31 ± 5	34	34
					21 ± 5	27 ± 5	24	45
					32 ± 5	32 ± 5	32	54
					37 ± 5	37 ± 5	37	45
				Dislocation 2: First (bottom pile-up)	76 ± 5	55 ± 5	66	73
					31 ± 5	36 ± 5	33	94
					11 ± 5	27 ± 5	19	45
					5 ± 5	5 ± 5	5	40
					5 ± 5	5 ± 5	5	25
					11 ± 5	5 ± 5	8	26
					79 ± 5	53 ± 5	66	34
					3 ± 5	5 ± 5	4	45
					81 ± 5	53 ± 5	67	54
					81 ± 5	76 ± 5	79	45
				Dislocation 3: Middle (bottom pile-up)	50 ± 5	59 ± 5	55	73
					17 ± 5	5 ± 5	11	94
					5 ± 5	29 ± 5	17	45
					32 ± 5	0 ± 5	16	40
					32 ± 5	66 ± 5	49	25
					27 ± 5	38 ± 5	32	26
					54 ± 5	29 ± 5	41	34
					5 ± 5	0 ± 5	3	45
					48 ± 5	53 ± 5	50	54
				4-2 (b)			$(\bar{1}\bar{1}1)[011]$	Dislocation 4: Last
169 ± 9	689 ± 9	429	6					
646 ± 9	103 ± 9	374	25					
Dislocation 5: Second to last	355 ± 9	473 ± 9	414					11
	532 ± 9	453 ± 9	492					6
				79 ± 9	110 ± 9	95	25	

<i>(Continuation)</i>								
Image	Sample	T (K)	Slip System	Dislocation in pile-up	d (left/up) (nm)	d (right/down) (nm)	Δd (nm)	Δt (s)
4-2 (c)	X1_21	293	$(\bar{1}11)[0\bar{1}1]$	Dislocation 6: Last	181 ± 10	186 ± 10	183	12
					112 ± 10	94 ± 10	103	27
4-2 (d)	X1_23	293	$(\bar{1}\bar{1}1)[0\bar{1}\bar{1}]$	Dislocation 7: Last	164 ± 5	181 ± 5	172	93
					108 ± 5	120 ± 5	114	63
				Dislocation 8: Second to last	85 ± 5	174 ± 5	129	93
					337 ± 5	282 ± 5	309	63
4-1 (a)			$(\bar{1}\bar{1}1)[011]$	Dislocation 1: First	157 ± 2	150 ± 2	153	8
					82 ± 2	81 ± 2	81	6
					96 ± 2	76 ± 2	86	4
					39 ± 2	57 ± 2	48	6
4-1 (b)	35/I2-Head22	96	$(\bar{1}\bar{1}1)[\bar{1}10]$	Dislocation 2: Last	193 ± 6	142 ± 6	168	7
					0 ± 6	82 ± 6	41	5
					207 ± 6	193 ± 6	200	4
					314 ± 6	236 ± 6	275	7
					231 ± 6	264 ± 6	248	26
					218 ± 6	151 ± 6	184	16
					173 ± 6	150 ± 6	162	19
					111 ± 6	104 ± 6	107	21
					150 ± 6	200 ± 6	175	17
139 ± 6	181 ± 6	160	11					
4-1 (c)	X1_21	102	$(\bar{1}11)[0\bar{1}1]$	Dislocation 3: Last	102 ± 9	141 ± 9	121	3
					45 ± 9	105 ± 9	75	13
					102 ± 9	48 ± 9	75	15
				Dislocation 4: Second to last	148 ± 9	139 ± 9	144	3
					140 ± 9	152 ± 9	146	13
					102 ± 9	82 ± 9	92	15
4-1 (d)	X1_29	109	$(\bar{1}\bar{1}\bar{1})[011]$	Dislocation 5: Middle	31 ± 4	80 ± 4	56	25
					76 ± 4	68 ± 4	72	30
					80 ± 4	68 ± 4	74	43
					4 ± 4	56 ± 4	30	36
					52 ± 4	69 ± 4	61	85
4-1 (e)			$(111)[\bar{1}10]$	Dislocation 6: Last	131 ± 22	819 ± 22	475	37
					694 ± 22	246 ± 22	470	30

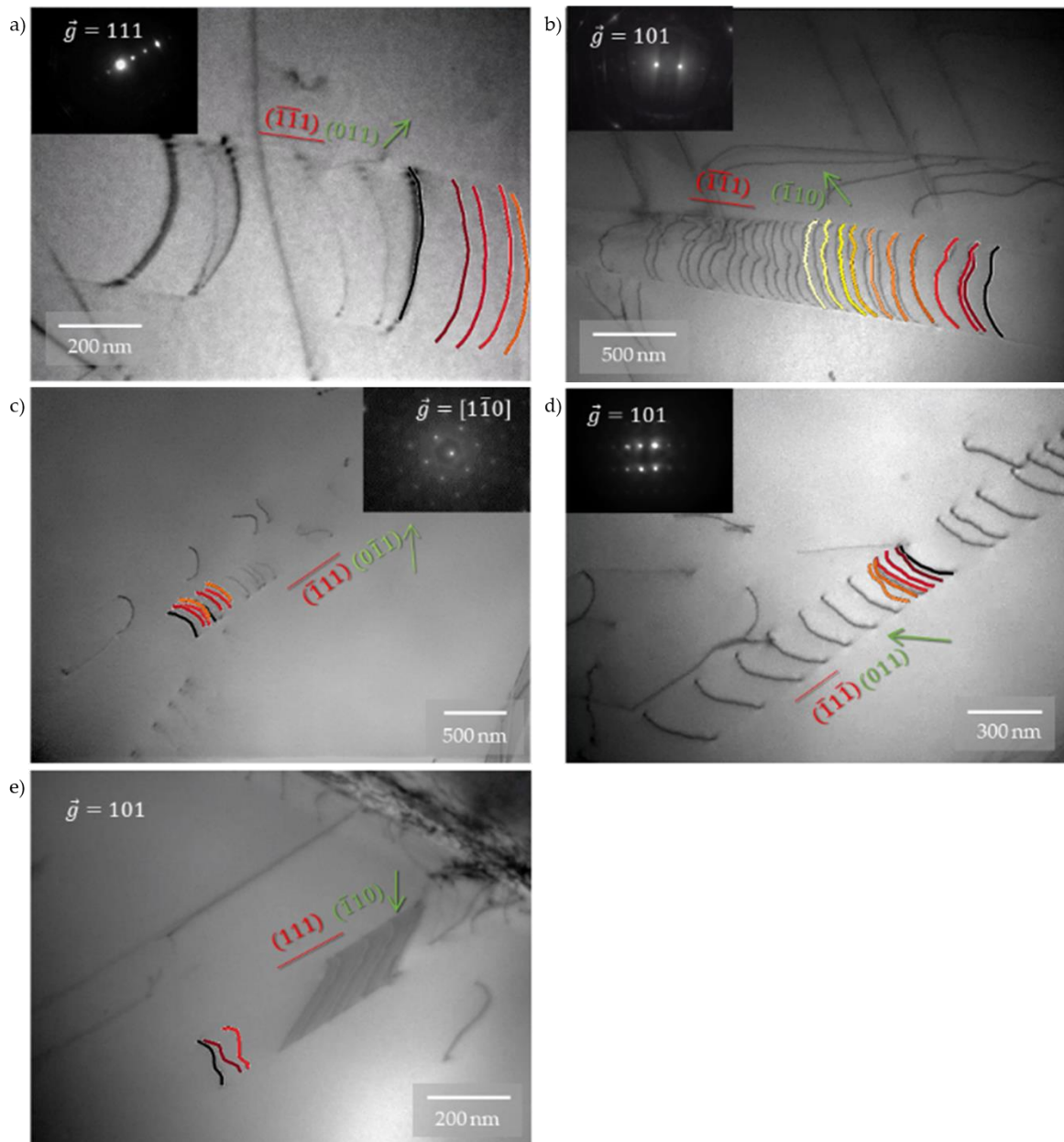


Figure 4-1 – Time track of dislocations jumps at LN₂T. Specimens: a) and b) 35/I2-Head22, c) X1-21, d) and e) X1-29.

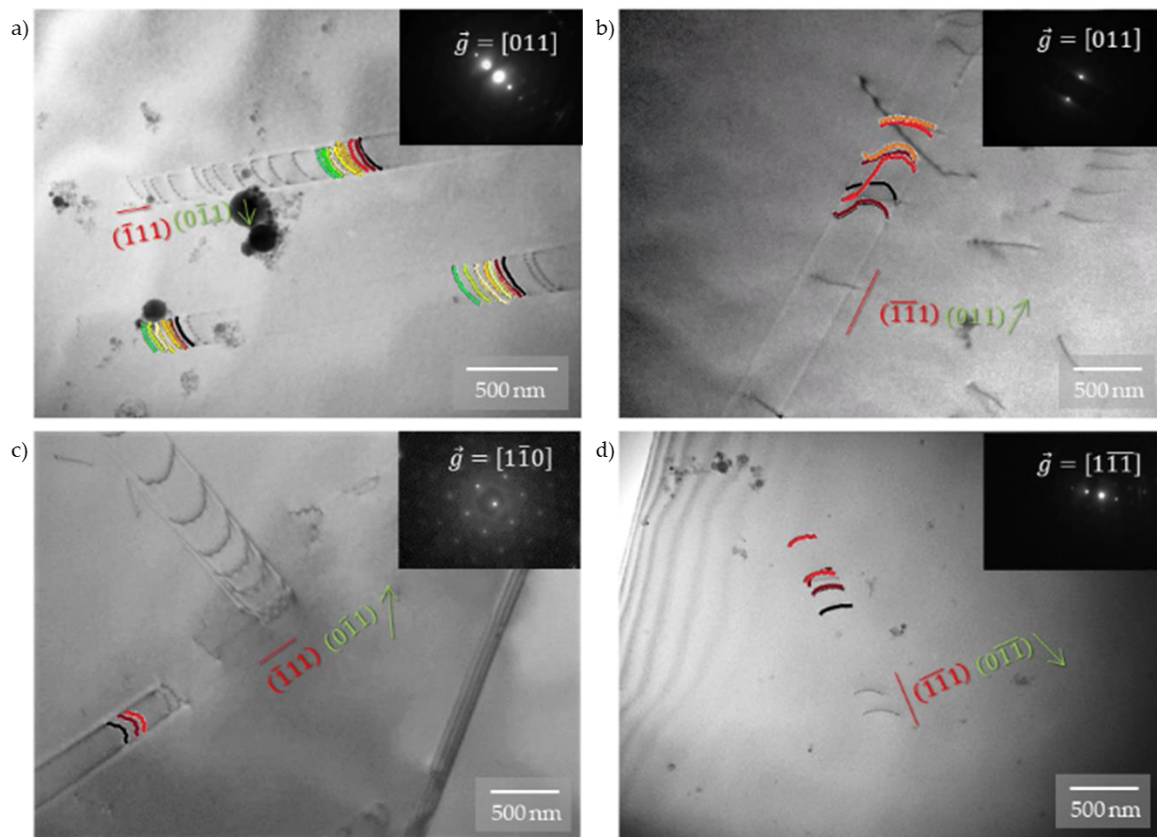


Figure 4-2 – Time track of dislocations jumps at RT. Specimens: a) X1-24 and b) X1-21, c) X1-23, d) X1-24.

The chosen dislocations for this calculation were perfect dislocations belonging to a “loose” pile-up (to be able to distinguish an individual dislocation, follow it and measure its distance). Once a loose pile-up was identified in a video sequence of an *in situ* TEM straining experiment, a single dislocation of said pile-up is chosen (notably, one that stays in the frame of the video for a certain duration). In a few cases, more than one dislocation was chosen from a pile-up or group of pile-ups in frame in a given sequence (as is the case of Figure 4-1(c) and Figure 4-2(a), (b) and (d)).

The selected dislocation moves forward and pauses, repeating this process several times. Still frames of the sequence were extracted for each “jump” (when the dislocation changes position, either by one or both extremities): the time difference between still pictures corresponds to the pause time.

Masks of the selected dislocations were obtained for each still frame (using Automated Dislocation Detection, by the MuDiLingo ERC project team in Forschungszentrum Jülich GmbH, Germany). The masks for a single dislocation were coloured with colour gradients from black to green (depending on how many still frames conformed a sequence), and superposed onto the TEM image at the start of the movement. Once the composed images

were built (as presented in the previous Figures), the distance between each mask (each “jump”) was measured.

Both Figures and the calculations presented in the Table indicate that dislocations move forward a bigger distance when strained at cryogenic temperatures, with a shorter time pause between jumps.

A further analysis of these movements was carried out and it is presented in Figure 4-3. When comparing the jump distance vs. pause time for each dislocation, it is clear that:

- They advance in sequences of “plateau”-like motion (parts (a) and (c) of the figure).
- The “plateaus” (jump distances) have an apparent periodicity within the movement of a single dislocation, especially when it is part of a denser pile-up. This is evidenced, for example, in the movement of dislocations 1 and 3 (RT, part (a) of the figure) and of dislocations 2 and 5 (LN₂T, part (c) of the figure). Table 4-1 shows that the values of each jump for each of these dislocations are at regular intervals.
- The jumps are shorter when the dislocation is part of a denser pile-up, if it is not the first or last dislocation of the pile-up, or if there are more pile-ups gliding in the vicinity of the one it belongs to. This means that the interaction with other dislocations affect the movement / distance covered by the selected dislocation.
- The mean distance for a jump at RT is 109 nm, and at LN₂T it is 129 nm (parts (b) and (d) of the figure).
- The mean pause times for a jump are $\bar{\Delta t}_{RT} = 45$ s vs. $\bar{\Delta t}_{LN_2T} = 19$ s.
- Dislocations seem to move to specific positions. Please refer, for example, to the case shown in part (b) of Figure 4-1: the selected dislocation (black mask) moves over time to positions that coincide with the position of other dislocations in the pile-up (the successive masks overlap with the dislocations in the TEM image). This seems to suggest that there is a pathway of atoms that block or permit the passage of dislocations (linked to chemical fluctuations), and this pathway changes with the temperature, suggesting that these chemical fluctuations act as obstacles to dislocation movement.

As presented in the last sections of Chapter 1, the lattice in the CoCrFeMnNi alloy is distorted by chemical fluctuations. It is the behaviour of dislocations traversing this distorted atomic landscape that will reveal what is happening in the crystal. In light of this, different questions arise from the above results: why do dislocations jump? And how does temperature influence the jumps (longer distance / shorter time)?

A possible explanation for the dislocations behaviour in CoCrFeMnNi is given by the solid solute strengthening (SSS) theory, which can be divided in two categories:

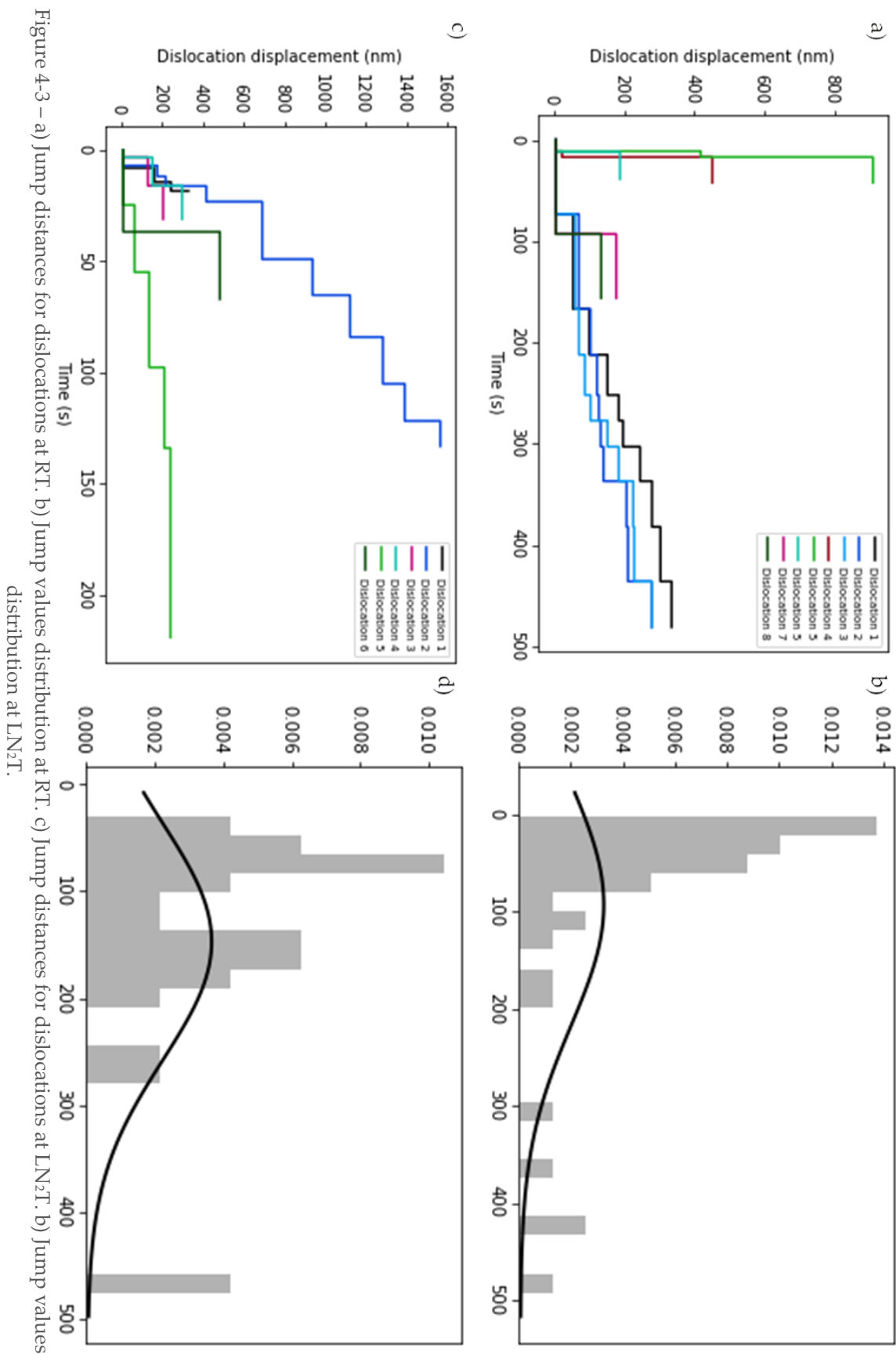


Figure 4-3 – a) Jump distances for dislocations at RT. b) Jump values distribution at RT. c) Jump distances for dislocations at LN₂T. d) Jump values distribution at LN₂T.

- The strong pinning model: proposed by Friedel and Fleischer ^[3-5] (henceforth FF), it treats the solutes as individual point obstacles that pin the dislocations, which then bow out in the regions between the solutes and can break out from these obstacles upon increasing stress.
- The weak pinning model: proposed by Mott and Labusch ^[6-8] (henceforth ML), it considers the collective effect of a field of randomly distributed solute fluctuations lowering the dislocation energy. For the dislocations to escape these fluctuations, an additional shear stress is necessary to increase the yield strength.

Leyson and Curtin ^[9] studied the transition between the FF and the ML models as a function of temperature and solute concentration, concluding that ML better describes the phenomena in concentrated solid solutions.

Recent studies ^[10-13], using molecular dynamics (MD) simulations, have reported a non-uniform structure of the dislocation line with a variable dissociation distance along the line, between Shockley partial dislocations. This usually is associated with local composition fluctuations that strongly affect the local values of stacking fault energy, inducing a local phase instability.

Many simulation studies have been done to link the plastic deformation behaviour to the local chemical fluctuations (LCF) in HEAs (see ^[14,15]), as they cause the variation of local generalized stacking fault energy and lattice resistance. Tuning LCFs is reported to improve the strength and ductility in these alloys (see ^[16,17]). The influence of local chemical fluctuations (LCF) on the behaviour of dislocations is exemplified in several studies:

- Osetsky and Morris ^[18] (through MD in a random NiFe fcc alloy), who showed that low stacking fault energies allow partial dislocation lines to adopt a minimum energy configuration with a maximum concentration of Ni atoms. They also noted that the changes in Ni/Fe ratio and SF width occur in both directions –increasing or decreasing, reflecting only the event that the dislocation changed its current location due to a jump into the new local minimum energy configuration. They conclude that the process of dislocation motion in concentrated alloys consists of three repeating main stages:
 1. a moving dislocation reaches a local minimum energy configuration, where it is relatively pinned;
 2. stress accumulates until there is sufficient elastic stress to overcome the local energy barrier;
 3. dislocations quickly glide towards the next available minimum energy configuration.

- Li et al. ^[19] (MD in NiCoFe and NiCoFeCu fcc CSSAs), who observed that the SF widths in both alloys varied significantly along the dislocation line rather than remain constant, due to the local fluctuations of SFE induced by fluctuations in the local concentration in both equiatomic solid-solution alloys (this is in agreement with the results of Smith et al. ^[13], and to the results obtained on this work, for example, in Figures 3-14 and 3-19 of Chapter 3). Due to the random nature of atom distributions in both alloys, the solid solution energy barrier that the dislocation has to overcome for motion varies as the dislocation moves. In their simulations, after a short movement, if the solid solution energy barrier is too high for the dislocation to overcome the applied stress, the dislocation will stop.
- Yang et al. ^[20,21] (MD in Al_xCoCrFeNi alloy, previously studied experimentally by Xu et al. ^[22]), who describe the LCF and, to comprehend the reaction of dislocation and critical shear stress in different LCFs, proposed ^[21] applying a ladder-shape shear stress to six models with different atomic distributions (different LCFs) for each composition ($x=0, 0.1, 0.3$ and 0.5). The results based on dislocation displacement and time are shown in Figure 4-4. In this figure, all the displacement lines are composed of similar characteristics, including some flat regions or plateaus, abrupt increase in displacement and obvious serration usually happens during severe shear deformation. These plateaus correspond to immobile regions where the applied force is not large enough to overcome the lattice friction and move the dislocations. Once the applied force is sufficiently large, the dislocations are able to slip freely and there is an abrupt increase in dislocation displacement. Afterwards, the slipping dislocations may be stopped soon after in some regions with higher lattice friction than the current stress and another plateau will be shown in the displacement line. These two phenomena may happen alternately and dominate the early stage of deformation until the applied stress reaches the critical shear stress, at which the dislocations are completely free to slip.
- Utt et al. ^[23] (combination of *in-situ* TEM and atomistic simulations in CoCrFeMnNi alloy), who reported jerky glide of dislocations and associated it with the energetic landscape of pinning obstacles. Taking into consideration the randomness of atoms in CoCrFeMnNi, that could lead to lattice friction, they expected that the SFE surface vary based on local atomic arrangement. Dislocation mobility (Figure 4-5) is linked to the amount of pinning points and its strength. According to their models, the presence of both Co and Cr associated to Ni produces an increase in pinning point density and strength. They conclude that CoCrNi-enriched areas lead to more hindered paths and dislocation motion is jerkier in such areas.

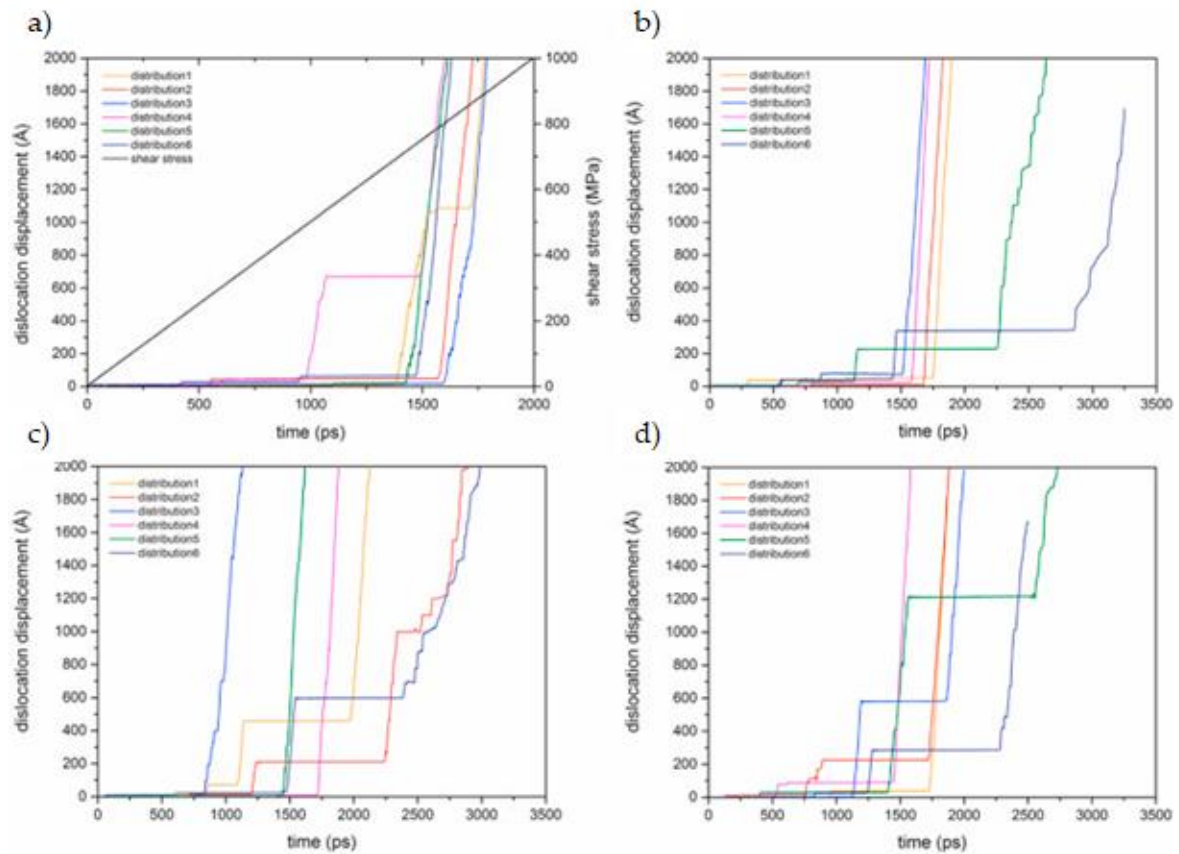


Figure 4-4 – Displacement lines for c) CoCrFeNi, d) $\text{Al}_{0.1}\text{CoCrFeNi}$, e) $\text{Al}_{0.3}\text{CoCrFeNi}$, f) $\text{Al}_{0.5}\text{CoCrFeNi}$ with different atomic distributions. Adapted from [21].

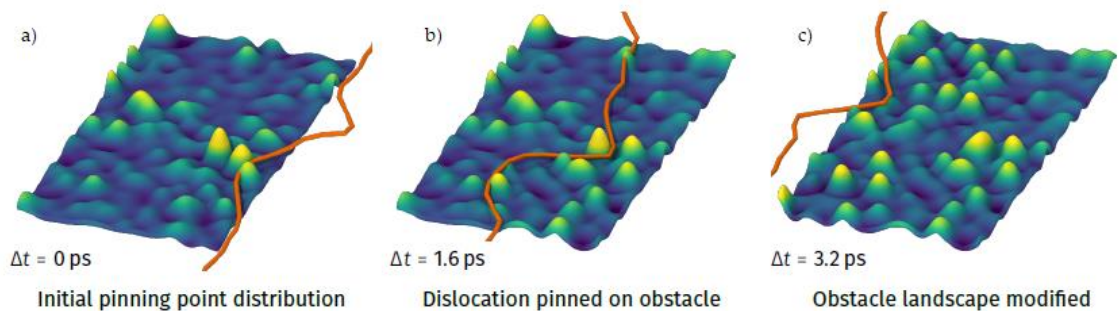


Figure 4-5 – A dislocation moving through its obstacle landscape, highlighting the pinning of the dislocation line. a) Proposed pinning point landscape around $x = -120$ Å, showing the initial configuration, b) a bowing out of the dislocation line due to pinning at the highest obstacle, and c) the modified dislocation pinning point landscape after the dislocation rearranged the local chemical environment. From [23].

Comparing the studies mentioned before to the results obtained by this work, a correlation can be found between the dislocations' motion in MD and what is seen during *in situ* TEM straining experiments: a dislocation move until it encounters a barrier (probably a LCF), it stops until the applied force is large enough for it to overcome the lattice friction and

move, and this steps are repeated over the covered distance, and, when plotted, the movement is “stair”-like, as in Figure 4-3(a) and (c) – this work, and Figure 4-4 – Yang et al. [21].

The local atomic landscape (LAL) of CoCrFeMnNi is conducive to enriched regions that could act as obstacles and others that have favourable shear bonds. These obstacles seem to be stronger at lower temperatures. This analysis is presented in the next section.

2. Obstacles

As already stated, the movement of dislocations is hindered by obstacles, which may be the origin of the LCFs and dislocation jumps. The pins could be second-phase particles, precipitates, or threading (sessile) dislocations [24]. The next figure (and Supplementary Video 7) exemplifies some of these cases.

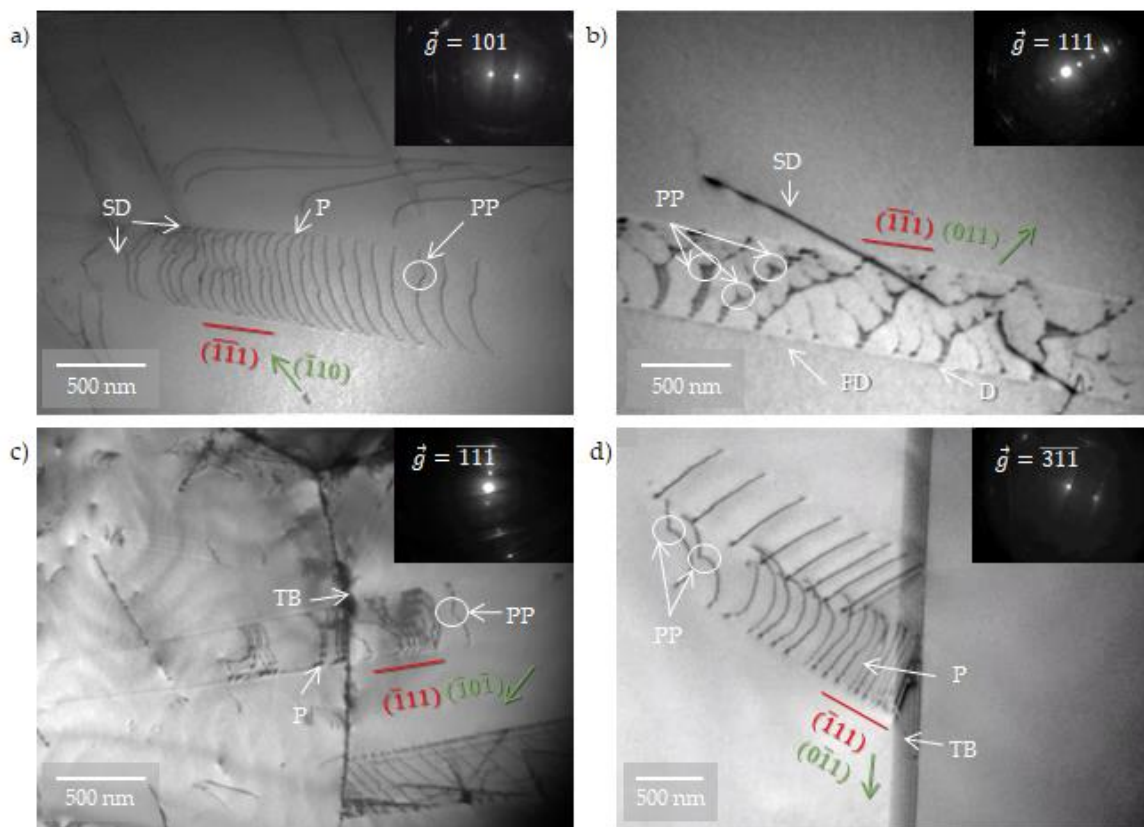


Figure 4-6 – Different examples of obstacles encountered by perfect (“P”) or dissociated (“D”) dislocations: pinning points (“PP”), sessile dislocations (“SD”), twin boundaries (“TB”), forest dislocations (“FD”). Obstacles can be detected as the curvature of the dislocation loop is distorted. a), b) and c) Specimen 35/I2-Head22, strained at $T = 96$ K. d) Specimen 35/I2-Head24, strained at $T = 293$ K. In red, the slip planes; in green, the Burgers vectors and their directions.

This section will be focusing on pinning points. The previous figure shows several pinning points (henceforth PP); let the focus be on the pile-up presented on part (a) of the figure (Figure 4-7).

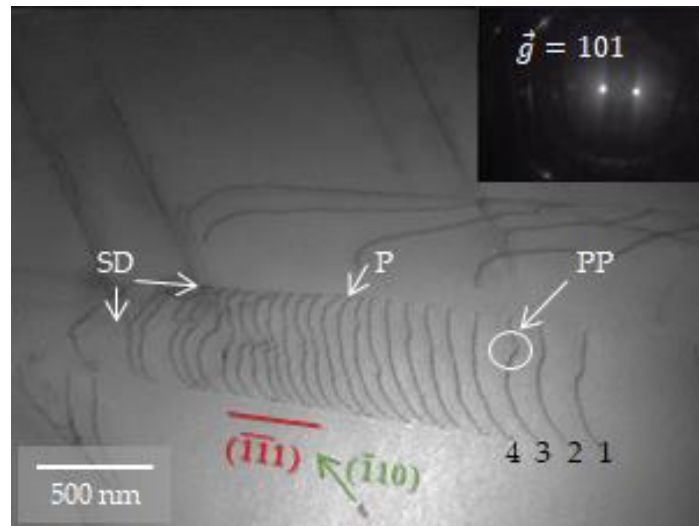


Figure 4-7 – Specimen 35/I2-Head22, strained at $T = 96$ K. In white, perfect dislocations “P”, sessile dislocations “SD” and pinning points “PP”; in black, identification of the dislocation position in the pile-up (for reference).

PPs are circled in white in the previous figures, curving the dislocation line (the one being anchored – dislocation 3 in the figure, for example), and seemingly also distorting the dislocations in proximity, as evidenced by the curvature of dislocations 2 and 1, which are not being pinned and present a change on their curvatures, nonetheless. The change in the curvature of the dislocation is characteristic of the presence of a PP, which blocks only a segment of the dislocation while the rest continues to move, getting curvier, until it reaches a stress large enough to overcome the obstacle and free itself, returning to a “smoother” curvature (as in the case of dislocation 4).

This process is better explained by Satoh et al. ^[25] as follows:

In an elementary process of dislocation-obstacle interaction, a gliding dislocation is pinned by obstacles and bows out to form arcs between the neighbouring pinning points, which induces cusps on the dislocation at obstacles. The apex angle of the dislocation cusp is referred to as the pinning angle φ . The dislocation breaks away by bypassing or cutting through the obstacle when the pinning angle reaches a critical value φ_c . Stronger obstacles have smaller critical angles. The obstacle strength factor $\alpha = \cos(\varphi_c/2)$ and the distance between the neighboring pinning points are the key parameters that relate the defect microstructure to the change in macroscopic mechanical properties. ^[25]

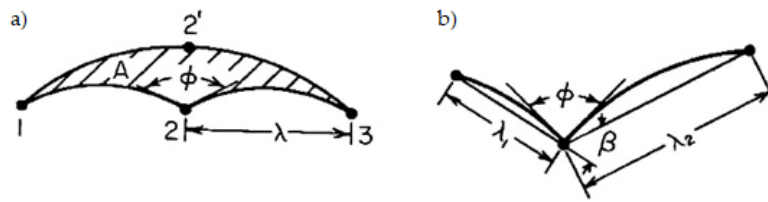


Figure 4-8 – a) A linear array of pins. Bowed out loop breaks pin at 2 and creates a new pin at obstacle 2'. b) A more general pin array. From [24].

Figure 4-8 presents the case where a dislocation is pinned by an obstacle. The balance of simple line tension of the dislocation and pinning force leads to the Orowan result (valid when the spacing λ is large compared to the size R of the obstacle and if the obstacles are equally spaced and in a straight line):

$$\tau_o = \frac{\mu b}{\lambda} \cos\phi$$

Equation 4-1 – Strength of an obstacle as a function of the line tension modification.

where τ_o is the shear stress on the glide plane, μ is the shear stress, λ is the obstacle spacing, and ϕ is the bow-out angle. Friedel [3,26] considered the more general arrangement of Figure 4-8(b). At steady state, the breaking of obstacle 2 in part (b) of the figure, on average, led to the formation of a new obstacle at 2'. In a simple line tension model, the radius of curvature of the dislocation line is $r = \mu b / \tau$. The work done by the applied stress is τb times the area swept ΔA [24]. Equating ΔA with the mean free path between particles, λ^2 , results in:

$$\tau_o = \frac{\mu b}{\lambda} \cos^4\left(\frac{\phi}{2}\right)$$

Equation 4-2 – Generalized case for the strength of an obstacle.

However, as these equations are only valid for obstacles that pin a dislocation in equally spaced segments (ideal case), experimentally it is not simple to calculate the strength of PPs, as obstacles pin the dislocation in (frequently) more than one segment and bow it out non-symmetrically. It is also important to correct the projected TEM image onto the real slip plane to obtain the real values of ϕ and λ (see Chapter 2 for the trigonometric reasoning).

Calculating the strength of a PP from *in situ* TEM still images is not an easy task. Consider the example presented in parts (c) and (d) of Figure 4-6, where specimens were strained at $T = 96$ K and $T = 293$ K, respectively. Figure 4-9 presents the measurements for each of

these examples (considering that λ_1' , λ_2' and ϕ' are projections, as stated above). Table 4-2 gives the resulting τ_o at both temperatures, calculated using Equation 4-2.

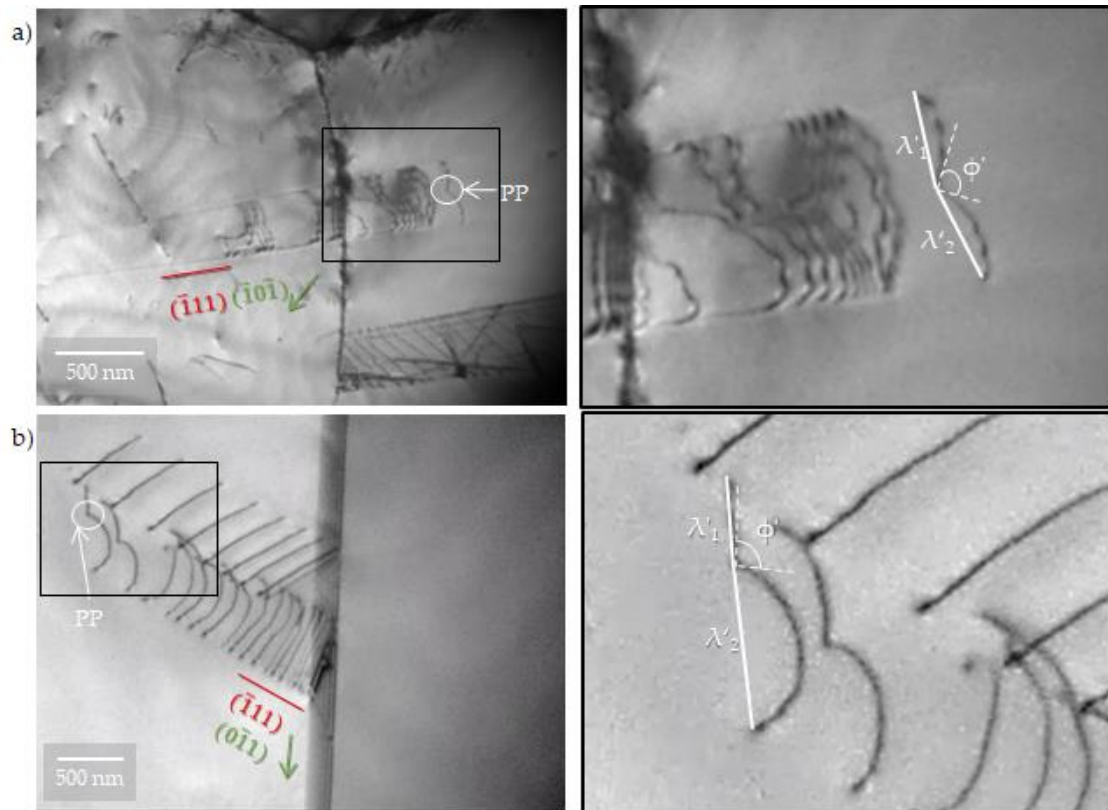


Figure 4-9 – Angles of curvatures due to pinning points at: a) cryogenic temperature, b) room temperature. The inserts are magnifications of the black frames in their respective images (1:3 scale).

Table 4-2 – Pinning point strength calculation (using Equation 4-2).

	b (nm) ¹	μ (GPa) ²	ϕ (°)	λ_1 (nm)	λ_2 (nm)	$\Delta\lambda$ (nm)	τ_o	
							(MPa)	(μb^2)
RT	0.254	80	131	300 ± 6	534 ± 6	417 ± 6	1.4 ± 0.4	0.0003
LN₂T	0.255	85	119	272 ± 6	310 ± 6	291 ± 6	4.8 ± 1.3	0.0009

¹ From [27].

² From [28].

PPs were not only present in the above examples. They were observed during the majority of *in situ* TEM straining experiments, both at RT and at cryogenic temperatures. They appeared to be either fewer in number or easier to overcome at RT than at LN₂T (please compare the last supplementary video to Supplementary Video 8), seeming to suggest that temperature plays a role in strengthening PPs, which is not accounted for in the previous equations.

The results in the table above were calculated using the $\Delta\lambda$ values, as the PPs are not in the ideal position (middle of the dislocation loop, bending the dislocation into two equal segments). This alone introduces an error into the results given by Equation 4-2 (hence the large error in the results). The tendency of τ_0 is, however, noteworthy: the strength of the PP at 96 K is approximately three times larger than at 293 K, allowing to conclude that PPs at cryogenic temperature are indeed stronger than at RT.

As stated in Oliveros et al. [29],

Because pinning points act similarly on partial or perfect dislocation, they, combined with a low SFE, will equally pin the leading and trailing partials of dissociated dislocations... A random orientation of the applied shear will favour the motion of the two partial dislocations of a dissociated perfect dislocation in the same direction (please refer to the blue region in Figure 3-26 of Chapter 3). This combined action of the stress on a pair of dislocations favours the overcoming of an obstacle. In the case where the stress acts to separate the dislocations, the stacking fault will pull the two partial dislocations together. In this context weak obstacles will not separate these partial dislocations. However, if obstacles become stronger, as it seems to be the case at low temperature, the probability that the trailing partial is retained by one of them increases. This will favour the dissociation and the development of long stacking faults and twins in the crystal as the deformation proceeds [1].

Again, a possible explanation accounting for PPs is the LCF (considered to influence dislocation multiplication and motion [16,17,30,31]). To elaborate on this notion, and in the frame of the MuDiLingo ERC project, Zhang et al. [32] started a completely new approach in which the dislocations are used as probes and their movements and curvature may "image" the local crystalline and chemical landscape. Even non detectable precipitates or defects (such as a forest dislocations) may appear through a change of curvature or a non-homogeneous motion through the alloy.

A comprehensive topological study of pinning points was carried out on the 35/I2-Head22 specimen shown in Supplementary Video 7 and in Figure 4-7 (strained at $T = 96$ K, by the MuDiLingo ERC team in France). Approaches (made by the MuDiLingo ERC team in Germany) including data-mining and reconstruction of the dislocation microstructure in 3D from the TEM image (Figure 4-10) were involved (see their study for the methods).

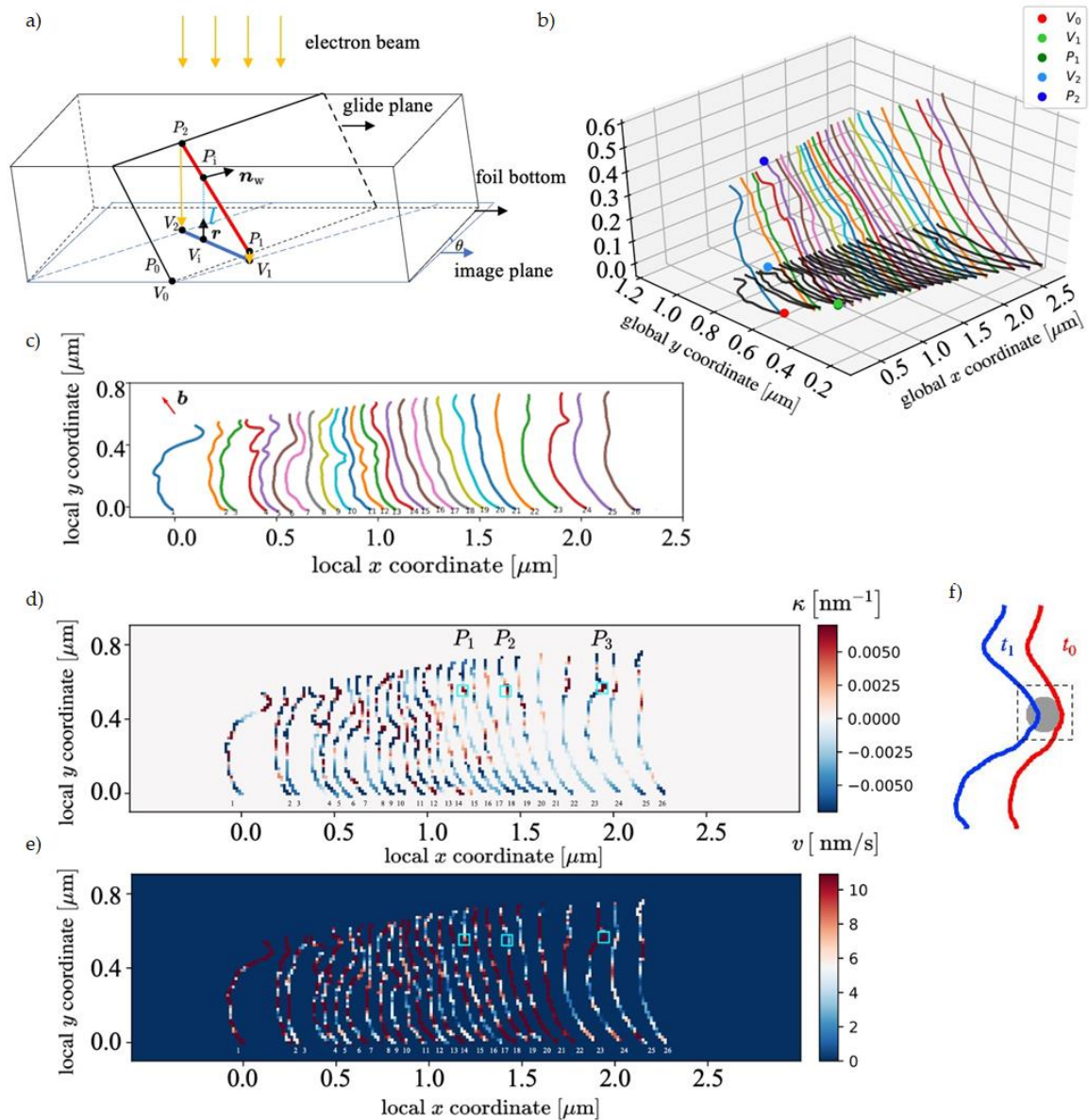


Figure 4-10 – a) Schematic showing the planar and linear feature in a foil projected on the image plane. b) A 3D plot of the piled-up dislocations of Figure 4-7 in the world coordinate system. c) Distribution of the piled-up dislocations on the $(\bar{1}\bar{1}\bar{1})$ slip plane. The red arrow represents the direction of the Burgers vector. d) Schematic of dislocation velocity calculation. e) Coarse-grained dislocation velocity calculated based on data in two frames; cyan boxes indicate position of PPs. f) Schematic of dislocation geometry around the local pinning point, showing two different configurations of dislocation at different times. Adapted from [32].

In HEAs, and unlike other types of obstacles (such as particles of different phases), pinning points due to LCF may not be directly visible during the TEM observations. Nevertheless, their effect on dislocation curvature is clear, as already stated. For this reason, Zhang et al. [32] assume that high curvature regions along a dislocation are potential locations for PPs. In view of this, they identified three possible PPs in the considered pile-up, calculating the dislocation curvature when the dislocation moves around an “effective zone” close to the

PP (Figure 4-10(f)). These possible PPs are indicating using a cyan box in parts (d-e) of the figure.

Adapting Equation 4-2, they calculated the strength of each of the three PPs identified (which they called P_1 , P_2 and P_3), also taking into consideration that, because they are in a pile-up, dislocations experience the influence of other dislocations. They computed the strength evolution (based on the bending angle evolution), showing that for P_1 and P_2 , the passing of a dislocation slightly increases the strength, and the inverse is true for P_3 . This result is shown in Figure 4-11, where the fluctuation of the strength evolution is evident. Also, comparing the values shown in the figure to the values calculated in Table 4-2 (even though they are not the same pinning points), the results prove that this novel method is more accurate than the results obtained from Equation 4-2.

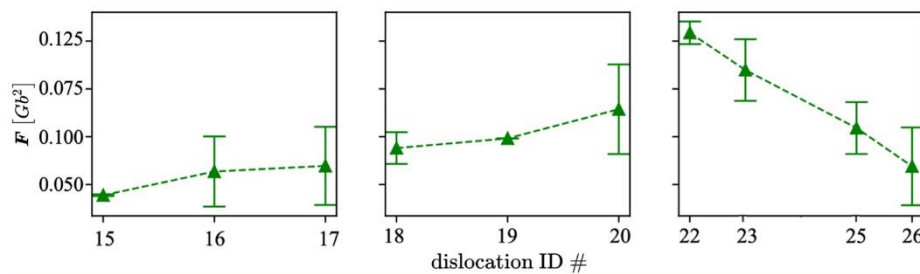


Figure 4-11 – Strength of the local pinning point estimated by different dislocations passing-by. The rough locations are marked with cyan boxes in Figure 4-10(e). From left to right, P_1 , P_2 , and P_3 ; the time spans corresponding to their strength changes are 1.3-14.2s, 14.4-24.5s, and 0-23.6s, respectively. Adapted from [32].

To access the 4th dimension (time) of the experiment, Zhang et al. [32] performed a spatio-temporal coarse graining of the dislocation microstructure through their shape change (local line curvature) and their velocity. These are the two “signals” received through the moving dislocations. The results are shown in Figure 4-12, an observation on how the average curvature and velocity vary along the x direction.

In Figure 4-12(b), the curvature at the head of the pile up is higher in average (dislocations are more bent under higher stress, as should be in a pile-up), and decreases from the head to the tail. Exceptions happen when there are local PPs, identified in part (a) of the figure. As seen from parts (a) and (c) of the figure, areas with a higher curvature difference in the dislocations’ lines coincide with higher velocity areas (see, for example, regions I and IV). Close to an isolated PP, there should be a fluctuation in the velocity due to the pinning-depinning mechanism, as shown on the right of region III and the left of region IV; by contrast, in region II, the velocity is reduced to almost a constant value, and the velocity increment in region I corresponds to dislocations interacting with sessile dislocations

acting as obstacles (Figure 4-7 and Supplementary Video 7). This indicates that regions III and IV are a pinning point-rich regions where dislocation are frequently pinned ^[32].

In CoCrFeMnNi, contrary to conventional solute-hardened alloys, the effective strength of the pinning points (lattice distortion from local ordering) may evolve in a “random” manner. Some pinning points are hardened while others are weakened, as different atomic bonds are broken and reconstructed by dislocation glide ^[32]. As in metallic materials, the bonding is principally mediated by electrons shared by the atoms, although some covalent bonds may also be present, the ensuing atomic interactions are short-ranged because of the screening provided by the shared electrons ^[33].

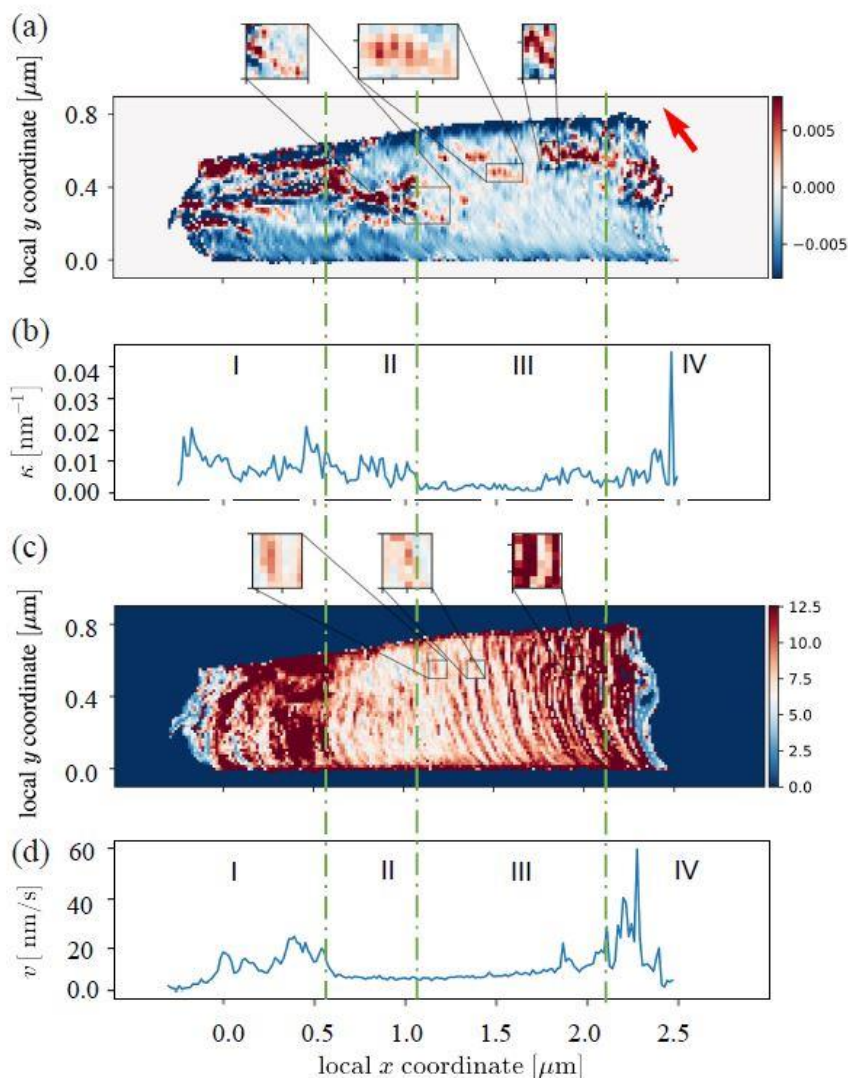


Figure 4-12 - Spatial-temporal averaging of curvature and velocity based on still images taken from Supplementary Video 7. a) Distribution of curvature with a pixel size of 15 nm. b) The average of the curvature along the y -axis. c) Distribution of velocity with a pixel size of 15 nm. d) The average velocity along the y -axis. From ^[32].

The cohesive energy for atomic bonds is the lowest for Mn-pairs (Mn-Mn, Mn-Cr, Mn-Co, Mn-Ni, Mn-Fe; all < 0.122 eV) and the highest for Fe-pairs (Fe-Fe, Fe-Ni, Fe-Co, Fe-Cr; all > 0.227 eV), with high cohesive energy also for Ni-Ni (0.230 eV) and Ni-Co (0.229 eV) pairs (the values for the cohesive energy were calculated in modelling by Gröger et al. [33], adapting the long-range Lennard-Jones potential. Due to the randomness of the alloy, they determined through their model that 80% of nearest neighbour bonds are between unlike elements [33]). The CoCrNi-enriched areas proposed by Utt et al. [23] as high-pinning zones have an approximate cohesive energy of 0.227 eV (assuming a equimolar distribution of elements in the alloy – as is the case, this value was calculated as the average of the pairs-cohesive energy from the values of Gröger et al. [33]).

Thus, when dislocations recreate Mn-bonds, the possible pinning-point is weakened until a new dislocation recreates a stronger bond; and when dislocations encounter a Fe-bond or a Ni-Co bond, for example, the former will present a stronger obstacle to its movement. The stronger-bonded LAL forming a pinning-point-enriched area also confirms the existence of LCFs in the CoCrFeMnNi alloy.

To explore the underlying reasons for dislocation pinning, Bu et al. [34] chose the bcc HfNbTiZr HEA to perform *in situ* TEM straining and STEM post-mortem characterization, to analyse the pinning points in their specimen. Even though the mechanisms behind the behaviour of fcc pinning points vs. bcc pinning points are different, their results can help visualise what happens in an fcc alloy with a high LCF region. Figure 4-13, a HAADF-STEM image, shows that enrichment of heavy Hf and/or Nb elements leads to an abrupt rise of contrast intensity in the Z-sensitive image, revealing the existence of local chemical inhomogeneity at the pinning point. Bu et al. [34] performed geometric phase analysis (GPA), which shows that the inhomogeneous distribution of those heavy elements will lead to a local lattice strain fluctuation due to the mismatch of the atomic radius.

These authors, attributed the pinning in the HfNbTiZr HEA to the interaction between dislocations and chemical fluctuations [34]. Such pinning effect is similar to the de-trapping events of nanoscale segments induced by LCF, which have been revealed by molecular dynamic methods in fcc [35] and bcc [36] HEAs. A more suitable example is presented by Li et al. [35], where they modelled the LCFs in a CoCrNi fcc MPEA through MD simulation.

In their simulation, Li et al. [35] present the LCF for specimens annealed at different T_a , measuring the LCF by the pairwise multicomponent short-range order parameter (see their methods for this calculation). Figure 4-14 presents their results. In part (a) of the figure, they suggest that their model CoCrNi system develops local Ni segregation and Co–Cr ordering with decreasing T_a . They compare their results using embedded-atom

method (EAM) model to previous DFT results ^[15,37] on the same alloy; both methods capture the Co–Cr ordering, which is consistent with the equilibrium phase diagram to form Co–Cr intermetallic phase ^[38]. The increase of LCF with decreasing T_a indicates deviations from the configurational entropy of an ideal solution $S_{c,ideal}$, which is shown in part (b) of the figure. Li et al. ^[35] report that a HEA rarely reaches $S_{c,ideal}$ ($\sim 95\%$ at $T_a = 1650$ K). With decreasing T_a , S_c turns away from $S_{c,ideal}$ fairly early and loses half of its magnitude when LCFs becomes obvious. As such, they conclude that a truly random SS is only an extreme state of HEAs and difficult to reach in practice, and that a HEA at a given composition possesses partial chemical order.

Parts (c) to (e) of the figure show three representative atomic configurations that show nanoscale Ni clusters and interconnected Co–Cr clusters with relatively random compositions and orientations. Randomly distributed Ni nanoscale precipitates break up the Co–Cr domains into finer regions. This LCF persists across the T_a range Li et al. ^[35] examined up to $T_a = 1650$ K. They highlight that, when kinetically permitted, all the HEAs evolve toward the ground state, and that the partially ordered system is actually the norm for single-phase HEA solutions ^[35].

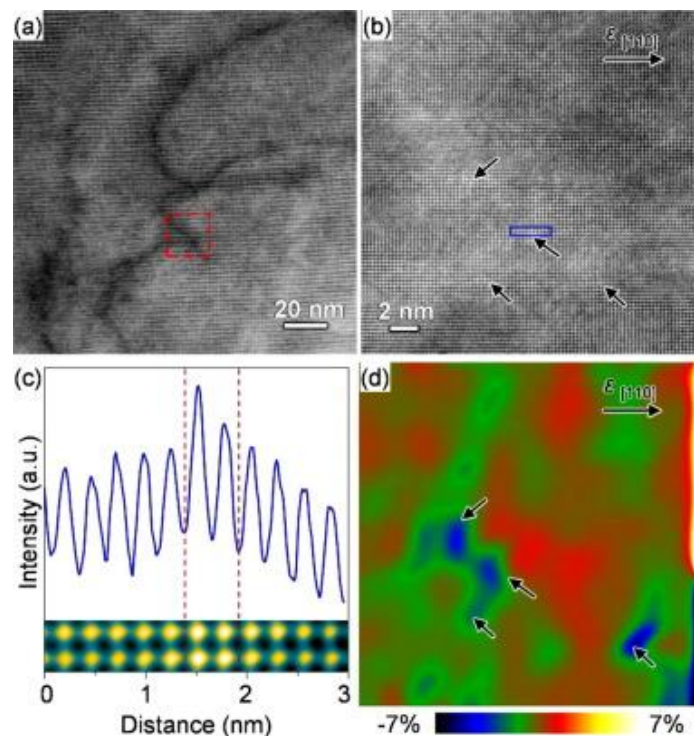


Figure 4-13 – LCF induced pinning. a) A low-magnification BF-STEM image of a pinned dislocation. b) The high-resolution HAADF-STEM image corresponding to the square area in (a). c) Intensity line profiles of the blue squared region in (b), inset is the corresponding enlarged HAADF-STEM image. d) The GPA of (b) showing the strain fluctuation around the pinning point, indicating local chemical inhomogeneities. From ^[34].

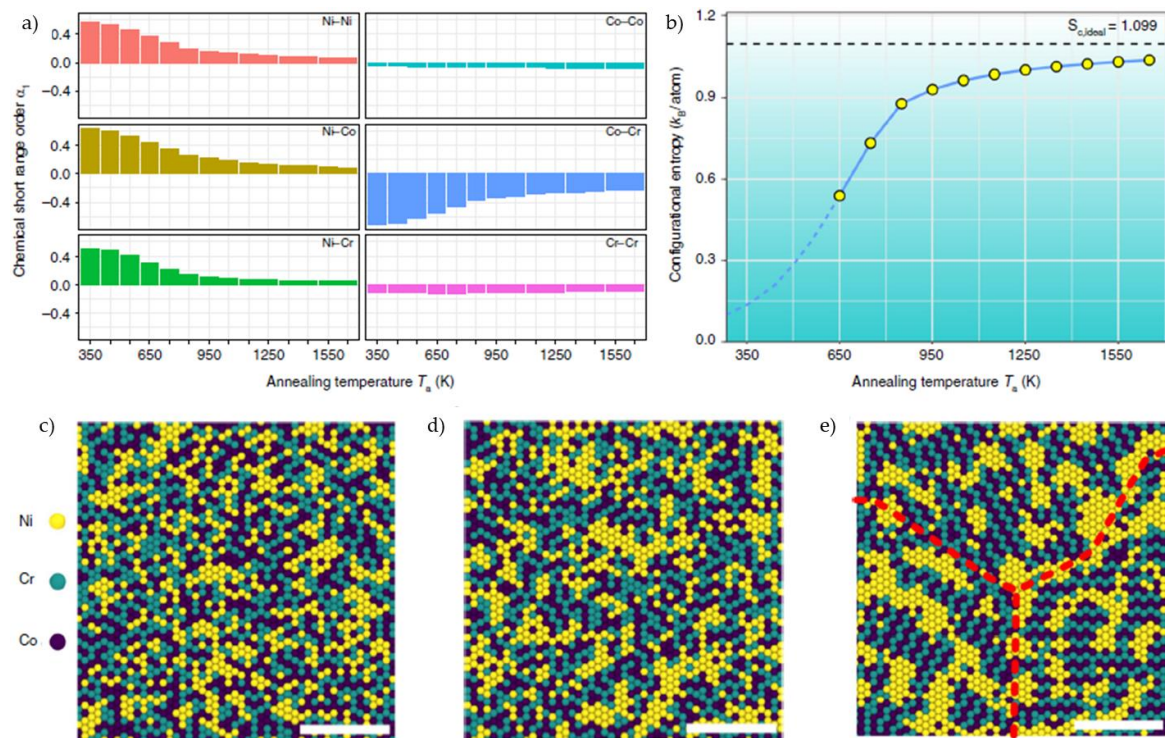


Figure 4-14 – LCF at different annealing temperatures T_a . a) Pairwise chemical short-range order parameter α_1 (see the methods section of the paper) at different annealing temperatures. b) Configurational entropy of the CoCrNi solution and its temperature dependence. Points are data estimated through the cluster variation method (CVM) with pair approximation, connected using a blue line as a guide for the eye. This approximation becomes increasingly inadequate at high LCF; thus, a dashed line is used instead to project the trend at low T_a . Black dashed line: $S_{c,ideal}$. c) - e) Representative configurations at $T_a = 1350$, 950, and 650 K, respectively. The red dashed lines indicate the Co–Cr domain boundaries. Scale bar = 3 nm. All atomic configurations are viewed on the (111) plane. Adapted from [35].

To further their analysis, Li et al. [35] also modelled a dislocation moving in a lattice CoCrNi with various LCFs (Figure 4-15). Due to the nanoscale LCF heterogeneities, the dislocation line is wavy and does not move smoothly, but through a series of forward slip of local segments and detraps from its local LCF environment (part (a) of the figure, where the nanoscale swept areas between the start and final states are highlighted in red). Each event of slip forward is called a nanoscale segment detraping (NSD). In order to evaluate the LCF effects on the barriers associated with a typical nanoscale segmented slip process, Li et al. [35] calculated the minimum energy path (MEP) in part (b) of the figure, where a typical nanoscale segment movement traverses a MEP consisting of multiple finer events with variable barriers, reflecting the complex nature of the underlying energy landscape in concentrated alloys. Both NSD and the calculated MEP correlate with the dislocation motion and conclusions presented in Section 1 for the CoCrFeMnNi alloy.

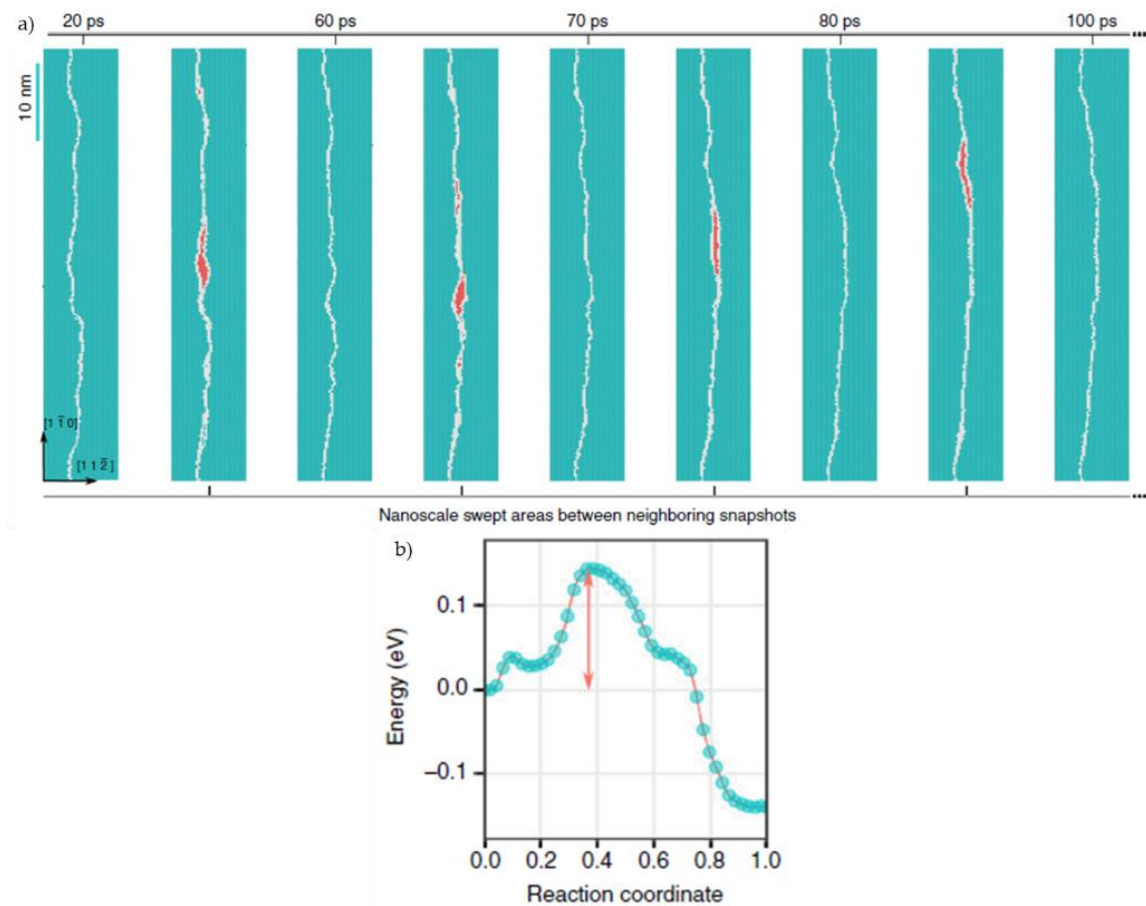


Figure 4-15 – Dislocation motion via NSD mechanism. a) Correlated nanoscale processes for a leading partial dislocation (white) in a specimen with $T_a = 950$ K. Applied $T = 300$ K, applied shear stress = 300 MPa. The swept areas between two neighbouring snapshots when the dislocation settles down briefly without motion (e.g., 20 and 60 ps) are highlighted in red. b) The calculated minimum energy path of a NSD process for a specimen with $T_a = 950$ K subjected to a local shear stress of 400 MPa. Adapted from [35].

Guo et al. [39], investigated the effect of the LCF on the deformation behaviour of CoCrFeMnNi at RT by the hybrid MD and Monte Carlo (MC) simulations. They increased the MC cycles and found the LCF of the system evolves towards a more stable state (see Figure 4-16, showing the LCFs of system under different MC cycles, with the LCFs measured by the pairwise multicomponent short-range order parameter [40]).

As shown in part (a) of the figure, all the absolute values of are close to zero at 0 ps, which means the distribution of the atoms is random. When increasing the MC cycles, Co and Fe gradually gathered with each other. In addition to Fe, Co also preferred to gather with Co. Part (b) shows the atomic configurations of the CoCrFeMnNi system under different MC cycles. Compared with the sample with no LCF at 0 ps, Co-Fe, Mn-Ni and Cr rich regions formed at 250 ps. As the system became more stable, the enrichment degree of different

compositions became higher [39]. Experimentally, the nano-scale precipitates of MnNi-, CoFe-, and Cr-rich regions have been found in CoCrFeMnNi [41,42].

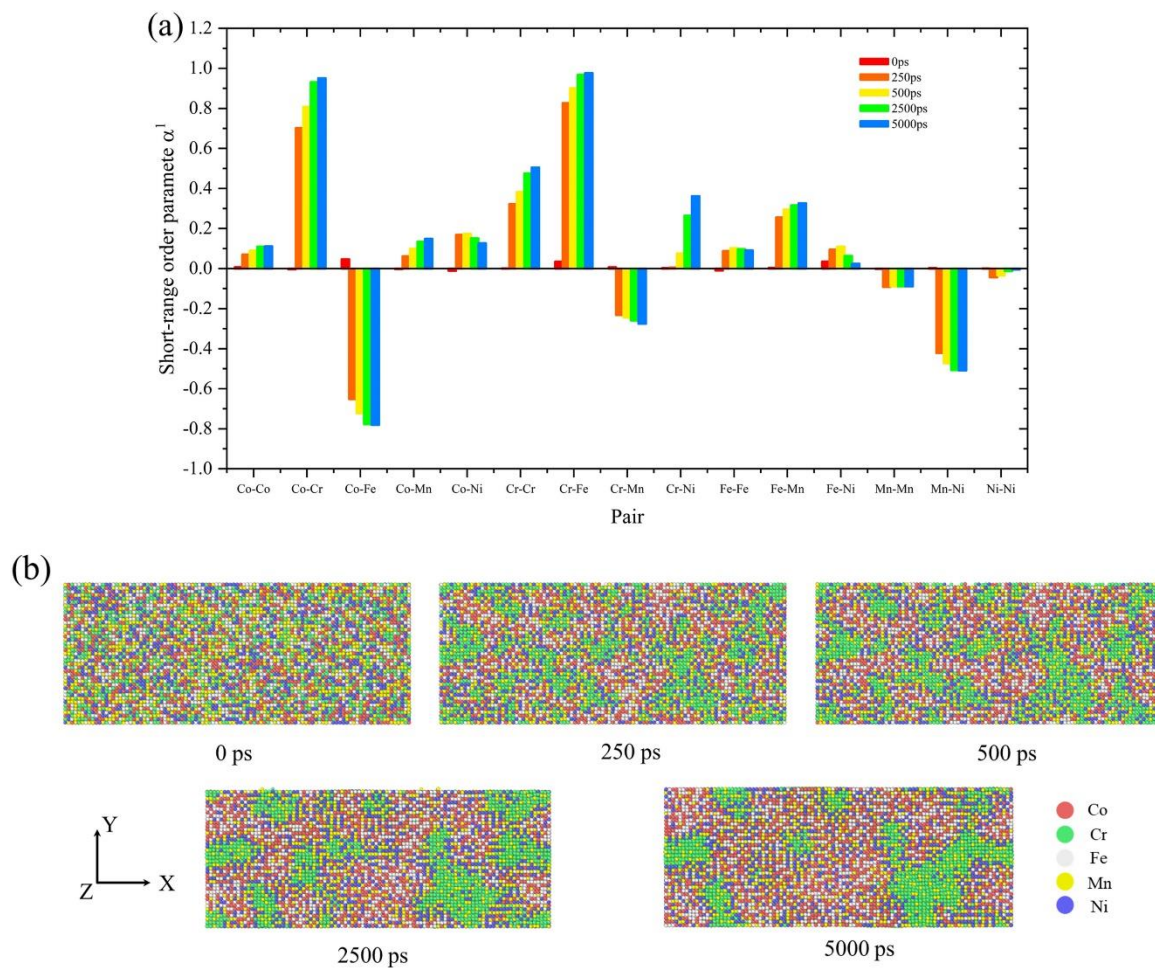


Figure 4-16 – Local chemical fluctuation of HEA CoCrFeMnNi system under different MC cycles. a) Pairwise chemical short-range order parameter. b) Atomic configurations. From [39].

Guo et al. [39] also showed the dislocation distribution at the beginning stage of the dislocation formation (Figure 4-17). They found the following:

In the 0 ps-sample, the composition feature in the position where dislocation formed were similar to the system. However, in the other samples, the atoms around the dislocation lines were mainly Cr atoms. This means that the positions where the dislocations formed were all Cr-rich regions, and the dislocations were easier to form in the Cr-rich regions than in the other regions (e.g., Mn-Ni, Co-Fe). With increasing MC cycles, Cr-rich regions became larger and dislocations became much easier to form, which explained why the yield strength of the samples gradually decreased. During MD and MC hybrid simulation, the system becomes more stable, the LCF becomes higher and the distribution and size of Cr-rich region also change.

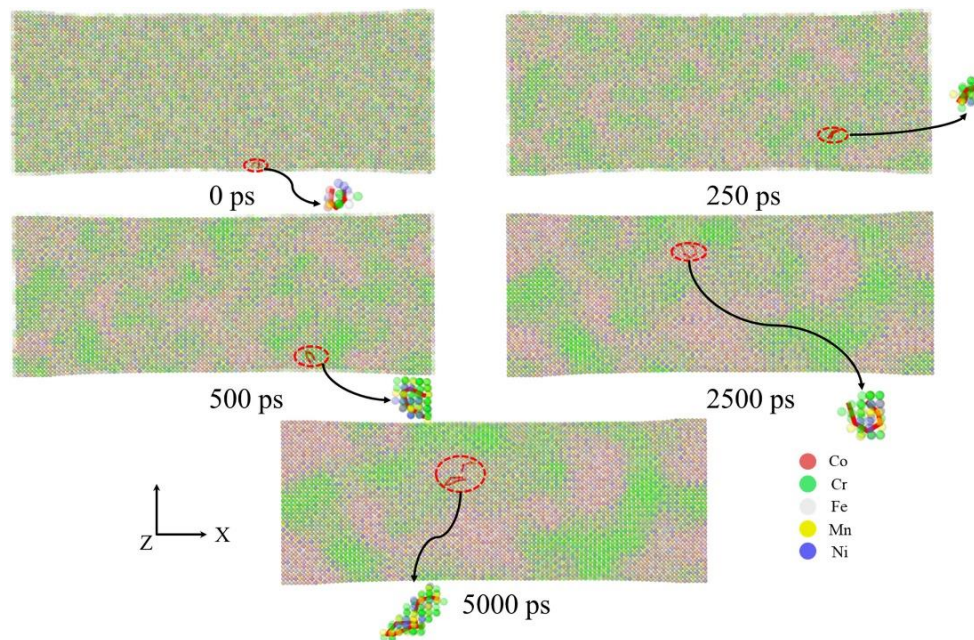


Figure 4-17 – Dislocation distribution at the beginning of the dislocation formation. Bu et al. designed the atoms to be semi-transparent, to observe the distribution of dislocation lines in the simulation cell. The depth of the colour is inconsistent, however all green atoms (dark or light), are Cr. From ^[39].

To conclude this section, this study would like to highlight the process developed by Zhang et al. ^[32] (spatio-temporal coarse graining data analysis), which presents an advantageous and more detailed technique to fully identify pinning points, compared to the experimental one shown at the start of this section. It allowed for a better understanding of pinning points and led to conclude that they are the results of atomic clusters that, when swept by a dislocation, fluctuate in strength, due to the atomic nature of said clusters. This allowed to conclude on the existence of LCFs in the CoCrFeMnNi alloy.

This section also briefly talked about short-range order existence in the CoCrFeMnNi alloy. This will be presented in more detail in the next section.

3. Pairs of perfect dislocations

As mentioned in Chapter 3, when a slip system is activated in a previously "virgin" zone, it is usually headed by a pair of perfect (undissociated) dislocations. The pair of dislocations open the path in a slip system that was previously not active. This phenomenon occurs both at room and at cryogenic temperatures. However, it is more recurrent at low temperatures (out of 26 different grains analysed at LN₂T, 16 presented at least one pair of dislocations heading deformation, meaning a 61.5% of occurrence. In contrast, at RT, pairs of perfect dislocations were present in 11 out of 30 grains studied

during *in situ* TEM straining, an occurrence of 36.7%). Some examples are presented in Figure 4-18 (parts (a) and (b) show pairs at RT, and (c) and (d) at LN₂T), aside from the ones previously presented in the last chapter.

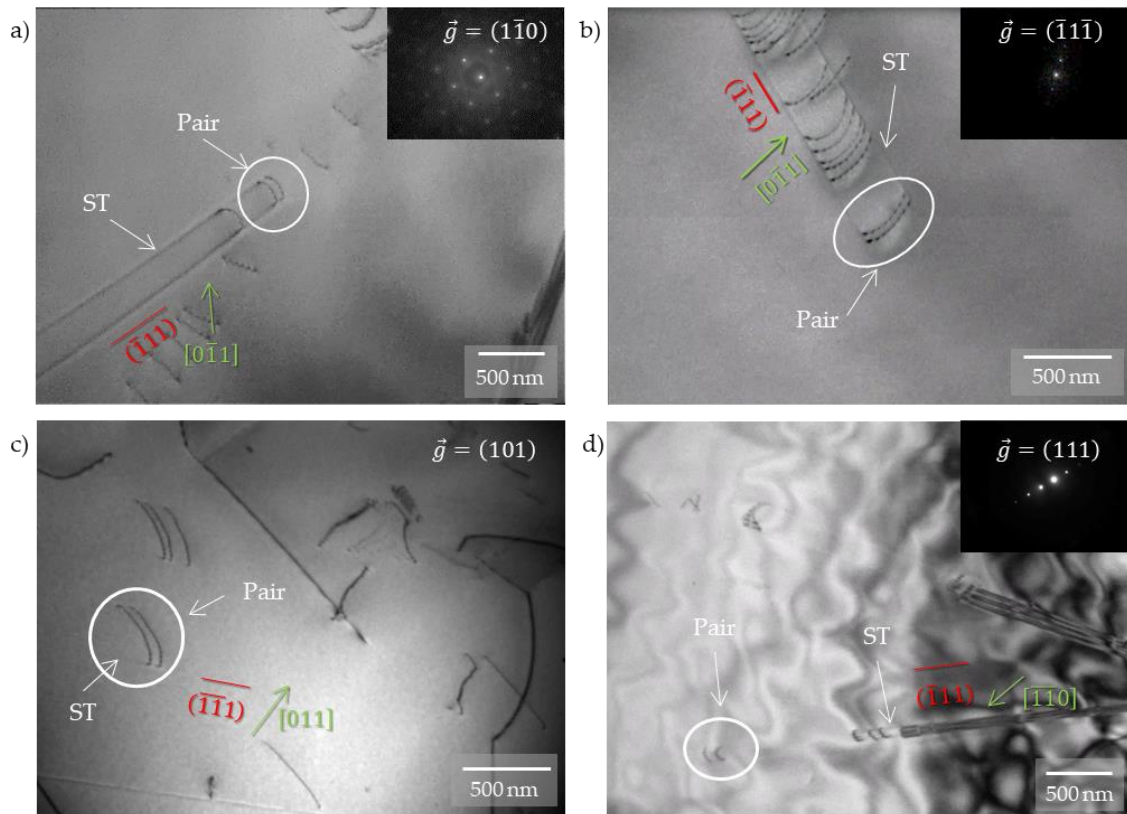


Figure 4-18 – *In situ* TEM straining BF images showing perfect dislocations moving in pairs at the head of a pile-up (or when starting slip system activation). All images show the pairs framed in white, slip planes in red, Burgers vectors in green and their corresponding \vec{g} . The slip traces of the pile-up (“ST”) are also indicated in white. a) Specimen X1-21, strained at $T = 293$ K. b) Specimen 35/I2-Head10, strained at $T = 293$ K. c) Specimen 35/I2-Head22, strained at $T = 96$ K. d) Specimen 35/I2-Head28, strained at $T = 103$ K.

The slip traces (indicated in the figure as “ST”) are a good indicator on whether the slip system is active in a “virgin” zone or not. In most cases, and depending on the imaging conditions, dislocations will leave behind a marked path in the form of straight lines at either side (this was previously presented in Chapter 2). Looking at the STs in the figure above, it is clear that they are behind the pair of perfect dislocations, indicating that they are opening the path in a previously inactive area of the crystal, in a specific slip plane.

It is worth noting that these pairs are not largely dissociated Shockley partials, but full perfect dislocations moving together, one behind the other (as seen in the previous figure). Once the pair moves a certain distance, more dislocations will appear, forming a pile-up (maintaining, however, the spacing between them and the original pair). This is indicative

of short-range order (SRO – the regular and predictable arrangement of the atoms over a short distance, usually with one or two atom spacing ^[43]).

Short-range ordering in fcc alloys has been linked to planar slip dislocation morphologies ^[44]. The phenomenon is typically attributed to the energy of a diffuse anti-phase boundary (DAPB), which is formed when the motion of leading dislocations on a slip plane diminishes the state of SRO. The DAPB energy gives rise to an athermal friction stress for the lead dislocation, and a “slip plane softening” effect ^[44] for subsequent dislocations gliding on the same slip plane after the SRO has been destroyed ^[45]. Subsequent dislocations following the initial dislocation would experience a lower energy barrier by gliding on the same path and avoiding the DAPB energy barrier ^[30]. Such an effect on mechanical properties can have profound implications on the deformation behaviour of single-phase concentrated solid solutions, including HEAs ^[46].

An antiphase boundary (APB) separates two domains of the same ordered phase ^[47,48]. It results from symmetry breaking that occurs during ordering processes, which can start at different locations in a disordered lattice. An APB forms when two such regions contact so that they display wrong compositional bonds across the interface, as illustrated in Figure 4-19 ^[49,50]. When the exact structure of the interfacial region is not known and, in addition, vary with solute content, it is called diffuse anti-phase boundary (DAPB) ^[51].

For systems with some degree of ordering, Fisher ^[52] proposed that the energy increase (per unit area) can serve as an estimate for chemical short range order. This energy is often referred to as a diffuse anti-phase boundary energy (γ^{DAPB}), since this is the amount of energy needed to disrupt the localized order of the nearby atoms ^[53].

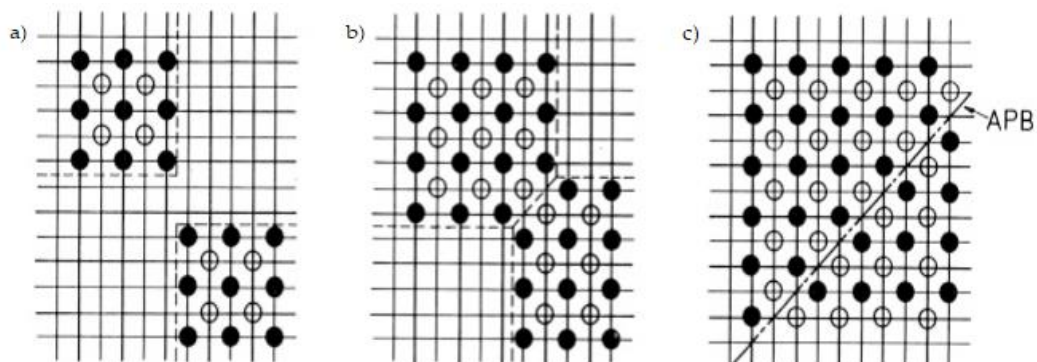


Figure 4-19 – Formation of an APB when ordered regions in which A (open circles) and B (filled circles) atoms occupying different sub-lattices grow together: a) nucleation of ordered domains on different sub-lattices, b) contact of domains, and c) the resulting APB (dashed line). From ^[50].

The pair of perfect dislocations activating a “virgin” area of the crystal evidences the existence of a specific ordering with a DAPB barrier that is broken with the passing of, not one, but two $a/6[110]$ -type dislocations. Once this barrier is overcome, the slip plane is softened and further dislocations can glide, forming a pile-up (parts (a) and (b) of Figure 4-18). The fact that the passing of two perfect dislocations breaks the DAPB evidences a particular order that seem to have the magnitude of $\sim 1 - 2|\vec{b}|$ ($\sim 0.255 - 0.51$ nm). The order is reestablished after these two dislocations cross.

The case of SRO in pile-ups in TEM thin foil specimens was studied by Saada and Douin^[54]. They explain it as follows:

The glide of a dislocation D_0 on a given plane G of a short-range-ordered alloy destroys, at least partially, the SRO, which needs an energy γ_0 per unit surface swept by the dislocation and corresponds to a frictional force γ_0 per unit length opposing the motion of D_0 .

Dislocation D_0 ... introduces some disorder (DAPB)... Whenever the order is completely destroyed by the glide of a single dislocation, the energy necessary to create this defect is γ_0 . In this case, dislocations following D_0 feel no frictional force resulting from the destruction of order. As a consequence, plastic flow occurs as groups of piled-up dislocations. However, there is no reason to assume that local order is completely destroyed by the glide of the first dislocation. The SRO should change after the passage of each dislocation, and successive dislocations trail a different fault. Assuming that, after the passage of a sufficient number of dislocations p^* , the local order is not affected any longer by the passage of other dislocations, the frictional stress $(\gamma_p - \gamma_{p-1})/b$ resulting from the SRO becomes negligible for $p > p^*$ (since $\gamma_p \approx \gamma_{p-1}$) and thus plastic flow will occur as groups of piled-up dislocations.^[54]

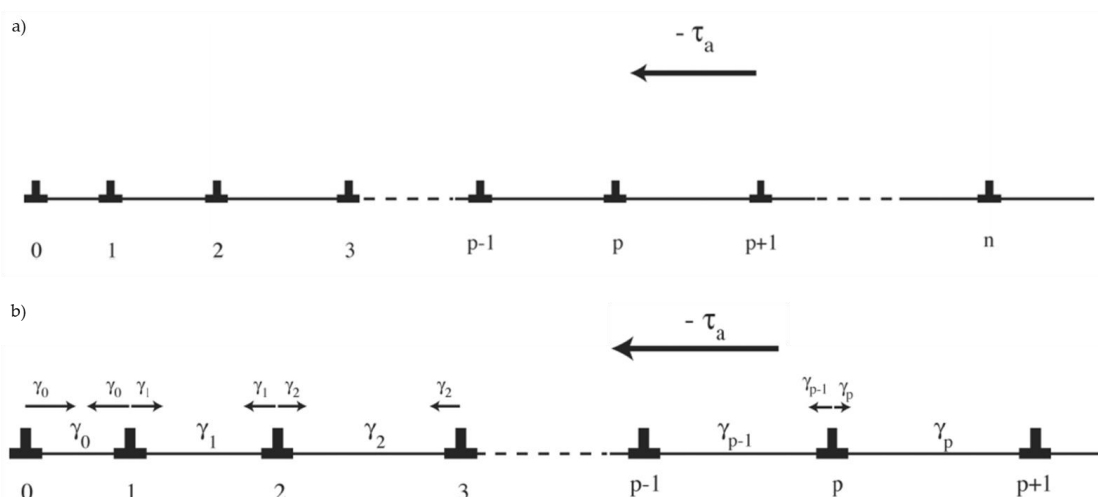


Figure 4-20 - Schematic diagrams of a general pile-up, under the effect of homogeneous applied stress $-\tau_a$, in a: a) disordered alloy, b) short-range-ordered alloy. Adapted from^[54].

Since all dislocations undergo the same applied stress $-\tau_a$, the total force F_p on the dislocation p is:

$$F_p = -b\tau_a + \gamma_p - \gamma_{p-1} + S_p + R_p, \quad 0 < p \leq n$$

Equation 4-3 – Force on a dislocation in a pile-up in a SRO alloy. From [54].

where R_p is the total elastic force exerted on the dislocation p by the other dislocations and S_p is the frictional force that each dislocation may experience owing to lattice friction and/or local interaction with foreign atoms. Pettinari-Sturmel et al. [55] applied this reasoning successfully to calculate the SRO values for a nickel-based super alloy.

Applying the former mathematical reasoning in the CoCrFeMnNi alloy is not possible, as the frictional force obtained from a perfect pile-up is not yet known. However, in the case of this work, an approximation can be obtained only taking into consideration the pair of perfect dislocations (considering them as isolated, as only they suffice to overcome the DAPB). This means that $\gamma_0 = \gamma^{DAPB}$, and the other variables do not apply when taking into consideration dislocations 0 and 1 (from the schematics above and from the schematics in Figure 4-21).

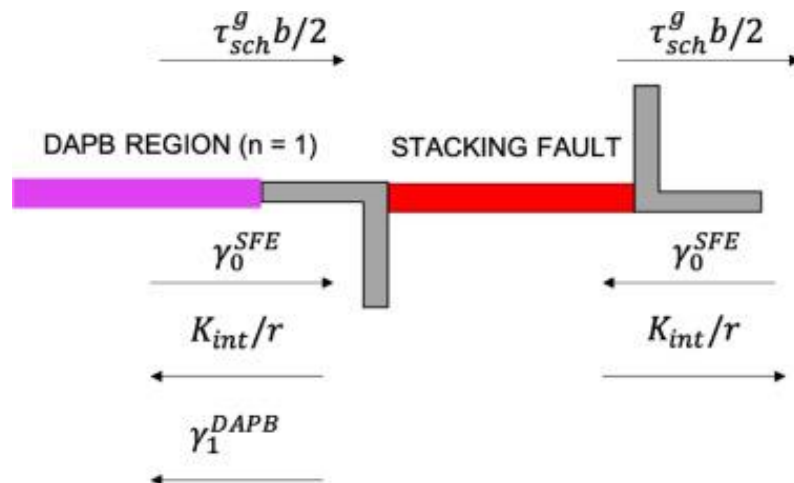


Figure 4-21 – The force balance on each partial dislocation associated with the head dislocation in a planar array due to an applied Schmid stress, the SFE, the DAPB energy, and the elastic repulsion between the partial dislocations. From [46].

The results of this approximation are given in Table 4-3, calculated for the separation (“ d ”) between the two perfect dislocations in the examples given in Figure 4-18, using Equation 3-3 (and the same parameters used when calculating the SFE values in Chapter 3).

Table 4-3 – Diffuse anti-phase boundary energy calculation using Equation 3-3.

Figure	T (K)	d (nm)	γ^{DAPB} (mJ/m ²)
4-16 (a)	293	126 ± 8	3 ± 1
4-16 (b)	293	62 ± 4	5 ± 2
4-16 (c)	96	115 ± 6	3 ± 1
4-16 (d)	103	167 ± 7	2 ± 1
			3

SRO analysis have been conducted in fcc HEAs, as, for example, in the case of Zhang et al. [30]. They studied a CoCrNi fcc alloy to determine the existence of SRO. Using high resolution TEM imaging (HRTEM), combined to diffraction contrast, they evaluate the size and shape of the SRO-enhanced domains through energy-filtered dark-field imaging (Figure 4-22). Parts (a) and (b) of the figure present two dark-field images formed by using two different objective aperture positions (as marked in part (c)). While each dark-field image shows mostly different sets of SRO-enhanced domains that are preferentially scattering to different parts of reciprocal space, there are a number of domains they could identified in both images (examples are marked by the arrows) [30]. They conclude that the existence of the same domains in images formed by separate and non-parallel directions of SRO-generated streaking is evidence for a non-planar shape of the SRO domains. However, as their dark-field images suggest, the domain boundaries are relatively diffuse, and there is no evidence of any specific shape that characterizes the SRO domains [30].

The existence of SRO has also been linked to cross-slip in fcc alloys [46] (Abu-Odeh and Asta [46] studied cross-slip in a model Ni-10%Al alloy through atomistic simulations, comparing configurations with random configurational disorder and SRO, and found that cross-slip activation barriers depend not only on the overall state of SRO in the alloy, but also on the presence or absence of a diffuse anti-phase boundary in the slip plane). This could help explain the activation of cross-slip present during the *in situ* TEM straining experiments of this work (as seen in Chapter 3) even with low SFE.

Aside from *in situ* TEM straining, the existence of SRO cannot be easily detected with other techniques, as its presence is revealed by moving dislocations at the very onset of plasticity. A possibility would be the use of atom probe tomography (APT), which offers the possibility of performing 3D imaging and chemical composition measurements at the atomic scale (around 0.1 – 0.3 nm resolution in depth and 0.3 – 0.5 nm laterally). Coupling this technique to *in situ* TEM straining experiments could lead to the identification of the SRO domains in the CoCrFeMnNi alloy, provided that, when straining, pairs of perfect dislocations move through “virgin” areas already mapped using APT.

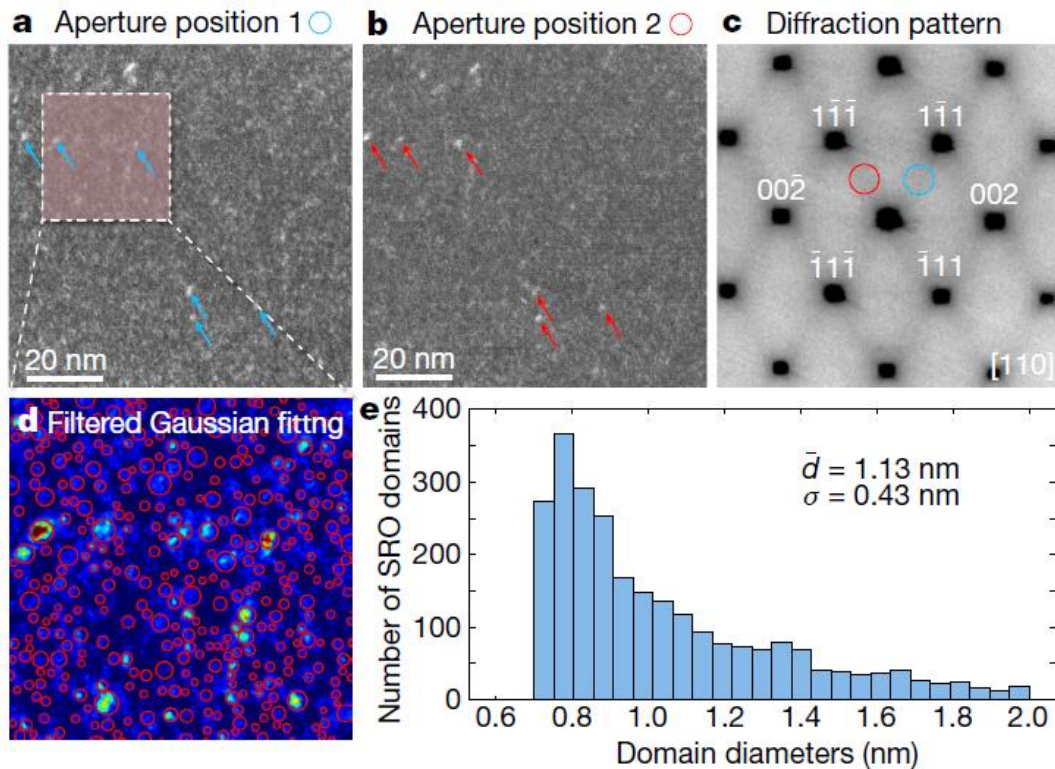


Figure 4-22 – Evidence for the three-dimensional structure of the domains and their size distribution. a)- b) Energy-filtered dark-field images from different diffuse superlattice peaks; examples showing the same domain contrast are marked with the arrows. c) Energy-filtered diffraction patterns of the region of interest; the red and blue circles indicate the dark-field imaging conditions of a) and b). The contrast is reversed for better visibility. d) Magnified view of the boxed part of the dark-field image in a), with identified SRO domains marked by the red circles. The dark-field image is pseudo-coloured for better visibility. e) The histogram of identified domain diameters. The average value \bar{d} and the standard deviation σ are listed in the box. From [30].

4. Conclusions

Taking into consideration the previous sections, several conclusions can be made:

- Two remarks arise from the results at cryogenic temperatures: dislocations move through longer jumps and the obstacles are stronger than at room temperature.
- The obstacles can be linked to local chemical fluctuations, which can either increase or decrease in strength when dislocations glide, as these locally rearrange the atomic landscape through their passage. This fluctuating strength is a novel result comparing, for example, to precipitation-hardened fcc alloys.
- In the randomly disordered fcc lattice of the CoCrFeMnNi alloy, the pair of perfect dislocations that activate slip and move a long distance in a “virgin area” of the crystal evidence a specific order.
- The spacing between the pair of perfect dislocations can be considered a DAPB. From the pair spacing, its approximate value was calculated to be $\gamma^{\text{DAPB}} \approx 3 \text{ mJ/m}^2$.

- From the analysis of the different grains that presented SRO evidence, in the “virgin” region of the crystal it seems that no obstacles hinder the movement of the pair of dislocations – as they travel a long distance. However, after their passing, subsequent dislocations gliding seem to break and reconstruct atomic bonds. The passing of dislocations effectively modifies the local atomic landscape, creating LCFs that lead to cluster-enriched areas that act as stronger (or weaker) pinning-points-enriched areas.

All these statements present the complexity of the atomic landscape, which changes locally with each dislocation passing ^[32]. However, the external factors also influence dislocation movement, such as applied stress (discussed in previous chapters) and temperature. The *in situ* TEM straining experiments have shown that a decrease in temperature influences both the distance of the dislocation jump and the easiness for dislocations to overcome a PP, as well as the probability of finding a pair of perfect dislocations heading an active slip system.

The atoms are not rearranged when the temperature changes, but their kinetic energy is reduced as a product of the decreasing temperature, increasing the obstacles (clusters) strength and limiting the local rearrangement. This influence of the temperature, especially in the occurrence of pairs of perfect dislocations (SRO), lead to several questions: is diffusion helping to restore a thermodynamically favourable local SRO? Or is this SRO more stable with low T? Further analysis (out of scope for this work, unfortunately) are needed to understand the effect of the dislocations moving through this local SRO domains, and the effect they can also have on the behaviour of dislocations in the CoCrFeMnNi alloy.

At last, the spatio-temporal coarse graining data-mining developed during this work ^([32]), coupled with the *in situ* TEM straining experiments, allowed to perform analysis inaccessible results in experimentation only, proving to be a powerful tool that can be implemented to further and better the understanding on the strengthening mechanisms of “regular” and “complex” alloys.

5. References

- [1] F. Otto, A. Dlouhý, Ch. Somsen, H. Bei, G. Eggeler, E. P. George, *Acta Materialia* **2013**, *61*, 5743–5755.
- [2] Z. Zhang, M. M. Mao, J. Wang, B. Gludovatz, Z. Zhang, S. X. Mao, E. P. George, Q. Yu, R. O. Ritchie, *Nature Communications* **2015**, *6*, DOI 10.1038/ncomms10143.
- [3] J. Friedel, *Dislocations*, Pergamon Press, Great Britain, **1964**.
- [4] R. L. Fleischer, *Acta metall.* **1961**, *9*, 996–1000.

- [5] R. L. Fleischer, *Acta metall.* **1963**, *11*, 203–209.
- [6] N. F. Mott, *London Edinburgh Dublin Philos. Mag. J. Sci.* **1952**, *43*, 1151–1178.
- [7] R. Labusch, *Phys. Stat. Sol. (b)* **1970**, *41*, 659–669.
- [8] R. Labusch, *Acta metall.* **1972**, *20*, 917–927.
- [9] G. P. M. Leyson, W. A. Curtin, *Philos. Mag.* **2013**, *93*, 2428–2444.
- [10] S. Zhao, Y. N. Osetsky, Y. Zhang, *J. Alloys Compd* **2017**, *701*, 1003–1008.
- [11] Y. N. Osetsky, G. M. Pharr, J. R. Morris, *Acta mat.* **2019**, *164*, 741–748.
- [12] C. Varvenne, A. Luque, W. G. Nöhring, W. A. Curtin, *Phys. Rev. B* **2016**, *93*, 104201.
- [13] T. M. Smith, M. S. Hooshmand, B. D. Esser, F. Otto, D. W. McComb, E. P. George, M. Ghazisaeidi, M. J. Mills, *Acta Materialia* **2016**, *110*, 352–363.
- [14] S. Liu, Y. Wei, *Extreme Mech. Lett.* **2017**, *11*, 84–88.
- [15] J. Ding, Q. Yu, M. Asta, R. O. Ritchie, *Proc. Natl. Acad. Sci. USA* **2018**, *115*, 8919.
- [16] Q. Ding, Y. Zhang, X. Chen, X. Fu, D. Chen, S. Chen, L. Gu, F. Wei, H. Bei, Y. Gao, M. Wen, J. Li, Z. Zhang, T. Zhu, R. O. Ritchie, Q. Yu, *Nature* **2019**, *574*, 223–227.
- [17] Z. Lei, X. Liu, Y. Wu, H. Wang, S. Jiang, S. Wang, X. Hui, Y. Wu, B. Gault, P. Kontis, D. Raabe, L. Gu, Q. Zhang, H. Chen, H. Wang, J. Liu, K. An, Q. Zeng, T.-G. Nieh, Z. Lu, *Nature* **2018**, *563*, 546–550.
- [18] Y. N. Osetsky, J. Morris, *Acta mat.* **2022**, *222*, 117457.
- [19] W. Li, S. I. Rao, Q. Wang, H. Fan, J. Yang, J. A. El-Awady, *Materialia* **2020**, *9*, 100628.
- [20] Y.-C. Yang, C. Liu, C.-Y. Lin, Z. Xia, *Scr. Mater.* **2020**, *178*, 181–186.
- [21] Y.-C. Yang, C. Liu, C.-Y. Lin, Z. Xia, *Mater. Sci. Eng. A* **2021**, *815*, 141253.
- [22] X. D. Xu, P. Liu, Z. Tang, A. Hirata, S. X. Song, T. G. Nieh, P. K. Liaw, C. T. Liu, M. W. Chen, *Acta mat.* **2018**, *144*, 107–115.
- [23] D. Utt, S. Lee, A. Stukowski, S. H. Oh, G. Dehm, K. Albe, *arXiv:2007.11489 [cond-mat, physics:physics]* **2020**.
- [24] J. P. Hirth, *J Supercond Nov Magn* **2012**, *25*, 561–563.
- [25] Y. Satoh, T. Hatano, N. Nita, K. Nogiwa, H. Matsui, *Mater. Trans.* **2014**, *55*, 413–417.
- [26] J. Friedel, in *Les Dislocations*, Gauthier-Villars, Paris, **1956**.
- [27] G. Laplanche, P. Gadaud, O. Horst, F. Otto, G. Eggeler, E. P. George, *Journal of Alloys and Compounds* **2015**, *623*, 348–353.
- [28] A. Haglund, M. Koehler, D. Catoor, E. P. George, V. Keppens, *Intermetallics* **2015**, *58*, 62–64.

- [29] D. Oliveros, A. Fraczkiewicz, A. Dlouhy, C. Zhang, H. Song, S. Sandfeld, M. Legros, *Mat. Chem. Phys.* **2021**, 272, 124955.
- [30] R. Zhang, S. Zhao, J. Ding, Y. Chong, T. Jia, C. Ophus, M. Asta, R. O. Ritchie, A. M. Minor, *Nature* **2020**, 581, 283–287.
- [31] M. Laurent-Brocq, A. Akhatova, L. Perrière, S. Chebini, X. Sauvage, E. Leroy, Y. Champion, *Acta mat.* **2015**, 88, 355–365.
- [32] C. Zhang, H. Song, D. Oliveros, A. Fraczkiewicz, M. Legros, S. Sandfeld, *Acta mat.* [Submitted for publication] **2022**.
- [33] R. Gröger, V. Vitek, A. Dlouhý, *Modelling Simul. Mater. Sci. Eng.* **2020**, 28, 075006.
- [34] Y. Bu, Y. Wu, Z. Lei, X. Yuan, H. Wu, X. Feng, J. Liu, J. Ding, Y. Lu, H. Wang, Z. Lu, W. Yang, *Materials Today* **2021**, 46, 28–34.
- [35] Q.-J. Li, H. Sheng, E. Ma, *Nat Commun* **2019**, 10, 3563.
- [36] B. Chen, S. Li, H. Zong, X. Ding, J. Sun, E. Ma, *PNAS* **2020**, 117, 16199–16206.
- [37] A. Tamm, A. Aabloo, M. Klintonberg, M. Stocks, A. Caro, *Acta mat.* **2015**, 99, 307–312.
- [38] H. Okamoto, *JPE* **2003**, 24, 377–378.
- [39] S. Guo, H. Chen, M. Wang, *Journal of Alloys and Compounds* **2021**, 868, 159215.
- [40] D. de Fontaine, *J Appl Cryst* **1971**, 4, 15–19.
- [41] E. J. Pickering, R. Muñoz-Moreno, H. J. Stone, N. G. Jones, *Scr. Mater.* **2016**, 113, 106–109.
- [42] D.-H. Lee, J.-A. Lee, Y. Zhao, Z. Lu, J.-Y. Suh, J.-Y. Kim, U. Ramamurty, M. Kawasaki, T. G. Langdon, J.-I. Jang, *Acta mat.* **2017**, 140, 443–451.
- [43] F. J. Owens, C. P. J. Poole, *The Physics and Chemistry of Nanosolids*, John Wiley & Sons, **2008**.
- [44] V. Gerold, H. P. Karnthaler, *Acta Metallurgica* **1989**, 37, 2177–2183.
- [45] A. Abu-Odeh, D. L. Olmsted, M. Asta, *Scripta Materialia* **2022**, 210, 114465.
- [46] A. Abu-Odeh, M. Asta, *Acta mat.* **2022**, 226, 117615.
- [47] R. Kikuchi, J. W. Cahn, *Acta metall.* **1979**, 27, 1337–1353.
- [48] M. J. Marcinkowski, *Electron Microscopy and Strength of Crystals*, John Wiley, New York, USA, **1963**.
- [49] F. Zhu, P. Haasen, R. Wagner, *Acta metall.* **1986**, 34, 457–463.
- [50] J. M. Howe, in *Physical Metallurgy* (Eds.: D.E. Laughlin, K. Hono), Elsevier, Oxford, **2014**, pp. 1317–1451.

- [51] J. E. Krzanowski, S. M. Allen, *Surf. Sci.* **1984**, *144*, 153–175.
- [52] J. C. Fisher, *Acta metall.* **1954**, *2*, 9–10.
- [53] E. Antillon, C. Woodward, S. I. Rao, B. Akdim, T. A. Parthasarathy, *Acta mat.* **2020**, *190*, 29–42.
- [54] G. Saada, J. Douin, F. Pettinari-Sturmel, A. Coujou, N. Clément, *Philosophical Magazine* **2004**, *84*, 807–824.
- [55] F. Pettinari-Sturmel, A. Coujou, N. Clément, *Mater. Sci. Eng. A* **2005**, *400–401*, 114–117.

Chapter 5

GENERAL CONCLUSIONS AND PERSPECTIVES

A large array of CoCrFeMnNi specimens were strained using the *in situ* TEM technique, both at room and at cryogenic temperatures. This allowed to observe the activation of plasticity mechanisms in real time.

1. Conclusions

The main message of this work is that *in situ* TEM straining is a powerful technique to access the crystallographic information of the specimen, all while observing / analysing the behaviour of dislocations. And coupling this technique with modelling / simulation ones – such as the coarse graining data-mining approach shown in Chapter 4, the results obtained are more accurate. Because both techniques are based on the behaviour of the dislocations, access is granted to previously inaccessible domains, such as the obstacles position and their strength's fluctuation, and also using dislocations to probe the local mechanical properties of the alloy (for example, local CRSS or SFE).

Through this approach, the locally measured and calculated τ and σ stresses could be favourably compared to macroscopic calculations in the literature. Also, the dissociation of a perfect dislocation into two Shockley partials (typical of fcc alloys) changes as a function of the crystal orientation, the applied stress, temperature, but also as a function of the local atomic arrangement. This shows that the SFE fluctuates along the dislocation line and along the pile-up (in average, SFE is low, in the range of 8-15 mJ/m²), leading to conclude that dislocations alter the local atomic landscape of the alloy.

CoCrFeMnNi behave as a typical low SFE fcc metal: perfect dislocations glide in {111} planes with a Burgers vector of $1/2[110]$, and dissociate on $1/6[112]$ Shockley partials, twinning is expected to occur with more frequency at low temperatures, and cross-slip is difficult. Nevertheless, twinning occurred with the same frequency, regardless of the temperature range of the experiment, with no evidence of a critical twinning activation stress. This led to conclude that perfect slip, large dissociation of perfect dislocations and twinning are all controlled by the crystal orientation of the specimen.

The plasticity mechanism activated in a region of the specimen seems to be governed by the “Escaig split”, which is a variation of the Peach-Koehler shear stress acting on both partial dislocations, for the slip system with the highest Schmid factor. The stress difference τ'_a between the shear acting on the edge component of each partial dislocation favours the constriction of the dislocation when positive (when in the (001) direction, activating only perfect glide) or its dissociation when negative (when in the (111) direction, activating twinning). This, as for any fcc alloy, also holds true for the CoCrFeMnNi alloy.

Twinning was, however, more frequently observed at low temperature, and this could be the result of a lowering of the stacking fault energy and a more effective pinning of both partial dislocations (stronger obstacles), which will favour the slower speed of the trailing dislocation, favouring the extension of stacking faults that serve as seeds for twinning. Also, a direct influence of temperature in the behaviour of dislocation was observed by means of the length of their jumps (larger at cryogenic temperatures).

Both of these phenomena (length of jumps and strength of obstacles) can be linked to local chemical fluctuations, which can either increase or decrease with gliding dislocations, as these locally rearrange the atomic landscape when passing. Possible “clusters” or atomic-bonds facilitate the movement of dislocations while others hinder it, either acting as barriers to overcome in their movement (jumps) or as obstacles (pinning-points). The fact that the obstacle strength fluctuates seems to suggest this is a correct assumption, as the dislocation destroys / recreates bonds while gliding. The behaviour of pinning-points in the CoCrFeMnNi alloy is different than in “regular” precipitation-hardened fcc alloys, for example, seemingly suggesting that they are a novel phenomenon present in HEAs or that a further analysis of obstacles in classical alloys must be made using this novel technique (spatial-temporal coarse graining data-mining).

Another interesting phenomenon observed during the *in situ* TEM straining experiments was the pair of perfect dislocations activating slip and moving a long distance in a “virgin area” of the randomly disordered fcc lattice of the CoCrFeMnNi alloy. This evidences the existence of order (SRO). As these dislocations maintain an invariant separation between them, this could be linked to a diffuse anti-phase boundary (DAPB), that seems to have a magnitude of $\sim 1 - 2 |\vec{b}|$. The spacing between the perfect dislocations in the pair allowed to calculate an approximation of the energy barrier: $\gamma^{\text{DAPB}} \approx 3 \text{ mJ/m}^2$.

From the analysis of the different grains that presented SRO evidence, two main observations arise:

- a) the pairs of perfect dislocations were more frequently observed at cryogenic temperatures than at room temperature, and

- b) in the “virgin” region of the crystal it seems that no obstacles hinder the movement of the pair of dislocations – as they travel a long distance. However, after their passing, subsequent dislocations gliding seem to break and reconstruct atomic bonds. The passing of dislocations effectively modifies the local atomic landscape, creating LCFs that lead to cluster-enriched areas that act as stronger (or weaker) pinning-points-enriched areas.

The main difference between a classic fcc alloy and CoCrFeMnNi is its randomness:

- a) Randomness of the atomic landscape: the presence of a SRO at the onset of plasticity that is broken after the glide of two perfect dislocations, facilitating the formation of pile-ups of dislocations that, when gliding, can lead to the formation of LCF domains.
- b) Random evolution of the pinning points strength (contrary to conventional precipitate-hardened alloys) due to the lattice distortion from LCFs.

All these statements present the complexity of the atomic landscape, which changes locally with each dislocation passing. The atoms are not rearranged when the temperature changes, but their kinetic energy is reduced as a product of the decreasing temperature, increasing the obstacles (clusters) strength and limiting the local rearrangement. This influence of the temperature, especially in the occurrence of pairs of perfect dislocations (SRO), lead to several questions: is diffusion helping to restore a thermodynamically favourable local SRO? Or is this SRO more stable with low T? Further analysis (out of scope for this work, unfortunately) are needed to understand the effect of the dislocations moving through this local SRO domains, and the effect they can also have on the behaviour of dislocations in the CoCrFeMnNi alloy.

2. Perspectives

It is clear that the local atomic landscape greatly influences the behaviour of dislocations and, thus, of the plasticity mechanisms activated in CoCrFeMnNi. A more comprehensive study, coupling *in situ* TEM straining experiments together with numerical simulations and chemical analysis could help elucidate the true role SRO and of LCFs in this alloy.

As evidenced by section 2 of Chapter 4, it is clear that collaborations between experimental and numerical methods (as this study, for example, as part of the MuDiLingo project) using a data-mining approach via dislocations as probes to trace back to the alloy mechanical and chemical properties can be a successful line of work. Combining the results obtained from *in situ* TEM straining (or other loading tests) experiments with simulations or / and machine learning to replicate dislocation behaviour under different conditions allows for more accurate simulations and to obtain results from conditions otherwise difficult to access in an experimental set-up.


Further analysis on the behaviour of pinning points at different temperatures could be critical to understand the mechanical properties of this alloy. And supplementary *in situ* TEM experiments focusing on dislocation motion to better comprehend the role of LCF domains that influence jumps at various temperatures could be key to comprehend the plasticity mechanisms of, not only CoCrFeMnNi, but other multi-principal element alloys.

Appendix 1

SUPPLEMENTARY VIDEOS

The following QR codes link to each supplementary video:

Video	Specimen	Found in Chapter	QR code
1	35/I2-Head13	3	
2	35/I2-Head14	3	

3	35/I2-Head24	3	
4	35/I2-Head12	3	
5	35/I2-HeadB	3	

6	X1-21	4	
7	35/I2-Head22	4	
8	35/I2-Head24	4	

Appendix 2

CRITICAL RESOLVED SHEAR STRESS CALCULATION

1. Basis

As already explained in Chapter 1, the plastic properties of crystalline metals are distinctly anisotropic. Slip occurs along close-packed directions on (mainly) close-packed planes. A given slip system becomes active when the resolved shear stress on it reaches a critical value (law of critical resolved shear stress) ^[1].

Considering the forces acting in a crystal when slip begins, the law of resolved shear stress is

$$f = \sigma b$$

Equation 4 – Mott and Nabarro formula.

where f depends only on the resolved component σ of the total stress system through the glide of the dislocation ^[1].

Expanding on this, Figure 23 presents the schematics for a total stress σ_{tot} acting along a direction inclined with respect to a plane that can be resolved into a normal stress component σ acting in the normal direction of that plane and a tangential, shearing stress component τ acting along the plane ^[2], where:

$$\sigma = \sigma_{tot} \cos \theta$$

$$\tau = \sigma_{tot} \sin \theta$$

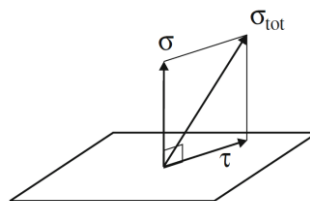


Figure 23 – The geometrical fundamentals of Schmid's law. From ^[2].

It can be anticipated that slip sets in if the shear stress component acting along the considered specific slip plane and in the considered specific slip direction surpasses a critical value ^[2]. This critical value is called the critical resolved shear stress, τ_{crit} (or CRSS). The related equations and mathematical deduction will be developed in the next subsection.

The expression for the critical shear stress in terms of the acting load stress σ_{tot} and the orientation of the crystal is the Schmid law (see ^[2] for the mathematical deduction). Its validity is demonstrated by investigating the onset of yielding of a single crystal as a function of its orientation: whereas the value of σ_{tot} needed to establish plastic deformation varies greatly as a function of orientation of the crystal, the value of τ_{crit} remains essentially constant ^[2].

Therefore, the critical resolved shear stress (CRSS from now on) can be said to be dependent on dislocation glide in a crystal. According to Salehinia and Bahr ^[3], in the absence of pre-existing dislocations, the inception of plasticity in single crystals is directly related to the nucleation of dislocations. The Schmid law states that yielding should occur once the shear stress on the slip plane, in the slip direction, is equal to the CRSS. Conventionally it is assumed that this CRSS is constant for a given material, regardless of the loading condition. This law is well established for FCC structures when pre-existing dislocations are present in the material, a condition for which deformation mechanisms are more stress dependent than being thermally controlled ^[3].

2. Locally measuring the CRSS

Figure 24(a) presents a dislocation segment pinned at its extremities. The schematics can be seen as an intersection for three dislocation segments, with points A and B fixed, under a constant shear stress τ in plane P ^[4]. The pinned segment (between points A and B) is submitted to a force

$$\vec{F} = \tau b$$

Equation 5 – Peach-Koehler expression ^[5].

oriented to X_1 . Figure 24(b) shows the displacement around a dislocation loop, not pinned.

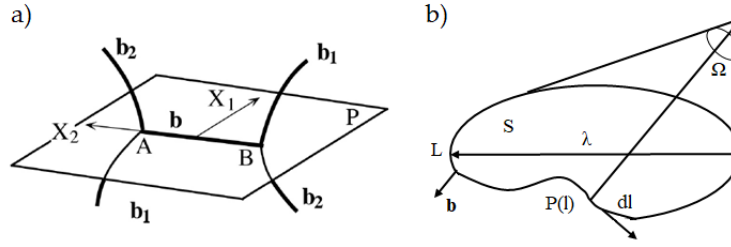


Figure 24 – a) A dislocation segment pinned at both extremities (from [4]). b) Displacement around a dislocation loop L (from [6]).

A curved dislocation line (as in Figure 24(b)) is less stable than a straight line and, accordingly, tends to straighten itself [6]. An elastic string under a tension T , when lengthened by dI , takes a supplementary energy TdI . Thus, the line tension can be seen as the energy per unit length

$$T = \frac{\mu b^2}{4\pi K} \ln \frac{\lambda}{b_0}$$

Equation 6 – Line tension of a dislocation. From [6].

where μ is the elastic modulus, λ is the diameter of the curve shown in Figure 24(b), and b_0 represents the diameter of a dislocation with a solid core in a crystal (the exact value chosen for b_0 is generally of little importance; for the reasoning and calculations, please refer to [6]), and where

$$\frac{1}{K} = \cos^2\psi + \frac{\sin^2\psi}{1 - \nu}$$

where ψ represents the character of the dislocation (when $\psi = 0^\circ$, the dislocation has a screw character, and an edge character when $\psi = 90^\circ$) and ν is the Poisson's ratio [6].

If the dislocation line makes an angle ψ with its Burgers vector, it can be decomposed into a screw dislocation and a coaxial edge dislocation, with Burgers vectors $b\cos\psi$ and $b\sin\psi$ respectively [6]. The energy and the line tension depend little on the exact nature of the dislocation, since the value of K lies between 1 and $(1 - \nu > 0.5)$ for pure screw and pure edge dislocations.

So, if $\ln \frac{\lambda}{b_0} \approx 4\pi K$ in Equation 6, then

$$T \approx \mu b^2$$

Equation 7 – Line tension for a screw dislocation. From [6].

These formulas are obtained assuming an isotropic medium [6]. In an anisotropic medium, there are complications because the energy W of a dislocation line does not depend only on its geometrical form but on its orientation with respect to the lattice. The anisotropic medium can depend on the anisotropy of the elastic constants or, less likely, from that of the core energy [6]. In an isotropic medium, $T = W$; however, the value of the effective line tension T against arbitrary deformations of the line is no longer equal to W [6].

Considering the dislocation segment from Figure 24(a) and supposing that this segment can move in the direction of an applied force \vec{F} and that its extremities are fixed, it will curve, as shown in Figure 25(a). Assuming that W varies with the angle θ of the line with the vertical axis in the figure, T is given by

$$T = \left(W + \frac{d^2W}{d\theta^2} \right)_{\theta=0}$$

Equation 8 – Change of T when W varies with respect of θ [6].

when considering the screw-edge difference ($\theta \neq 0$), where θ represents the dislocation character, thus making $\theta = \psi$.

This formula was first given by de Wit and Koehler [7]. In many cases, the term in $d^2W/d\theta^2$ alters T only by a small numerical factor, and can thus be safely neglected in rough estimates [6].

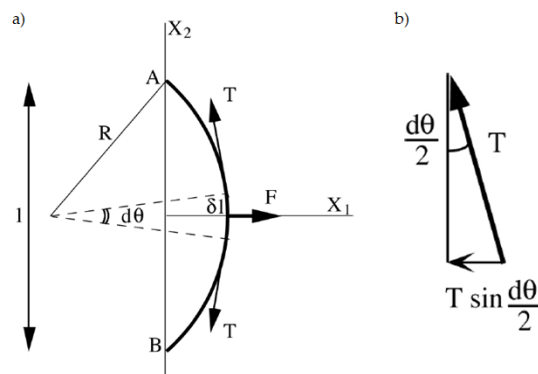


Figure 25 – a) Curvature of a length of dislocation under a force \vec{F} . b) Its forces at equilibrium. From [4].

Coming back to the curved segment of the dislocation and assuming that the loop can move, it does so in the direction of \vec{F} . The curve (at equilibrium) is obtained from the relationship between the line tension T and the force \vec{F} (Figure 25 (a) and (b)). Since its ends are fixed, it will take an equilibrium curvature $1/R$ obtained by equating the force $Td\theta$ of the line tension on the arc dl to the applied force Fdl . Hence

$$R = \frac{dl}{d\theta} = \frac{T}{F}$$

where T is given by Equation 7 and F is given by Equation 5. This, thus, gives the expression

$$R = \frac{\mu b}{\tau}$$

Equation 9 – Locally measured CRSS [6].

The bigger the dislocation loop, the smaller the stress τ to increase the size of the loop [4]. This relationship gives the basis for the technique to directly measure (in a TEM straining experiment) the stress of a dislocation, that is, the CRSS.

When assuming an isotropic medium, $T = W$, the resulting dislocation loop has a circular shape. When T has the value given by Equation 8, the shape of the loop resembles an ellipse (for more details, please refer to Appendix 3).

- [1] A. Cottrell, *An Introduction to Metallurgy*, The Institute Of Materials, London, England, **1975**.
- [2] E. J. Mittemeijer, *Fundamentals of Materials Science*, Springer Berlin Heidelberg, Berlin, Heidelberg, **2011**.
- [3] I. Salehinia, D. F. Bahr, *Int. J. Plast.* **2014**, *52*, 133–146.
- [4] J. Douin, *Mécanique des milieux continus: introduction à la plasticité des matériaux*, Diderot Éd., **1997**.
- [5] M. Peach, J. S. Koehler, *Phys. Rev.* **1950**, *80*, 436–439.
- [6] J. Friedel, *Dislocations*, Pergamon Press, Great Britain, **1964**.
- [7] G. de Wit, J. S. Koehler, *Phys. Rev.* **1959**, *116*, 1113–1120.

Appendix 3

SHAPE OF A DISLOCATION LOOP

Author: J. Douin ^[1].

The shape of a dislocation loop is given by the condition of minimum free energy E_t for a given stress. Assuming linear elasticity, the stress is proportional to the deformation, which corresponds here to a given area S of the loop. The shape of the loop will then be given by the condition that minimizes E_t assuming constant S . In what follows, we will neglect the self-interaction between dislocation segments. The influence of the self-interaction has been proven to be negligible provided the size of the loop is not too small (in the order or less than $100b$).

If $E(\theta)$ is the self-energy by unit length of the segment of dislocation with character θ , the total energy E_t of the loop L is:

$$E_t = \oint E(\theta) dL$$

At a point A of the loop L with Cartesian co-ordinates (x, y) , $dL = (\dot{x}^2 + \dot{y}^2)^{1/2} d\theta$, where $\dot{x} = \partial x / \partial \theta$, and the energy of the dislocation loop writes:

$$E_t = \oint (\dot{x}^2 + \dot{y}^2)^{1/2} E(\theta) d\theta$$

The area of the loop is given by:

$$S = \oint (x\dot{y} - \dot{x}y) d\theta$$

Let's call (r, θ) the polar co-ordinates of a point A of the loop L . We can construct the tangent of L in A and draw the vector \overline{OM} normal to this tangent, with modulus $|\overline{OM}| = p$.

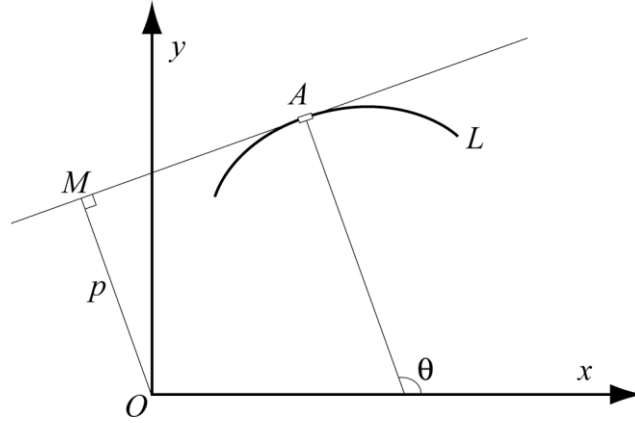


FIGURE 26 – POLAR COORDINATES OF A POINT IN A LOOP

According to the figure (above), $p = x \cos \theta + y \sin \theta$, which corresponds to the variables change:

$$x = p \cos \theta - \dot{p} \sin \theta$$

$$y = p \sin \theta - \dot{p} \cos \theta$$

We can then rewrite the total energy E_t and the area S of the loop as:

$$E_t = \oint (p + \dot{p}) E(\theta) d\theta$$

$$S = \frac{1}{2} \oint (p + \dot{p}) d\theta$$

where, again, we want to minimize E_t assuming constant S . In such case, the lagrangien L_g :

$$L_g = E_t - \lambda S$$

where λ is the so-called Lagrange multiplier, and must fulfil the 2nd order Euler-Lagrange equation giving the condition of extremum for E_t with constant S :

$$\frac{\partial L_g}{\partial p} - \frac{d}{d\theta} \frac{\partial L_g}{\partial \dot{p}} + \frac{d^2}{d\theta^2} \frac{\partial L_g}{\partial \ddot{p}} = 0$$

This equation leads to:

$$p + \dot{p} = \frac{1}{\lambda} \left(E(\theta) + \frac{\partial^2 E(\theta)}{\partial \theta^2} \right)$$

and the general solution of this differential equation is:

$$p(\theta) = C \sin(\theta - \beta\beta) + \frac{E(\theta)}{\lambda}$$

where C and β are arbitrary constants. The first term of the above equation has a 2π period and if we choose the origin of the calculation in such a way that the loop has a centre of symmetry, i.e. its centre, then $C = 0$. We then get:

$$p(\theta) = E(\theta)/\lambda$$

Finally, the local curvature R in every point of the dislocation loop must obey the relation $R = T/\tau b$, where T is the line tension of the dislocation segment. R can be rewritten as $R = dL/d\theta = (\dot{x}^2 + \dot{y}^2)^{1/2} = p + \ddot{p}$, then with $T = \left(E(\theta) + \frac{\partial^2 E(\theta)}{\partial \theta^2}\right)$, it simply follows that $\lambda = \tau b$. The shape of the loop is finally given by [2]:

$$x = \frac{1}{\tau b} \left(\cos \theta E(\theta) - \sin \theta \frac{\partial E(\theta)}{\partial \theta} \right)$$

$$y = \frac{1}{\tau b} \left(\sin \theta E(\theta) + \cos \theta \frac{\partial E(\theta)}{\partial \theta} \right)$$

[1] J. Douin, **n.d.**

[2] P. M. Hazzledine, H. P. Karnthaler, A. Korner, *Phys. Stat. Sol. (a)* **1984**, 81, 473–484.

Appendix 4

STACKING FAULT CHARACTERISATION

Williams and Carter ^[1] explained the steps to characterise a stacking fault in TEM in their book, chapter 24. Following these steps, BF and DF images of the SFs in specimen 35/I2-Head12 were taken, using two different \vec{g} vector to image them. The important remark is:

For the geometry of the DF, if the origin of the g -vector is placed at the centre of the SF in the DF image, the vector g points away from the bright outer fringe if the fault is extrinsic and toward it if it is intrinsic (200, 222, and 440 reflection); if the reflection is a 400, 111, or 220 the reverse is the case (see Figure 27). ^[1]

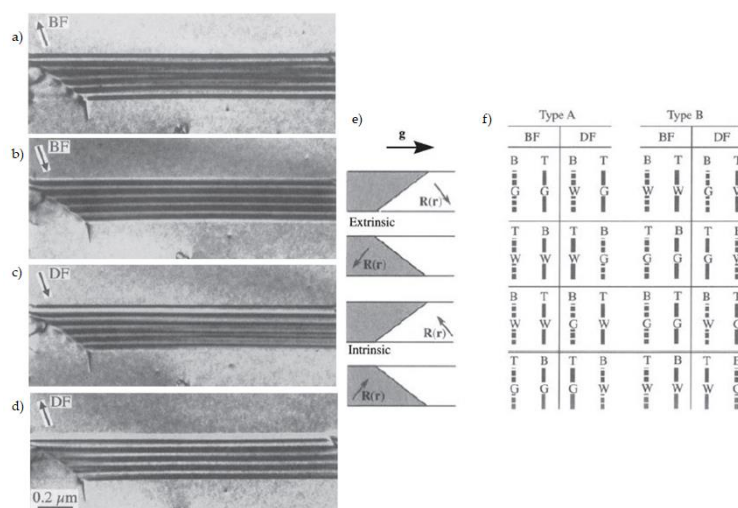


Figure 27 – a) - d) Four strong-beam images of an SF recorded using $\pm g$ BF and $\pm g$ DF. The beam was nearly normal to the surfaces; the SF fringe intensity is similar at the top surface but complementary at the bottom surface. The rules are summarized in e) and f), where G and W indicate that the first fringe is grey or white, and (T,B) indicates top/bottom. From ^[1].

Using the Williams and Carter procedure, two-beam BF and DF images were obtained on the SFs lying along (111) plane, a first set with $\vec{g} = \pm[00\bar{1}]$ (Figure 28) and a second set with $\vec{g} = \pm[1\bar{1}\bar{1}]$ (Figure 29). In the first set of images, \vec{g} points away from the dark outer fringe, and in the second, it points away from the bright outer fringe, suggesting an intrinsic SF.

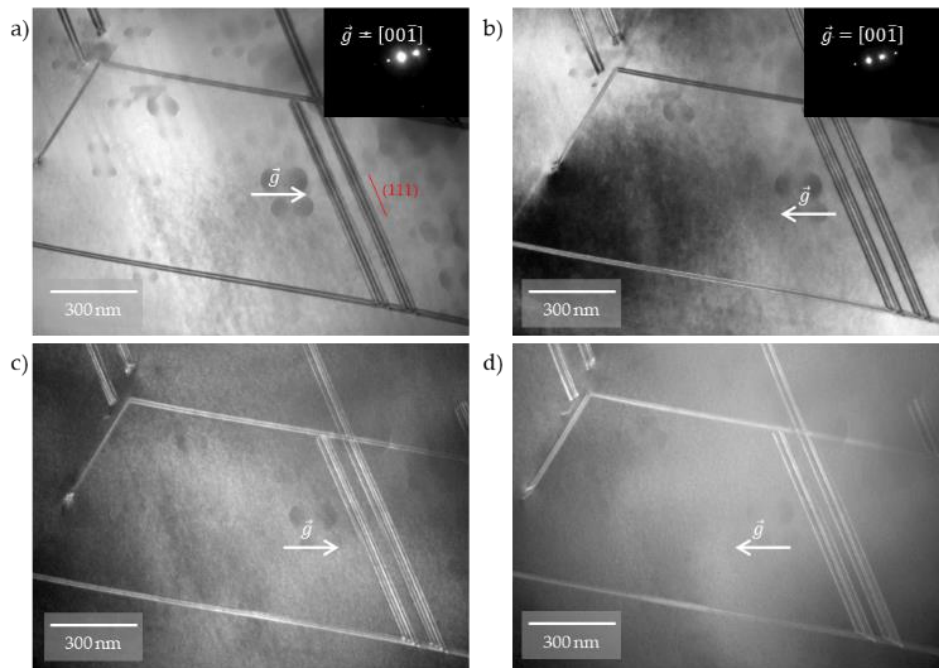


Figure 28 – TEM characterisation of specimen 35/I2-Head12, strained at $T=293$ K. a) BF image taken at $\vec{g} = +[00\bar{1}]$. b) BF image taken at $\vec{g} = -[00\bar{1}]$. c) and d) show the respective DF images. \vec{g} direction is indicated by the white arrow.

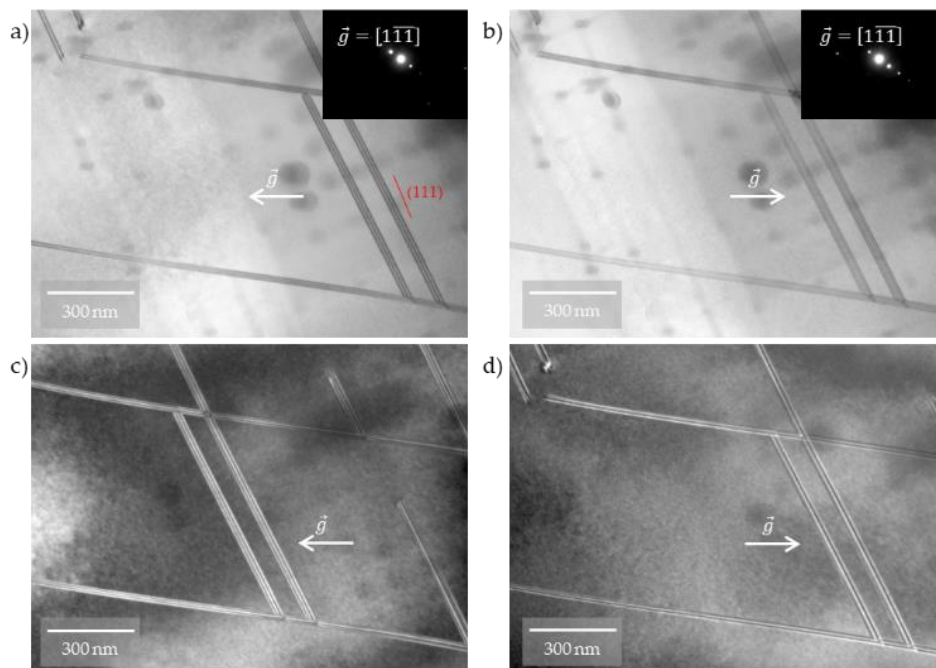


Figure 29 – Same specimen. a) BF at $\vec{g} = +[1\bar{1}\bar{1}]$. b) BF at $\vec{g} = -[1\bar{1}\bar{1}]$. c) and d) Respective DF images. \vec{g} direction is indicated by the white arrow.

- [1] D. B. Williams, C. B. Carter, in *Transmission Electron Microscopy: A Textbook for Materials Science* (Eds.: D.B. Williams, C.B. Carter), Springer US, Boston, MA, 1996, pp. 379–399.

Appendix 5

ABSTRACT – ENGLISH

The aim of this work is to give a comprehensive compendium of plasticity mechanisms, more specifically dislocation behaviour, in single-phase equiatomic CoCrFeMnNi, a high entropy alloy that crystallizes in the fcc structure. Its mechanical properties include high strength, particularly at low temperatures, good ductility and a large number of slip systems, on which its plasticity largely depends.

To have a better understanding of its properties and its plasticity mechanisms, *in situ* TEM straining experiments were carried out at room and cryogenic temperatures to analyse dislocation behaviour and movements.

Dislocations behave as they do in a classic fcc low SFE alloy: perfect $a/2[110]$ dislocations glide in $\{111\}$ -type planes, and they dissociate into $a/6[112]$ Shockley partials. The mechanisms responsible for plasticity are planar slip and twinning. They both occur at the two testing temperatures in this study, leading to conclude that the dissociation of dislocations that lead to twin formation is dominated by the crystalline orientation of the specimen.

The strengthening mechanisms are a result of the classical dislocation/obstacle interaction, but also of the local lattice distortions subject to moving dislocations. This is evidenced in the *in situ* TEM straining experiments as obstacles than pin dislocations (evidenced by the curvature of dislocations loop while moving under applied stress). These obstacles seem to be stronger at low temperature, a fact that is further studied in this work. The pinning points seem to be a result of the local atomic landscape of CoCrFeMnNi alloy, which also causes dislocations to move in the reported “jerky” manner for the alloy.

Appendix 6

ABSTRACT – FRANÇAIS

L'objectif de ce travail est de donner un aperçu complet des mécanismes de plasticité, plus particulièrement, du comportement des dislocations, dans l'alliage CoCrFeMnNi, un alliage à haute entropie équiatomique monophasé cristallisant dans la structure cfc. Ses propriétés mécaniques comprennent une résistance élevée, en particulier à basse température, une bonne ductilité et un grand nombre de systèmes de glissement, dont dépend largement sa plasticité.

Pour mieux comprendre ses propriétés et ses mécanismes de plasticité, des expériences de déformation MET *in situ* ont été réalisées aux températures ambiante et cryogénique pour analyser le comportement et les mouvements des dislocations.

Les dislocations se comportent comme dans un alliage cfc classique avec une faible énergie de faute d'empilement : des dislocations parfaites de type $a/2$ [110] glissent dans des plans type {111}, et elles se dissocient en partielles de Shockley $a/6$ [112]. Les mécanismes responsables de la plasticité sont le glissement planaire et le maclage. Au cours des essais de traction de cette étude, ils ont été observés aux deux températures d'essai, ce qui permet de conclure que la dissociation des dislocations qui conduit à la formation du maclage est dominée par l'orientation cristalline de l'échantillon.

Les mécanismes de déformation sont le résultat de l'interaction classique dislocation/obstacle, mais aussi des distorsions locales du réseau soumis aux dislocations en mouvement. Ceci est mis en évidence dans les expériences de déformation MET *in situ* sous forme d'obstacles qui épinglent les dislocations (mis en évidence par la courbure de la boucle des dislocations en mouvement sous une contrainte appliquée). Ces obstacles semblent être plus forts à basse température, un fait qui est étudié plus en détail dans ce travail. Les points d'épinglement semblent être le résultat du paysage atomique local de l'alliage CoCrFeMnNi, ce qui provoque également le déplacement "saccadé" des dislocations qui a été rapporté pour cette alliage.

Appendix 7

RESUME DE LA THESE EN FRANÇAIS

Pour caractériser les mécanismes élémentaires de plasticité dans l'alliage à haute entropie (AHE) CoCrFeMnNi en utilisant la technique de déformation MET in situ, quelques définitions de base sur la plasticité et sur les alliages à haute entropie sont nécessaires. Elles seront données dans ce chapitre. La technique de déformation MET in situ sera expliquée dans le chapitre suivant, ainsi que la préparation des échantillons et les procédures expérimentales. Puis, le chapitre 3 expliquera l'analyse et les principaux résultats issus de ces expériences, ainsi que la discussion et les perspectives qui en découlent.

1. Bibliographie et état de l'art

Un alliage métallique conventionnel peut être une solution solide (une seule phase, où tous les grains métalliques sont de la même composition) ou un mélange de phases métalliques (deux ou plusieurs solutions, formant une microstructure de différents cristaux au sein du métal). En revanche, les alliages à haute entropie sont des alliages à solution solide multiéléments sans métal solvant primaire.

Contrairement aux méthodes traditionnelles de fabrication des alliages, Cantor et al. ^[1] et Yeh et al. ^[2] ont eu l'idée de préparer des alliages multi-composants équiatomiques ou quasi équiatomiques ^[3]. Yeh a popularisé le terme "AHEs", en indiquant qu'en thermodynamique, l'entropie configurationnelle d'un alliage binaire

$$\Delta S_{\text{conf}} = -R(X_A \ln X_A + X_B \ln X_B)$$

Entropie configurationnelle d'un alliage binaire

est maximale lorsque les éléments sont en proportions équiatomiques, et que l'entropie configurationnelle maximale dans tout système augmente avec le nombre d'éléments (N) ($\Delta S_{\text{conf,max}} = R \ln N$), et qu'elle aurait un effet important sur la cinétique de formation des phases, la déformation du réseau et les propriétés de l'alliage résultant, en améliorant la solubilité entre les composants constitutifs et en conduisant à des phases et des microstructures plus simples.

L'alliage Cantor est un alliage quinaire équiatomique, composé de cobalt, chrome, fer, manganèse et nickel. Il appartient à la famille des métaux de transition 3d et est un AMEP de type I (structure cfc).

1.1. Propriétés mécaniques de l'alliage Cantor

Plusieurs rapports sur le comportement de cet alliage ont été publiés. Gali et George ^[4] ont montré expérimentalement que la résistance présente une forte dépendance à la température en dessous de 473 K, qui s'affaiblit à des températures élevées jusqu'à 1273 K, et une dépendance modeste à la vitesse de déformation à de faibles températures homologues. Dans leur revue, George et al. ^[5] soulignent que la résistance et la ductilité de l'alliage augmentent toutes deux avec la diminution de la température (jusqu'à la gamme cryogénique), avec des résistances ultimes supérieures à 1 GPa et des allongements de 60 % à 77 K. Ils remarquent également une ductilité élevée, causée par le retard dans le rétrécissement car le taux d'érouissage est inversement proportionnel à la température.

Otto et al. ^[6] ont montré des courbes de contrainte-déformation d'ingénierie représentatives pour des échantillons de CoCrFeMnNi de différentes tailles de grain (échantillons à grain fin = 4,4 μm , échantillons à gros grain = 155 μm) à six températures différentes (essais de traction effectués à une vitesse de déformation d'ingénierie de 10^{-3} s^{-1} , à 77 K, 293 K, 473 K, 673 K, 873 K et 1073 K). Ces courbes sont présentées à la figure 1. La déformation technique dans ces courbes est le rapport entre le déplacement de la traverse et la longueur initiale de l'éprouvette (12,7 mm). Ils ont obtenu les valeurs les plus élevées de la limite d'élasticité, de la résistance à la rupture et de l'allongement à la rupture à la température de l'azote liquide (77 K), et ont constaté qu'une augmentation de la température entraîne une diminution monotone de la limite d'élasticité et de la résistance à la rupture.

Ils ^[6] ont également quantifié (Figure 2) les dépendances à la température et à la taille de grain de la limite d'élasticité σ_y , de la résistance à la traction ultime σ_{uts} et de l'allongement à la rupture ϵ_f du décalage de 0,2 %, constatant que les résistances et la ductilité présentent de fortes dépendances à la température, avec leurs maxima également à 77 K, et que pour toutes les tailles de grain, σ_y et σ_{uts} diminuent de façon monotone avec l'augmentation de la température.

Dans leur revue, George et al. ^[5] résument les propriétés mécaniques du CoCrFeMnNi, et concluent (comme Gludovatz et al. ^[7]) qu'il présente une résistance, une ductilité et une ténacité à la rupture exceptionnelles. Sa ténacité à l'amorçage de fissure (K_{JIC}) est de $\sim 220 \text{ MPa} \cdot \text{m}^{1/2}$, à peu près indépendante de la température, de la température ambiante

jusqu'à 77 K, tandis que sa ténacité à la propagation de fissure dépasse $\sim 300 \text{ MPa} \cdot \text{m}^{1/2}$ (la résistance à la fissuration augmente avec la longueur de la fissure).

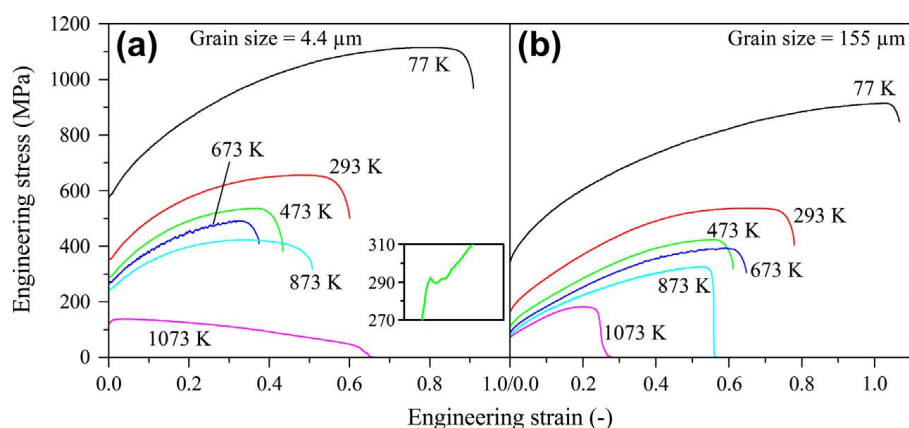


Figure 30 – Courbes de contrainte-déformation techniques représentatives de l'alliage CoCrFeMnNi aux six températures d'essai pour : a) les grains fins et b) les grains grossiers. L'encart en a) montre une petite chute de charge après la déformation pour un échantillon à grain fin qui a été testé à 473 K. D'après [6].

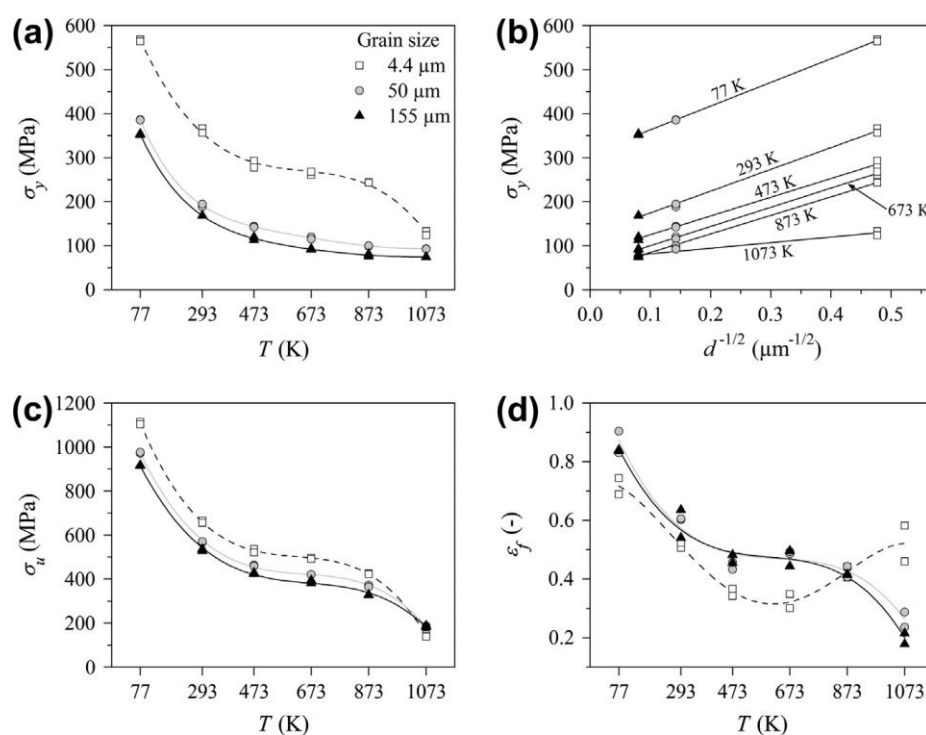


Figure 31 – Dépendance de la température et de la taille des grains pour : a) - b) la limite d'élasticité à 0,2% de décalage (σ_y), c) la résistance ultime à la traction (σ_{uts}), et d) l'allongement à la rupture (ϵ_f). D'après [6].

George et al. [5] concluent que, même si une augmentation de la résistance et de la ductilité avec la diminution de la température est observée dans d'autres alliages cfc (comme dans les aciers inoxydables austénitiques), le caractère unique de l'alliage Cantor réside dans le

maintien d'une haute ténacité à des températures cryogéniques (contrairement à la plupart des matériaux qui deviennent plus fragiles lorsque la température diminue).

1.2. Comportement des dislocations dans l'alliage Cantor

Pendant un essai de traction, le glissement des dislocations est le principal mécanisme de déformation. À température ambiante, le glissement se produit par glissement planaire de $1/2 \langle 110 \rangle$ dislocations parfaites sur les plans $\{111\}$ ^[6,8,9]. Ces dislocations parfaites se divisent en $1/6 \langle 112 \rangle$ dislocations partielles de Shockley, qui, selon Okamoto et al. ^[8], lient un défaut d'empilement avec des distances de division moyennes allant de $\sim 3,5 - 4,5$ nm pour l'orientation du bord à $\sim 5 - 8$ nm pour l'orientation de la vis, ce qui donne une énergie de défaut d'empilement de $30 \pm 5 \text{ mJ} \cdot \text{m}^{-2}$. Otto et al. ^[6] concluent que les séparations partielles relativement importantes (surtout lorsqu'elles sont normalisées par le vecteur de Burgers) impliquent que le glissement transversal est difficile dans cet alliage, ce qui est cohérent avec le glissement plan et les longs empilements de dislocations qu'ils ont observés aux joints de grains.

À des grossissements plus faibles, les dislocations sont longues et courbées de façon régulière sur les plans $\{111\}$ sans direction de ligne préférée, ce qui implique des mobilités similaires des segments de bord et de vis ^[5,8]. Zhang et al. ^[10] ont réalisé des expériences de contrainte MET in situ qui suggèrent que les partiels de Shockley sont plus mobiles que les parfaits (non dissociés), qui sont très lents. Néanmoins, George et al. ^[5] mettent en garde contre le fait de tirer des conclusions sur la mobilité des dislocations à partir d'observations in situ, car aucune information concernant la contrainte de cisaillement localement résolue agissant sur les dislocations mobiles n'était disponible au moment de leur revue (2019).

Laplanche et al. ^[9] ont étudié l'évolution de la microstructure du CoCrFeMnNi à différentes températures et ont conclu qu'elle est nettement différente lorsque la déformation est effectuée à des températures cryogéniques. À 77 K, la distribution des dislocations et l'évolution de leur densité avec la déformation est initialement similaire à celle de la température ambiante. Ils ^[9] ont montré sur cette figure (avec les mêmes conditions de grossissement et de contraste, $\vec{g} = (111)$, et des niveaux de déformation réels similaires) que l'évolution microstructurale est associée à la formation d'empilements de dislocations. Aux alentours de 20% de déformation, des déformations plus importantes entraînent des densités de dislocation plus élevées et finalement leur réorganisation en structures cellulaires. Ils ont mesuré les densités de dislocation après déformation à 293 K et 77 K jusqu'à 20% de déformation en utilisant le MET.

1.3. Maillage mécanique

Le maillage mécanique est un processus de déformation concurrent du glissement des dislocations. La nucléation du maillage mécanique est assistée par des concentrations de contraintes pour surmonter la contrainte de cisaillement résolue critique pour le maillage, $\tau^{\text{CCRC-twin}}$ [11], qui, selon la théorie de Venables, est [11-13]

$$\tau^{\text{CCRC-twin}} = \frac{\gamma b}{b_1(nb - b_1)}$$

Contrainte critique de maillage, selon Venables.

où γ est l'Énergie de Faute d'Empilement (EFE), b est le vecteur de Burgers de la dislocation unitaire, b_1 est le vecteur de Burgers de la dislocation partielle de Shockley, et n est le facteur de concentration de contrainte (ce qui explique pourquoi des macles ont été observés dans certaines zones d'un même cristal alors que dans d'autres, une forte densité de dislocation a été trouvée). Selon Meyers et al. [14], une faible EFE est une condition nécessaire pour l'activation du maillage mécanique. Diao et al. [11] ont comparé les valeurs EFE de différents alliages/éléments, en soulignant ceux pour lesquels l'activation du maillage est plus facile.

La morphologie résultante des macles mécaniques a des épaisseurs allant de quelques dizaines de nanomètres à quelques micromètres [6,7,9,11]. La structure cristallographique des limites de macles faillées est caractérisée par une différence d'orientation $\Sigma 3$, par rapport à la matrice.

Dans leur étude de 2016, Laplanche et al. [9] ont conclu que le durcissement par dislocation uniquement n'est pas suffisant pour atteindre le taux d'érouissage observé et donc que le maillage est nécessaire pour expliquer l'augmentation de la combinaison résistance-ductilité lorsque la température diminue. Par conséquent, ils suggèrent que l'évolution microstructurale est similaire à 77 K et 293 K, et que pour des déformations inférieures à ~7,4%, il n'y a que la plasticité des dislocations et la densité des dislocations augmente de manière similaire aux deux températures, et qu'après cette déformation, le maillage est activé comme mode de déformation supplémentaire.

Sur la base d'une moyenne de 10 essais à 77K et 293 K, Laplanche et al. [9] ont constaté que la limite d'élasticité technique σ_y augmentait de 265 ± 10 MPa à 460 ± 30 MPa et que σ_{uts} augmentait de 600 ± 40 MPa à 1060 ± 70 MPa lorsque la température diminuait. Parallèlement à ce gain de résistance, ils ont également constaté que la ductilité en traction augmentait d'environ 50 % lorsque la température tombait à 77 K.

Leurs résultats sont présentés à la Figure 3. Le panneau (c) montre le taux d'écroissage réel normalisé par le module de cisaillement $((d\sigma/d\varepsilon)/\mu)$ en fonction de la déformation réelle. Là, le taux d'écroissage présente une décroissance monotone avec l'augmentation de la déformation à 293 K, divergeant du taux d'écroissage à 77 K, qui révèle trois étapes distinctes : d'abord, une diminution continue du taux d'écroissage de $\sim\mu/20$ à $\sim\mu/30$ à $\sim 10\%$ de déformation vraie (similaire à ce qui est observé à 293 K) ; ensuite, à des déformations plus importantes (10-35 %), le taux d'écroissage reste presque constant autour de $\mu/30$; et enfin, le taux d'écroissage diminue jusqu'à la rupture à $\sim 44\%$.

Sur cette base, Laplanche et al. ^[9] concluent qu'à 77 K, la déformation vraie à laquelle des macles peuvent être observés de manière cohérente est comprise entre 6,0% et 8,8%, soit $7,4 \pm 1,4\%$, et ils désignent cette valeur comme la "contrainte de maclage" $\sigma_{tw} = 720 \pm 30$ MPa à 77 K, qui, selon eux, est la contrainte critique où le maclage devrait être observé. Cette contrainte de maclage est caractéristique d'un matériau et d'une taille de grain donnés, par conséquent, le maclage devrait être observé également à température ambiante tant que la contrainte dans les éprouvettes de traction atteint cette valeur. Cependant, George et al. ^[5] mettent en garde contre ce résultat, car le matériau polycristallin étudié par l'équipe de Laplanche avait une taille de grain relativement petite de $17 \mu\text{m}$ et, selon Meyers et al. ^[15], la prédisposition au maclage est renforcée lorsque la taille de grain augmente.

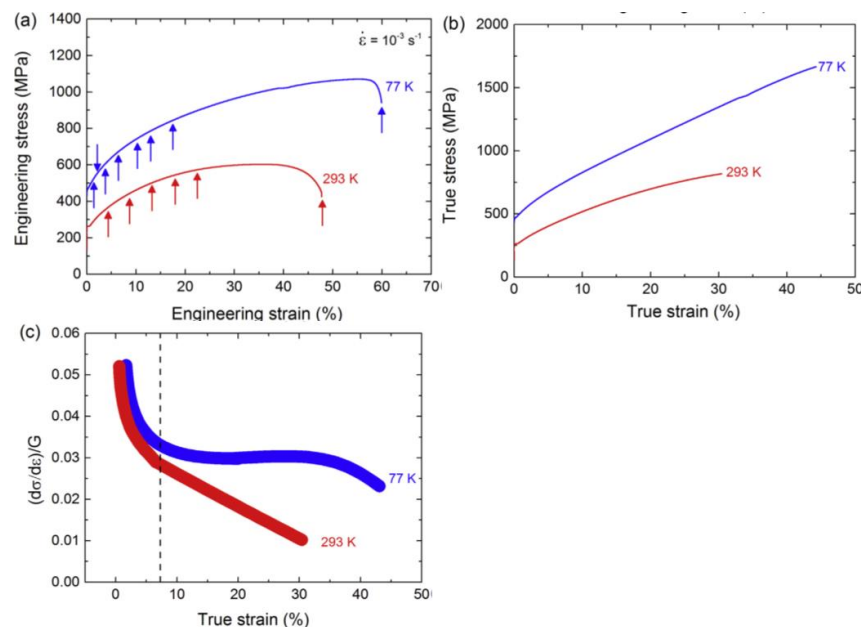


Figure 32 – Courbes représentatives : a) d'ingénierie et b) de contrainte-déformation vraie d'essais de traction à 77 K et 293 K. Les flèches en a) indiquent les déformations auxquelles plusieurs essais de traction supplémentaires ont été interrompus pour étudier l'évolution de la microstructure. c) Taux d'écroissage vrai normalisé par le module de cisaillement en fonction de la déformation vraie. D'après ^[9].

1.4. Énergie de défaut d'empilement et ordre à courte distance dans le CoCrFeMnNi

Comme nous l'avons déjà dit, les macles entravent généralement le mouvement des dislocations et induisent un renforcement, mais les systèmes de macles multiples peuvent également améliorer la ductilité, par exemple, dans les aciers à plasticité induite par macles (TWIP) ou le CoCrFeMnNi, qui ont de faibles énergies de défaut d'empilement et, par conséquent, des séparations relativement grandes entre les partiels de Shockley [16,17].

Plusieurs études de simulation (Monte Carlo basé sur la DFT, modélisation *ab initio*, simulation de dynamique moléculaire) [17-21] ont été réalisées pour prédire le degré d'influence de l'ordre chimique local sur l'EFS dans le CoCrFeMnNi et ses dérivés ("entropie moyenne", alliages à trois éléments, c'est-à-dire CoCrNi, etc. - voir Figure 4), ainsi que l'énergie de maclage, la différence d'énergie entre les phases cubique face centrée et hexagonale (qui régit les effets TRIP et TWIP) et l'énergie de formation des défauts ponctuels, qui sont tous des paramètres connus pour affecter de façon marquée la résistance et la déformation des AHE à base de CoCrNi [5].

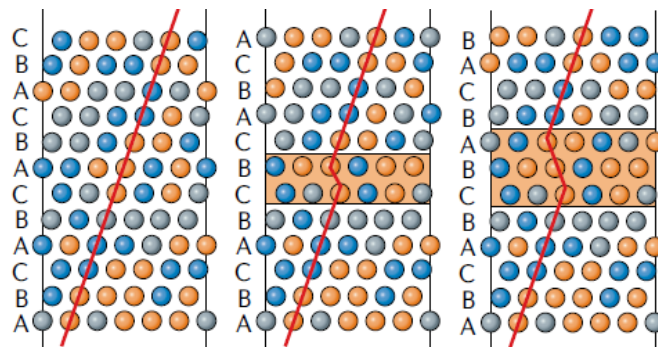


Figure 33 – Rôle de l'ordonnancement chimique local sur l'énergie de défaut d'empilement calculée par DFT pour les alliages CoCrNi en solution solide. Vue latérale des configurations atomiques dans une structure cfc originale (à gauche), avec des défauts d'empilement intrinsèques (au milieu) et des défauts d'empilement extrinsèques (à droite). L'ombre orange indique la faille d'empilement (ABC représente les plans (111) empilés). D'après [21].

Zaddach et al. [22] ont mesuré le EFE pour le CoCrFeMnNi par diffraction des rayons X et ont obtenu une valeur entre 18.3 - 27.3 mJ/m². Huang et al. [18] l'ont quantifiée à température ambiante par mesure expérimentale et par calculs *ab initio* (en utilisant une super-cellule de neuf couches cfc (111) avec un SF intrinsèque), et ont obtenu une valeur de ~21 mJ/m². Ils ont également étudié la dépendance de la température du EFE (Figure 5), suggérant que le CoCrFeMnNi est plus susceptible de se déformer par gémissement avec la diminution de la température. Zhao et al. [19] ont également calculé cette dépendance à la température, trouvant un coefficient de dépendance $d\gamma/dT = 0,11 \text{ mJ/m}^2/\text{K}$.

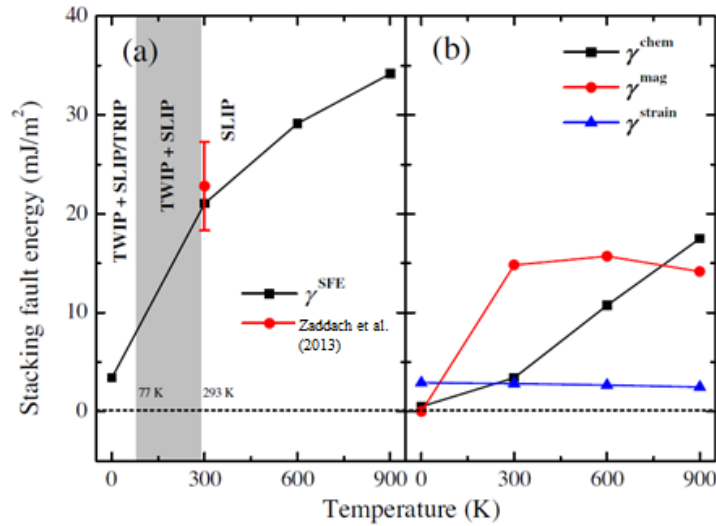


Figure 34 – EFE théorique de l'alliage à haute entropie CoCrFeMnNi. a) EFE total $\gamma^{EFE} = \gamma^{chem} + \gamma^{mag} + \gamma^{strain}$. b) Contribution individuelle : partie chimique γ^{chem} , partie magnétique γ^{mag} et partie déformation γ^{strain} . D'après [18].

Smith et al. [16] ont réalisé des observations MET à haute résolution sur l'alliage Cantor et ont montré que la séparation entre les dislocations partielles est très variable (d'un facteur deux) en différents points le long de la dislocation. Leurs calculs suggèrent que cela peut être dû à des variations de la composition locale, affectant l'énergie locale des défauts d'empilement et donc la séparation partielle (Figure 6).

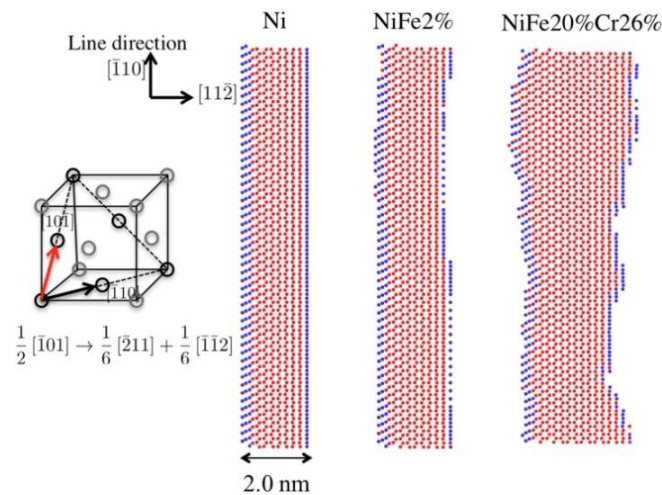


Figure 35 – Variations de la distance de dissociation d'une dislocation mixte $\frac{1}{2}[10\bar{1}]$ dans un alliage concentré Ni-20 at%Fe-26 at%Cr par rapport au Ni pur et à un alliage dilué Ni-2at%Fe. Les dislocations sont créées dans une géométrie globale avec des conditions limites périodiques dans la direction de la ligne. Les atomes bleus appartiennent aux dislocations partielles, tandis que les atomes rouges comprennent la région de défaut d'empilement entre les partiels. La distance de dissociation varie le long de la ligne de dislocation dans l'alliage concentré. D'après

[16].

Huang et al. [18] ont calculé l'énergie de défaut d'empilement en fonction de la température pour l'alliage Cantor, et ont conclu qu'elle diminue brusquement à ~ 3.4 mJ/m² à 0 K. Comme des énergies de défaut d'empilement plus faibles améliorent la capacité de maillage [23,24], ces calculs sont cohérents avec l'observation expérimentale que l'alliage Cantor tend à se jumeler plus facilement lorsque la température diminue [25].

Le rôle de l'ordre chimique local dans les AHE reste une question ouverte car peu d'expériences l'ont confirmé expérimentalement [5]. Une étude, réalisée par Zhang et al. [26], a utilisé la structure fine d'adsorption aux rayons X étendue sur le CoCrNi et a suggéré que les atomes de Cr affichent une préférence pour la liaison aux atomes de Ni et de Co plutôt qu'aux autres atomes de Cr, ce qui, selon George et al. [5], est cohérent avec les prédictions Monte Carlo basées sur la DFT. Cependant, une confirmation expérimentale supplémentaire est nécessaire pour affirmer que cet ordre chimique local existe réellement dans des solutions solides AHE apparemment aléatoires.

2. Méthodologie expérimentale et résultats

2.1. Échantillons et montage expérimental

Trois types de échantillons de CoCrFeMnNi ont été utilisés dans les expériences de déformation MET *in situ* :

Échantillon	Co %	Cr %	Fe %	Mn %	Ni %
35/I2-Head	20	20	20	20	20
X1	20	20	20	20	20
1484Recuit	20	15	26	17	22

Les lingots de chaque type ont d'abord été découpés en échantillons rectangulaires de 3 x 1,5 mm, avec une épaisseur variant de 500 à 800 nm, en utilisant l'usinage par électro-décharge [27]. Ensuite, les échantillons ont été mécaniquement amincis avec du papier SiC dans la région de 30 μ m. Les échantillons rectangulaires ont été, comme étape finale, électropolis dans une unité de polissage à double jet Tenupol de Struers en utilisant un électrolyte d'acide perchlorique à 10% et d'éthanol à 90% pour créer des régions transparentes aux électrons autour d'un trou central, typiquement d'une épaisseur de 50 à 500 nm [27]. La transparence des électrons dépend à la fois de la tension du MET, du numéro atomique moyen des espèces chimiques contenues dans l'échantillon (plus il est grand, moins il est transparent) et, pour les matériaux cristallins, du vecteur de diffraction utilisé pour former les images. Pour l'alliage Cantor étudié dans cette thèse, des régions jusqu'à 800 nm d'épaisseur ont pu être suivies dans des conditions de diffraction spécifiques (voir ci-dessous). De plus, les dislocations ont été caractérisées dans des zones

dont l'épaisseur ne dépassait pas 100 nm afin de garantir une longueur de ligne suffisante. Le processus de préparation a été réalisé par le Service de Préparation des Échantillons du laboratoire CEMES-CNRS. Le processus détaillé peut être trouvé sur ^[28]. L'échantillon final est collé sur une grille en Cu à l'aide d'une colle au 2-cyanoacrylate d'éthyle (Figure 7).

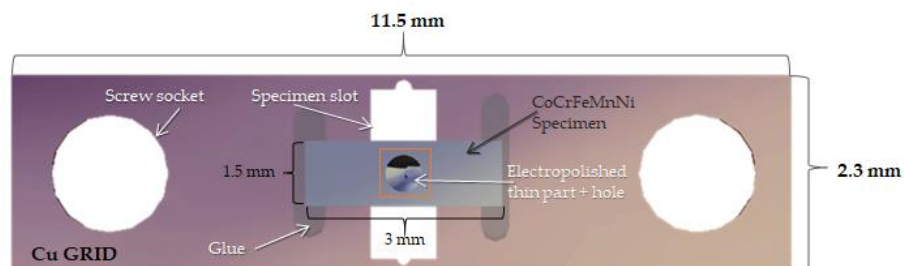


Figure 36 – Modèle d'un échantillon collé sur une grille de Cu. Le cadre orange montre la zone électro-zinguée de l'échantillon avec le trou percé.

Une fois l'échantillon collé sur la grille en Cu, il est ensuite fixé au support de déformation uniaxiale (α tilt) utilisé pour les expériences de déformation MET in situ au moyen de deux vis. Le support utilisé est un support Gatan commercial, modèle 671, refroidi par N₂ liquide, fonctionnant d'environ 100°C (réservoir de N₂ vide et chauffage par résistance) jusqu'à des températures cryogéniques (réservoir de N₂ plein) (Figure 8) piloté par un contrôleur extérieur relié au thermocouple fixé aux mâchoires de l'échantillon. Le support, une fois rempli de N₂, est capable de se stabiliser à une température d'environ 100 K en 30 minutes, lorsqu'un bon vide est atteint dans l'enveloppe du réservoir ^[27]. Le mécanisme d'élongation est composé d'une mâchoire fixe et d'une mâchoire mobile, cette dernière étant déplacée par un contrôleur motorisé avec un seul bouton poussoir qui démarre ou arrête le processus d'élongation, à des vitesses allant de 10 nm/s à 1 μ m/s.

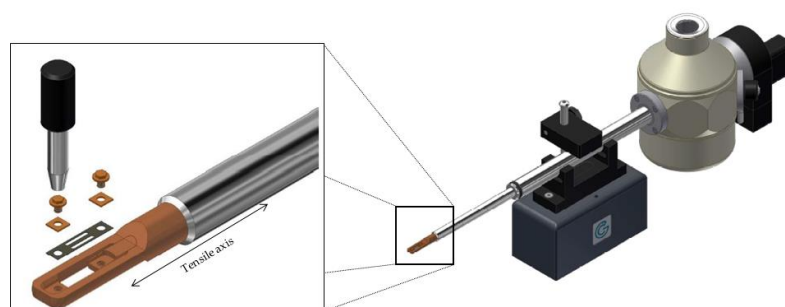


Figure 37 – Support Gatan LN2 avec échantillon mis en place. Images propriété de Gatan®. Insertion montrant la zone de l'échantillon, la grille de traction et les deux vis pour la fixer.

Une fois l'échantillon chargé sur le support, ce dernier est inséré dans le MET. Les expériences de traction in situ ont été réalisées sur un MET JEOL 2010 LaB₆ fonctionnant

à 200 KeV. En fonction de la température souhaitée pour une expérience spécifique, le réservoir du support est rempli ou non de N₂ liquide (pour les essais à température ambiante : TA, ou à la température de l'azote liquide : TAL). La stabilisation de la température nécessite entre quelques minutes et environ une demi-heure avant de commencer le filtrage, selon le degré de froid souhaité. Une fois l'équilibre thermique atteint grâce au transfert de chaleur par conduction entre le support et l'échantillon, la déformation peut commencer.

Pendant les expériences in situ, de courtes impulsions de déformation (de l'ordre de 10^{-3} s⁻¹) sont appliquées, séparées par des périodes plus longues pendant lesquelles les mouvements des dislocations sont observés. En moyenne, la vitesse de déformation des expériences in situ est de l'ordre de 10^{-4} à 10^{-5} s⁻¹ [27]. La contrainte maximale appliquée dans l'échantillon correspond à la région où le bord du trou est parallèle à l'axe de déformation [29], car le trou introduit une concentration de contrainte. De plus, dans les zones avec des fractures préexistantes sur le bord du trou, il y a plus de tendance à déclencher la déformation en réponse à l'application de la contrainte [30].

La figure 9 montre un échantillon, électropoli pour obtenir une zone mince où un trou a été percé selon la méthode de préparation déjà présentée. La partie (c) de la figure montre le bord du trou autour duquel on peut distinguer plusieurs grains différents (délimités par des lignes pointillées blanches). Chaque grain a sa propre orientation cristalline, qui peut être déterminée pendant l'essai de contrainte MET in situ.

Comme on peut le voir sur l'image, la taille de chaque grain varie de quelques microns à plusieurs dizaines de microns. Il y a beaucoup plus de grains présents dans un échantillon, mais pendant une expérience de contrainte MET in situ, on n'a accès qu'aux zones transparentes aux électrons de l'échantillon, c'est-à-dire uniquement les grains dans la partie amincie de l'échantillon autour du trou. Cela ne laisse que quelques grains où la déformation plastique peut être observée. Parmi ces grains, seuls ceux qui sont voisins du trou et perpendiculaires à l'axe de déformation auront une concentration de contraintes suffisamment importante pour déclencher une déformation plastique, ce qui réduit encore les zones où les systèmes de glissement s'activeront.

Pour mieux cibler les grains où la déformation peut être observée, l'orientation du cristal doit être connue afin d'identifier les plans de glissement possibles et leurs directions. De plus, le calcul des facteurs de Schmid pour chaque combinaison plan de glissement/vecteur de Burgers est un bon indicateur des systèmes de glissement les plus susceptibles de s'activer sous déformation en traction [29].

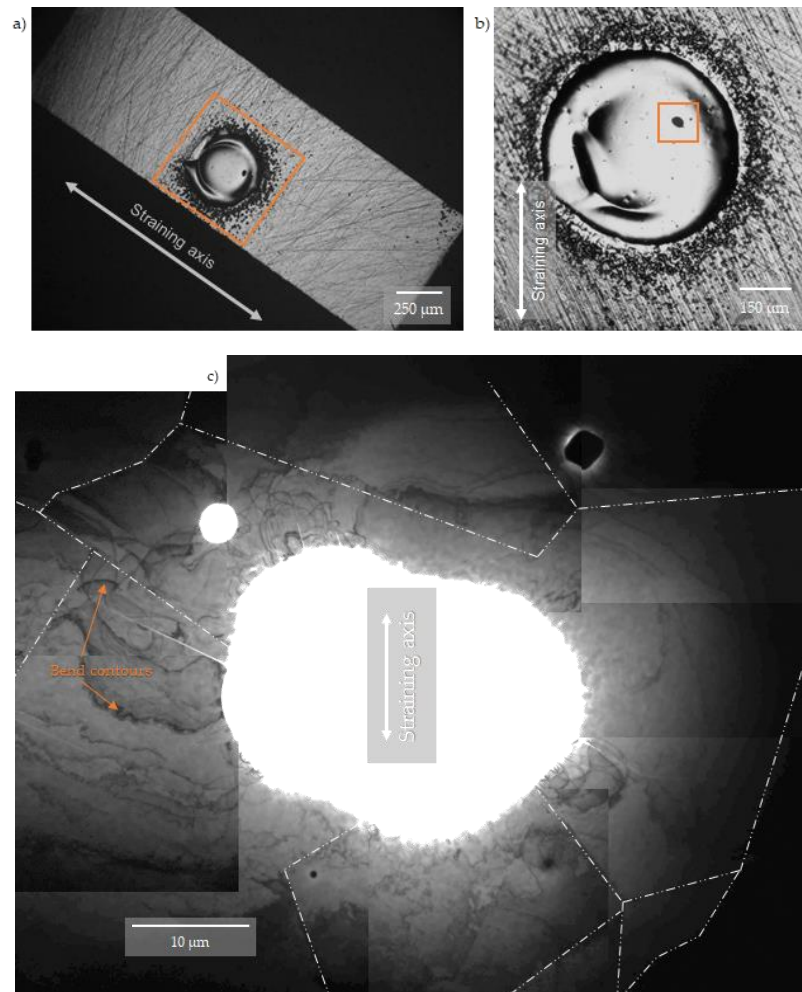


Figure 38 – a) Image au microscope optique d'un échantillon ; le cadre orange indique la zone amincie par électropolissage et le trou. b) Image au microscope optique à un plus fort grossissement montrant la zone mise en évidence dans la partie précédente. Le deuxième cadre orange indique le trou autour duquel la déformation sera observée. c) Image MET composée du trou électropoli, montrant plusieurs grains autour de celui-ci (lignes pointillées blanches), identifiés en raison de la différence de contraste entre les zones lors du basculement ; les flèches orange signalent des exemples de contours de flexion. Toutes les images indiquent la direction correspondante de l'axe de déformation sur l'expérience.

En tout, le chapitre 2 a présenté les échantillons et la technique utilisés dans cette étude. Les bases théoriques ont été données et les différents paramètres qui peuvent être déterminés à partir des expériences de déformation MET in situ ont été présentés.

Le chapitre 2 explique comment :

- Identifier les dislocations en MET (parfaites - non dissociées et dissociées en partielles de Shockley, et maillage).
- Indexer ces dislocations pour connaître leur système de glissement (plan de glissement et vecteur de Burgers).

- Obtenir l'orientation cristallographique d'un grain étudié (grâce aux diagrammes de diffraction obtenus à partir de l'expérience in situ).
- Calculer l'épaisseur locale de l'échantillon (et, par extension, d'autres mesures projetées) à partir de l'image MET projetée.

3. Mécanismes de plasticité dans l'alliage CoCrFeMnNi

Les dislocations dans l'alliage CoCrFeMnNi se comportent comme suit (selon, entre autres, ^[6,8,9]) :

- Le glissement est initié par le glissement planaire de $1/2 \langle 110 \rangle$ dislocations parfaites sur les plans $\{111\}$ qui peuvent se diviser en $1/6 \langle 112 \rangle$ partiels de Shockley.
- Pour que le glissement se produise, une contrainte critique " σ_{tw} " (ou "contrainte de glissement") doit être atteinte, selon Laplanche et al. ^[9].
- Le maillage est observé à basse température (77 K) au-dessus de la contrainte critique, uniquement après le glissement planaire de dislocations parfaites.
- Peu ou pas de maillage est observé à température ambiante (voir ^[9,31]). Une exception est l'étude faite par Kireeva et al. ^[32], où ils ont observé un maillage à température ambiante, à une contrainte beaucoup plus faible que l'étude de Laplanche et al. mentionnée précédemment.
- Le glissement croisé est difficile dans cet alliage, selon Otto et al. ^[6].

3.1. Calcul de la contrainte de cisaillement résolue critique (CCRC)

Lors de la réalisation d'une expérience de déformation MET in situ, la contrainte appliquée exacte n'est pas connue (comme expliqué au chapitre 2). Cependant, la CCRC peut être mesurée localement en utilisant le rayon de courbure d'une boucle de dislocation, en utilisant l'équation suivante :

$$R = \frac{\mu b}{\tau}$$

Courbure d'une boucle de dislocation.

où R est le rayon de courbure, μ est le module d'élasticité, b est le vecteur de Burgers et τ est la CCRC.

En utilisant cette équation, les valeurs CCRC pour un réseau de 24 dislocations isolées mais actives provenant de différents échantillons ont été mesurées, à la fois à la température ambiante et à la température de l'azote liquide.

Les moyennes calculées dans les tableaux montrent que la résistance (mesurée localement) à TA est de (222 ± 9) MPa et à TAL de (291 ± 12) MPa. Ces résultats sont en accord avec la tendance selon laquelle l'alliage Cantor est plus résistant lorsque la température diminue. En raison du large éventail de systèmes de glissement mesurés, la dispersion des valeurs est également importante. Selon le rayon et la forme de chaque dislocation mesurée, les valeurs de τ changent, ce qui permet de conclure que la direction du système de glissement (son orientation) joue un rôle important sur la résistance de l'échantillon.

τ et σ mesurés localement pour un réseau de dislocations sur des échantillons déformés à $T = 293\text{K}$.

	Échantillon	Système de glissement	Facteur de Schmid m	τ (MPa)	σ_{exp} (MPa)
1	35/I2-Head13	$(\bar{1}11)[0\bar{1}1]$	0.46	90 ± 3	194 ± 7
2	35/I2-Head14	$(1\bar{1}1)[\bar{1}01]$	0.27	140 ± 3	518 ± 11
3	35/I2-Head14	$(1\bar{1}1)[011]$	0.46	70 ± 3	153 ± 6
4	35/I2-Head14	$(\bar{1}11)[101]$	0.45	170 ± 3	379 ± 7
5	35/I2-Head15	$(1\bar{1}\bar{1})[101]$	0.33	40 ± 2	121 ± 7
6	35/I2-Head24	$(\bar{1}\bar{1}1)[\bar{1}0\bar{1}]$	0.44	60 ± 2	137 ± 6
7	35/I2-Head24	$(111)[0\bar{1}1]$	0.22	30 ± 3	137 ± 12
8	35/I2-Head30	$(\bar{1}\bar{1}1)[1\bar{1}0]$	0.34	80 ± 2	236 ± 7
9	35/I2-Head30	$(111)[1\bar{1}0]$	0.14	50 ± 2	353 ± 18
10	35/I2-Head43B	$(\bar{1}11)[101]$	0.27	40 ± 2	151 ± 9
11	X1-21	$(\bar{1}11)[0\bar{1}1]$	0.38	26 ± 2	69 ± 6
Moyenne				72 ± 2	222 ± 9

τ et σ mesurés localement pour un réseau de dislocations sur des échantillons déformés à des températures cryogéniques.

	Échantillon	Système de glissement	Facteur Schmid m	T	τ (MPa)	σ_{exp} (MPa)
1	35/I2-Head22	$(\bar{1}11)[011]$	0.40	96	90 ± 3	226 ± 7
2	35/I2-Head22	$(\bar{1}11)[0\bar{1}1]$	0.32	96	150 ± 2	467 ± 7
3	35/I2-Head28	$(\bar{1}\bar{1}1)[1\bar{1}0]$	0.11	103	70 ± 3	660 ± 32
4	35/I2-Head28	$(\bar{1}11)[0\bar{1}1]$	0.46	103	120 ± 3	261 ± 6
5	35/I2-Head28	$(\bar{1}\bar{1}1)[\bar{1}10]$	0.36	103	62 ± 2	173 ± 7
6	35/I2-Head28	$(\bar{1}11)[\bar{1}\bar{1}0]$	0.46	103	135 ± 3	293 ± 6
7	35/I2-Head29	$(\bar{1}\bar{1}1)[1\bar{1}0]$	0.41	104	160 ± 3	388 ± 7
8	35/I2-Head29	$(1\bar{1}1)[\bar{1}01]$	0.46	104	55 ± 3	120 ± 6
9	35/I2-Head29	$(111)[0\bar{1}1]$	0.06	104	28 ± 2	452 ± 39
10	X1-21	$(\bar{1}11)[\bar{1}\bar{1}0]$	0.48	102	39 ± 2	82 ± 5
11	X1-21	$(\bar{1}11)[0\bar{1}1]$	0.38	102	30 ± 2	79 ± 6
Moyenne					85 ± 3	291 ± 12

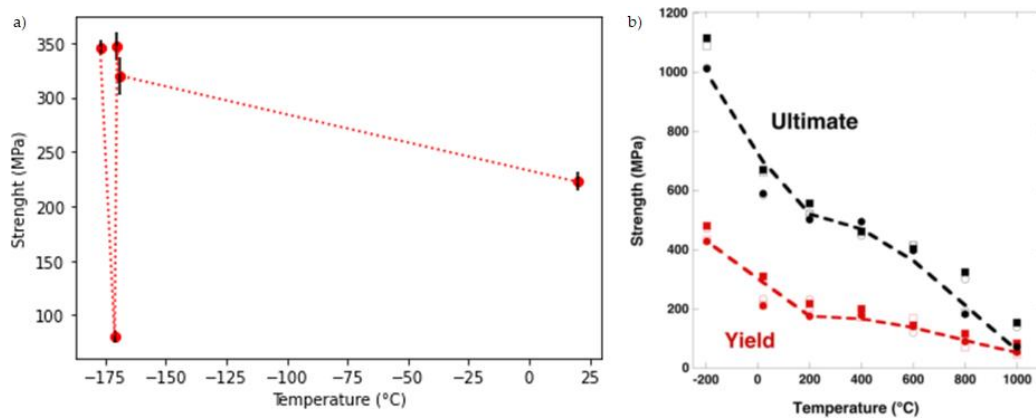


Figure 39 – Résistance à la traction en fonction de la température pour les alliages CoCrFeMnNi. a) Calculée expérimentalement dans cette étude, pour des éprouvettes rectangulaires de 3 x 1 mm. En rouge, la position des moyennes pour chaque température testée ; en noir, leurs barres d'erreur respectives. b) Résultats de Gali et George ^[4], pour des échantillons en forme d'arête de chien de sections de 10 x 2.5 x 0.63 mm déformés dans une machine d'essai de traction.

D'après le graphique de la partie (a) de la figure, il est clair qu'il y a une tendance à la diminution de la résistance avec l'augmentation de la température. La seule exception est donnée par l'échantillon testé à 102 K (-171 °C). Cela peut être dû au fait que la mesure a été prise à faible déformation ou au fait qu'il ne s'agit pas du même type d'échantillon (X1 vs. 35/I2-Head).

En comparant ces résultats à ceux décrits dans la littérature (par exemple, les essais de traction *ex situ* réalisés par Gali et George ^[4]), on peut conclure que les essais de traction *in situ* sur le CoCrFeMnNi sont analogues aux essais de traction macroscopiques (voir Figure 10), donc

$$\sigma_{\text{exp}} \approx \sigma_y$$

(σ_{uts} n'a pas été mesurée expérimentalement car les échantillons n'ont jamais été déformés jusqu'à la rupture pendant les expériences de traction *in situ*). Il est important de mentionner que la figure 10(a) a été construite en utilisant la moyenne de σ_{exp} pour chaque plage de température mesurée (96, 102, 103, 104 et 293 K) et que T a été convertie de K en °C pour faciliter la comparaison avec la partie (b) de la figure.

3.2. Mouvement des dislocations

- Le glissement planaire dans CoCrFeMnNi suit ce qui est attendu dans un métal cfc typique : les dislocations avec un vecteur de Burgers de $1/2\langle 110 \rangle$ glissent dans le plan $\{111\}$, et se dissocient asymétriquement en deux partiels de Shockley de type $1/6\langle 112 \rangle$.

- La valeur de la dissociation change en fonction de l'orientation du cristal, de la contrainte appliquée, de la température, mais aussi en fonction de l'arrangement atomique local. En moyenne, cette EFE est faible, de l'ordre de 8 à 15 mJ/m².
- La dissociation d'une dislocation parfaite peut donc se produire sans obstacle à condition que l'orientation soit favorable. Cela conduit au développement de failles d'empilement étendues. Ces failles d'empilement étendues servent de germes à l'expansion des macles mécaniques.
- Malgré cette faible EFE, le glissement transversal est fréquemment observé dans cet alliage. Cela semble être une réponse à l'activation du mécanisme de Friedel-Escaig lorsque les dislocations sont arrêtées sur des obstacles forts (joints de grains, macles).

3.3. Maclage

Les expériences MET in situ présentées jusqu'à présent montrent que l'activation du maclage ne dépend pas d'une contrainte critique ou de la température. Cependant, il est clair qu'une contrainte de cisaillement appliquée est capable de diviser la dissociation asymétrique des dislocations parfaites, même au moment ou juste avant le début de la déformation plastique [27].

La figure 11 reproduit la variation de la contrainte de cisaillement de Peach-Kohler agissant sur les deux dislocations partielles \vec{b}_{p1} et \vec{b}_{p2} qui composent une dislocation parfaite \vec{b} pour le système de glissement avec le facteur de Schmid le plus élevé. La différence de contrainte τ'_a entre le cisaillement agissant sur la composante de bord de chaque dislocation partielle (σ_{yz}^1 et σ_{yz}^2) va favoriser la constriction de la dislocation b lorsqu'elle est positive ou sa dissociation lorsqu'elle est négative. Cette contrainte d'Escaig est ensuite tracée dans un triangle stéréographique standard pour le système de glissement le plus favorable. Lorsque le cristal est chargé en tension, τ'_a atteint les plus fortes valeurs positives (zone rouge) près de l'orientation 001. Dans la région bleue, τ'_a est négatif et la contrainte appliquée tend à augmenter le fractionnement [33,34]. En compression, l'inverse se produirait.

Compte tenu de cela, une analyse des grains soumis à la contrainte à la température ambiante (où le système de glissement primaire a été activé) a été effectuée et chaque orientation cristallographique a été tracée dans un triangle stéréographique standard (veuillez considérer qu'il peut y avoir de légères variations de position parce que l'axe de contrainte a tendance à s'aligner parallèlement aux bords du trou dans les zones les plus minces ; par conséquent, dans une expérience donnée où plusieurs grains sont soumis à la contrainte en même temps, les orientations des grains sont recueillies lorsque l'axe de traction réel est à $\pm 15^\circ$ de l'axe macroscopique).

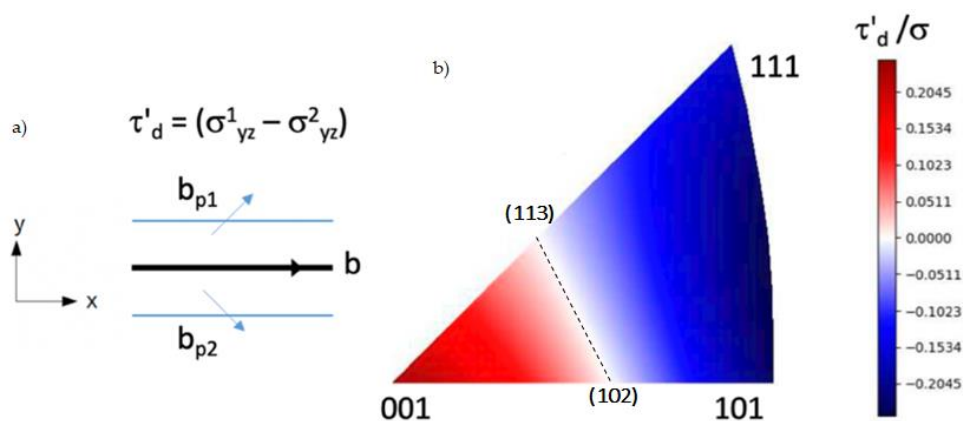


Figure 40 – Division d'Escaig de deux dislocations partielles en fonction de la direction de la contrainte appliquée en traction. a) b_{p1} et b_{p2} (type $a/6\langle 112 \rangle$) composent une dislocation parfaite b (type $a/2\langle 110 \rangle$) divisée dans le plan (xy) . τ'_d est la différence entre les contraintes de Peach-Koehler agissant sur les composantes des bords de b_{p1} et b_{p2} . b) Signe et amplitude de τ'_d en fonction de la direction de la contrainte appliquée dans le triangle stéréographique standard. Figure réalisée par Frédéric Momprou, d'après [27]. La ligne pointillée montre la limite d'orientation où les composantes subissent une contrainte égale (directions (113) à (102)).

Le triangle stéréographique standard a été construit à partir des angles d'Euler de chaque grain étudié, par rapport à l'axe de traction, en utilisant le logiciel ATEX [35]. Le résultat à température ambiante est présenté dans la Figure 12, et pour la température cryogénique dans la Figure 13 (chaque point correspond à l'axe de déformation du grain déformé) : les points bleus représentent les orientations où le maillage était activé, et les points rouges où seul le glissement parfait était actif ; les points gris représentent les grains où seuls les systèmes de glissement secondaires étaient actifs.

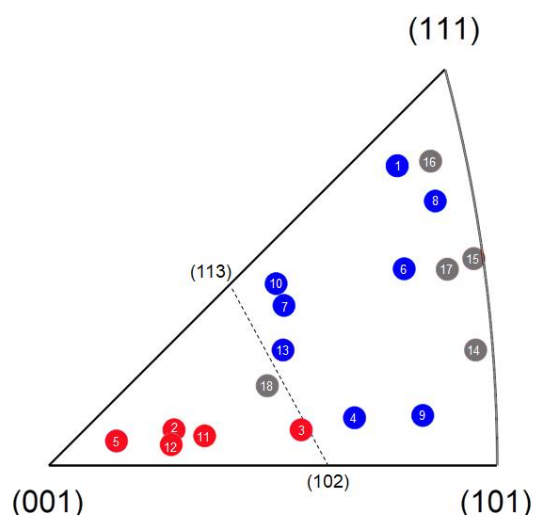


Figure 41 – Dépendance de l'orientation du micro maillage (points bleus) par rapport au glissement parfait des dislocations (points rouges) dans un triangle standard à température ambiante. Adapté de [27]. La limite est donnée par la ligne pointillée (directions (113) à (102)). Les points gris montrent les grains où des systèmes autres que le primaire ont été activés.

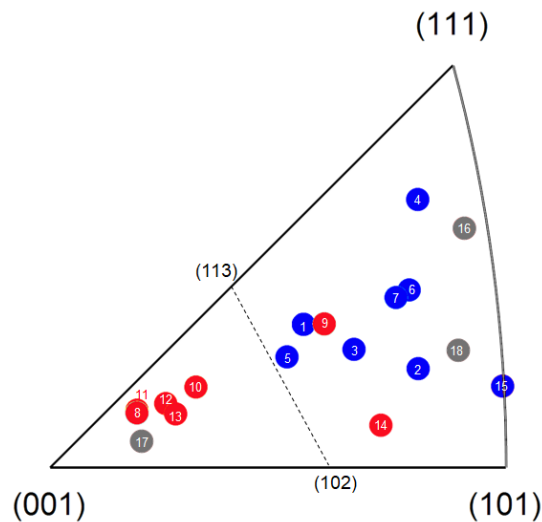


Figure 42 – Dépendance de l'orientation du micro maillage (points bleus) par rapport au glissement parfait des dislocations (points rouges) dans des triangles standards à des températures cryogéniques. Adapté de [27]. La limite est donnée par la ligne pointillée (directions (113) à (102)). Les points gris montrent les grains où des systèmes autres que le primaire ont été activés.

4. Mouvement des dislocations dans le paysage atomique local

Pour aider à élucider la véritable différence entre le comportement des dislocations aux deux températures étudiées, le même échantillon a été déformé à la fois à TA et à TAL. Les résultats de cette analyse montrent que, sous l'influence d'un certain τ , les dislocations se déplacent vers l'avant. Elles le font, non pas avec un déplacement régulier, mais dans ce qui a été défini comme un mouvement "saccadé" ou "lent" (qui a suggéré une friction élevée du réseau [6,10]). Ce mouvement saccadé des dislocations est présenté dans ce travail comme des "sauts". Ces sauts sont mis en évidence lors d'une contrainte MET in situ comme des dislocations se déplaçant vers l'avant, puis faisant une pause pendant un certain temps, et enfin "sautant" dans une nouvelle position.

4.1. Mouvement des dislocations

Pour comprendre la signification de ces sauts, un ensemble de dislocations se déplaçant en pile-up a été choisi, à la fois à TA et à TAL, et la distance de leurs sauts a été calculée. Les figures 14 et 15 présentent ces dislocations. Leur mouvement a été suivi dans le temps, et les figures le présentent de la manière suivante : la dislocation choisie est surlignée en noir, chaque saut effectué par la dislocation est marqué en rouge (suivi de jaune et de vert lorsque cela est pertinent).

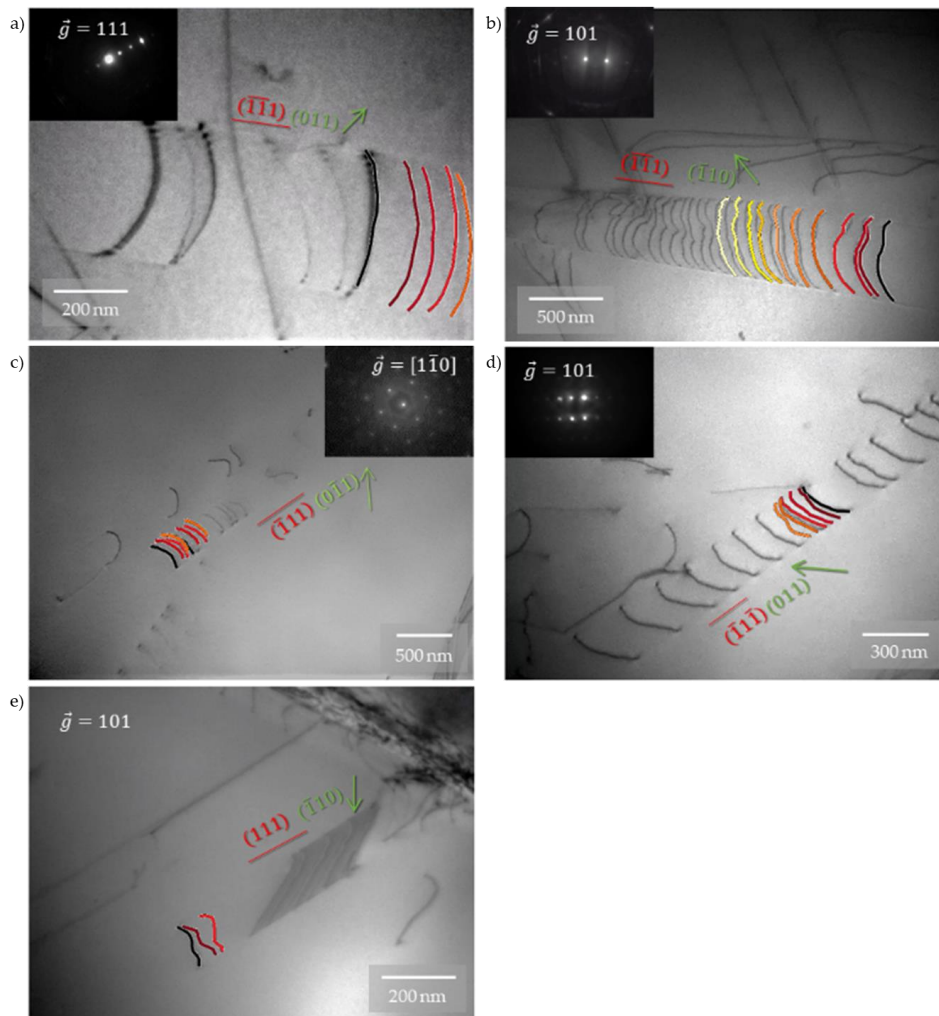


Figure 43 – Suivi temporel des sauts de dislocations à TAL. Échantillons : a) et b) 35/I2-Head22, c) X1-21, d) et e) X1-29.

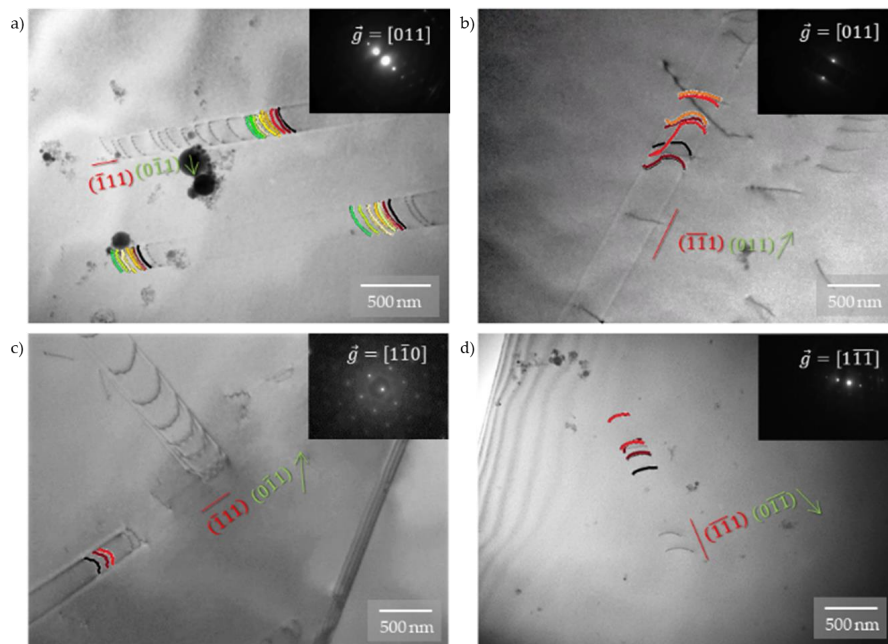


Figure 44 – Suivi temporel des sauts de dislocations à TA. Échantillons : a) X1-24, b) X1-21, c) X1-23, d) X1-24.

Une analyse plus approfondie de ces mouvements a été effectuée et elle est présentée dans la figure 16. En comparant la distance de saut en fonction du temps de pause pour chaque dislocation, il est clair que :

- Elles avancent dans des séquences de mouvement de type "plateau" (parties (a) et (c) de la figure).
- Les "plateaux" (distances de saut) ont une périodicité apparente dans le mouvement d'une seule dislocation, surtout lorsqu'elle fait partie d'un empilement plus dense. Ceci est mis en évidence, par exemple, dans le mouvement des dislocations 1 et 3 (TA, partie (a) de la figure) et des dislocations 2 et 5 (TAL, partie (c) de la figure).
- Les sauts sont plus courts lorsque la dislocation fait partie d'un empilement plus dense, si elle n'est pas la première ou la dernière dislocation de l'empilement, ou s'il y a plus d'empilements glissant dans le voisinage de celui auquel elle appartient. Cela signifie que l'interaction avec les autres dislocations affecte le mouvement / la distance parcourue par la dislocation sélectionnée.
- La distance moyenne pour un saut à TA est de 109 nm, et à TAL elle est de 129 nm (parties (b) et (d) de la figure).
- Les temps de pause moyens pour un saut sont $\bar{\Delta t}_{TA} = 45$ s contre $\bar{\Delta t}_{TAL} = 19$ s.
- Les dislocations semblent se déplacer vers des positions spécifiques. Veuillez-vous référer, par exemple, au cas présenté dans la partie (b) de la figure 14 : la dislocation sélectionnée (masque noir) se déplace au fil du temps vers des positions qui coïncident avec la position d'autres dislocations dans l'empilement (les masques successifs se superposent aux dislocations dans l'image MET). Cela semble suggérer qu'il existe un chemin d'atomes qui bloque ou permet le passage des dislocations (lié aux fluctuations chimiques), et ce chemin change avec la température, ce qui suggère que ces fluctuations chimiques agissent comme des obstacles au mouvement des dislocations.

Comme présenté dans les dernières sections du chapitre 1, le réseau dans l'alliage CoCrFeMnNi est déformé par les fluctuations chimiques. C'est le comportement des dislocations traversant ce paysage atomique déformé qui révélera ce qui se passe dans le cristal. À la lumière de ces éléments, différentes questions découlent des résultats ci-dessus : pourquoi les dislocations sautent-elles ? Et comment la température influence-t-elle les sauts (distance plus longue / temps plus court) ?

De nombreuses études de simulation ont été réalisées pour relier le comportement de déformation plastique aux fluctuations chimiques locales (FCL) dans les AHE (voir [21,36]), car elles provoquent la variation de l'énergie de défaut d'empilement généralisé local et de la résistance du réseau. On rapporte que le réglage des FCL améliore la résistance et la ductilité de ces alliages (voir [37,38]).

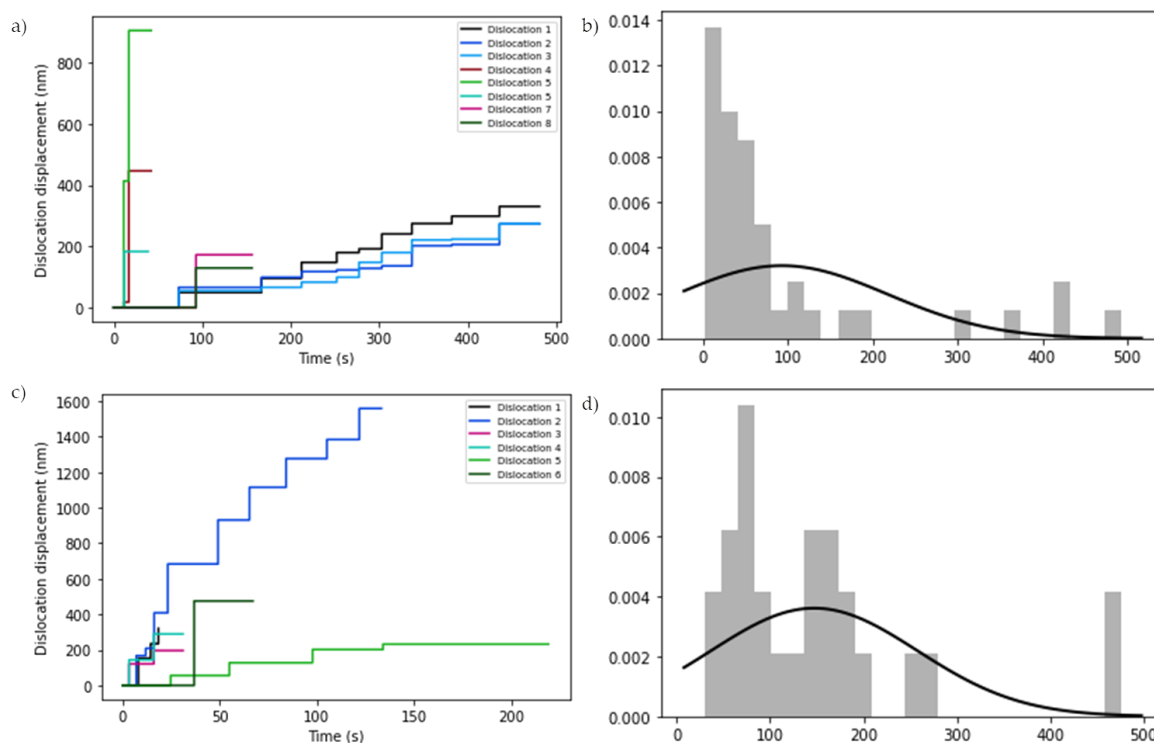


Figure 16 - a) Distances de saut pour les dislocations à TA. b) Distribution des valeurs de saut à TA. c) Distances de saut pour les dislocations à TAL. b) Distribution des valeurs de saut à TAL.

Le paysage atomique local (PAL) du CoCrFeMnNi est propice aux régions enrichies qui pourraient agir comme des obstacles et d'autres qui ont des liaisons de cisaillement favorables. Ces obstacles semblent être plus forts à basse température. Cette analyse est présentée dans la section suivante.

4.2. Obstacles

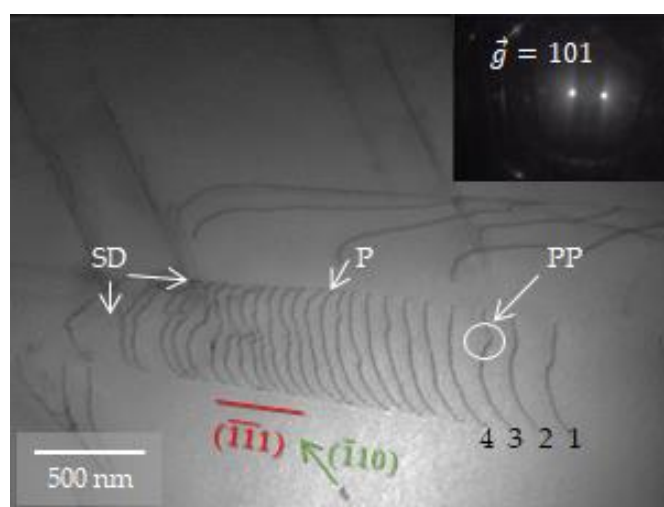


Figure 45 – Échantillon 35/I2-Head22, déformé à T = 96 K. En blanc, dislocations parfaites "P", dislocations sessiles "DS" et points d'épingleage "PE" ; en noir, identification de la position de la dislocation dans l'empilement (pour référence).

Les PE sont encerclés en blanc dans les figures précédentes, courbant la ligne de dislocation (celle qui est ancrée - dislocation 3 dans la figure, par exemple), et apparemment aussi déformant les dislocations à proximité, comme le montre la courbure des dislocations 2 et 1, qui ne sont pas épinglées et présentent néanmoins un changement sur leurs courbures. Le changement de courbure de la dislocation est caractéristique de la présence d'un PE, qui ne bloque qu'un segment de la dislocation tandis que le reste continue à se déplacer, en s'incurvant, jusqu'à ce qu'il atteigne une contrainte suffisamment importante pour surmonter l'obstacle et se libérer, revenant à une courbure plus "lisse" (comme dans le cas de la dislocation 4).

Le calcul de la résistance d'un PE à partir d'images fixes MET in situ n'est pas une tâche facile. Considérons l'exemple présenté dans la Figure 18, où les échantillons ont été déformés à $T = 96\text{ K}$ et $T = 293\text{ K}$, respectivement. La figure présente les mesures pour chacun de ces exemples (en considérant que λ_1' , λ_2' et ϕ' sont des projections, comme indiqué ci-dessus).

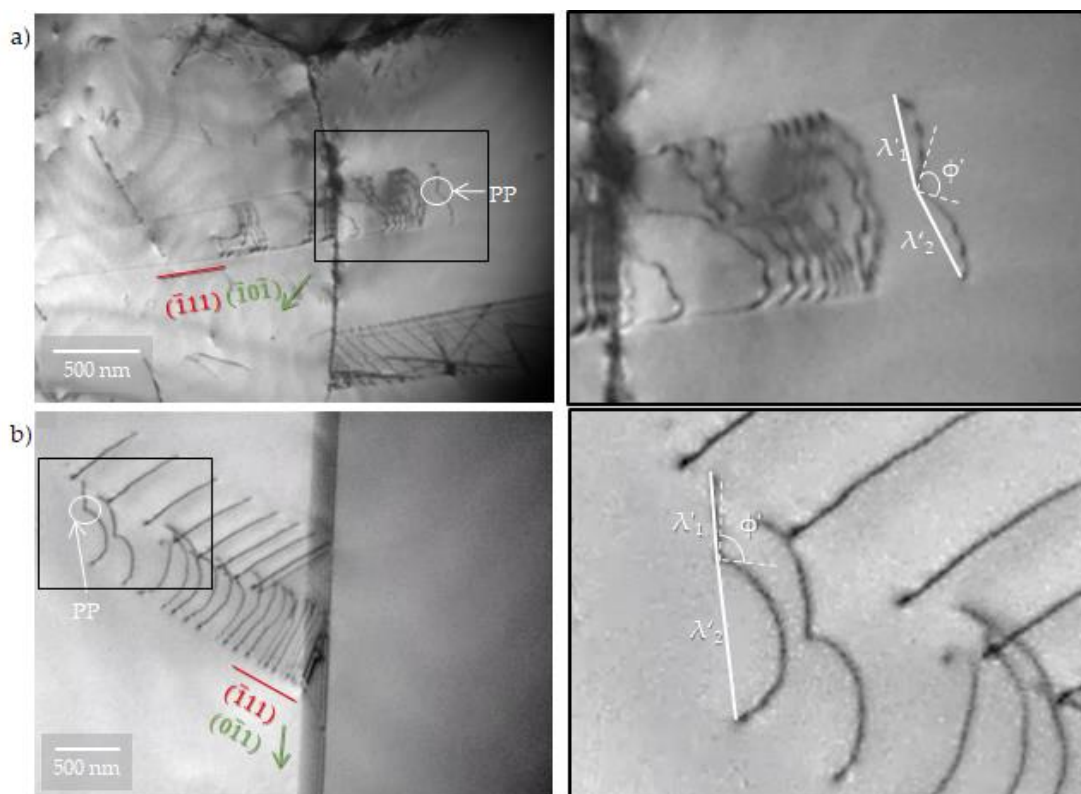


Figure 46 – Angles de courbures dus aux points d'épinglage à : a) température cryogénique, b) température ambiante. Les encarts sont des agrandissements des cadres noirs dans leurs images respectives (échelle 1 :3).

Les PE n'étaient pas seulement présents dans les exemples ci-dessus. Ils ont été observés pendant la majorité des expériences de stratification MET in situ, à la fois à TA et à des

températures cryogéniques. Ils semblaient être soit moins nombreux, soit plus faciles à surmonter à TA qu'à TAL, ce qui semble suggérer que la température joue un rôle dans le renforcement des PE.

Calcul de la résistance des points d'épinglage.

	b (nm) ¹	μ (GPa) ²	φ (°)	λ₁ (nm)	λ₂ (nm)	Δλ (nm)	τ_o	
							(MPa)	(μb ²)
TA	0.254	80	131	300 ± 6	534 ± 6	417 ± 6	1.4 ± 0.4	0.0003
TAL	0.255	85	119	272 ± 6	310 ± 6	291 ± 6	4.8 ± 1.3	0.0009

¹ D'après [39].

² D'après [40].

Les résultats du tableau ci-dessus ont été calculés en utilisant les valeurs $\Delta\lambda$, car les PE ne sont pas dans la position idéale (milieu de la boucle de dislocation, pliant la dislocation en deux segments égaux). Ce seul fait introduit une erreur dans les résultats (d'où la grande erreur dans les résultats). La tendance de τ_o est cependant remarquable : la force du PE à 96 K est environ trois fois plus grande qu'à 293 K, ce qui permet de conclure que les PE à température cryogénique sont effectivement plus forts qu'à TA.

Une fois encore, une explication possible des PE est le FCL (considéré comme influençant la multiplication et le mouvement des dislocations [37,38,41,42]). Pour développer cette notion, et dans le cadre du projet ERC MuDiLingo, Zhang et al. [43] ont lancé une approche complètement nouvelle dans laquelle les dislocations sont utilisées comme des sondes et leurs mouvements et courbures peuvent "imager" le paysage cristallin et chimique local. Même des précipités ou des défauts non détectables (comme une forêt de dislocations) peuvent apparaître à travers un changement de courbure ou un mouvement non-homogène dans l'alliage.

Une étude topologique complète des points d'épinglage a été réalisée sur l'échantillon 35/I2-Head22 (déformé à T = 96 K, par l'équipe ERC MuDiLingo en France). Des approches (réalisées par l'équipe ERC MuDiLingo en Allemagne) comprenant l'exploration de données et la reconstruction de la microstructure des dislocations en 3D à partir de l'image MET (Figure 17) ont été impliquées (voir leur étude pour les méthodes).

Dans le CoCrFeMnNi, contrairement aux alliages conventionnels durcis par soluté, la force effective des points de pincement (distorsion du réseau due à l'ordonnement local) peut évoluer de manière "aléatoire". Certains points de pincement sont durcis tandis

que d'autres sont affaiblis, car différentes liaisons atomiques sont brisées et reconstruites par le glissement des dislocations ^[43]. Comme dans les matériaux métalliques, la liaison est principalement médiée par les électrons partagés par les atomes, bien que certaines liaisons covalentes puissent également être présentes, les interactions atomiques qui en résultent sont de courte portée en raison de l'écran fourni par les électrons partagés ^[44].

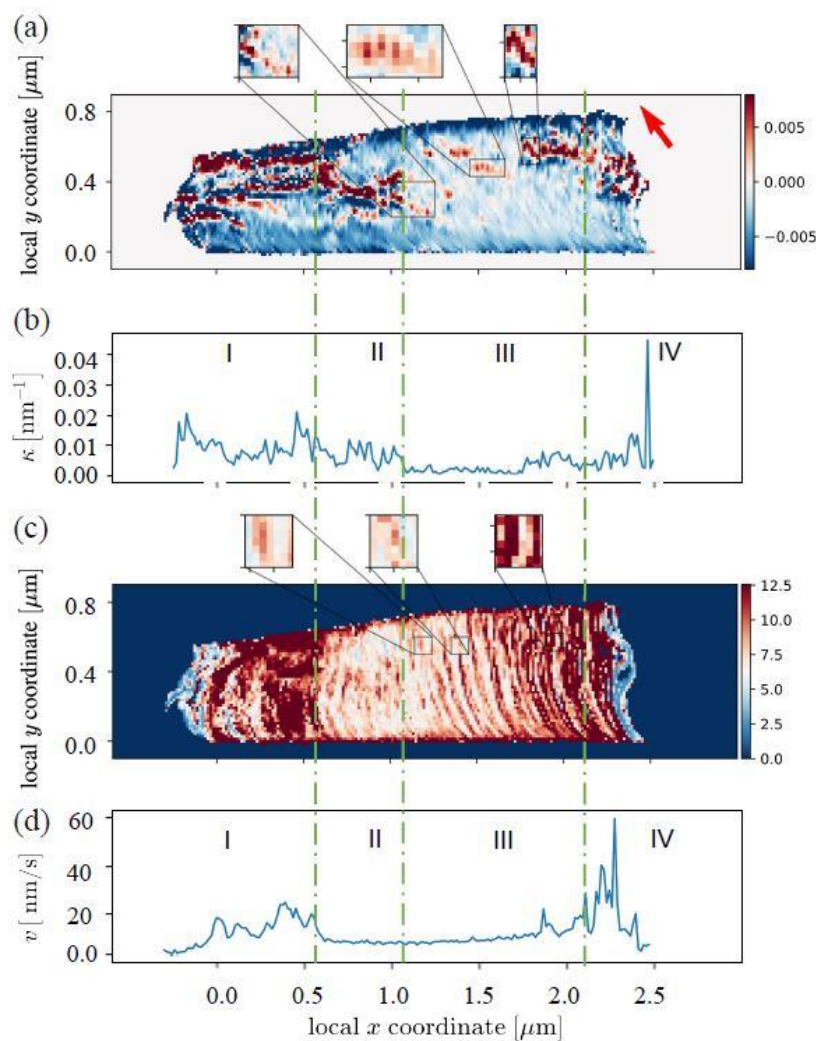


Figure 47 - Moyenne spatio-temporelle de la courbure et de la vitesse à partir d'images fixes tirées de la vidéo supplémentaire 7. a) Distribution de la courbure avec une taille de pixel de 15 nm. b) La moyenne de la courbure le long de l'axe y. c) Distribution de la vitesse avec une taille de pixel de 15 nm. d) La vitesse moyenne le long de l'axe y. D'après ^[43].

L'énergie cohésive pour les liaisons atomiques est la plus faible pour les paires Mn (Mn-Mn, Mn-Cr, Mn-Co, Mn-Ni, Mn-Fe ; toutes $< 0,122$ eV), et la plus élevée pour les paires Fe (Fe-Fe, Fe-Ni, Fe-Co, Fe-Cr ; toutes $> 0,227$ eV), avec une énergie de cohésion élevée également pour les paires Ni-Ni (0,230 eV) et Ni-Co (0,229 eV) (les valeurs de l'énergie de cohésion ont été calculées par modélisation par Gröger et al. ^[44], en adaptant le potentiel de Lennard-Jones à longue portée. En raison du caractère aléatoire de l'alliage, ils ont

déterminé par leur modèle que 80 % des liaisons les plus proches sont entre des éléments différents ^[44]). Les zones enrichies en CoCrNi proposées par Utt et al. ^[45] comme zones à fort piquage ont une énergie de cohésion approximative de 0,227 eV (en supposant une distribution équimolaire des éléments dans l'alliage - comme c'est le cas, cette valeur a été calculée comme la moyenne de l'énergie de cohésion des paires à partir des valeurs de Gröger et al. ^[44]).

Ainsi, lorsque les dislocations recréent des liaisons Mn, le point de pincement éventuel est affaibli jusqu'à ce qu'une nouvelle dislocation recrée une liaison plus forte ; et lorsque les dislocations rencontrent une liaison Fe ou une liaison Ni-Co, par exemple, la première constituera un obstacle plus fort à leur mouvement. Le LAL à liaison plus forte formant une zone enrichie en points d'épingle confirme également l'existence de FCL dans l'alliage CoCrFeMnNi.

Pour conclure cette section, cette étude aimerait mettre en évidence le processus développé par Zhang et al. ^[43] (analyse spatio-temporelle des données de gros grain), qui présente une technique avantageuse et plus détaillée pour identifier complètement les points de pincement, par rapport à la technique expérimentale présentée au début de cette section. Elle a permis de mieux comprendre les points de pincement et de conclure qu'ils sont le résultat d'amas atomiques qui, lorsqu'ils sont balayés par une dislocation, fluctuent en force, en raison de la nature atomique de ces amas. Ceci a permis de conclure à l'existence de FCL dans l'alliage CoCrFeMnNi.

4.3. Ordre à courte distance

Lorsqu'un système de glissement est activé dans une zone précédemment "vierge", il est généralement dirigé par une paire de dislocations parfaites (non dissociées). La paire de dislocations ouvre le chemin dans un système de glissement qui n'était pas actif auparavant. Ce phénomène se produit aussi bien à température ambiante qu'à température cryogénique. Cependant, il est plus récurrent à basse température (sur 26 grains différents analysés à TAL, 16 présentaient au moins une paire de dislocations en cours de déformation, soit une fréquence de 61,5%. En revanche, à TA, des paires de dislocations parfaites étaient présentes dans 11 des 30 grains étudiés lors de la déformation MET in situ, soit une occurrence de 36,7%). Quelques exemples sont présentés dans la Figure 20 (les parties (a) et (b) montrent les paires à TA, et (c) et (d) à TAL), en plus de ceux présentés précédemment dans le dernier chapitre.

Il faut remarquer que ces paires ne sont pas des partiels de Shockley largement dissociés, mais des dislocations parfaites complètes se déplaçant ensemble, l'une derrière l'autre (comme on le voit sur la figure précédente). Une fois que la paire se déplace sur une

certain distance, d'autres dislocations apparaissent, formant un empilement (en conservant toutefois l'espacement entre elles et la paire d'origine). Cela indique un ordre à courte distance (OCD - l'arrangement régulier et prévisible des atomes sur une courte distance, généralement avec un ou deux atomes d'espacement ^[46]).

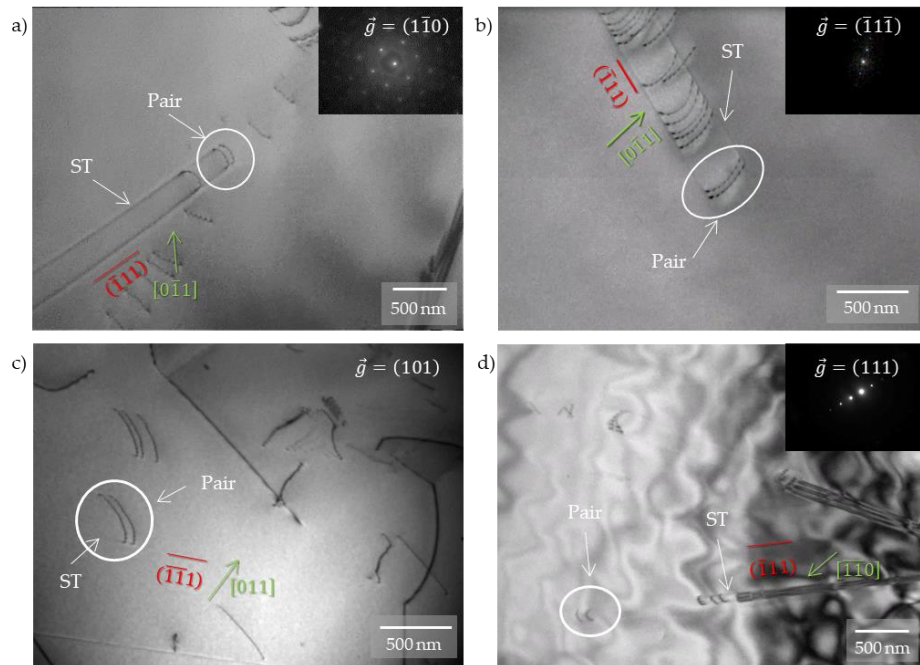


Figure 48 – Images MET champ clair de déformation in situ montrant des dislocations parfaites se déplaçant par paires à la tête d'un empilement (ou lors de l'activation du système de glissement). Toutes les images montrent les paires encadrées en blanc, les plans de glissement en rouge, les vecteurs de Burgers en vert et leurs \vec{g} correspondants. Les traces de glissement du pile-up ("ST") sont également indiquées en blanc. a) Échantillon X1-21, déformé à $T = 293$ K. b) Échantillon 35/I2-Head10, déformé à $T = 293$ K. c) Échantillon 35/I2-Head22, déformé à $T = 96$ K. d) Échantillon 35/I2-Head28, déformé à $T = 103$ K.

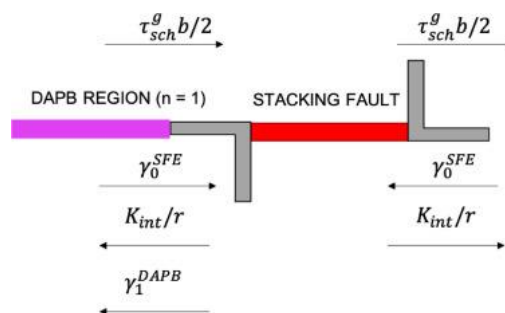


Figure 49 – Le bilan des forces sur chaque dislocation partielle associée à la dislocation de tête dans un réseau planaire en raison d'une contrainte de Schmid appliquée, de la EFE, de l'énergie FAD et de la répulsion élastique entre les dislocations partielles. D'après ^[49].

L'ordre à courte distance dans les alliages cfc a été lié à des morphologies planes de dislocation par glissement ^[47]. Le phénomène est généralement attribué à l'énergie d'une

frontière antiphase diffuse (FAD), qui se forme lorsque le mouvement des dislocations principales sur un plan de glissement diminue l'état d'OCD. L'énergie de la FAD donne lieu à une contrainte de friction athermique pour la dislocation principale, et à un effet de "ramollissement du plan de glissement" ^[47] pour les dislocations suivantes qui glissent sur le même plan de glissement après la destruction du OCD ^[48]. Les dislocations suivantes qui suivent la dislocation initiale subissent une barrière d'énergie plus faible en glissant sur le même chemin et en évitant la barrière d'énergie de la FAD ^[41]. Un tel effet sur les propriétés mécaniques peut avoir des implications profondes sur le comportement de déformation des solutions solides concentrées monophasiques, y compris les AHE ^[49].

Une frontière d'antiphase (FA) sépare deux domaines de la même phase ordonnée ^[50,51]. Elle résulte de la rupture de symétrie qui se produit pendant les processus d'ordonnement, qui peuvent commencer à différents endroits dans un réseau désordonné. Un APB se forme lorsque deux régions de ce type entrent en contact de sorte qu'elles présentent des liaisons de composition erronées à travers l'interface ^[52,53]. Lorsque la structure exacte de la région interphase n'est pas connue et, de plus, varie avec la teneur en soluté, on parle de frontière antiphase diffuse (FAD) ^[54].

L'application du premier raisonnement mathématique dans l'alliage CoCrFeMnNi n'est pas possible, car la force de frottement obtenue à partir d'un empilement parfait n'est pas encore connue. Cependant, dans le cas de ce travail, une approximation peut être obtenue en ne prenant en compte que la paire de dislocations parfaites (en les considérant comme isolées, car elles seules suffisent à surmonter la FAD). Cela signifie que $\gamma_0 = \gamma^{\text{FAD}}$, et que les autres variables ne s'appliquent pas lorsqu'on prend en considération les dislocations 0 et 1 (d'après les schémas ci-dessus et d'après les schémas de la Figure 21).

Les résultats de cette approximation sont donnés dans le tableau suivant, calculés pour la séparation ("d") entre les deux dislocations parfaites dans les exemples donnés à la Figure 20, en utilisant l'équation de calcul de la EFE du chapitre 3.

Calcul de l'énergie de la frontière d'antiphase diffuse.

Figure	T (K)	d (nm)	γ^{FAD} (mJ/m ²)
4-16 (a)	293	126 ± 8	3 ± 1
4-16 (b)	293	62 ± 4	5 ± 2
4-16 (c)	96	115 ± 6	3 ± 1
4-16 (d)	103	167 ± 7	2 ± 1
			3

En dehors de la déformation MET in situ, l'existence de l'OCD ne peut pas être facilement détectée avec d'autres techniques, car sa présence est révélée par des dislocations en mouvement au tout début de la plasticité. Une possibilité serait d'utiliser la tomographie par sonde atomique (TSA), qui offre la possibilité de réaliser des mesures d'imagerie 3D et de composition chimique à l'échelle atomique (résolution d'environ 0,1 à 0,3 nm en profondeur et 0,3 à 0,5 nm latéralement). Le couplage de cette technique à des expériences de déformation MET in situ pourrait conduire à l'identification des domaines OCD dans l'alliage CoCrFeMnNi, à condition que, lors de la déformation, les paires de dislocations parfaites se déplacent dans les zones "vierges" déjà cartographiées à l'aide de la TSA.

5. Conclusions et perspectives

5.1. Conclusions

Le message principal de ce travail est que la déformation MET in situ est une technique puissante pour accéder aux informations cristallographiques de l'échantillon, tout en observant / analysant le comportement des dislocations. En couplant cette technique avec des techniques de modélisation/simulation - comme l'approche d'exploration de données à gros grain présentée au chapitre 4 - les résultats obtenus sont plus précis. Comme les deux techniques sont basées sur le comportement des dislocations, elles permettent d'accéder à des domaines auparavant inaccessibles, comme la position des obstacles et la fluctuation de leur force, et aussi d'utiliser les dislocations pour sonder les propriétés mécaniques locales de l'alliage (par exemple, le CCRC ou le EFE local).

De l'analyse des différents grains qui présentaient des preuves d'OCD, deux observations principales ressortent :

- a) les paires de dislocations parfaites ont été observées plus fréquemment à des températures cryogéniques qu'à température ambiante, et
- b) dans la région "vierge" du cristal, il semble qu'aucun obstacle n'entrave le mouvement de la paire de dislocations - car elles parcourent une longue distance. Cependant, après leur passage, les dislocations suivantes qui glissent semblent rompre et reconstruire les liaisons atomiques. Le passage des dislocations modifie effectivement le paysage atomique local, créant des FCL qui conduisent à des zones enrichies en clusters qui agissent comme des zones enrichies en points d'accrochage plus forts (ou plus faibles).

La principale différence entre un alliage cfc classique et le CoCrFeMnNi est son caractère aléatoire :

- a) Caractère aléatoire du paysage atomique : présence d'un OCD au début de la plasticité qui est rompu après le glissement de deux dislocations parfaites, facilitant la

formation d'empilements de dislocations qui, en glissant, peuvent conduire à la formation de domaines FCL.

- b) Évolution aléatoire de la résistance des points de pincement (contrairement aux alliages conventionnels durcis par précipitation) en raison de la distorsion du réseau due aux FCL.

Toutes ces affirmations présentent la complexité du paysage atomique, qui change localement à chaque passage de dislocation. Les atomes ne sont pas réarrangés lorsque la température change, mais leur énergie cinétique est réduite en raison de la diminution de la température, ce qui augmente la force des obstacles (clusters) et limite le réarrangement local. Cette influence de la température, notamment dans l'apparition de paires de dislocations parfaites (OCD), conduit à plusieurs questions : la diffusion contribue-t-elle à restaurer un OCD local thermodynamiquement favorable ? Ou ce OCD est-il plus stable avec une T basse ? Des analyses plus poussées (hors de portée de ce travail, malheureusement) sont nécessaires pour comprendre l'effet des dislocations se déplaçant à travers ces domaines OCD locaux, et l'effet qu'elles peuvent également avoir sur le comportement des dislocations dans l'alliage CoCrFeMnNi.

5.2. Perspectives

Il est clair que le paysage atomique local influence grandement le comportement des dislocations et, par conséquent, des mécanismes de plasticité activés dans le CoCrFeMnNi. Une étude plus complète, couplant des expériences de déformation MET in situ avec des simulations numériques et des analyses chimiques, pourrait aider à élucider le véritable rôle de l'OCD et des FCL dans cet alliage.

Comme le montre la section 2 du chapitre 4, il est clair que les collaborations entre les méthodes expérimentales et numériques (comme cette étude, par exemple, dans le cadre du projet MuDiLingo) utilisant une approche d'exploration de données via les dislocations comme sondes pour remonter aux propriétés mécaniques et chimiques de l'alliage peuvent être une ligne de travail fructueuse. La combinaison des résultats obtenus à partir d'expériences de déformation MET in situ (ou d'autres essais de chargement) avec des simulations et/ou l'apprentissage automatique pour reproduire le comportement des dislocations dans différentes conditions permet de réaliser des simulations plus précises et d'obtenir des résultats dans des conditions autrement difficiles d'accès dans un dispositif expérimental.

Une analyse plus poussée du comportement des points d'épinglage à différentes températures pourrait être essentielle pour comprendre les propriétés mécaniques de cet alliage. Et des expériences MET in situ supplémentaires se concentrant sur le mouvement

des dislocations pour mieux comprendre le rôle des domaines FCL qui influencent les sauts à différentes températures pourraient être essentielles pour comprendre les mécanismes de plasticité, non seulement du CoCrFeMnNi, mais aussi d'autres alliages à éléments principaux multiples.

6. Références bibliographiques

- [1] B. Cantor, I. T. H. Chang, P. Knight, A. J. B. Vincent, *Mater. Sci. Eng. A* **2004**, 375–377, 213–218.
- [2] J. W. Yeh, S. K. Chen, S. J. Lin, J. Y. Gan, T. S. Chin, T. T. Shun, C. H. Tsau, S. Y. Chang, *Adv. Eng. Mater.* **2004**, 6, 299–303.
- [3] B. S. Murty, J. W. Yeh, S. Ranganathan, P. P. Bhattacharjee, in *High-Entropy Alloys*, Elsevier, **2019**, pp. 13–30.
- [4] A. Gali, E. P. George, *Intermetallics* **2013**, 39, 74–78.
- [5] E. P. George, D. Raabe, R. O. Ritchie, *Nat. Rev. Mater.* **2019**, 4, 515–534.
- [6] F. Otto, A. Dlouhý, Ch. Somsen, H. Bei, G. Eggeler, E. P. George, *Acta Materialia* **2013**, 61, 5743–5755.
- [7] B. Gludovatz, A. Hohenwarter, D. Catoor, E. H. Chang, E. P. George, R. O. Ritchie, *Science* **2014**, 345, 1153–1158.
- [8] N. L. Okamoto, S. Fujimoto, Y. Kambara, M. Kawamura, Z. M. T. Chen, H. Matsunoshita, K. Tanaka, H. Inui, E. P. George, *Sci Rep* **2016**, 6, 35863.
- [9] G. Laplanche, A. Kostka, O. M. Horst, G. Eggeler, E. P. George, *Acta Materialia* **2016**, 118, 152–163.
- [10] Z. Zhang, M. M. Mao, J. Wang, B. Gludovatz, Z. Zhang, S. X. Mao, E. P. George, Q. Yu, R. O. Ritchie, *Nature Communications* **2015**, 6, DOI 10.1038/ncomms10143.
- [11] H. Y. Diao, R. Feng, K. A. Dahmen, P. K. Liaw, *Curr. Opin. Solid State Mater. Sci.* **2017**, 21, 252–266.
- [12] J. A. Venable, *Philos. Mag.* **1961**, 6, 379–396.
- [13] J. W. Christian, S. Mahajan, *Prog. Mater. Sci.* **1995**, 39, 1–157.
- [14] M. A. Meyers, A. Mishra, D. J. Benson, *Progress in Materials Science* **2006**, 51, 427–556.
- [15] M. A. Meyers, O. Vöhringer, V. A. Lubarda, *Acta Materialia* **2001**, 49, 4025–4039.
- [16] T. M. Smith, M. S. Hooshmand, B. D. Esser, F. Otto, D. W. McComb, E. P. George, M. Ghazisaeidi, M. J. Mills, *Acta Materialia* **2016**, 110, 352–363.

- [17] Z. Zhang, H. Sheng, Z. Wang, B. Gludovatz, Z. Zhang, E. P. George, Q. Yu, S. X. Mao, R. O. Ritchie, *Nat Commun* **2017**, *8*, 14390.
- [18] S. Huang, W. Li, S. Lu, F. Tian, J. Shen, E. Holmström, L. Vitos, *Scripta Materialia* **2015**, *108*, 44–47.
- [19] S. Zhao, G. M. Stocks, Y. Zhang, *Acta mat.* **2017**, *134*, 334–345.
- [20] I. V. Kireeva, Y. Chumlyakov, Z. Pobedennaya, D. Kuksgauzen, I. Karaman, H. Sehitoglu, Tomsk, Russia, **2016**, p. 020090.
- [21] J. Ding, Q. Yu, M. Asta, R. O. Ritchie, *Proc. Natl. Acad. Sci. USA* **2018**, *115*, 8919.
- [22] A. J. Zaddach, C. Niu, C. C. Koch, D. L. Irving, *JOM* **2013**, *65*, 1780–1789.
- [23] N. Bernstein, E. B. Tadmor, *Phys. Rev. B* **2004**, *69*, 094116.
- [24] E. B. Tadmor, N. Bernstein, *J. Mech. Phys. Solids* **2004**, *52*, 2507–2519.
- [25] E. P. George, W. A. Curtin, C. C. Tasan, *Acta mat.* **2020**, *188*, 435–474.
- [26] F. X. Zhang, S. Zhao, K. Jin, H. Xue, G. Velisa, H. Bei, R. Huang, J. Y. P. Ko, D. C. Pagan, J. C. Neufelnd, W. J. Weber, Y. Zhang, *Phys. Rev. Lett.* **2017**, *118*, 205501.
- [27] D. Oliveros, A. Fraczkiewicz, A. Dlouhy, C. Zhang, H. Song, S. Sandfeld, M. Legros, *Mat. Chem. Phys.* **2021**, *272*, 124955.
- [28] D. Oliveros, M. Legros, D. Lamirault, *In Situ TEM Tensile Specimen Preparation*, **2019**.
- [29] A. Coujou, Ph. Lours, N. A. Roy, D. Caillard, N. Clement, *Acta metall. mater.* **1990**, *38*, 825–837.
- [30] A. Rajabzadeh, Etude Expérimentale et Théorique de La Migration de Joints de Grains, Couplée à Un Cisaillement, Université Toulouse III Paul Sabatier, **2013**.
- [31] Q. Ding, X. Fu, D. Chen, H. Bei, B. Gludovatz, J. Li, Z. Zhang, E. P. George, Q. Yu, T. Zhu, R. O. Ritchie, *Materials Today* **2019**, *25*, 21–27.
- [32] I. V. Kireeva, Y. I. Chumlyakov, Z. V. Pobedennaya, I. V. Kuksgausen, I. Karaman, *Materials Science & Engineering A* **2017**, *705*, 176–181.
- [33] F. D. León-Cázares, C. M. F. Rae, *Crystals* **2020**, *10*, 445.
- [34] S. M. Copley, B. H. Kear, *Acta Metallurgica* **1968**, *16*, 227–231.
- [35] B. Beausir, J.-J. Fundenberger, *ATEX*, Université De Lorraine, Metz, France, **2017**.
- [36] S. Liu, Y. Wei, *Extreme Mech. Lett.* **2017**, *11*, 84–88.
- [37] Q. Ding, Y. Zhang, X. Chen, X. Fu, D. Chen, S. Chen, L. Gu, F. Wei, H. Bei, Y. Gao, M. Wen, J. Li, Z. Zhang, T. Zhu, R. O. Ritchie, Q. Yu, *Nature* **2019**, *574*, 223–227.

- [38] Z. Lei, X. Liu, Y. Wu, H. Wang, S. Jiang, S. Wang, X. Hui, Y. Wu, B. Gault, P. Kontis, D. Raabe, L. Gu, Q. Zhang, H. Chen, H. Wang, J. Liu, K. An, Q. Zeng, T.-G. Nieh, Z. Lu, *Nature* **2018**, *563*, 546–550.
- [39] G. Laplanche, P. Gadaud, O. Horst, F. Otto, G. Eggeler, E. P. George, *Journal of Alloys and Compounds* **2015**, *623*, 348–353.
- [40] A. Haglund, M. Koehler, D. Catoor, E. P. George, V. Keppens, *Intermetallics* **2015**, *58*, 62–64.
- [41] R. Zhang, S. Zhao, J. Ding, Y. Chong, T. Jia, C. Ophus, M. Asta, R. O. Ritchie, A. M. Minor, *Nature* **2020**, *581*, 283–287.
- [42] M. Laurent-Brocq, A. Akhatova, L. Perrière, S. Chebini, X. Sauvage, E. Leroy, Y. Champion, *Acta mat.* **2015**, *88*, 355–365.
- [43] C. Zhang, H. Song, D. Oliveros, A. Fraczkiewicz, M. Legros, S. Sandfeld, *Acta mat.* [Submitted for publication] **2022**.
- [44] R. Gröger, V. Vitek, A. Dlouhý, *Modelling Simul. Mater. Sci. Eng.* **2020**, *28*, 075006.
- [45] D. Utt, S. Lee, A. Stukowski, S. H. Oh, G. Dehm, K. Albe, *arXiv:2007.11489 [cond-mat, physics:physics]* **2020**.
- [46] F. J. Owens, C. P. J. Poole, *The Physics and Chemistry of Nanosolids*, John Wiley & Sons, **2008**.
- [47] V. Gerold, H. P. Karnthaler, *Acta Metallurgica* **1989**, *37*, 2177–2183.
- [48] A. Abu-Odeh, D. L. Olmsted, M. Asta, *Scripta Materialia* **2022**, *210*, 114465.
- [49] A. Abu-Odeh, M. Asta, *Acta mat.* **2022**, *226*, 117615.
- [50] R. Kikuchi, J. W. Cahn, *Acta metall.* **1979**, *27*, 1337–1353.
- [51] M. J. Marcinkowski, *Electron Microscopy and Strength of Crystals*, John Wiley, New York, USA, **1963**.
- [52] F. Zhu, P. Haasen, R. Wagner, *Acta metall.* **1986**, *34*, 457–463.
- [53] J. M. Howe, in *Physical Metallurgy* (Eds.: D.E. Laughlin, K. Hono), Elsevier, Oxford, **2014**, pp. 1317–1451.
- [54] J. E. Krzanowski, S. M. Allen, *Surf. Sci.* **1984**, *144*, 153–175.